The Dissertation Committee for Yubing Wang Certifies that this is the approved version of the following dissertation:

PROBABILISTIC ASSESSMENTS OF THE SEISMIC STABILITY OF SLOPES: IMPROVEMENTS TO SITE-SPECIFIC AND REGIONAL ANALYSES

Committee:

Ellen M. Rathje, Supervisor

Brady R. Cox

Robert B. Gilbert

Lance Manuel

Jennifer A. Miller

PROBABILISTIC ASSESSMENTS OF THE SEISMIC STABILITY OF SLOPES: IMPROVEMENTS TO SITE-SPECIFIC AND REGIONAL ANALYSES

by

Yubing Wang, B.E.; M.S.E.

Dissertation

Presented to the Faculty of the Graduate School of

The University of Texas at Austin

in Partial Fulfillment

of the Requirements

for the Degree of

Doctor of Philosophy

The University of Texas at Austin

May 2014

To My Beloved Wife and Parents…

Acknowledgements

I would like to give my highest gratitude and respect to Dr. Ellen M. Rathje, who has been my supervisor over the last five years. Her encouragement, support, and guidance let me advance along the path of knowledge. She is not only my academic advisor but also my life mentor. Her passion, enthusiasm, and kindness positively influence my personality. Her significant contribution of time and knowledge to this dissertation is gratefully acknowledged.

I would like to greatly thank my dissertation committee Dr. Bray R. Cox, Dr. Robert B. Gilbert, Dr. Lance Manuel, and Dr. Jennifer A. Miller for their valuable feedback on this dissertation. Dr. Gilbert inspired me to think from the engineering perspective when I was learning theories in his classes. Dr. Miller and Dr. Manuel considerably broadened my knowledge in their fields of study. Dr. Cox provided very valuable comments on my study.

I would like to thank Dr. Randall M. Jibson at the USGS, for the beneficial technical discussions with him. I also want to thank Fugro Consultants Inc. for the data used in this study, and I am glad that I will work for this company after my graduation.

Financial support for part of this dissertation was provided by the USGS, Department of the Interior, under grant G12AP20083. This support is greatly acknowledged. The Department of Physics at the University of Texas at Austin offered teaching assistantship to me. I sincerely appreciate this opportunity which financially supported my study and improved my oral communication in English.

I also want to thank my friends for brightening my life during the past five years in Austin. In this foreign country, the days that I spent with all of you filled my life with pleasure and happiness.

Last, but never the least, I would like to give my greatest appreciation and love to my wife and parents for their unconditional encouragement, support and love. My parents never doubted me and always supported me. My beloved wife, Ying Lai, came into my life during the darkest days, and she made every day after bright and cheerful.

PROBABILISTIC ASSESSMENTS OF THE SEISMIC STABILITY OF SLOPES: IMPROVEMENTS TO SITE-SPECIFIC AND REGIONAL ANALYSES

Yubing Wang, Ph.D.

The University of Texas at Austin, 2014

Supervisor: Ellen M. Rathje

Abstract: Earthquake-induced landslides are a significant seismic hazard that can generate large economic losses. Predicting earthquake-induced landslides often involves an assessment of the expected sliding displacement induced by the ground shaking. A deterministic approach is commonly used for this purpose. This approach predicts sliding displacements using the expected ground shaking and the best-estimate slope properties (i.e., soil shear strengths, ground water conditions and thicknesses of sliding blocks), and does not consider the aleatory variability in predictions of ground shaking or sliding displacements or the epistemic uncertainties in the slope properties.

In this dissertation, a probabilistic framework for predicting the sliding displacement of flexible sliding masses during earthquakes is developed. This framework computes a displacement hazard curve using: (1) a ground motion hazard curve from a probabilistic seismic hazard analysis, (2) a model for predicting the dynamic response of the sliding mass, (3) a model for predicting the sliding response of the sliding mass, and (4) a logic tree that incorporates the uncertainties in the various input parameters. The developed probabilistic framework for flexible sliding masses is

applied to a slope at a site in California. The results of this analysis show that the displacements predicted by the probabilistic approach are larger than the deterministic approach due to the influence of the uncertainties in the slope properties. Reducing these uncertainties can reduce the predicted displacements.

Regional maps of seismic landslide potential are used in land-use planning and to identify zones that require detailed, site-specific studies. Current seismic landslide hazard mapping efforts typically utilize deterministic approaches to estimate rigid sliding block displacements and identify potential slope failures. A probabilistic framework that uses displacement hazard curves and logic-tree analysis is developed for regional seismic landslide mapping efforts. A computationally efficient approach is developed that allows the logic-tree approach to be applied for regional analysis. Anchorage, Alaska is used as a study area to apply the developed approach. With aleatory variability and epistemic uncertainties considered, the probabilistic map shows that the area of high/very high hazard of seismic landslides increases by a factor of 3 compared with a deterministic map.

Table of Contents

List of Tables

List of Figures

Chapter 1 Introduction

1.1 RESEARCH SIGNIFICANCE

A landslide is the downslope movement of soil or rock materials (i.e., sliding mass). Most slopes are stable under static conditions, but when an earthquake occurs the seismically-induced ground shaking is often sufficient to cause failures of slopes which were marginally to moderately stable under static conditions.

Tremendous amounts of damage have been caused by earthquake-induced landslides in previous earthquakes. In some earthquakes, landslides have been responsible for more than half of the total damage caused by all the seismic hazards. In the 1964 Alaska earthquake, earthquake-induced landslides caused an estimated 56% of the total cost of damage (Youd 1978, Wilson and Keefer 1985). More than half of all deaths in large (M>6.9) earthquakes in Japan between 1964 and 1980 were caused by seismic landslides (Kobayashi 1981). The 1920 Haiyuan earthquake (M=8.5) in the Ningxia Province of China induced hundreds of large landslides, which took away 100,000 lives (Close and McCormick 1922). Predicting earthquake-induced landslides is essential for reducing losses of lives and properties caused by earthquakes, thus it is an important activity for geotechnical engineers.

Predicting earthquake-induced landslides often involves an assessment of the expected sliding displacement induced by the ground shaking. The current deterministic approach predicts sliding displacements using the expected ground shaking and the best-

estimate slope properties (i.e., soil shear strengths, ground water conditions and thicknesses of sliding blocks). In the deterministic approach, neither the aleatory variability in predictions of ground shaking or sliding displacement nor the epistemic uncertainties in the slope properties are considered. Such aleatory variability and epistemic uncertainties have significant influence on the predicted seismic performance of slopes, and should be taken into account to properly evaluate the seismic risk associated with earthquake-induced landslides. Rathje and Saygili (2008) proposed a probabilistic approach using displacement hazard curves to deal with the aleatory variability, and they introduced a logic-tree analysis for slope properties to take epistemic uncertainties into account (Rathje and Saygili 2009). However, this probabilistic approach is based on a rigid sliding block analysis, which assumes the sliding mass is a rigid block sliding on a plane and ignores the dynamic response of deep/soft soil masses.

In this dissertation, a probabilistic framework for predicting the sliding displacement of flexible sliding masses during earthquakes is developed. This framework computes a displacement hazard curve using: (1) a ground motion hazard curve from a probabilistic seismic hazard analysis, (2) a model for predicting the dynamic response of the sliding mass, (3) a model for predicting the sliding response of the sliding mass, and (4) a logic tree that incorporates the uncertainties in the various input parameters. After developing the framework, the practical implementation of the approach is demonstrated through application to an actual site in California. This example demonstrates how the developed framework can be implemented using existing ground motion hazard information from the U.S. Geological Survey and conventional geotechnical site characterization. The influence of different sources of uncertainty are explored through this example.

On a regional scale, the locations of potential seismic landslides across a region can be mapped through the computation of sliding displacements. Seismic landslide hazard maps are used in land-use planning and emergency-response planning, and to identify zones that require detailed, site-specific studies. The United States Geological Survey (USGS) and California Geological Survey (CGS) have been creating seismic landslide hazard maps (e.g., Jibson et al. 2000, McCrink 2001) by assigning hazard categories across areas based on displacements computed using the deterministic approach. Yet there are significant uncertainties regarding the input parameters used to predict displacement, particularly when applied at a regional scale. In this dissertation, a logic-tree approach that describes the epistemic uncertainties in the slope properties is used to incorporate uncertainty into the regional mapping of seismic landslide hazard. The direct application of the logic-tree approach is very time-consuming for regional mapping, thus this dissertation develops an efficient computational scheme (i.e., the Mean λ_D Threshold approach) that allows the logic-tree approach to be applied more easily to regional analysis. As a result, we develop a practical approach to rigorously incorporating variability and uncertainty into seismic landslide hazard mapping without significantly increasing the computational complexity compared with the deterministic approach. Anchorage, Alaska is selected as a study area to demonstrate the logic-tree approach. The application of the approach to a real study area allows the influence of different sources of uncertainty on the seismic landslide hazard map to be quantified, and it allows for a comparison with various deterministic approaches.

1.2 SCOPE OF RESEARCH

This dissertation focuses on the development of probabilistic analysis to predict the earthquake-induced sliding displacements of flexible slopes and the improvement of probabilistic seismic landslide hazard mapping.

Chapter 1 briefly discusses the significance of modeling earthquake-induced landslides and the current approaches to site-specific and regional analyses.

Chapter 2 introduces sliding displacements for the evaluation of seismic landslide potential. The sliding resistance of a slope is characterized as a yield acceleration, which can be computed through a seismic slope stability analysis. An infinite slope model is adopted for shallow landslides, and slice methods are used to perform the seismic slope stability analysis for deep failures. Empirical models for rigid and flexible sliding displacements are presented along with supplemental empirical models for the seismic loading parameters and mean period of ground motion.

Chapter 3 presents the current deterministic and probabilistic approach to predicting sliding displacements. The dynamic response of flexible sliding masses is investigated and compared with the behavior of rigid sliding blocks. The probabilistic approach is extended to flexible sliding masses by considering the dynamic response. A logic-tree analysis is introduced to incorporate epistemic uncertainties in shear strengths, as well as the aleatory variability in the prediction of the mean period of the ground motion.

Chapter 4 demonstrates the application of the probabilistic framework for flexible sliding displacements. The Lexington Elementary School site, located in a region with frequent seismic activity, is selected to perform the probabilistic analysis. The interpolation of shear strength data, the calculation of yield accelerations, and the

specification of the ground motion hazard are discussed to construct a logic tree. The importance of uncertainties is revealed by exploring the influence of the logic-tree analysis on the dynamic response and sliding displacements.

Chapter 5 first reviews the current seismic landslide mapping procedures using the deterministic approach and through displacement hazard curves. The procedure to create a logic tree for regional mapping based on epistemic uncertainties in slope properties and among empirical displacement models is discussed. The Mean λ_D Threshold approach is developed to reduce the heavy loads of computation required to implement the regional logic-tree analysis.

Chapter 6 describes the application of the probabilistic seismic landslide hazard mapping approach developed in Chapter 5. Anchorage, Alaska, which has a significant seismic hazard from crustal faults and a subduction zone, is selected as the study area. The topography, geology, ground water conditions and ground motion hazard are described and characterized to determine the values and associated weights used in the logic-tree analysis. The results show the significance of logic-tree analysis for regional mapping.

Chapter 7 presents the conclusions of this dissertation, and discusses future improvements on the study of this dissertation.

Chapter 2 Evaluating Seismic Landslide Potential

2.1 INTRODUCTION

Under static conditions, a landslide/slope failure occurs when a slope is "permanently" destabilized by extra driving forces and/or reduced shear strengths that are commonly due to increased pore water pressures. During an earthquake, extra driving forces are applied to the slope due to the inertial forces related to earthquake shaking. The inertial forces vary with time in the same way that acceleration with time during earthquake shaking. Although the maximum seismic loading during earthquake shaking may exceed the shear strength of the soil, the exceedance of the strength may occur for only a short time and the cumulative deformation of the sliding mass may not be large enough to cause considerable damage.

The first efforts for estimating the influence of seismic shaking on slopes were initiated in the 1950s. Terzaghi (1950) developed a static limit-equilibrium analysis based on adding an earthquake force to the sliding mass. His concept was so valuable that it was widely known and accepted as pseudo-static analysis (Jibson 2011). A few years later the finite element method (FEM), which is also known as stress-deformation analysis, was developed and applied to the computation of permanent deformation in the soil mass. However, finite element analysis requires much more detailed information on the soil properties and site conditions such that, even today, it is only performed for important projects by well-trained engineers. To bridge the gap between these two types

of analyses, Newmark (1965) proposed a rigid sliding block analysis for assessing the sliding displacement and failure of slopes during earthquakes. In this approach, accelerations that are greater than the yield acceleration result in downslope movement of a slope mass. The yield acceleration (k_y), when multiplied by the mass of the sliding mass, represents the horizontal destabilizing force that results in a factor of safety of 1.0. The yield acceleration can be computed through a pseudo-static slope stability analysis. Acceleration-time histories are required for the computation of cumulative sliding displacements during the ground shaking. The magnitude of sliding displacement relates well with observations of seismic performance of slopes (e.g., Jibson et al. 2000), and thus has been a useful parameter in seismic design and hazard assessment. Since the development of the rigid sliding block approach in the 1960s, it has been extended to flexible sliding masses.

This chapter introduces the limit equilibrium analyses used to compute the k_y required for sliding displacement analyses. The procedures to estimate sliding displacements for rigid and flexible sliding masses are also presented.

2.2 SEISMIC SLOPE STABILITY ANALYSIS

Under static conditions, the factor of safety (FS_{static}) is used to evaluate slope stability. The factor of safety is calculated from the force and/or moment equilibrium of a potential failure surface. The factor of safety is defined as the ratio of shear strength to the equilibrium shear stresses on the potential failure surface. A stable slope has a static factor of safety greater than 1.0. A failure occurs when the static factor of safety drops

below 1.0 and it cannot reach above 1.0 until the failure stops and a new force/moment equilibrium is established,

During an earthquake, the soil mass on a slope experiences inertial forces due to the ground shaking. The seismic loading force can be represented by the mass of the soil (W/g) multiplied by a seismic coefficient (k), $F = k \cdot W/g$. The seismic coefficient varies with time in much the same way as an earthquake acceleration-time history. If the maximum seismic loading force exceeds the sliding resistance of the slope, the seismic factor of safety ($FS_{seismic}$) falls below 1.0. However, the time during which $FS_{seismic}$ is less than 1.0 may be small and failure may not occur. Therefore, $FS_{seismic}$ may not be the best representation of the seismic stability of a slope. Instead the sliding displacement induced by the seismic loading provides a better assessment of the seismic performance of slopes. The computation of sliding displacements requires the yield acceleration k_y to characterize the sliding resistance. k_y represents the seismic loading that initiates instability and is equal to the seismic coefficient that produces $FS_{seismic} = 1.0$. A pseudo-static analysis, which assumes the seismic loading as a static force, is performed to calculate k_y.

In natural slopes, a common failure mode for seismic landslides is a thin, veneer slope failure (Keefer 2002). Jibson (2011) noted that about 90% of earthquake-induced landslides are shallow slides and falls in rock and debris. Considering various studies, the depth of shallow seismic landslides has been defined as: (1) about 1 to 2 m (Kieffer et al. 2006, Parise and Jibson 2000), (2) about 1 to 5 m (Harp and Jibson 1996), and (3) less than 3 m (Keefer 1984, 1999 and 2002). Jibson et al. (2000) used a thickness (t) of 2.4 m (8 ft) for a seismic landslide hazard map in Southern California, which was representative of typical failures in the 1994 Northridge earthquake. In this case, the depth of the failure surface (typically several meters) is much smaller than the length of

the slope failure (dozens of meters to hundreds of meters) and an infinite slope model can be used to assess the stability of the slope.

Figure 2.1 shows an infinite slope model for static conditions. W is the weight of the failure block, σ and τ are the normal and shear stresses on the failure surface, c' is the effective cohesion, ϕ' is the effective friction angle, γ is the material unit weight, γ_w is the unit weight of water, α is the slope angle, *t* is the slope-normal thickness of the rigid block, and *m* is the proportion of the block thickness that is saturated and thus represents pore water pressure. The static Factor of Safety can be expressed as:

$$FS_{static} = \frac{c' + (\gamma - m \cdot \gamma_w) \cdot t \cos\alpha \cdot \tan\phi'}{\gamma \cdot t \cdot \sin\alpha} = \frac{c'}{\gamma \cdot t \cdot \sin\alpha} + \frac{\tan\phi'}{\tan\alpha}\left(1 - m \cdot \frac{\gamma_w}{\gamma}\right) \qquad (2.1)$$

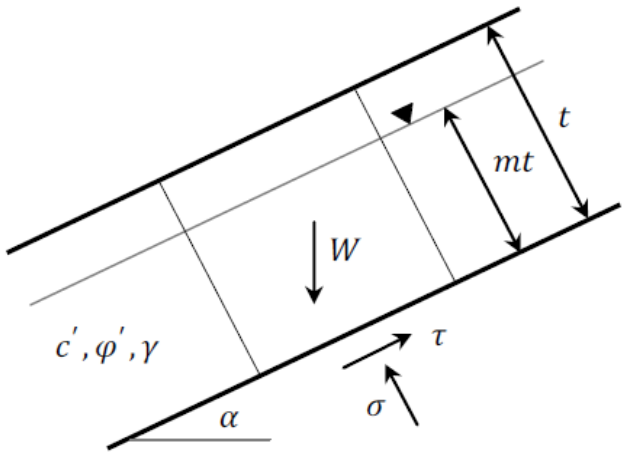

Figure 2.1 Infinite Slope Model under Static Condition

By assuming ground shaking parallel to the slope, the yield acceleration that produces $FS_{seismic} = 1.0$ can be calculated as:

$$FS_{seismic} = \frac{c' + (\gamma - m \cdot \gamma_w) \cdot t\cos\alpha \cdot \tan\phi'}{\gamma \cdot t \cdot \sin\alpha + \gamma \cdot t \cdot k_y/g} = 1.0$$

$$k_y = (FS_{static} - 1)g \cdot \sin\alpha \quad (2.2)$$

where g is the acceleration of gravity. The ground shaking can also be assumed as horizontal, but in most cases the resulting yield acceleration only has a small difference (Saygili, 2008).

The yield acceleration is calculated by using the static factor of safety derived from an effective stress analysis of the infinite slope model. However, the effective stress analysis under seismic conditions requires the knowledge of excess pore water pressures generated by the seismic loading on the failure surface. For gravels and coarse sands, no excess pore water pressure is built up due to the rapid drainage of soils. For silts and clays, undrained shear strengths with zero friction angles are used in Equation 2.1, so that a total stress analysis is performed and the excess pore water pressures are not required for the FS_{static} calculation. For fine sands, soil liquefaction can be triggered if the high excess pore water pressures are established, but the liquefaction mechanism is beyond the scope of this dissertation.

Seismic landslides can also occur as deep rotational/translational slides. Softer/deeper soil masses typically have deeper failures, and the failure depth can be up to dozens of meters. Keefer (1984) describes common deep failures (depth > 3 m) as coherent slides, including rock and soil slumps, rock and soil block slides, and some slow earth flows. Harp and Jibson (1996) found that deep, coherent landslides (depth > 5 m) triggered by the 1994 Northridge Earthquake were far less numerous than shallow landslides, but their contribution to the total volume of landslide materials is significant

due to their much larger volume per slide. Limit equilibrium analyses of circular and/or non-circular failure surfaces are required to evaluate the factor of safety of these types of failures. Many methods of slices (e.g., Spencer 1967) have been developed for the analysis of these types of failure surfaces. In these approaches, the soil mass sitting on a failure surface is divided into slices (Figure 2.2), and force and/or moment equilibriums are satisfied in each slice. For seismic conditions, a seismic force is applied to each slice based on the seismic coefficient and weight of the slice. The yield acceleration is the seismic coefficient that produces $FS_{seismic} = 1.0$ under the pseudo-static condition (i.e., the seismic loading is applied as a static force on the soil mass).

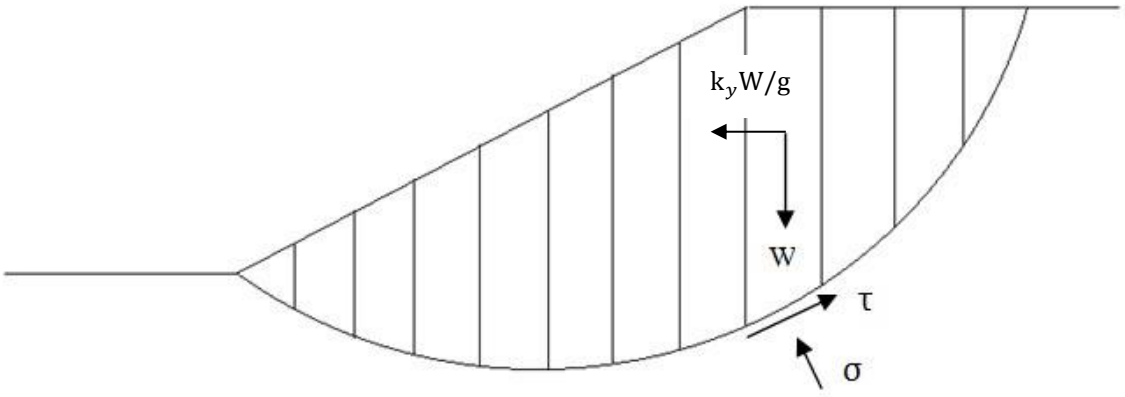

Figure 2.2 Slices of a slope under pseudo-static conditions

2.3 SLIDING BLOCK DISPLACEMENTS

Sliding block displacements are computed for a given yield acceleration (k_y) and earthquake ground motion. For rigid sliding block analysis, the slope is considered a rigid block sitting on a base (i.e. failure surface). Given an acceleration-time history, sliding starts when the acceleration-time history exceeds the yield acceleration and it continues until the relative velocity between the sliding block and base drops back to zero. Figure 2.3 shows a schematic of the rigid sliding block analysis. At point X, where the ground acceleration reaches the level of the yield acceleration, sliding starts. The relative acceleration between the base and k_y is numerically integrated to obtain the relative velocity, and the relative velocity is numerically integrated to obtain the relative sliding displacement. At point Y, the ground acceleration decreases to the k_y level, but the sliding does not stop due to non-zero relative velocity. At point Z, the relative velocity becomes zero and sliding stops. Sliding is triggered each time the ground acceleration exceeds the k_y level. To calculate the relative displacement between the sliding block and base for the entire time history, the relative acceleration-time is integrated twice with respect to time in the ranges when sliding occurs.

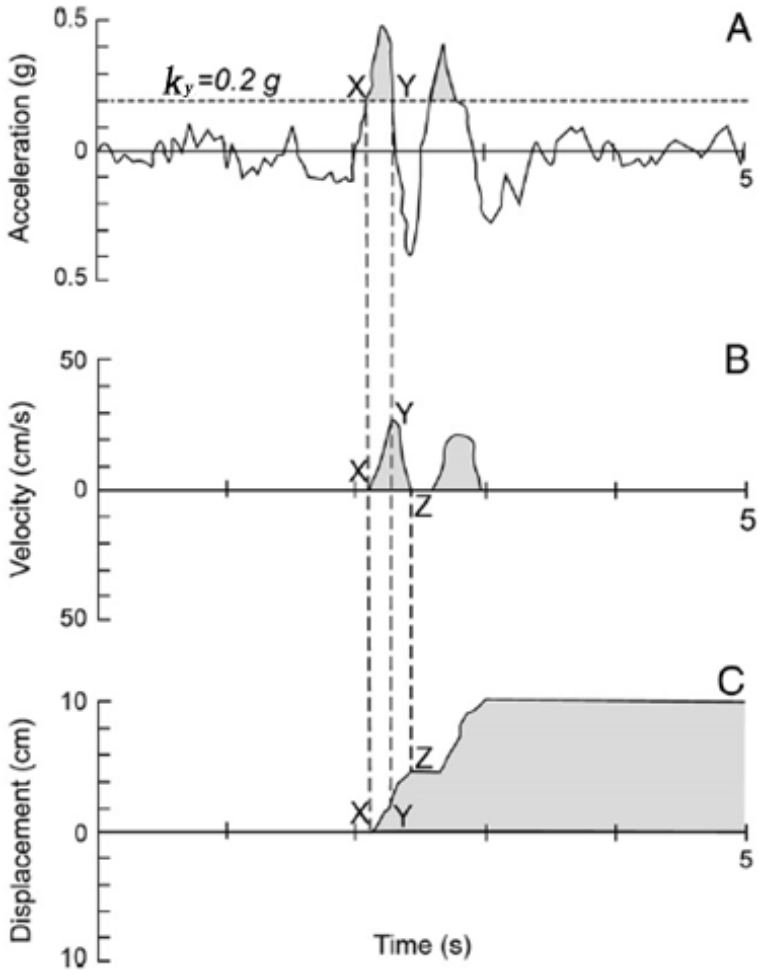

Figure 2.3 Illustration of rigid sliding block analysis (adapted from Wilson and Keefer 1983 by Jibson et al. 2000)

The rigid sliding block assumption is good for computing sliding displacements of shallow landslides, because the seismic behaviors at different depths only have negligible difference within the thin soil mass. Therefore the seismic coefficient (k)-time histories of shallow soil masses can be assumed the same as the input acceleration-time histories on the base (Figure 2.4a). However, such assumption is not appropriate for deeper and/or softer sliding masses, which behave as flexible bodies subjected to high

frequency input signals (Figure 2.4b). The dynamic response of flexible sliding masses must be taken into account for the computation of flexible sliding displacements through a decoupled sliding block analysis (e.g., Makdisi and Seed 1978). In this analysis, the seismic loading force induced by the spatially variable accelerations within the sliding mass at any time is represented by an equivalent, average seismic coefficient, k (Figure 2.4b). The k-time history can be computed from dynamic analysis of the sliding mass and this k-time history is used in the sliding block analysis to predict displacements.

The dynamic response of flexible sliding masses can be computed through two-dimensional (2-D) finite element analysis. Alternatively, modeling the sliding mass as a one-dimensional (1-D) soil column can provide an adequate estimate of the seismic loading for flexible sliding masses (Rathje and Bray 2001, Vrymoed and Calzascia 1978). This 1-D modeling simplification is convenient for computing the average k-time history of a flexible sliding mass from an input acceleration-time history.

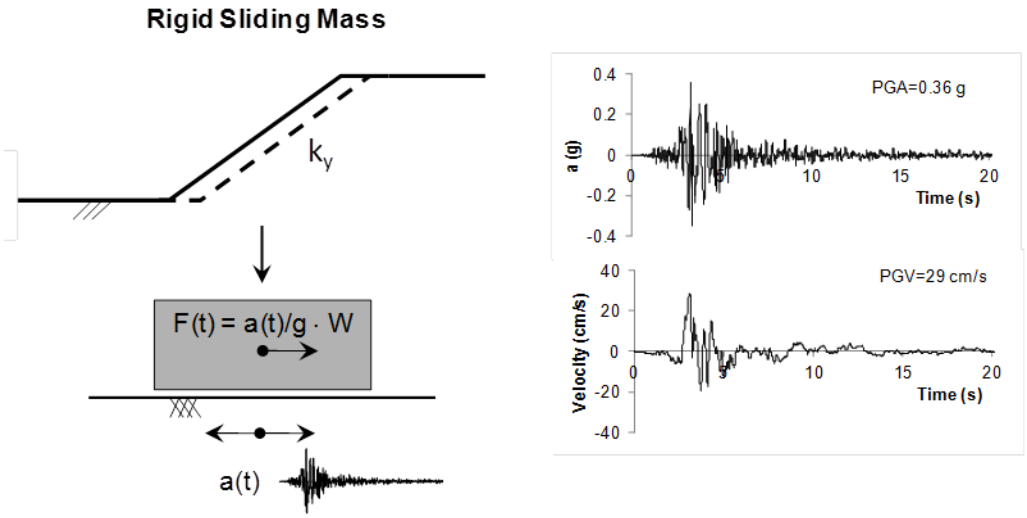

(a)

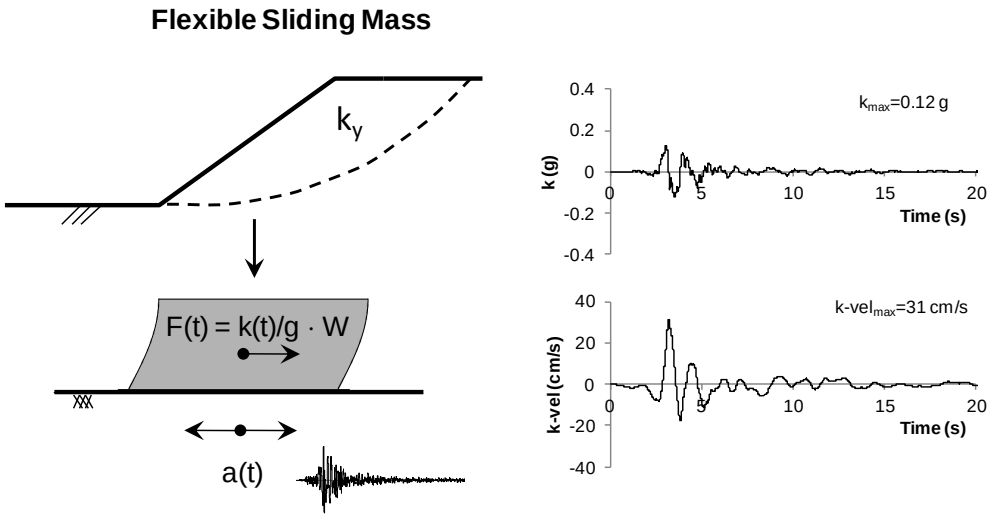

(b)

Figure 2.4 Seismic loading for (a) rigid sliding masses and (b) flexible sliding masses (Rathje et al. 2013)

2.4 EMPIRICAL MODELS FOR RIGID SLIDING DISPLACEMENT

Sliding block analysis requires the yield acceleration of a slope and the acceleration-time history at a site. Because of the variable nature of earthquake ground motions, a suite of at least 7 to 10 acceleration-time histories are commonly used for analysis. However, the identification, selection, and scaling of appropriate acceleration-time histories is a difficult and time-consuming process. Instead of directly using acceleration-time histories to predict rigid sliding block displacements, many empirical models have been proposed in the past decades for computing sliding block displacements based on various characteristics of ground shaking and the yield acceleration. Theses empirical displacement models are from the regression analysis of thousands of cases in which the complete sliding block analysis was conducted.

Ground motion parameters (GMs), such as Peak Ground Acceleration (PGA), Peak Ground Velocity (PGV), mean period of ground motion (T_m) and Arias Intensity (I_a), have been used individually or in combination to represent the level of ground shaking in empirical displacement models. The general form of an empirical displacement model is expressed as:

$$\ln(D) = f(\mathbf{k}_y, \text{GMs}) \tag{2.3}$$

Here, the natural logarithm of the predicted sliding displacement (D) is a function of the yield acceleration and the ground motion parameters (GMs). The most commonly available ground motion parameters for seismic hazard predictions are PGA, response spectral acceleration, and PGV. Bray and Travasarou (2007), Jibson (2007), and Rathje and Saygili (2009) have proposed empirical displacement models for rigid sliding masses

that use PGA to represent the level of ground shaking and earthquake magnitude (M) to provide an indirect measure of frequency content. Because only one ground motion parameter is used in these models, they are considered scalar models. If more than one ground motion parameter is included in an empirical model, the standard deviation (i.e., variability) of the predicted sliding displacement can be significantly reduced (Saygili and Rathje 2008). Saygili and Rathje (2008) proposed a rigid sliding block model using PGA and PGV as the ground motion parameters, and such a model is a vector model. Jibson (2007) proposed vector models using PGA and I_a.

Four empirical displacement models are used to compute rigid sliding displacements in following chapters: Bray and Travasarou (2007, BT07), Jibson (2007, J07), Rathje and Saygili (2009, RS09), and Saygili and Rathje (2008, SR08). The three scalar models (BT07, J07 and RS09) and one vector model (SR08) are expressed as:

J07	$\log D = -2.710 + \log\left[\left(1 - \frac{k_y}{PGA}\right)^{2.335}\left(\frac{k_y}{PGA}\right)^{-1.478}\right] + 0.424 \cdot M$ $\sigma_{\log D} = 0.454$ (2.4a)
BT07	$P[D = 0] = 1 - \Phi(-1.76 - 3.22\ln(k_y) + 3.52\ln(PGA))$ $\ln D = -0.22 - 2.83\ln(k_y) - 0.333(\ln(k_y))^2 + 0.566\ln(k_y)\ln(PGA)$ $+3.04\ln(PGA) - 0.244(\ln(PGA))^2 + 0.278(M - 7)$ $\sigma_{\ln D} = 0.66$ (2.4b)

RS09	$\ln D = 4.89 - 4.85\left(\frac{k_y}{PGA}\right) - 19.64\left(\frac{k_y}{PGA}\right)^2 + 42.49\left(\frac{k_y}{PGA}\right)^3 - 29.06\left(\frac{k_y}{PGA}\right)^4 + 0.72\ln(PGA) + 0.89(M-6)$ $\sigma_{\ln D} = 0.732 + 0.789\left(\frac{k_y}{PGA}\right) - 0.539\left(\frac{k_y}{PGA}\right)^2$ (2.4c)
SR08	$\ln D = -1.56 - 4.58\left(\frac{k_y}{PGA}\right) - 20.84\left(\frac{k_y}{PGA}\right)^2 + 44.75\left(\frac{k_y}{PGA}\right)^3 - 30.50\left(\frac{k_y}{PGA}\right)^4 - 0.64\ln(PGA) + 1.55\ln(PGV)$ $\sigma_{\ln D} = 0.405 + 0.524\left(\frac{k_y}{PGA}\right)$ (2.4d)

where D is the rigid sliding displacement in units of cm, PGA and k_y are in units of g, and PGV is in units of cm/s. The BT07 model requires one first to calculate the probability of zero displacement (P[D = 0]), then the calculated D value is conditional on the probability of non-zero displacement (P[D > 0]).

Figure 2.5 plots the displacement predicted by each of the four models as a function of k_y for deterministic ground motions representing M = 7.5 and a distance of 5 km. Using a ground motion prediction equation for rock conditions, the corresponding median PGA is 0.35 g and PGV is 42 cm/s. For all of the models, the predicted sliding displacement decreases with increasing yield acceleration. However, at any given value of k_y the displacements predicted by the various models vary by a factor of 3.

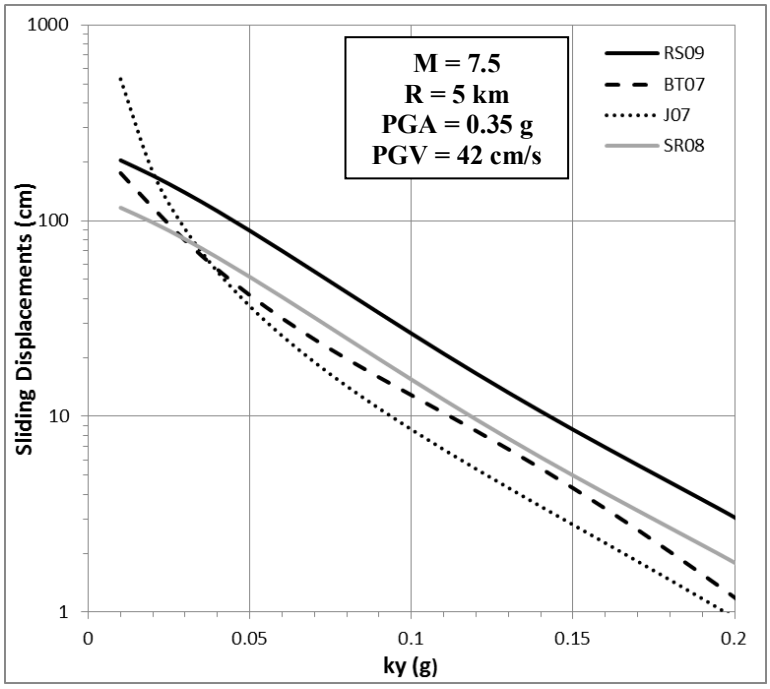

Figure 2.5 Predicted sliding displacements as a function of k_y

The ground motion values used in the empirical displacement models can be specified from a deterministic seismic hazard analysis (DSHA), in which a ground motion prediction equations (GMPE) is used to predict the ground shaking based on the expected earthquake magnitude (M), site-to-source distance (R), and shear wave velocity (e.g., $V_{s,30}$ = average shear wave velocity within 30-m depth). Today it is more common to specify ground motions from a probabilistic seismic hazard analysis (PSHA). PSHA computes a seismic hazard curve which provides the annual probability (or frequency) of exceedance of different ground motion levels. PSHA accounts for all M and R within the study area and their probability of occurrence, as well as the aleatory variability in ground motions. The ground motion hazard curves are used to identify ground motions associated with a prescribed seismic hazard level (e.g., often 10% or 2% probability of

exceedance in 50 years). Seismic hazard deaggregation provides information about the contribution of different earthquake scenarios (M and R values) to the ground motion hazard.

2.5 EMPIRICAL MODELS FOR FLEXIBLE SLIDING DISPLACEMENT

Similar to rigid sliding block analysis, flexible sliding displacement can also be predicted using empirical models. However, these empirical models must predict both the dynamic response and sliding displacement of the sliding mass. Two seismic loading parameters, k_{max} and k-vel_{max}, for flexible sliding masses are analogous to the parameters PGA and PGV for rigid sliding masses and are used to represent the dynamic response of flexible sliding masses. k_{max} is the maximum seismic coefficient of the k-time history. k-vel is the integral of the k-time history over time, as shown in Figure 2.4b, k-vel_{max} is the maximum value of the k-vel-time history. Rathje and Antonakos (2011) developed empirical models for k_{max} and k-vel_{max} based on 400 site response analyses of 1-D soil columns, thus k_{max} and k-vel_{max} can be predicted without directly computing the k-time history from dynamic analysis. The empirical models for k_{max} and k-vel_{max} are expressed as:

For $T_s/T_m \geq 0.1$:

$$\ln(k_{max}/PGA) = (0.459 - 0.702 \cdot PGA) \cdot \ln((T_s/T_m)/0.1) + (-0.228 + 0.076 \cdot PGA) \cdot \ln((T_s/T_m)/0.1)^2$$

For $T_s/T_m < 0.1$:

$$\ln(k_{max}/PGA) = 0.0$$

$$\sigma_{\ln(k_{max}/PGA)} = 0.25 \quad (2.5a)$$

For $T_s/T_m \geq 0.2$: $\ln(\text{k-vel}_{max}/\text{PGV}) = (0.240) \cdot \ln((T_s/T_m)/0.2) + (-0.091 - 0.171 \cdot \text{PGA}) \cdot \ln((T_s/T_m)/0.2)^2$

For $T_s/T_m < 0.2$: $\ln(\text{k-vel}_{max}/\text{PGV}) = 0.0$

$$\sigma_{\ln(\text{k-vel}_{max}/\text{PGV})} = 0.25 \quad (2.5b)$$

where T_s is the natural period of the sliding mass, calculated as $T_s = 4H/V_s$ for 1-D soil columns with H the thickness of the sliding mass, V_s the average shear wave velocity of the sliding mass, and T_m is the mean period of the ground motion. A site with higher T_s is softer, and a larger T_m represents a motion that contains more energy at long periods.

Figure 2.6 and Figure 2.7 show the variations of k_{max}/PGA and k-vel_{max}/PGV as a function of T_s/T_m developed by Rathje and Antonakos (2011) using the results of 400 1-D site response analyses. The empirical model predicts k_{max} = PGA at $T_s/T_m \leq 0.1$, indicating rigid sliding conditions. k_{max} is larger than PGA for PGA < 0.2 g and for $T_s/T_m < 0.5$, and the ratio of k_{max}/PGA generally decreases with increasing PGA or T_s/T_m. For k-vel_{max} the rigid sliding conditions extend to $T_s/T_m \leq 0.2$. k-vel_{max} can be slightly greater than PGV for small PGA values, and k-vel_{max}/PGV deceases slowly with increasing PGA or T_s/T_m.

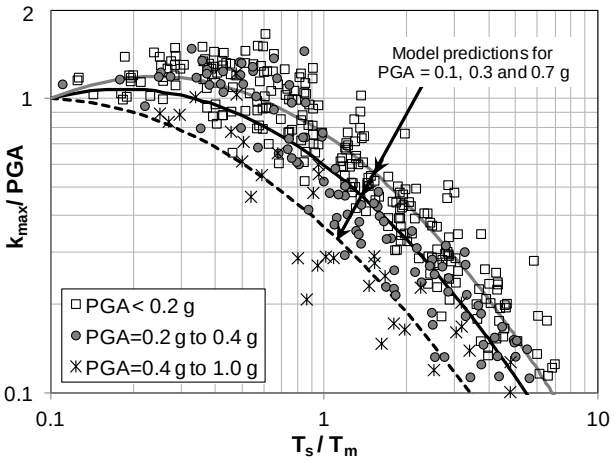

Figure 2.6 Variation of k_{max}/PGA as a function of T_s/T_m (Rathje and Antonakos 2011)

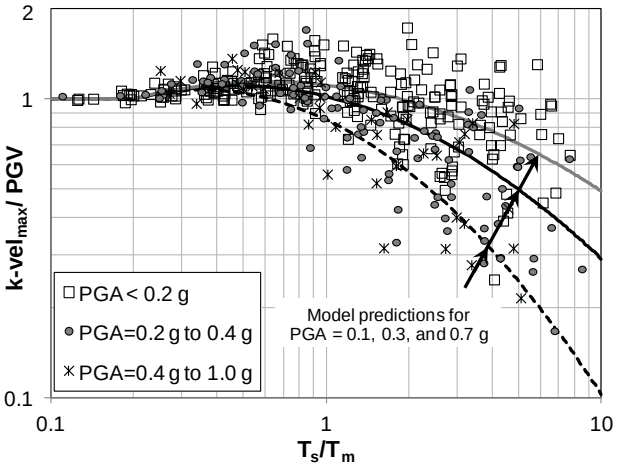

Figure 2.7 Variation of k-vel_{max}/PGV as a function of T_s/T_m (Rathje and Antonakos 2011)

The mean period T_m represents the frequency content of an earthquake ground motion and was firstly proposed by Rathje el al. (1998). When the frequency content of a ground motion closely matches the natural period of a sliding mass, the dynamic response is enhanced due to resonance. The calculation of T_m utilizes the Fourier Amplitude Spectrum, averaging the periods weighted by the Fourier amplitudes of the ground motion. Rathje et al. (2004) developed an empirical model for T_m as a function of earthquake moment magnitude (M), closest distance to the fault rupture (R, unit of km), site classifications (Rodriguez-Marek et al. 2001), and forward directivity (FD).

$$\ln(T_m) = -1.0 + 0.18 \cdot (M - 6) + 0.0038 \cdot R + 0.078 \cdot S_C + 0.27 \cdot S_D + 0.40 \cdot (1 - R/20) \cdot FD$$

$$\sigma_{\ln(T_m)} = \sqrt{(\sigma_{\text{site class}})^2 + 0.17^2} \tag{2.6}$$

where magnitude is limited to 7.25 for M > 7.25. S_C and S_D are indicator variables for site classes (S_C = 0 and S_D = 0 for site class B, S_C = 1 and S_D = 0 for site class C, and S_C = 0 and S_D = 1 for site class D). $\sigma_{\text{site class}}$ is 0.42 for site class B, 0.38 for site class C, and 0.31 for site class D. FD indicates forward directivity conditions (FD = 1 for sites with M ≥ 6.0, R ≤ 20 km, azimuth angle ≤ 30°, and rupture length ratio ≥ 0.5, FD = 0 otherwise).

T_m generally increases with increasing M and R, because larger magnitude earthquakes generate more energy at long periods and short-period motions are attenuated faster with increasing distance. However, T_m is larger with closer distance to the earthquake source when forward directivity is taken into account. Sites with softer

soil have larger T_m values, because short-period motions are damped out and long-periods are amplified during the propagation in deeper/softer soils.

With predictions of the seismic loading parameters, Rathje and Antonakos (2011) also developed empirical models for flexible sliding displacements based on the RS09 and SR08 models. k_{max} and k-vel_{max} are used in lieu of PGA and PGV in Equations 2.4c and 2.4d, and additional modification terms are added to the RS09 and SR08 models. The scalar and vector empirical models are expressed as:

$$\ln(D_{k_{max},M}) = \ln(D_{PGA,M}) + \begin{cases} 3.69 \cdot T_s - 1.22 \cdot T_s^{\,2}, & T_s \leq 1.5 \text{ s} \\ 2.78 \quad , & T_s > 1.5 \text{ s} \end{cases}$$

$$\sigma_{lnD} = 0.694 + 0.322\left(\frac{k_y}{k_{max}}\right) \tag{2.7a}$$

$$\ln(D_{k_{max},k-vel_{max}}) = \ln(D_{PGA,PGV}) + \begin{cases} 1.42 \cdot T_s, & T_s \leq 0.5 \text{ s} \\ 0.71 \quad , & T_s > 0.5 \text{ s} \end{cases}$$

$$\sigma_{lnD} = 0.40 + 0.284\left(\frac{k_y}{k_{max}}\right) \tag{2.7b}$$

where $D_{PGA,M}$ and $D_{PGA,PGV}$ represents the median displacements predicted by the RS09 and SR08 rigid sliding block models. k_{max} and k-vel_{max} are used in lieu of PGA and PGV for the calculation of $D_{PGA,M}$ and $D_{PGA,PGV}$.

The displacements computed by empirical models are not exact predictions of actual, measureable displacements. Sliding displacement analysis only models seismic displacements directly caused by the ground shaking. Soil materials may weaken by the sliding displacement, leading to reduction of the static factor of safety and continuing

post-seismic displacement. The predicted results indicate the likelihood of continuing deformation and the occurrence of landslides, which means that a larger displacement represents a higher probability of landslide occurrence (Jibson et al. 2000). In fact, Jibson et al. (1998, 2000) developed an empirical relationship between predicted rigid sliding displacements and actual landslide occurrence based on the observed landslides triggered by the 1994 Northridge earthquake. These probabilities were used by USGS (Jibson and Michael 2009) to define seismic hazard categories based on the estimated displacements and probability of landslide occurrence (Table 2.1). The displacement thresholds currently used by the California Geological Survey (McCrink and Real 1996, McCrink 2001) for its seismic landslide maps are 5cm, 15cm, and 30cm, which result in four landslide hazard categories (very low, low, moderate, and high). The CGS approach assumes no shear strength contribution from cohesion (c' = 0), thus the predicted displacements are relatively larger than the USGS approach. Therefore, the CGS thresholds are higher than the USGS thresholds for the same hazard categories. In this study, the USGS displacement thresholds are adopted to determine seismic landslide hazard categories.

Table 2.1 Seismic Hazard Categories based on Newmark Displacement (Jibson and Michael 2009)

Hazard Category	Sliding Displacement (cm)	Probability of Landslide (%)
Low	0 - 1	0 - 2
Moderate	1 - 5	2 - 15
High	5 - 15	15 - 32
Very High	> 15	> 32

2.6 SUMMARY

Rigid sliding block displacement can be used to evaluate seismic landslide potential of slopes. The computation of rigid sliding displacements requires the yield acceleration of the slope and the acceleration-time history. For shallow landslides, a pseudo-static infinite slope model is introduced to characterize a sliding block sitting on a base and to compute the yield acceleration. For deep failure surfaces, the yield acceleration is computed through a limit equilibrium analysis under the pseudo-static condition with the seismic factor of safety equal to 1.0.

To simplify the computation of rigid sliding displacement, many researchers have developed empirical displacement models using ground motion parameters rather than acceleration-time histories. These displacement models were introduced. Empirical models for flexible sliding masses are also available. Unlike rigid sliding blocks, the dynamic response of flexible sliding masses has significant influence on sliding displacements and must be taken into account. The empirical models for flexible sliding masses predict both the dynamic response and sliding displacement of the slope. For both rigid and flexible sliding masses, the predicted sliding displacements are used to indicate the likelihood of landslide occurrence and to assign seismic landslide hazard categories.

Chapter 3 Probabilistic Framework for Flexible Sliding Displacements[1]

3.1 INTRODUCTION

Seismic landslide potential can be evaluated by computing sliding displacements using sliding block analysis. For shallow landslides, the dynamic response of sliding masses can be ignored, so rigid sliding displacements are appropriate for the evaluation of seismic landslide potential. However, the dynamic response of deeper/softer sliding masses is significantly different from rigid sliding masses. This dynamic response can be taken into account through a decoupled sliding block analysis, which uses the results from a dynamic response analysis as input into a rigid sliding block analysis. Empirical models provide a simple and fast way for predicting the dynamic response and sliding displacement without the need of choosing suitable ground motions for the analysis.

Empirical models predict sliding displacements as a function of ground motion parameters and site parameters. There is significant aleatory variability (i.e. large standard deviation, σ_{lnD}), also known as natural randomness, associated with each empirical model, so that a given set of input parameters relates to a large range of possible displacements. Earthquake ground motions also have significant aleatory variability. The current deterministic approach for computing sliding displacements either ignores or does not rigorously treated the aleatory variability in the expected

[1] This Chapter is based on a published paper authored by Rathje et al. (2013). Dr. Ellen Rathje and Yubing Wang did the major work. Dr. Peter Stafford provided feedback and assistance. Dr. Rathje's former students, George Antonakos and Dr. Gokhan Saygili, also contributed to this paper.

ground motion, dynamic response, and predicted displacement. Therefore, the deterministic approach may underestimate the seismic landslide potential.

Alternatively, Rathje and Saygili (2008) developed a probabilistic approach to incorporate the aleatory variability displacement calculation through the use of displacement hazard curves, which can quantify the hazard levels for different levels of slope displacement. The developed probabilistic approach is only applicable to rigid sliding displacement analysis. This chapter extends the probabilistic approach to flexible sliding masses by taking into account the dynamic response of slope. Additionally, a logic tree approach is introduced that allows one to incorporate the epistemic uncertainties associated with the slope properties (i.e., soil shear strengths, ground water table and thickness of sliding blocks) and different empirical displacement models.

3.2 PROBABILISTIC FRAMEWORK FOR RIGID SLIDING DISPLACEMENT

3.2.1 Deterministic Approach

The current deterministic approach computes the median displacement from a displacement prediction model given the expected ground motion intensity. The ground motion parameters, such as PGA and PGV, required by the empirical models are obtained from seismic hazard curves that may come from site-specific probabilistic seismic hazard analysis or from the USGS website. A PGA hazard curve (Figure 3.1) provides a seismic hazard level (i.e., annual frequency of exceedance) for different values of PGA at a location of interest. The two most commonly used hazard levels are 0.0021 1/year (i.e., 10% probability of exceedance in 50 years) and 0.0004 1/year (i.e., 2% probability

of exceedance in 50 years). These hazard levels represent approximately 500-year and 2500-year return periods for a motion, respectively. For the PGA hazard curve in Figure 3.1, the 10% in 50 year motion is 0.54 g and the 2% in 50 year motion is 0.88 g.

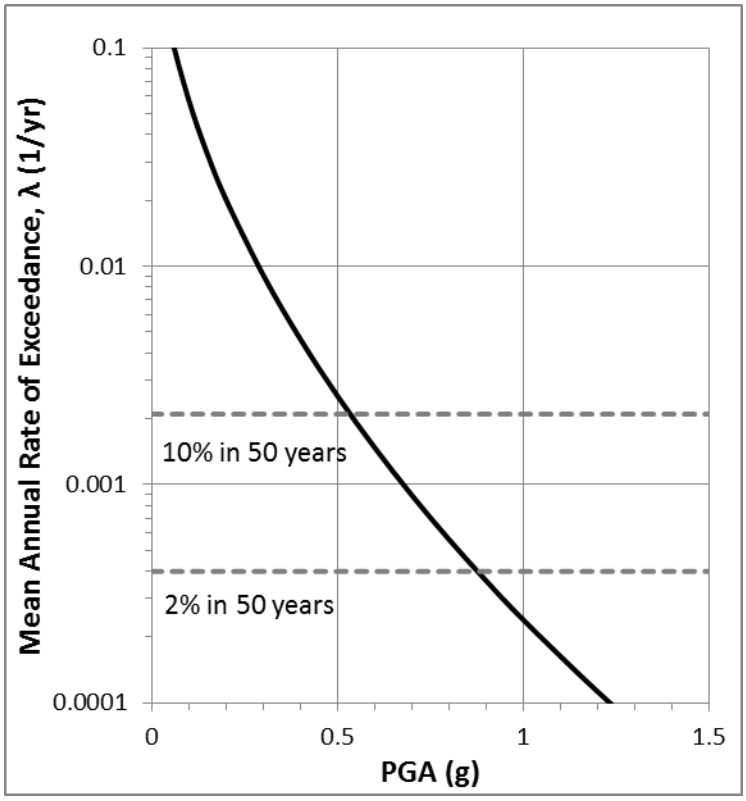

Figure 3.1 PGA Hazard Curve for a site in northern California (Rathje and Saygili 2011)

The current deterministic approach does not consider any aleatory variability in ground shaking and the sliding displacement predictions, or epistemic uncertainty in the slope properties. Only a single value of each input parameter (shear strength, yield acceleration, ground motion level) is used to calculate the sliding displacement. For example, the k_y value of a site is computed from specified slope properties by using

Equations 2.1 and 2.2, and the sliding displacement can be predicted by using Equation 2.3 with the PGA value derived from a ground motion hazard curve (e.g., Figure 3.1) at a selected seismic hazard level. The predicted median sliding displacement is compared with a determined acceptable value or thresholds (e.g., Table 2.1) to evaluate the seismic landslide potential.

3.2.2 Displacement Hazard Curve

A displacement hazard curve (e.g. Figure 3.3), similar to a ground motion hazard curve (e.g. Figure 3.1), directly relates the predicted sliding displacement (i.e. slope performance) with the seismic hazard level (i.e. mean annual rate of exceedance). Rathje and Saygili (2008) proposed a scalar approach, which utilizes an empirical displacement model with only one (i.e., a scalar) ground motion parameter (typically PGA), to compute a displacement hazard curve from a ground motion hazard curve. The standard deviation $\sigma_{\ln D}$ of the empirical displacement model is included in the computation of the displacement hazard curve. Later, Saygili and Rathje (2009) modified their scalar approach by adding earthquake magnitude (M), because the scalar empirical model without magnitude did not provide unbiased estimates of the sliding displacement relative to magnitude.

In the scalar approach, the mean annual rate of exceedance (λ_D) for a displacement level x is defined as:

$$\lambda_D(x) = \sum_i \sum_k P[D > x | PGA_i, M_k] \cdot P[M_k | PGA_i] \cdot P[PGA_i] \qquad (3.1)$$

where D is sliding displacement, $P[D > x|PGA_i, M_k]$ is the probability of D > x given the occurrence of acceleration level PGA_i and earthquake magnitude M_k, $P[M_k|PGA_i]$ is the conditional probability of M_k given PGA_i, and $P[PGA_i]$ is the mean annual probability of occurrence of ground motion level PGA_i. The double summation represents numerical integration over bins for PGA and M, and it represents the combined application of the total probability theorem and conditional probability.

For a given PGA_i and M_k, the empirical model provides a lognormal distribution of the displacement with mean μ_{lnD} (or median D = exp (μ_{lnD})) and standard deviation σ_{lnD}. Given a displacement level x, the probability of D > x can be calculated by using the cumulative distribution function for the normal distribution as:

$$P[D > x|PGA_i, M_k] = 1 - \Phi\left(\frac{x-\mu_{lnD}}{\sigma_{lnD}}\right) \tag{3.2}$$

$P[PGA_i]$ is the annual probability of occurrence of acceleration level PGA_i and it can be approximated from the annual probability of exceedance as:

$$\begin{aligned} P[PGA_i] &= P\left[PGA > PGA_{i-\frac{1}{2}}\right] - P\left[PGA > PGA_{i+\frac{1}{2}}\right] \\ &= \frac{P[PGA > PGA_{i-1}] + P[PGA > PGA_i]}{2} \\ &\quad - \frac{P[PGA > PGA_i] + P[PGA > PGA_{i+1}]}{2} \\ &= \frac{\lambda_{i-1} + \lambda_i}{2} - \frac{\lambda_i + \lambda_{i+1}}{2} = \frac{\lambda_{i-1} - \lambda_{i+1}}{2} \end{aligned} \tag{3.3}$$

where $P[PGA > PGA_{i-1/2}]$ and $P[PGA > PGA_{i+1/2}]$ represent the annual probability of exceedance associated with PGA values halfway between adjacent PGA values (i.e. PGA_{i-1}, PGA_i and PGA_{i+1}). Assuming that the annual probability and annual rate of exceedance are approximately the same for rare events, the hazard values λ_{i-1}, λ_i and λ_{i+1} from the PGA hazard curve can represent the annual probability of exceedance of PGA_{i-1}, PGA_i and PGA_{i+1}.

Theoretically, the annual probability of exceedance $P[PGA > PGA_i]$ can be derived from the annual rate of exeedance λ_i by using the Poisson process as:

$$P[PGA > PGA_i] = 1 - e^{-\lambda_i t} \tag{3.4}$$

where t is equal to 1 year for annual probability. Figure 3.2 shows that the ratio of λ_i to $P[PGA > PGA_i]$ is between 1.0 and 1.05 for low annual rate of exceedance (λ<0.1). The PGA values associated with high annual rate of exceedance are small enough that they will not cause damage to slopes and structures. Therefore, for the λ values considered in real engineering problems, the annual probability of exceedance can be approximated by using the annual rate of exceedance.

Equation 3.3 assumes that hazard values over one PGA bin vary linearly and that the annual probabilities for the PGA levels estimated in this way will be closer to the exact values with smaller bin sizes. If the discretization of the PGA hazard curve is small enough, there is no need to account for the nonlinear variation of hazard values over the bin.

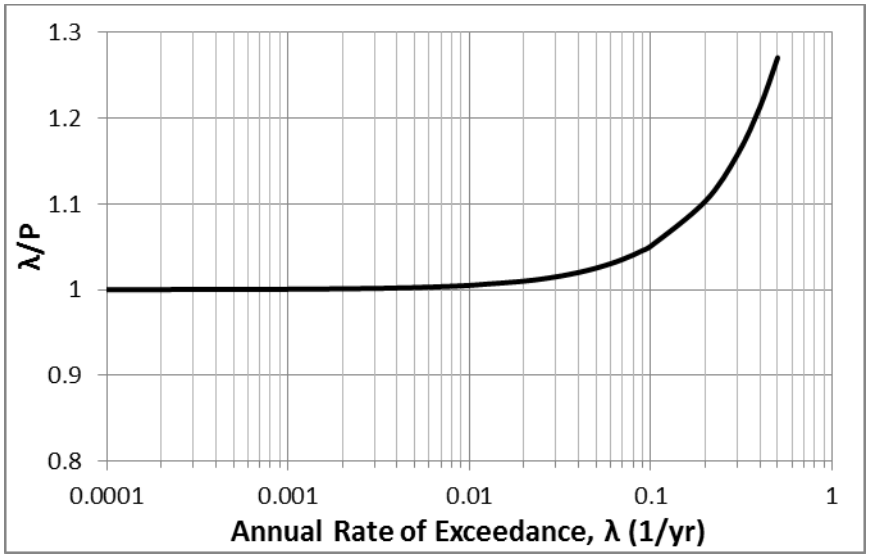

Figure 3.2 Ratio of Annual Rate to Annual Probability of Exceedance

$P[M_k|PGA_i]$ can be derived from the seismic hazard deaggregation for PGA, which is available on the USGS website or is commonly provided with a site-specific PSHA. The seismic hazard deaggregation describes the contributions of all combinations of earthquake magnitude (M_k) and source-to-site distance (R_l) given a PGA level. The sum of all contributions to a given PGA hazard level is equal to 1.0. The expression of a hazard deaggregation is $P[M_k, R_l|PGA > PGA_i]$. Therefore, the conditional probability $P[M_k|PGA_i]$ can be obtained from the total probability theorem (Equation 3.5) as (Bradley 2010):

$$P[M_k|PGA_i] = \sum_l P[M_k, R_l|PGA_i] \tag{3.5}$$

$$P[M_k, R_l|PGA_i] = \frac{P[M_k, R_l, PGA > PGA_{i-1/2}] - P[M_k, R_l, PGA > PGA_{i+1/2}]}{P[PGA_i]} \tag{3.6}$$

$$P\left[M_k, R_l, PGA > PGA_{i-1/2}\right] = \frac{P[M_k, R_l, PGA > PGA_{i-1}] + P[M_k, R_l, PGA > PGA_i]}{2} \tag{3.7}$$

$$P[M_k, R_l, PGA > PGA_i] = P[M_k, R_l | PGA > PGA_i] \cdot P[PGA > PGA_i] \tag{3.8}$$

The two terms in the numerator of Equation 3.6 can be computed via Equation 3.7. Equation 3.8 is used to compute the two terms on the right side of Equation 3.7. Again, the annual probability of exceedance is assumed to be equal to the annual rate of exceedance for this calculation.

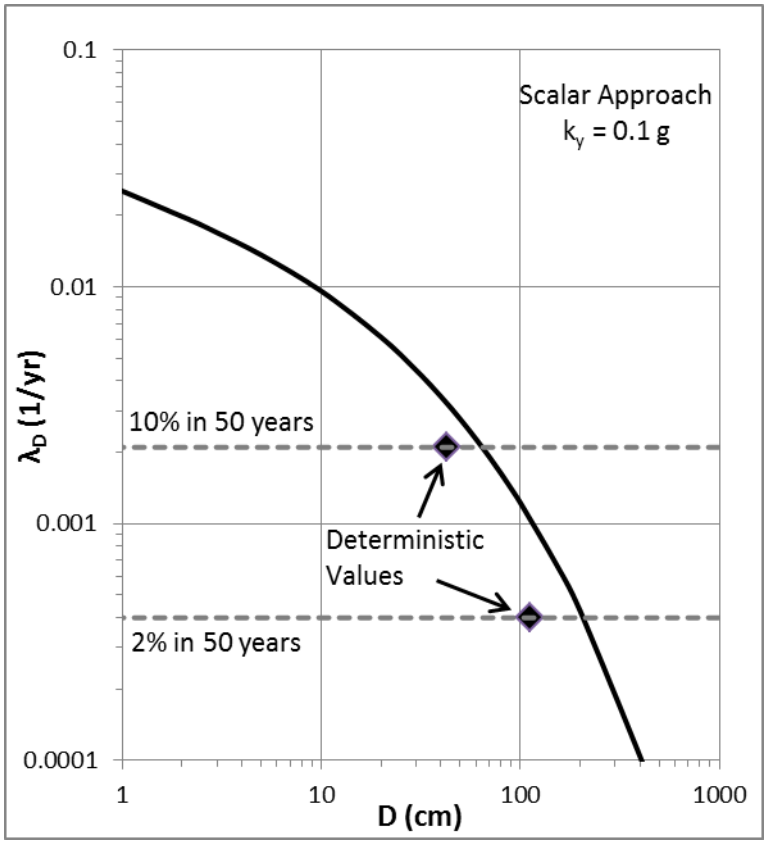

Figure 3.3 Displacement hazard curve for a site in northern California using the scalar approach

Finally, a displacement hazard curve is created by using Equation 3.1. One thing to be noted is that Equation 3.1 provides the annual probability of exceedance for a displacement level x due to the use of annual probability on the right side of the equation. However, the annual probability can be assumed equivalent to the annual rate, as validated before. Furthermore, the second conversion from the annual probability to the annual rate on the left side of Equation 3.1 can reduce the errors of the first conversion made on the right side of Equation 3.1.

Figure 3.3 shows a displacement hazard curve and deterministic displacement values from the same PGA hazard curve used for the displacement hazard curve (Figure 3.1). The scalar probabilistic approach results in greater displacements (67 cm and 208 cm) than the deterministic approach (43 cm and 113 cm), due to the consideration of aleatory variability.

If more than one ground motion parameter is included in an empirical model, the aleatory variability in the sliding displacement predictions can be significantly reduced (Saygili and Rathje 2008). Saygili and Rathje (2008) proposed several vector empirical displacement models (i.e., models that use a vector of ground motion parameters), and the model that includes both intensity (PGA) and frequency content (PGV) parameters was preferred to use for the vector probabilistic approach (Rathje and Saygili 2008). Similar to the scalar approach, for the vector approach the mean annual rate of exceedance (λ_D) for a displacement level x is defined as:

$$\lambda_D(x) = \sum_i \sum_j P[D > x | PGA_i, PGV_j] \cdot P[PGA_i, PGV_j] \quad (3.9)$$

where $P[D > x|PGA_i, PGV_j]$ is the probability of D > x given ground motion levels PGA_i and PGV_j, and $P[PGA_i, PGV_j]$ is the joint annual probability of occurrence of ground motion levels PGA_i and PGV_j.

For given values of PGA_i and PGV_j, a vector predictive model provides a lognormal distribution of the sliding displacement with mean μ_{lnD} and standard deviation σ_{lnD}. Given a displacement level x, the probability of D > x can be calculated by using Equation 3.2. $P[PGA_i, PGV_j]$ can be computed using a vector PSHA computer code (VPSHA, Bazzurro and Cornell 2002). Alternatively, the joint probability $P[PGA_i, PGV_j]$ can be derived from the scalar hazard information for PGA along with the seismic hazard deaggregation, GMPEs for PGA and PGV, and the correlation coefficient between PGA and PGV using:

$$P[PGA_i, PGV_j] = P[PGV_j|PGA_i] \cdot P[PGA_i] \tag{3.10}$$

where $P[PGA_i]$ is the annual probability of occurrence of ground motion level PGA_i and can be calculated from Equation 3.3. $P[PGV_j|PGA_i]$ is the conditional probability of PGV_j given PGA_i and is computed using:

$$P[PGV_j|PGA_i] = \sum_k \sum_l P[\,PGV_j|PGA_i, M_k, R_l] \cdot P[M_k, R_l|PGA_i] \tag{3.11}$$

where $P[M_k, R_l|PGA_i]$ is derived from the seismic hazard deaggregation (Equations 3.6 to 3.8). The PGA and PGV GMPEs and the correlation coefficient for PGA and PGV are required to compute $P[PGV_j|PGA_i, M_k, R_l]$ (Bazzurro and Cornell 2002, Rathje and

Saygili 2008). The conditional PGV required for $P[PGV_j|PGA_i, M_k, R_l]$ also follows a lognormal distribution with its conditional mean and standard deviation defined as:

$$\mu_{\ln PGV|PGA_i,M_k,R_l} = \mu_{\ln PGV|M_k,R_l} + \rho \frac{\sigma_{\ln PGV|M_k,R_l}}{\sigma_{\ln PGA|M_k,R_l}} (\ln PGA_i - \mu_{\ln PGA|M_k,R_l}) \quad (3.12)$$

$$\sigma_{\ln PGV|PGA_i,M_k,R_l} = \sigma_{\ln PGV|M_k,R_l} \cdot \sqrt{1-\rho^2} \quad (3.13)$$

where $\mu_{\ln PGA|M_k,R_l}$, $\sigma_{\ln PGA|M_k,R_l}$, $\mu_{\ln PGV|M_k,R_l}$ and $\sigma_{\ln PGV|M_k,R_l}$ are derived from GMPEs for PGA and PGV. The correlation coefficient ρ between PGA and PGV has been estimated as 0.6 (Rathje and Saygili 2008, Baker 2007). Thus, $P[PGV_j|PGA_i, M_k, R_l]$ can be obtained from a normal distribution with mean and standard deviation calculated from Equations 3.12 and 3.13.

Figure 3.4 shows hazard curves for displacement computed using the scalar and vector approaches for the same site as Figure 3.3. As shown in Figure 3.4, the vector approach predicts smaller displacements than the scalar approach at all seismic hazard levels. These reductions occur because more ground motion information is utilized in the vector approach (i.e., PGA and PGV vs. only PGA), so that the vector empirical displacement model predicts a smaller median displacement and a smaller standard deviation than the scalar empirical displacement model.

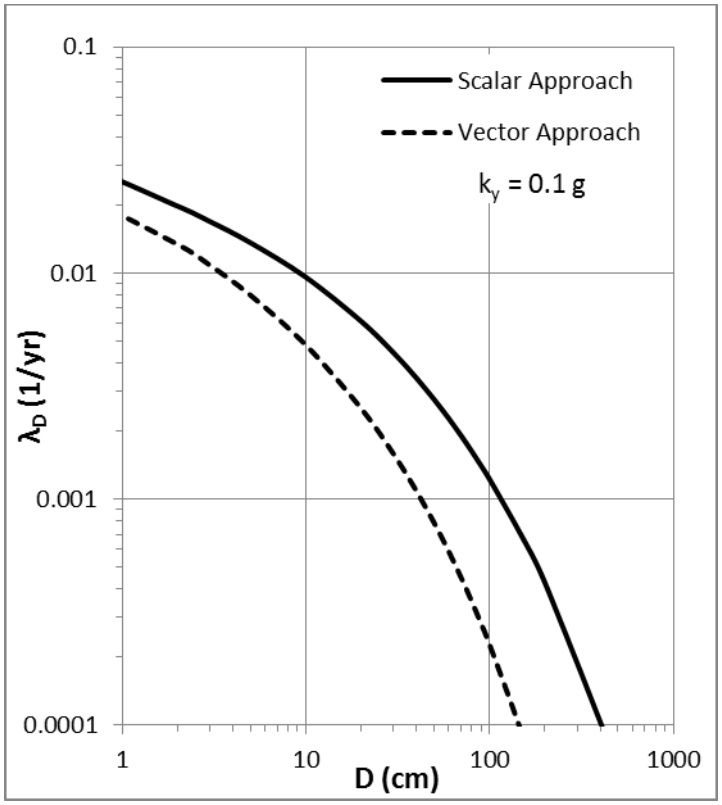

Figure 3.4 Displacement hazard curves for a site in northern California using both scalar and vector approaches

3.3 PROBABILISTIC ASSESSMENT OF THE DYNAMIC RESPONSE OF FLEXIBLE SLIDING MASSES

As discussed in Section 2.3, the dynamic response of sliding masses should be considered for deeper/softer slopes because they respond as flexible sliding masses. For these sites, the appropriate seismic loading time history is the seismic coefficient (k)-time history and this time history is used as input into a rigid sliding block analysis. Empirical models for flexible sliding masses (e.g. Rathje and Antonakos 2011) can be

used to predict the dynamic response, the corresponding seismic loading parameters, and the flexible sliding block displacements.

The parameters k_{max} and k-vel_{max} (introduced in Section 2.3) for flexible sliding masses are analogous to parameters PGA and PGV for rigid sliding masses and are used to represent the dynamic response of flexible sliding masses. Similar to PGA and PGV, seismic hazard curves can also be constructed for k_{max} and k-vel_{max}, although such curves are not explicitly required for the computation of flexible displacement hazard curves. The hazard curves of k_{max} and k-vel_{max} can be computed independently of one another as:

$$\lambda_{k_{max}}(y) = \sum_i \sum_k P[k_{max} > y | PGA_i, M_k] \cdot P[M_k | PGA_i] \cdot P[PGA_i] \quad (3.14)$$

$$\lambda_{k-vel_{max}}(z) = \sum_i \sum_j P[k - vel_{max} > z | PGA_i, PGV_j] \cdot P[PGA_i, PGV_j] \quad (3.15)$$

where $P[k_{max} > y | PGA_i, M_k]$ is the probability of $k_{max} > y$ given ground motion level PGA_i and earthquake magnitude M_k, and $P[k - vel_{max} > z | PGA_i, PGV_j]$ is the probability of k-$vel_{max} > z$ given ground motion levels PGA_i and PGV_j. All other components in Equation 3.14 and 3.15 are the same as shown in Equation 3.1 and 3.9, respectively. The distributions of k_{max} and k-vel_{max} are also assumed lognormal with means and standard deviations from empirical models (e.g. Equation 2.5). Thus, $P[k_{max} > y | PGA_i, M_k]$ and $P[k - vel_{max} > z | PGA_i, PGV_j]$ can be calculated using Equation 3.2. As seen in the empirical models for k_{max} and k-vel_{max}, the dynamic response of flexible sliding masses also depends on the site period T_s and the mean period of the ground motion T_m but these values are taken as constant.

Figure 3.5 to Figure 3.8 illustrate the dynamic response predictions of flexible masses by using the same hazard information as shown in Figure 3.1. The mean period

of the ground motion T_m is assumed deterministically to be equal to 0.5 s, and the ratio T_s/T_m selected for the calculations are 0.0, 0.25, 0.5, and 1.0. These conditions represent rigid sliding ($T_s = 0$) and flexible sliding for $T_s = 0.125$, 0.25 and 0.5 s.

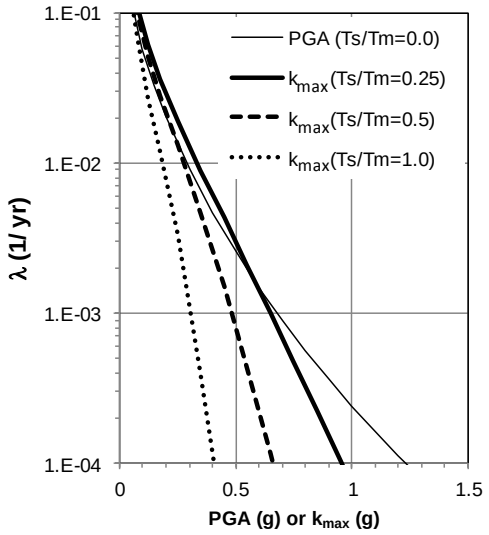

Figure 3.5 k_{max} hazard curves (T_m=0.5s)

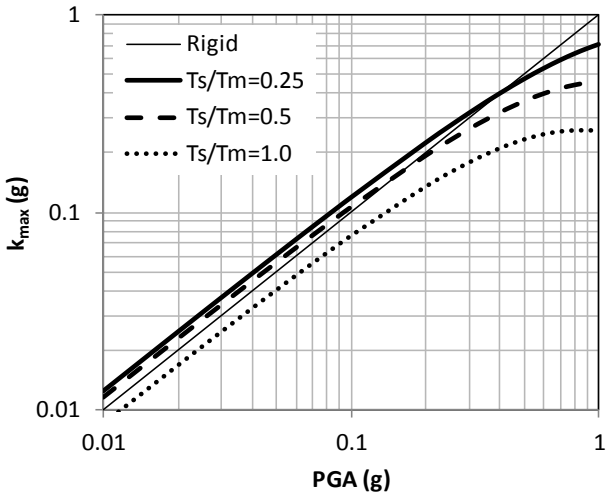

Figure 3.6 Variation of k_{max} with PGA from Equation 2.5a for different values of T_s/T_m

Figure 3.5 shows a series of k_{max} hazard curves with different T_s/T_m ratios, and Figure 3.6 displays the variation of k_{max} as a function of PGA for different T_s/T_m ratios. As seen in Figure 3.5, the seismic loading for a flexible sliding mass represented by k_{max} is generally smaller than for the rigid condition, except at higher values of λ with smaller PGA values. The reason is that the empirical model for k_{max} generally predicts k_{max} < PGA for larger PGA values (Figure 3.6). The predicted k_{max} is only greater than PGA for $T_s/T_m<0.5$ and for PGA smaller than about 0.2 g. Furthermore, the k_{max} generally decreases with increasing T_s/T_m ratio, which is also shown in Figure 3.5.

Intuitively, the dynamic response k_{max} should increase with increasing input ground motion PGA. However, the empirical model predicts a median k_{max} that reaches a maximum at a certain PGA and it starts decreasing for larger PGA. The reason for this behaviour is that the input PGA values used for deriving the empirical model are mostly less than 0.4 g, and only a few PGA values up to 1.0 g are considered. Therefore, the empirical model has a limitation when extrapolated beyond the range of input PGA used to develop it. This issue was not readily apparent when the model was developed because deterministic PGA values rarely exceed 0.7 to 0.8 g. Yet in probabilistic analyses we must integrate over the entire hazard curve and incorporate large PGA. A simple modification can be used to extend the application of the empirical model to high PGA levels. The PGA value that predicts the maximum k_{max} is defined as the PGA threshold, and k_{max} value is set equal to this maximum for PGA values greater than this threshold. The PGA threshold is a function of T_s/T_m, and it can be calculated by taking the derivative of Equation 2.5a with respect to PGA and setting it equal to zero. The resulting expression is:

$$\mathrm{PGA}_{\mathrm{threshold}} = \frac{1}{0.702 \cdot \ln\left(\frac{T_s}{T_m}/0.1\right) - 0.076 \cdot \left(\ln\left(\frac{T_s}{T_m}/0.1\right)\right)^2} \tag{3.16}$$

The influence of this modification can be seen in Figure 3.6 for T_s/T_m=1.0 with PGA threshold is 0.82 g and the corresponding maximum k_{max} is 0.26 gFigure 3.6.

Table 3.1 summarizes the predicted k_{max} values from both probabilistic and deterministic approaches at two commonly concerned seismic hazard levels for the three values of T_s/T_m. All probabilistic values are generally 10-25% greater than the corresponding deterministic values due to incorporating aleatory variability. For the cases shown the difference is largest for T_s/T_m=1.0 and λ=0.0004 1/yr, because the deterministic k_{max} is limited to its maximum median value given that the PGA (0.88 g) is larger than the PGA threshold, but the probabilistic k_{max} is can exceed the maximum due to the consideration of the standard deviation in the calculation.

Table 3.1 Probabilistic and deterministic k_{max} predictions

	k_{max} Comparisons					
	T_s/T_m = 0.25		T_s/T_m = 0.5		T_s/T_m = 1.0	
λ (1/yr)	Probabilistic	Deterministic	Probabilistic	Deterministic	Probabilistic	Deterministic
0.0021	0.55 g	0.50 g	0.42 g	0.38 g	0.27 g	0.24 g
0.0004	0.77 g	0.66 g	0.56 g	0.45 g	0.35 g	0.26 g

Note: λ = 0.0021 represents a 10% probability of exceedance in 50 years
λ = 0.0004 represents a 2% probability of exceedance in 50 years

Figure 3.7 shows a series of k-vel_{max} hazard curves for different T_s/T_m ratios, and Figure 3.8 displays the variation of k-vel_{max}/PGV as a function of PGA (not PGV) for different T_s/T_m ratios. Unlike for k_{max}, the k-vel_{max} hazard curves are much closer to the PGV hazard curve that represents the rigid condition. This behavior is a result of the ratio k-vel_{max}/PGV being slightly higher than 1.0 for $T_s/T_m<0.5$ and only slowly decreasing with increasing PGA (Figure 3.8) or T_s/T_m (Figure 2.7). As a consequence, the predicted k-vel_{max} from the empirical equation continues to increase with increasing PGA or PGV, and it does not reach a maximum for PGA<2.0 g. Because PGA values generally do not exceed 2.0 g in a seismic hazard curve, it is not necessary to develop a PGA or PGV threshold for the prediction of k-vel_{max}.

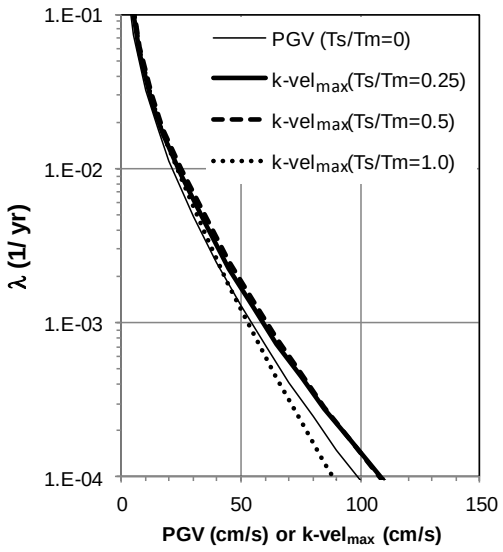

Figure 3.7 k-vel_{max} hazard curves (T_m=0.5s)

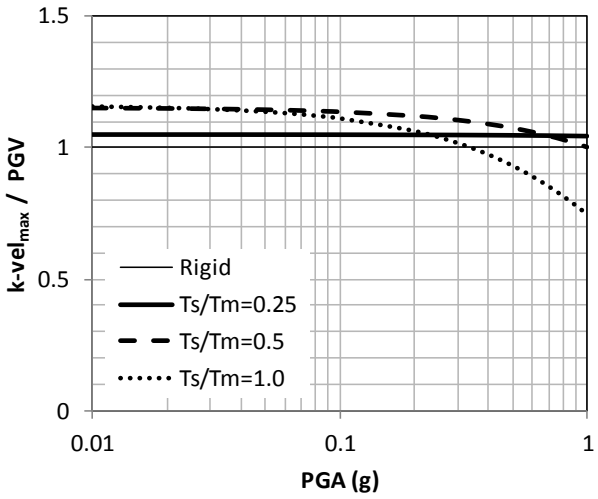

Figure 3.8 Variation of k-vel$_{max}$/PGV with PGA from Equation 2.5b for different values of T_s/T_m

Table 3.2 summarizes probabilistic and deterministic k-vel$_{max}$ values for 10% and 2% probabilities of exceedance in 50 years. The probabilistic values are generally 5-10% greater than the deterministic values, and such difference is smaller than for k_{max} in Table 3.2. Table 3.1 and Table 3.2 both shows larger difference between probabilistic and deterministic values as T_s/T_m increases. To further display this trend, Figure 3.9 illustrates the ratio between deterministic and probabilistic values as a function of T_s/T_m. It is clearly observed that the ratio decreases with increasing T_s/T_m, and the reduction of the ratio is larger for k_{max} than k-vel$_{max}$ at a given T_s/T_m value.

The deterministic k-vel$_{max}$ values are more similar to the probabilistic predictions because essentially perfectly correlated ($\rho \sim 1.0$) values of PGA and PGV are used for the deterministic predictions of k-vel$_{max}$, while a correlation coefficient of 0.6 are used for the calculation of P[PGA, PGV] in the probabilistic predictions of k-vel$_{max}$ (Equation 3.15, Section 3.2.2). As a result, the larger correlation coefficient considered in the

deterministic prediction leads to greater ground motion levels used in the deterministic calculation. Therefore, although the aleatory variability in the k-vel_{max} prediction is ignored in the deterministic calculation of k-vel_{max}, the difference between deterministic and probabilistic results is reduced by using larger ground motion levels for the deterministic k-vel_{max}.

Table 3.2 Probabilistic and deterministic k-vel_{max} predictions

	k-vel_{max} Comparisons					
	T_s/T_m = 0.25		T_s/T_m = 0.5		T_s/T_m = 1.0	
λ (1/yr)	Probabilistic	Deterministic	Probabilistic	Deterministic	Probabilistic	Deterministic
0.0021	46 cm/s	45 cm/s	48 cm/s	46 cm/s	43 cm/s	39 cm/s
0.0004	77 cm/s	74 cm/s	78 cm/s	72 cm/s	66 cm/s	56 cm/s

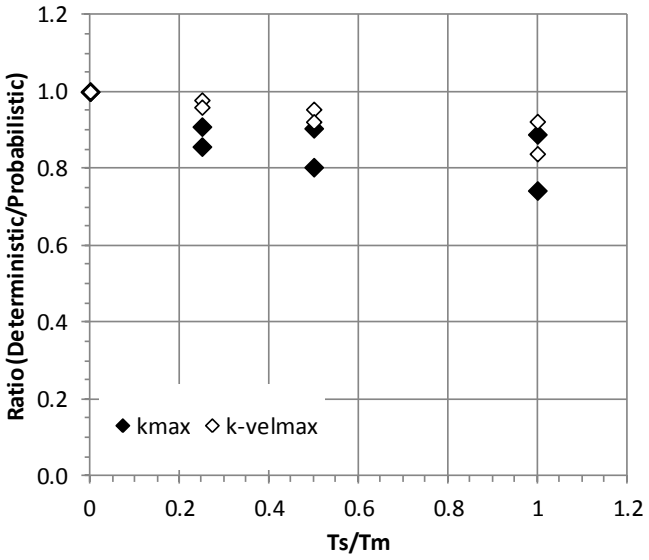

Figure 3.9 Ratio of deterministic to probabilistic predictions of k_{max} and k-vel_{max}

3.4 PROBABILISTIC ASSESSMENT OF THE SLIDING DISPLACEMENT OF FLEXIBLE SLIDING MASSES

For flexible sliding masses, the displacement hazard curve can be constructed in a similar way as for the rigid condition. The seismic loading parameters k_{max} and k-vel_{max} are used for the calculation of flexible sliding displacements rather than PGA and PGV. The computation of displacement hazard curves for flexible sliding masses also can be performed using scalar or vector approaches. For the scalar approach, the mean annual rate of exceedance (λ_D) for a displacement level x is defined as:

$$\lambda_D(x) = \sum_k \sum_m P[D > x | k_{max_m}, M_k] \cdot P\left[k_{max_m}, M_k\right] \quad (3.17)$$

where D is sliding displacement, $P[D > x|k_{max_m}, M_k]$ is the probability of D > x given the occurrence of seismic loading level k_{max_m} and earthquake magnitude M_k. $P[D > x|k_{max_m}, M_k]$ can be calculated by using the mean and standard deviation provided by the scalar empirical models for flexible sliding displacements. $P\left[k_{max_m}, M_k\right]$ is the joint annual probability of occurrence of k_{max_m} and M_k. The double summation represents numerical integration over bins for k_{max} and M, and it represents an application of the total probability theorem.

The joint annual probability of occurrence of $P\left[k_{max_m}, M_k\right]$ can be computed by using the annual probability of occurrence of ground motion level PGA_i (i.e. $P[PGA_i]$) and the conditional probability $P[M_k|PGA_i]$:

$$P\left[k_{max_m}, M_k\right] = \sum_i P\left[k_{max_m}\middle|PGA_i, M_k\right] \cdot P[M_k|PGA_i] \cdot P[PGA_i] \quad (3.18)$$

where $P[k_{max_m}|PGA_i, M_k]$ is the conditional probability of occurrence of k_{max_m} given PGA_i and M_k and is approximated from the cumulative density functions of two adjacent k_{max} levels as:

$$P[k_{max_m}|PGA_i, M_k] = \frac{P[k_{max} > k_{max_{m+1}}|PGA_i, M_k] - P[k_{max} > k_{max_{m-1}}|PGA_i, M_k]}{2} \quad (3.19)$$

These cumulative density functions are derived from the mean and standard deviation from the empirical predictive model for k_{max}. Although the earthquake magnitude M_k is not required for the k_{max} prediction, it is required in the scalar empirical displacement model for flexible sliding displacements and therefore must be carried through the calculation.

Using the same T_s (0.0, 0.125, 0.25 and 0.5 s) and T_m (0.5 s) values as Section 3.3, displacement hazard curves for the (k_{max}, M) model are computed and shown in Figure 3.10. The predicted flexible displacements with T_s/T_m=0.25 is greater than for the rigid condition. For larger T_s/T_m, the predicted displacements generally decrease with increasing T_s/T_m. These observations show that different sites (T_s) have different seismic behaviours with the same input ground motions (PGA hazard curve and T_m).

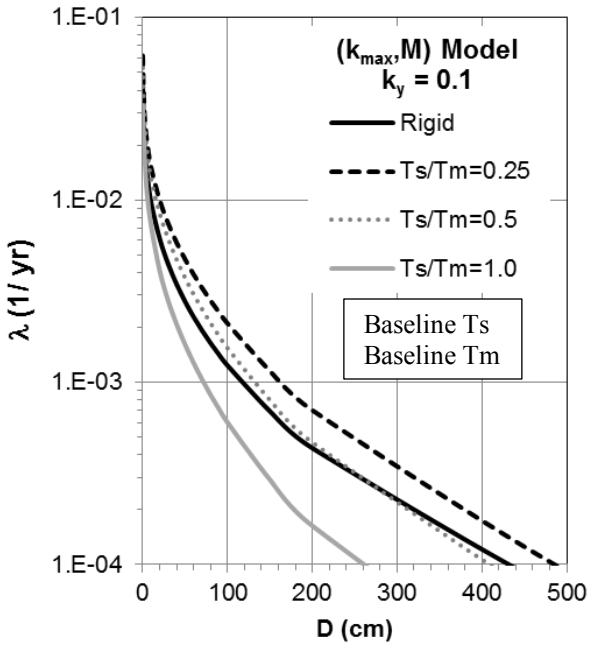

Figure 3.10 Displacement hazard curves for (k_{max}, M) model with baseline T_s and T_m

To further examine the impact of the absolute values of T_s and T_m on the predicted displacements, displacement hazard curves are computed by using different combinations of T_s and T_m. As discussed in Section 3.3, the empirical models for k_{max} and k-vel_{max} (Equation 2.5) depend only on the ratio of T_s/T_m but not the individual values of T_s or T_m. The empirical models for flexible displacements (Equation 2.7) have modification terms as a function of T_s and thus T_s directly influences the computed displacement.

To illustrate the impact of T_s on the predicted displacements, the ratio T_s/T_m is kept the same as before and the T_s values are increased and decreased by 30%. Note that this approach essentially increases Tm in the same way as Ts, and the dynamic responses of flexible sliding masses do not change with T_s. The resulting displacement hazard

curves for the -30% Ts, baseline Ts, and +30% Ts are shown in Figure 3.11. The displacement hazard curves show that the predicted displacements increase with increasing $T_{s,}$ although the predicted k_{max} and k-vel_{max} are the same for these analyses. The result indicates that the same dynamic responses generally induce larger sliding displacements in softer sliding masses.

To illustrate the effect of changing T_m alone, the baseline site periods (T_s = 0.0, 0.125, 0.25 and 0.5 s) are kept the same and T_m is increased and decreased by 30% (T_m = 0.35 and 0.65 s). Increasing T_m reduces Ts/Tm, and decreasing T_m does the opposite. The resulting displacement hazard curves are shown in Figure 3.12. Generally, an increase in T_m results in more displacement. It is noticeable that the impact of T_m is significantly greater for softer sites than for stiffer sites. For T_s=0.125 s, an increase in T_m from 0.35 s to 0.65 s increases predicted displacement by 30 ~ 40%, while the predicted displacements are increased by a factor of 2 ~ 3 for T_s=0.5 s.

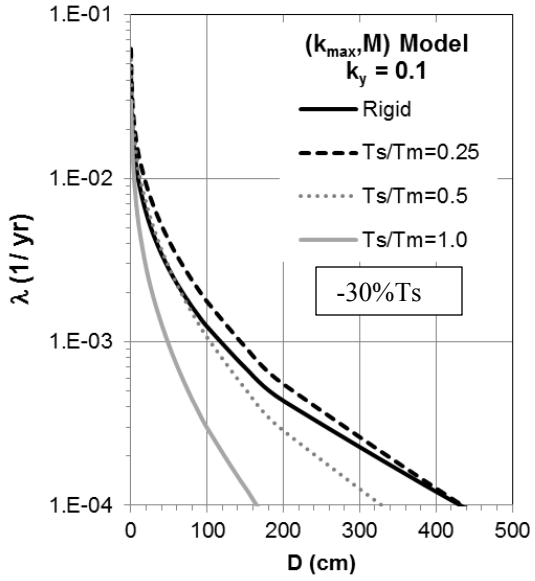

(a)

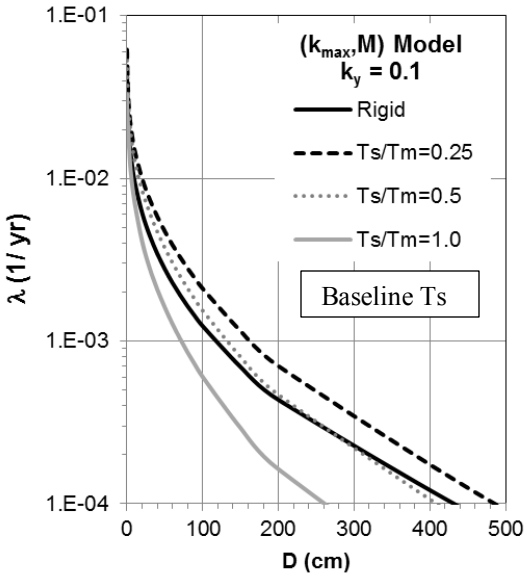

(b)

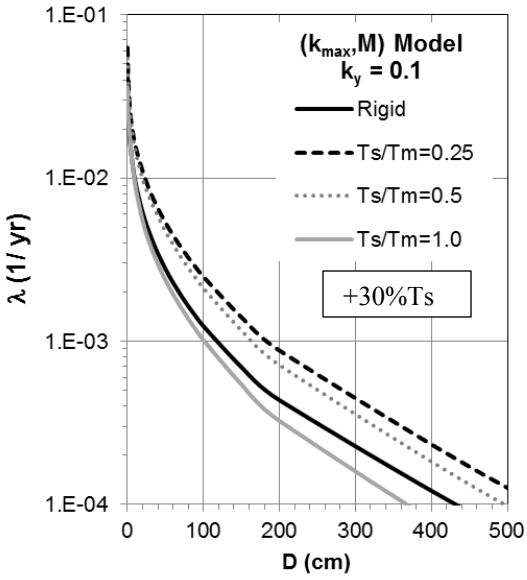

(c)

Figure 3.11 Displacement hazard curves for (k_{max}, M) model for different T_s with same Ts/T_m

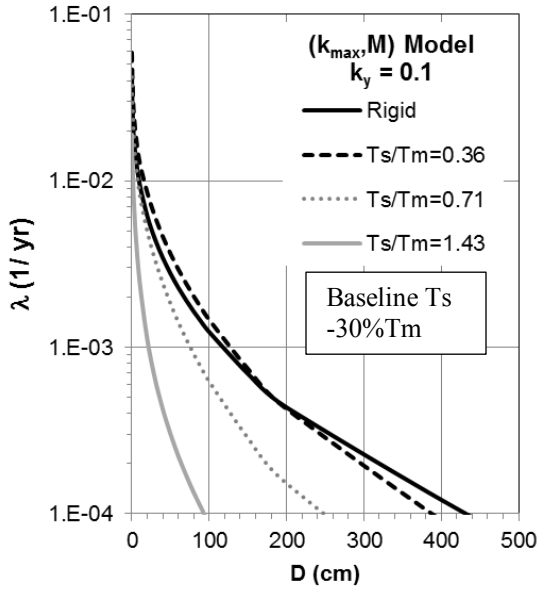

(a)

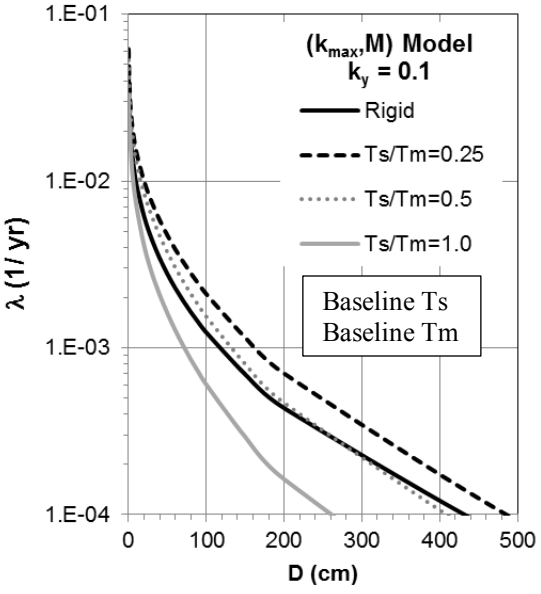

(b)

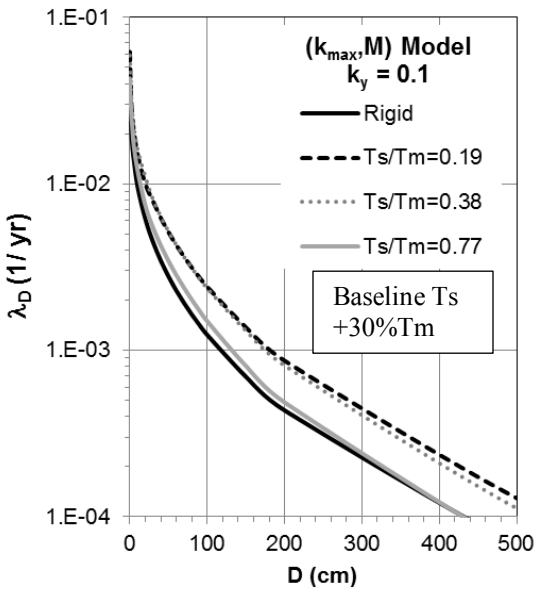

(c)

Figure 3.12 Displacement hazard curves for (k_{max}, M) model for different T_m with baseline T_s

Similar as the vector approach for rigid sliding, the flexible displacement hazard is computed by substituting PGA and PGV with k_{max} and k-vel_{max} in Equation 3.9, or the mean annual rate of exceedance (λ_D) for a displacement level x is defined as:

$$\lambda_D(x) = \sum_m \sum_n P[D > x | k_{max_m}, k-vel_{max_n}] \cdot P[k_{max_m}, k-vel_{max_n}] \quad (3.20)$$

where $P[D > x|k_{max_m}, k-vel_{max_n}]$ is the probability of D > x given the occurrence of seismic loading levels k_{max_m} and $k-vel_{max_n}$. $P[D > x|k_{max_m}, k-vel_{max_n}]$ can be calculated by using the mean and standard deviation provided by the vector empirical models for flexible sliding displacements. $P[k_{max_m}, k-vel_{max_n}]$ is the joint annual probability of occurrence of k_{max_m} and $k-vel_{max_n}$. This joint annual probability can be computed from $P[PGA_i, PGV_j]$ and the probabilities of obtaining k_{max_m} and $k-vel_{max_n}$ given PGA_i and PGV_j using:

$$P[k_{max_m}, k-vel_{max_n}] = \sum_i \sum_j P[k-vel_{max_n} | k_{max_m}, PGA_i, PGV_j] \cdot P[k_{max_m} | PGA_i, PGV_j] \cdot P[PGA_i, PGV_j] \quad (3.21)$$

where $P[k_{max_m} | PGA_i, PGV_j]$ is calculated from the empirical model for k-vel_{max} and its standard deviation. $P[k-vel_{max_n} | k_{max_m}, PGA_i, PGV_j]$ requires the conditional mean and standard deviation of k-vel_{max}, which are calculated by substituting PGA and PGV with k_{max} and k-vel_{max} in Equations 3.12 and 3.13. The correlation coefficient ρ between k_{max} and k-vel_{max} was evaluated by using the residuals of the computed values of k_{max} and k-vel_{max} from Rathje and Antonakos (2011) relative to the median values from their

empirical models. This approach is similar to the approach taken by Baker (2007) when considering the correlation between various ground motion parameters. Figure 3.13 shows moderate correlation between k_{max} and k-vel_{max} residuals. The computed correlation coefficient is 0.45.

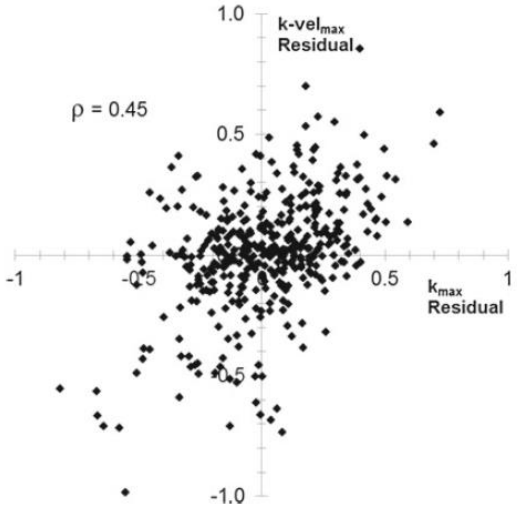

Figure 3.13 Correlation between k_{max} and k-vel_{max}

Using the same ideas as Figure 3.10 to 3.12, Figure 3.14 to 3.16 are created by using different combinations of T_s and T_m values. Comparing Figure 3.14 with Figure 3.10, the vector approach clearly predicts considerably less sliding displacements than the scalar approach due to the reduction of uncertainty by taking more ground hazard information into the computation. The difference is typically between a factor of 2 and 3, indicating the value of incorporating frequency content via k-vel_{max} when making displacement predictions.

Figure 3.14 shows that predicted flexible displacements with T_s/T_m=0.25 is greater than the rigid condition. For larger T_s/T_m, the predicted displacements generally decrease with increasing T_s/T_m while T_m is constant. As discussed for the scalar approach, Figure 3.15 (a) (b) and (c) illustrate that different site (different T_s) may have the same dynamic response k_{max} and k-vel_{max} with the same T_s/T_m, but the resulting sliding displacements should be different. One thing may be noticed is that, the displacement curves for T_s/T_m=1.0 in Figure 3.15 (a) and (c) are identical because the T_s values are 0.5 and 0.65, which provide the same modification term (i.e. constant modification term for $T_s \geq 0.5$) in the empirical model (Equation 2.7).

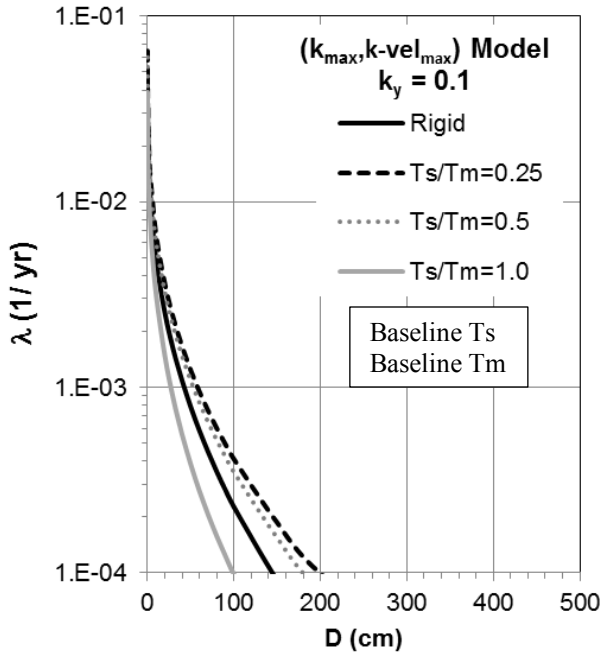

Figure 3.14 Displacement hazard curves for (k_{max}, k-vel_{max}) model with baseline T_s and T_m

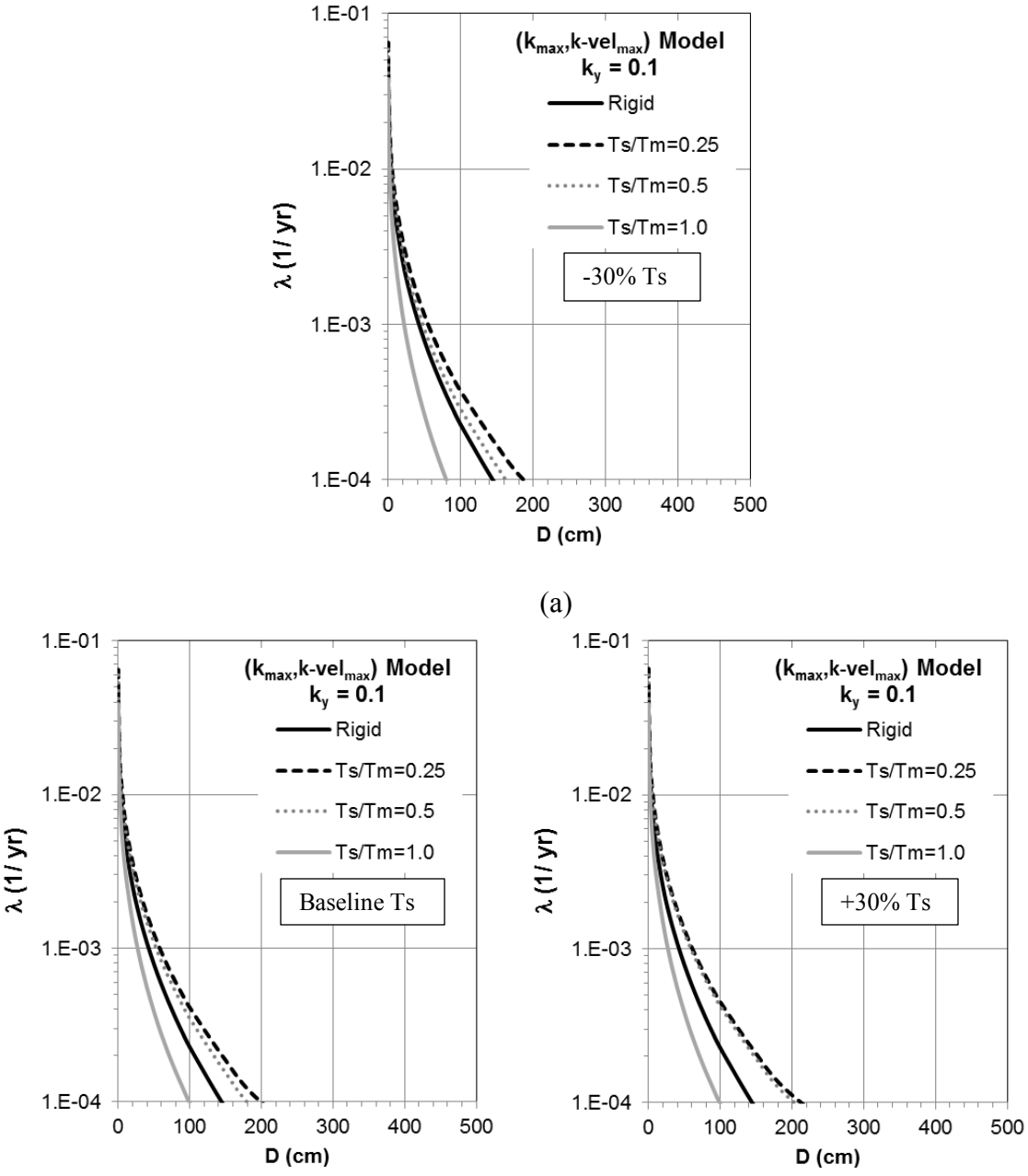

(a)

(b)

(c)

Figure 3.15 Displacement hazard curves for (k_{max}, k-vel_{max}) model for different T_s with same Ts/T_m

To illustrate the effect of changing T_m alone, the baseline site periods (T_s = 0.0, 0.125, 0.25 and 0.5 s) are kept the same and T_m is increased and decreased by 30% (T_m = 0.35 and 0.65 s). The resulting displacement hazard curves are shown in Figure 3.16. The displacement increment for T_s=0.125 s is about 10 ~ 20% with an increase in Tm from 0.35 s to 0.65 s, while the predicted displacements increases by a factor of 3 ~ 4 for T_s=0.5 s. Same as the scalar approach, the impact of T_m is significantly greater for softer sites than for stiffer sites.

Overall, the variation of vector displacement curves due to T_s/T_m in each plot is clearly smaller than the scalar displacement curves (Figure 3.10 to 3.12), because it is reduced by the small variation of k-vel_{max} hazard curves (Figure 3.7).

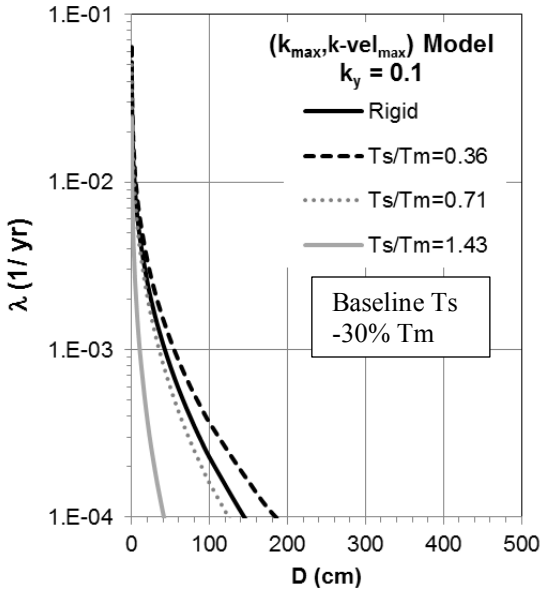

(a)

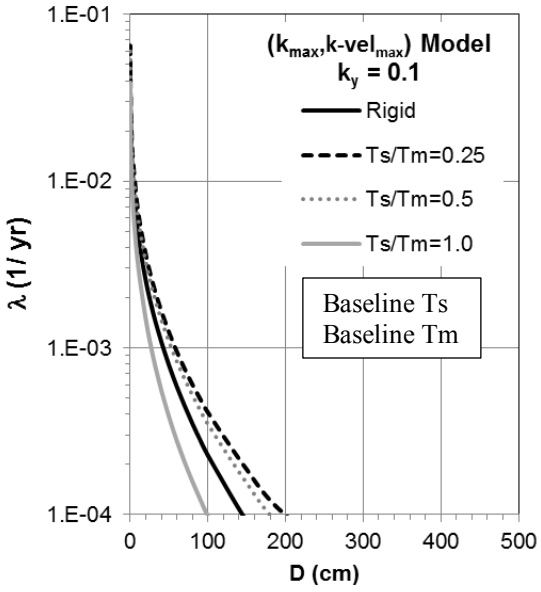

(d)

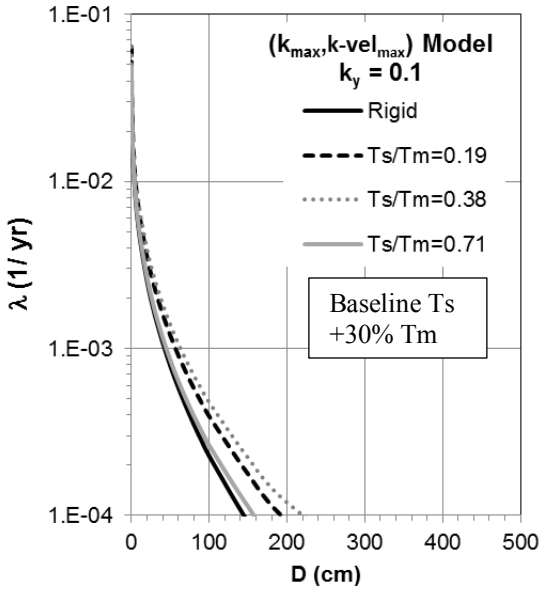

(e)

Figure 3.16 Displacement hazard curves for (k_{max}, k-vel_{max}) model for different T_m with baseline T_s

Again, the probabilistic predictions of sliding displacements are compared with the results from traditional deterministic analysis. Here, the deterministic analysis takes the ground motions (i.e., PGA and PGV) from a hazard curve for a given hazard level, uses these values to predict a median dynamic response (i.e., k_{max} and k-vel_{max}), and uses the median dynamic response to predict a median displacement.

Two common hazard levels (2% and 10% probability of exceedance in 50 years) and two k_y values (0.1 and 0.2 g) are selected for the comparison between deterministic and probabilistic analyses. These analyses were performed for the hazard defined in Figure 3.1 with T_m=0.5 s and T_s/T_m = 0.0, 0.25, 0.5, and 1.0 s using both scalar and vector models. Figure 3.17 plots the ratio of the deterministic to probabilistic displacements versus T_s/T_m for all of the analyses performed. These data clearly show that the deterministic analysis predicts smaller sliding displacements (except at T_s/T_m=0 for the vector model), and the under-prediction increases with larger T_s/T_m. The reason the underprediction because larger is that very small deterministic displacements are predicted due to the deterministic k_{max} approaching k_y. On the other hand, the probabilistic analysis considers the full k_{max} distribution, not only the median value, in the displacement calculation, such that larger displacements are predicted even if the median k_{max} is close to k_y.

For the case where the deterministic results are larger (i.e. vector model at T_s/T_m=0), the (k_{max}, k-vel_{max}) model directly chooses PGA and PGV from separate ground motion hazard curves at the same hazard level, which essentially assumes perfect correlation ($\rho \sim 1.0$) between PGA and PGV. But the probabilistic approach incorporates the correlation as $\rho \sim 0.6$ for the calculation of $P[PGA, PGV]$. Thus, the deterministic approach overestimates the PGV relative to PGA, and its over-prediction in ground motion balances out, or even larger than, the effect of ignoring the uncertainty in

the displacement prediction. Even with the overestimation of PGV, the deterministic approach still mostly under-predicts the sliding displacements via the (k_{max}, k-vel_{max}) model.

The small sample of analyses presented in Figure 3.17 indicates that the deterministic analysis maybe un-conservative and that performing fully probabilistic analysis can be important and helpful.

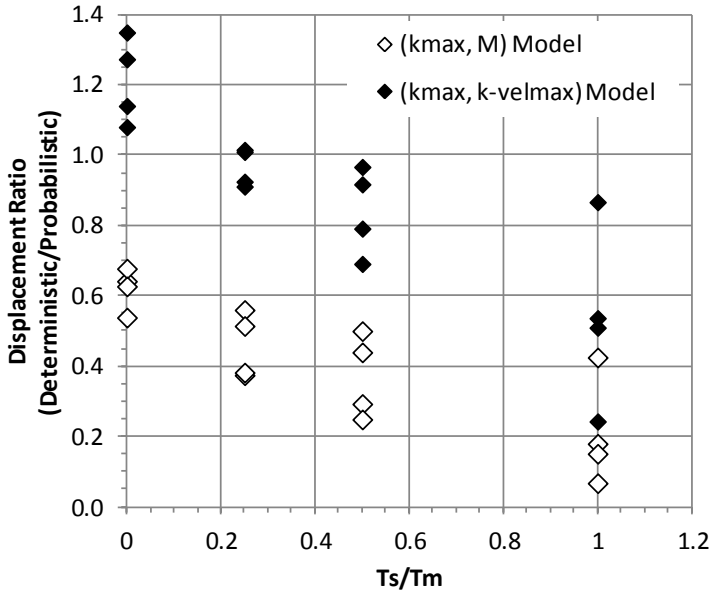

Figure 3.17 Ratio of deterministic to probabilistic predictions of displacements

3.5 INCORPORATING EPISTEMIC UNCERTAINTY

Uncertainties always exist when characterizing the slope properties (e.g., soil shear strengths, ground water conditions, and sliding block thickness) for a stability analysis. Ignoring these epistemic uncertainties and assuming a single set of slope

properties leads to a single value of k_y, which simplifies the computation of the dynamic response of the slope, but it may lead to an inaccurate assessment of the seismic slope performance during earthquakes.

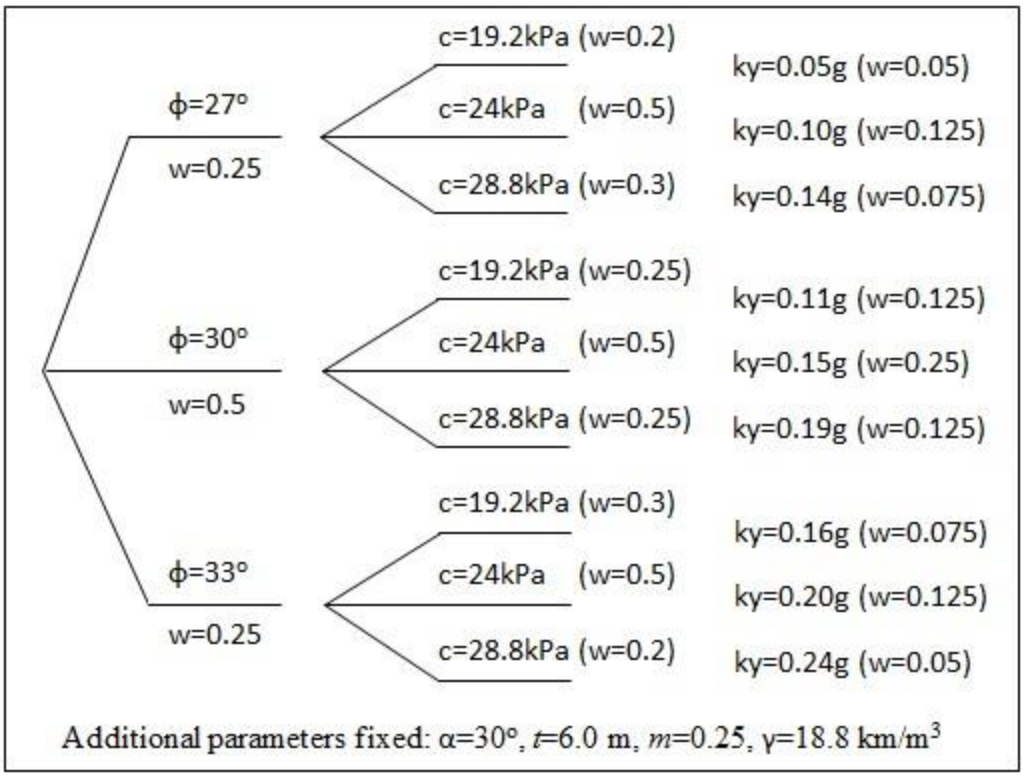

Figure 3.18 Logic tree for the assessment of yield acceleration

A logic tree analysis can be used to account for epistemic uncertainties in the assessment of the seismic slope stability hazard (Saygili 2008). A logic tree is made of nodes and branches, as illustrated in Figure 3.18. Nodes represent the input parameters under consideration and the branches associated with a node represent discrete, possible values for that parameter. Each branch is associated with a weight, and the weights from

all branches from one node must equal 1.0. Following branches through each node defines the input parameters for a single k_y value and the product of the weights of the branches represents the weight associated with that k_y.

For the logic tree shown in Figure 3.18, three discrete values are assumed for both c and ϕ resulting in nine possible values of k_y computed for an infinite slope analysis. The other parameters in the infinite slope analysis (i.e., slope angle, thickness, saturation ratio, and unit weight) are held constant. To incorporate the multiple values of k_y into the seismic displacement analysis, a displacement hazard curve is computed for each k_y given the ground motion hazard curve. The displacement hazard curves for the 9 k_y in the logic tree are shown by the gray curves in Figure 3.19. A mean displacement hazard curve (solid black line in Figure 3.19) is calculated from the multiple hazard curves and their weights. This averaging is done on the hazard levels (i.e., λ_D) for each displacement level. To illustrate the influence of epistemic uncertainties on the seismic displacement hazard, the displacement hazard curve for the best estimate k_y=0.15g (c=24kPa, ϕ=30^o) is also shown in Figure 3.19. The mean displacement hazard curve from the logic tree analysis is higher than the hazard curve using the best estimate k_y, indicating that the seismic slope performance is underestimated when one does not incorporate uncertainties in the soil properties.

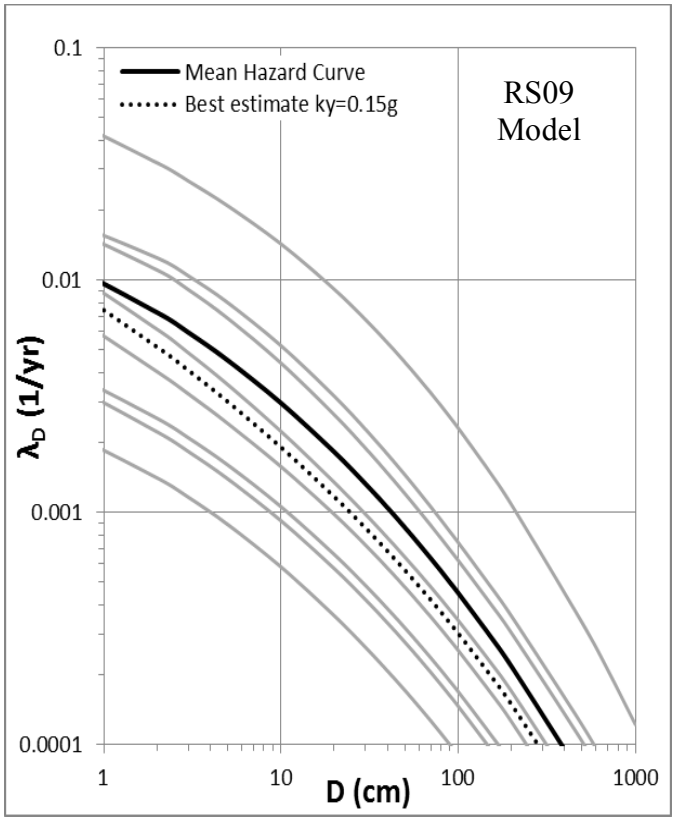

Figure 3.19 Rigid Displacement Hazard Curves for Logic Tree

A logic tree analysis can be applied to all uncertain parameters and models within the seismic slope stability analysis, including the sliding block properties (i.e. *t* and *m*) and sliding displacement models. The application of the logic tree approach should include each of these components.

3.6 SUMMARY

This chapter described the probabilistic framework for computing sliding block displacements for flexible slopes. The generation of displacement hazard curves from the empirical models for the seismic loading parameters (k_{max}, k-vel_{max}) and the scalar and vector displacement models was provided. Deterministic and probabilistic estimates of seismic loading and sliding displacements were compared. Finally, the logic tree approach was introduced to incorporate epistemic uncertainties existing in the slope properties, such as shear strengths, ground water conditions and sliding block thickness. The results show that the seismic slope performance is underestimated when uncertainties in soil properties are not incorporated in the analysis.

Chapter 4 Application of Probabilistic Framework: Lexington Elementary School

4.1 INTRODUCTION

In Chapter 3, the probabilistic framework for flexible sliding displacements was described and this framework was demonstrated using hypothetical values of yield acceleration k_y, site period T_s, and mean period of ground motion T_m. These parameters play a critical role in evaluating the seismic performance of slopes, and the estimation of these parameters for a site-specific analysis requires significant site information including the slope geometry, soil profile, field and lab testing, ground water conditions, seismic hazard assessment, etc. The available site information may not clearly lead to the required inputs for a probabilistic sliding displacement analysis, and engineering judgment may be required. Additionally, the uncertainties in the site information must be characterized, so that the logic tree analysis can be performed without overestimating or underestimating the uncertainties.

Lexington Elementary School (W-121.99 N37.18) in Santa Clara County, California is selected for the implementation of the probabilistic analysis. The school location is within less than a mile of the San Andreas Fault (Figure 4.1) in an area of high seismic hazard. The terrain around the site is slightly inclined from the west to the east with about an 8^o slope. Fugro Consultants Inc. (2011, 2012) performed static and dynamic slope stability analyses for the Lexington Elementary School using standard deterministic methods. Static and pseudo-static limit equilibrium slope stability analyses

were performed to determine the factor of safety and yield acceleration for the idealized soil profiles, which were developed based on local geology and laboratory test results. These values were then used to estimate the expected level of deformation from ground shaking for a 475-year return period. Because of the available subsurface and seismic hazard information for this site, it is well suited for application of the developed probabilistic method.

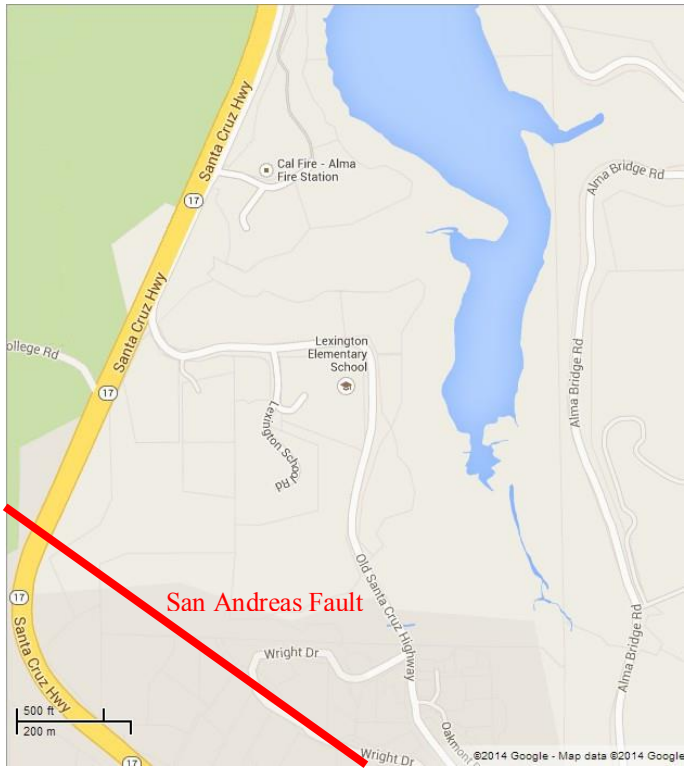

Figure 4.1 Map of Lexington Elementary School (Google Map)

This chapter first describes the available site information for the Lexington Elementary School. This information is used to identify the best estimate properties and their uncertainty, which are then used to perform a pseudo-static slope stability analysis for identifying the critical failure surface and associated yield acceleration. A logic tree is developed that incorporates the uncertainties in slope properties (e.g. shear strengths) and ground motions (i.e. mean period T_m). Then the full probabilistic analysis is performed to evaluate the seismic landslide potential of this site.

4.2 INPUT PARAMETERS

4.2.1 Site Conditions and Slope Geometry

As seen in Figure 4.1, Lexington Elementary School is located just east of the Santa Cruz Highway, and the Lexington reservoir is about 500 ft away to the east of the school site. The school site is about 400 ft long from east to west and 350 ft wide from north to south, and its elevation is about 760 ft above sea level. The terrain around the school is slightly sloped 8^o from west to east, but the slope that has the most significant landslide potential near the school site is sloped at about 18^o. The San Andreas Fault is less than a mile to the south, and it dominates the seismic hazard of this site. Although the 1989 Loma Prieta Earthquake (W-121.877 N37.04) occurred about 18 km away, there are no indications of previous landslide movements at the surface of the site or within about 170 ft of the ground surface (Fugro, 2011). However, future earthquakes may be much closer and stronger, so it is necessary to evaluate the seismic performance of the slopes at the school site.

Figure 4.2a shows a geologic cross-section of the school site and Figure 4.2b provides an idealized cross-section for stability analyses. The surficial soils (Qsur) are fluvial deposits and alluvial fan deposits (Qriver, Qfan). The underlying soil is the Plio-Pleistocene Santa Clara formation (QTsc), which consists of fluvial boulder to pebble gravel, sandstone, and siltstone locally including thin bedded lacustrine mudstone. The upper part of the Santa Clara formation has relatively smaller shear strengths, but beyond 200 ft depth (QTsc_deep) it can be treated as very dense soil or soft rock.

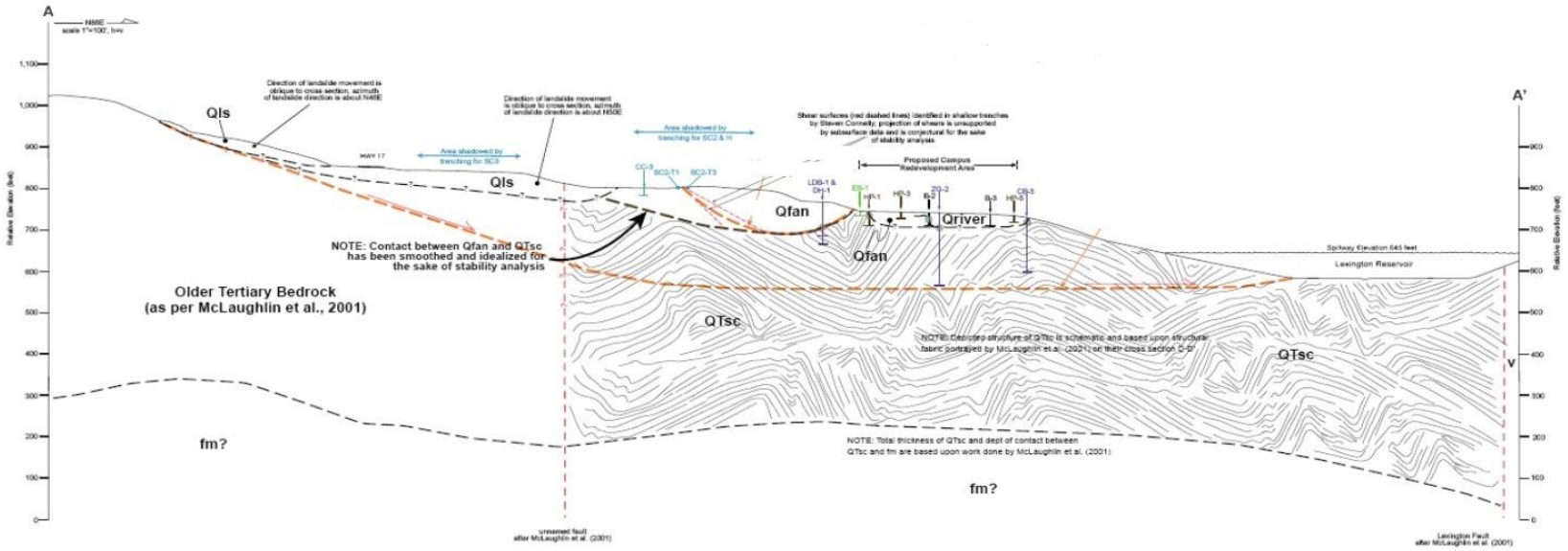
A
A'
Qls
Qls
Qfan
Qfan
Qriver
QTsc
QTsc
fm?
fm?
Older Tertiary Bedrock
(as per McLaughlin et al., 2001)
NOTE: Contact between Qfan and QTsc
has been smoothed and idealized for
the sake of stability analysis
Lexington Reservoir

(a)

Figure 4.2

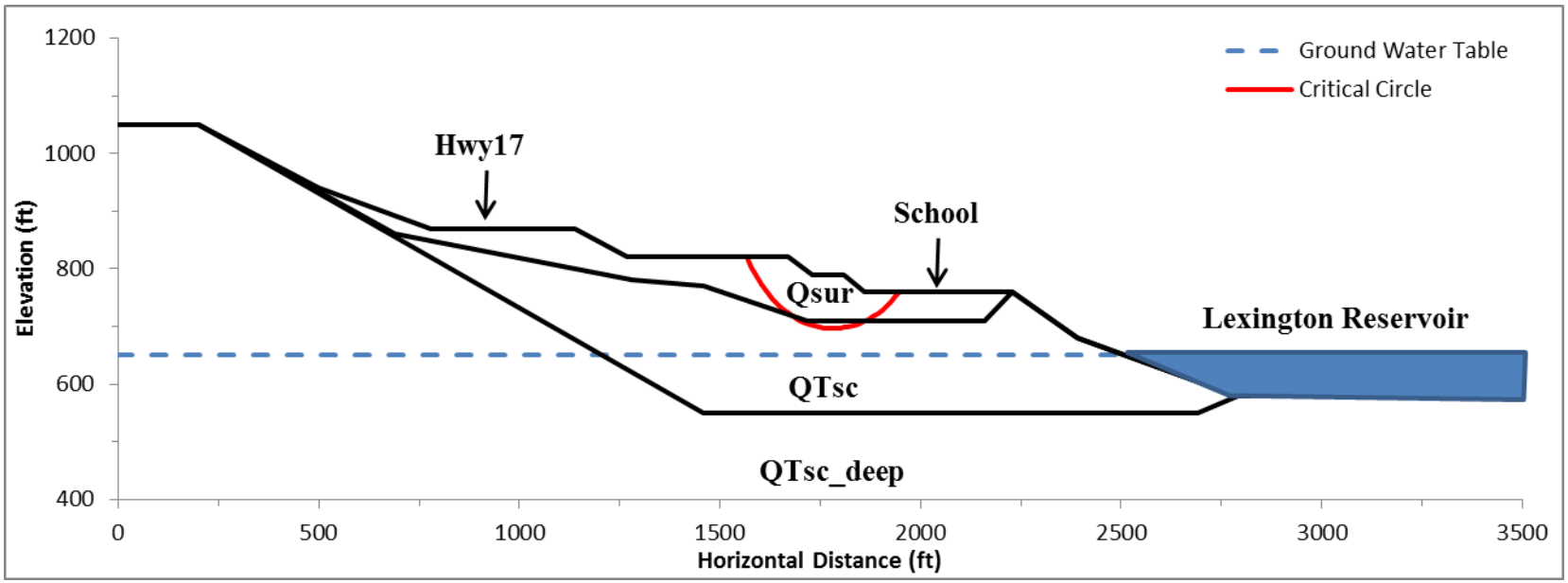

(b)

Figure 4.2 Site cross-section of Lexington Elementary School (a) geologic and (b) idealized

The ground water table rises slowly from the Lexington Reservoir, and the school site is very close to the reservoir (Figure 4.2). Therefore, the ground water table of the school site is assumed to be at the same elevation as the Lexington Reservoir (650 ft). Based on this assumption, the ground water table is located at about 110 ft depth at the site, within the upper Santa Clara formation (QTsc).

Slope stability analyses by Fugro (2011, 2012) found that a potential shallow failure surface near the school site (Figure 4.2b) was more critical than a large-scale deep failure that extended into the deep Santa Clara formation (QTsc_deep). In this case, the ground water beneath the site does not influence the slope stability analysis, because the shallow failure surface does not reach the ground water table (Figure 4.2b).

There is a vertical surcharge load of 1,500 psf corresponding to the building zone on the school site, but this load may help stabilize the shallow failure at the toe rather than drive the failure. To be conservative, this surcharge load is not considered for the slope stability analysis.

4.2.2 Shear Strengths and Shear Wave Velocity

The shear strengths of the surficial soils (Qsur) were interpreted based on laboratory test results from direct shear tests (DS) and unconsolidated-undrained triaxial compression tests (UTC) conducted by Pacific Crest Engineering (2011). The DS and UTC tests were performed at multiple values of normal stress and the total stress shear strength parameters (c and ϕ) were reported. In plotting the shear strength as a function of depth from the various tests and samples, the total normal stress at the sample depth was used along with the reported c and ϕ for that specimen to compute the shear strength.

The measured shear strengths of the surficial Qsur deposits are plotted versus depth in Figure 4.3. The data vary widely, indicating significant uncertainty in the strength of these materials. The best estimate shear strength profile developed by Fugro (2012) increases linearly with depth and is shown in Figure 4.3. Also shown are low strength and high strength profiles that we developed to account for the uncertainty in the shear strength characterization. The low and high strength profiles roughly represent 5^{th} and 95^{th} percentile levels of the measured shear strengths, respectively. The slope of the shear strength profile is assumed the same for the low, high, and best-estimate relationships.

The test results for the upper Santa Clara formation (QTsc) are shown in Figure 4.4. The deep Santa Clara formation (QTsc_deep) beyond 200 ft depth is very stiff and strong such that potential landslides will not extend into this layer. The best estimate shear strength profile developed by Fugro (2012) is shown in Figure 4.4, along with the corresponding values of c and ϕ. Low strength and high strength profiles were developed as part of this study to account for the variability in the test data (Figure 4.4). These profiles parallel the best estimate profile and thus are modeled through a change in cohesion combined with the best-estimate ϕ.

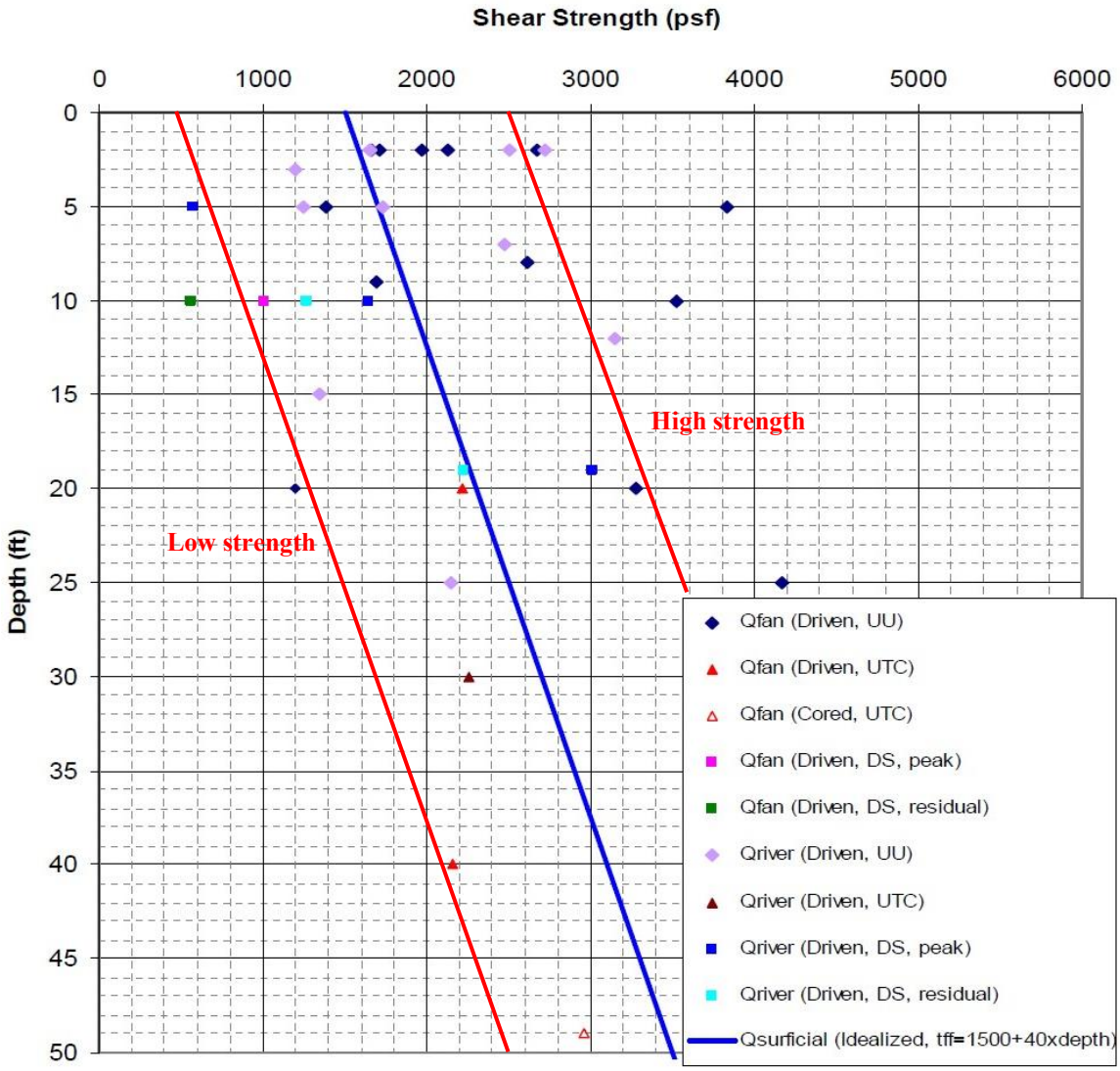

Figure 4.3 Shear strength of surficial deposits Qsur (Fugro, 2012)

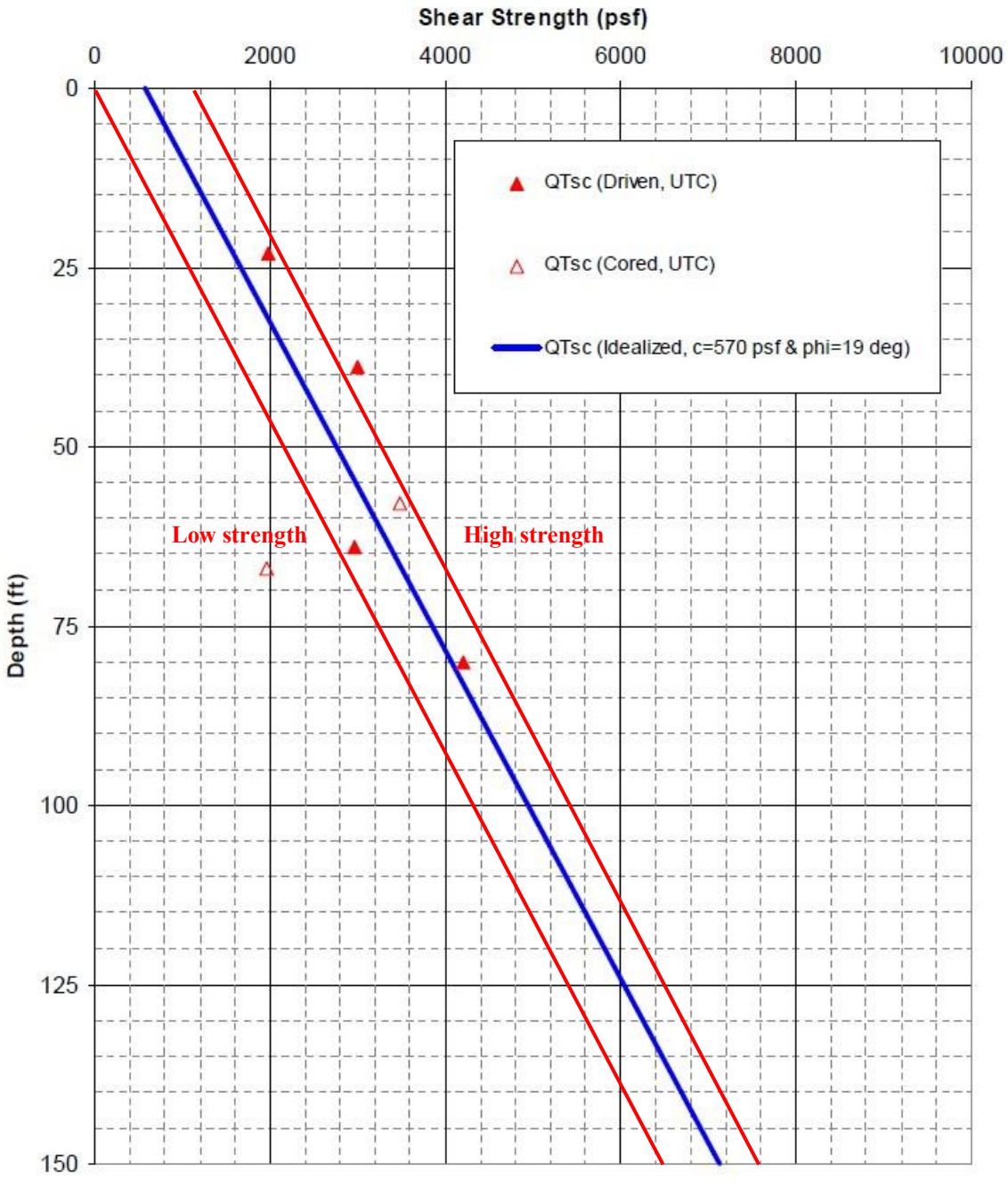

Figure 4.4 Shear strength of the upper Santa Clara formation (QTsc). Note depth is referenced to the top of QTsc. (Fugro, 2012)

A shear wave velocity (V_S) profile is required for the dynamic response analysis. In the absence of direct measurements, the V_S profile is estimated through empirical relationships. The V_S profile for the Qsur deposits was estimated by Fugro (2012) using an empirical relationship by Dickenson (1994) that relates Vs with the undrained shear strength, Su for alluvial soils in the San Francisco Bay Area. The data used by Dickenson (1994) to develop the relationship are shown in Figure 4.5 along with the best fit power law relationship. The power law relationship is given by:

$$V_S = A \cdot S_u{}^{n} \tag{4.1}$$

where A = 18 and n = 0.475 for V_S in units of ft/s and Su in units of psf. Most of the Su data in Figure 4.5 range from 0 to 3,000 psf, and this range is similar to the measured shear strengths shown in Figure 4.3 for the Lexington School site.

The scatter of data around the fitted curve in Figure 4.5 suggests uncertainty in the empirical model. Although Dickenson (1994) did not explicitly provide an estimation of the uncertainty in his model, the scatter of data is well represented by the dashed lines shown in Figure 4.5. These lines can be represented by a power law with the same exponent (n = 0.475) and values of A equal to $A_{low} = 15$ and $A_{high} = 21$.

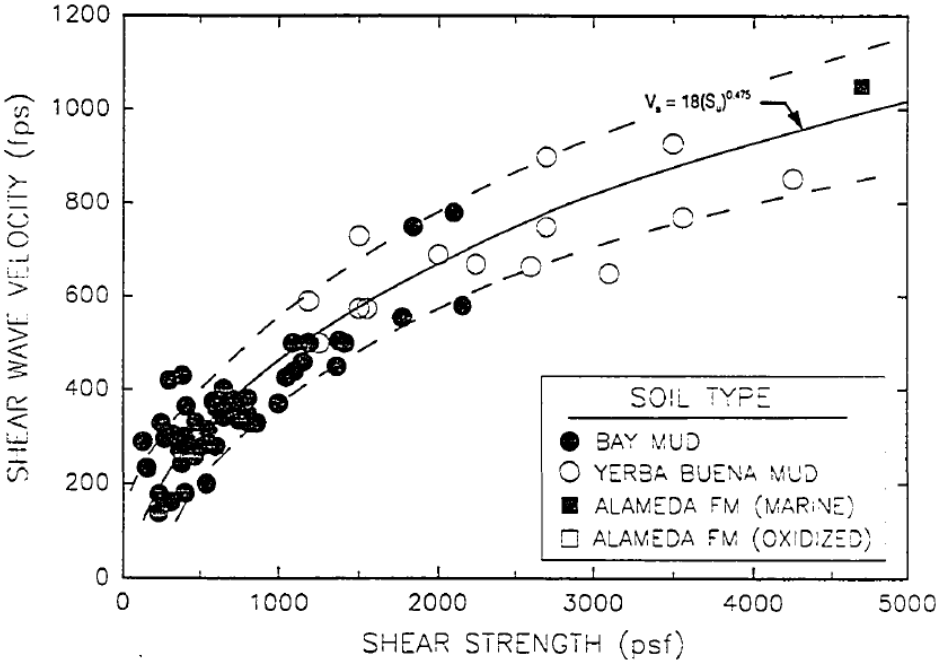

Figure 4.5 Variation of shear wave velocity with undrained shear strength of cohesive soils (Dickenson 1994)

The underlying QTsc material is older (Plio-Pleistocene) and stiffer than the Qsur deposits such that the relationship in Figure 4.5 is not appropriate. Instead, G_{max} is related to Su using another empirical model developed by Dickenson (1994) and then V_S is computed from G_{max} and the mass density (i.e., $V_S = \sqrt{G_{max}/\rho}$). This relationship between G_{max} and Su is linear and taken as:

$$G_{max} = B \cdot S_u \tag{4.2}$$

where Su and G_{max} are both in units of psf and B is a dimensionless model parameter. Dickenson (1994) recommended that the coefficient B depends on Su, overconsolidation ratio (OCR), Plasticity Index (PI) and effective confining stress. For

the QTsc material (PI = 15, OCR = 1), Fugro (2012) took B=1280 from a range of published values (500 ~1450) summarized by Dickenson (1994) from other researchers. Such selection is based on the assumption that V_S profile has no large change at boundaries between soil layers (Figure 4.6). Beyond 200 ft depth (i.e., QTsc_deep deposits), V_S=1800 ft/s was selected by Fugro (2012) as representative of "very dense soil or soft rock" conditions (NEHRP Soil Type C).

The uncertainties in V_S for the QTsc and QTsc_deep layers are assumed to be proportional to the uncertainty in Qsur. As a result, the high and low values of V_S for the QTsc deposits can be calculated by scaling the parameter B based on the baseline, low, and high values of A. The resulting B values are B_{low} = 890 and B_{high} = 1740. The resulting low and high values of V_S for QTsc_deep are 1,500 to 2,100 ft/s, and such values are compatible with the NEHRP site class C (1,200 ~ 2,500 ft/s) determined for the deep Santa Clara formation. The resulting baseline, low and high shear wave velocity profiles are illustrated in Figure 4.6 for the Lexington school site, and the best-estimate, low and high shear strengths are used to create Figure 4.6a, Figure 4.6b and Figure 4.6c respectively. It should be noted that the thickness of Qsur layer is about 50 ft directly below the school site (Figure 4.2b), but it is up to 80~90 feet thickness at the location of the potential shallow failure surface.

To develop the logic tree and associated weights for both the shear strength parameters and the shear wave velocity profiles, a normal distribution is assumed. The baseline values are taken to represent the mean (μ) and the low and high values are taken as the 5% and 95% values. To approximate a standard normal distribution N(0,1) with three points at 5%, 50%, and 95% (i.e., $\mu - 1.6\sigma$, μ, $\mu + 1.6\sigma$), the corresponding weights are 0.2, 0.6, and 0.2.

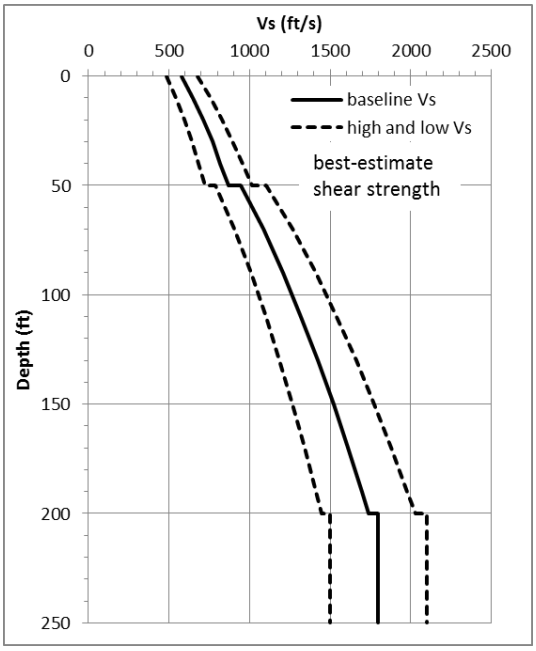

(a)

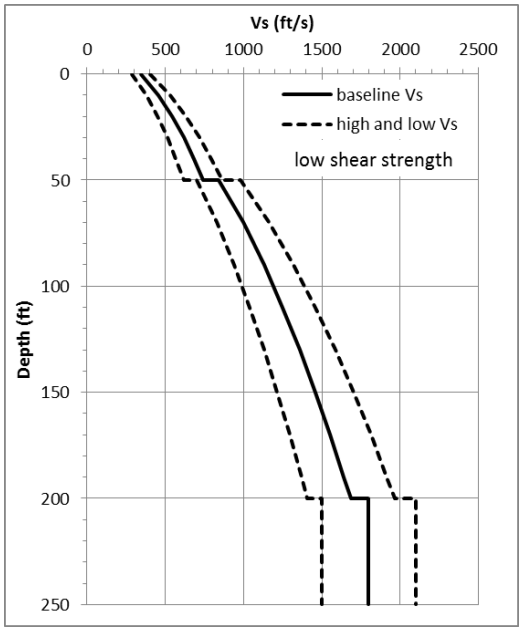

(b)

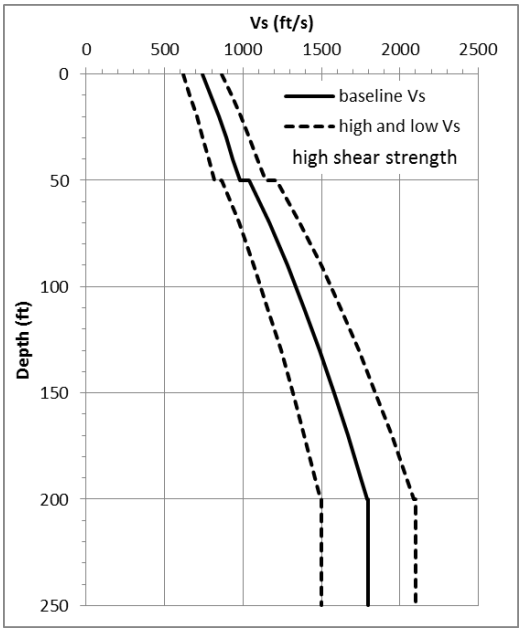

(c)

Figure 4.6 Baseline, low, and high shear wave velocity profiles based on (a) best-estimate, (b) low, and (c) high shear strengths

The logic tree branches for the shear strength and shear wave velocity profiles for each of the geologic units are summarized below.

Table 4.1 Logic tree for shear strengths

	Qsur	QTsc	Weight
Low	$\mathrm{Su} = 500 + 40 \cdot \mathrm{z}$	$\mathrm{c} = 0$ psf, $\phi = 19°$	0.2
Best Estimate	$\mathrm{Su} = 1500 + 40 \cdot z$	$\mathrm{c} = 570$ psf, $\phi = 19°$	0.6
High	$\mathrm{Su} = 2500 + 40 \cdot z$	$\mathrm{c} = 1140$ psf, $\phi = 19°$	0.2

*Note: Su in units of psf, z in units of feet.

Table 4.2 Logic tree for shear wave velocity

	Qsur	QTsc	Weight
Low	$\mathrm{V_S} = 15 \cdot \mathrm{S_u}^{0.475}$	$\mathrm{G_{max}} = 890 \cdot \mathrm{S_u}$	0.2
Baseline	$\mathrm{V_S} = 18 \cdot \mathrm{S_u}^{0.475}$	$\mathrm{G_{max}} = 1280 \cdot \mathrm{S_u}$	0.6
High	$\mathrm{V_S} = 21 \cdot \mathrm{S_u}^{0.475}$	$\mathrm{G_{max}} = 1740 \cdot \mathrm{S_u}$	0.2

*Note: $\mathrm{V_S}$ in units of ft/s, $\mathrm{G_{max}}$ in units of psf.

4.2.3 Yield Acceleration and Site Period

The yield acceleration k_y, which characterizes the sliding resistance of a slope against earthquake shaking, is required by empirical displacement models for predicting sliding displacements. With the slope geometry, soil profile and shear strengths, the yield acceleration k_y can be computed through a pseudo-static slope stability analysis, which uses an inertial force ($\mathrm{k} \cdot \mathrm{W}$) acting on the failure mass to represent the effects of earthquake shaking. The value of k that produces a pseudo-static factor of safety (FS)

equal to 1.0 (i.e., full shear strengths are mobilized to resist sliding along the critical failure surface) is the yield acceleration k_y of the slope.

The pseudo-static slope stability analysis can be fulfilled by various limit equilibrium methods. The Spencer's slice method is chosen for this analysis, because both force and moment equilibriums are enforced. The inertial force ($k \cdot W$) is applied to the center of gravity of each slice. No pore water pressure is considered in the static slope stability analysis because 1) the ground water table is much lower than the critical failure surface and 2) total stress analysis (undrained shear strengths) is used for Qsur and QTsc layers.

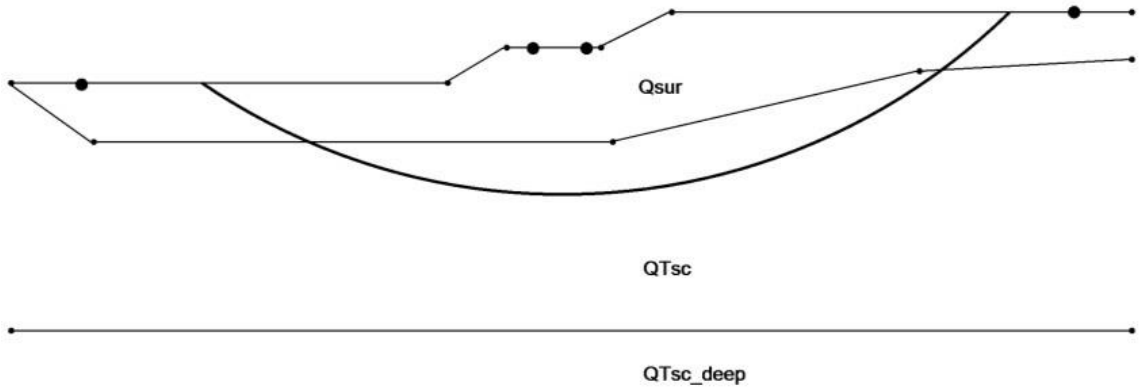

Figure 4.7 Critical failure surface with best-estimate shear strengths under pseudo-static condition

Assuming that the seismic loading acting on the slope is horizontal, the k_y value can be computed under the pseudo-static condition. The critical failure surface with best-estimate shear strengths is shown in Figure 4.7, and the associated yield acceleration

is 0337 g. The failure mass extends into the QTsc layer with a maximum thickness (H_{max}) of 151.9 ft. The average thickness (H_{avg}) across the entire failure surface is 90.4 ft.

Similarly, k_y values for the low and high shear strengths are computed by the pseudo-static analyses and result in k_y values of 0.241 g and 0.390 g, respectively. The k_y value changes significant (i.e., -28% ~ +16%) with changes in shear strength. The results of all k_y computations are summarized in Table 4.3, and the critical failure surfaces for the low and high shear strengths are shown in Figure 4.8 and Figure 4.9. The maximum thickness (H_{max}) and average thickness (H_{avg}) of the failure surface decreases by 65% when using the low shear strength, indicating that the critical failure surface becomes shallower with smaller shear strength. The critical failure surface computed for high shear strength is deeper than the one with best-estimate shear strength. Any changes in the thickness of the failure surface will influence the site period used in the sliding displacement analysis.

Table 4.3 Results of pseudo-static slope stability analyses

Shear Strength	k_y (g)	H_{max} (ft)	H_{avg} (ft)	Weight
High	0.390	189.3	116.3	0.2
Best-Estimate	0.337	151.9	90.4	0.6
Low	0.241	48.6	32.2	0.2

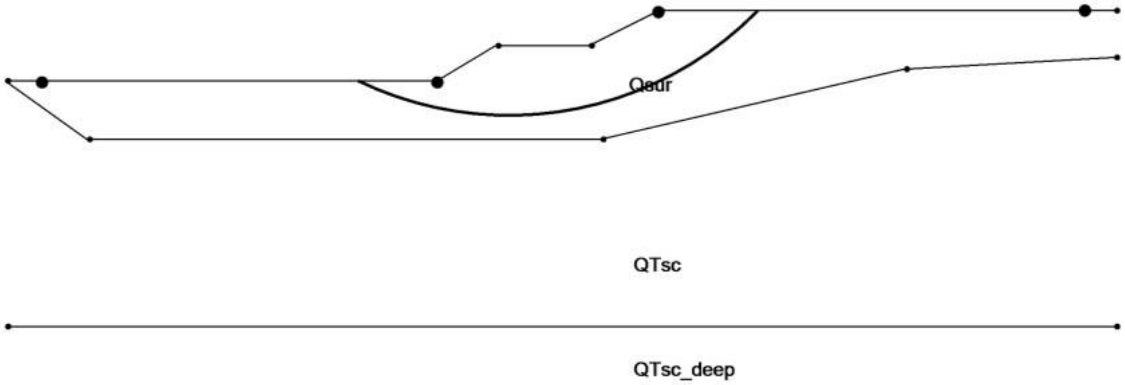

Figure 4.8 Critical failure surface with high shear strengths under static condition

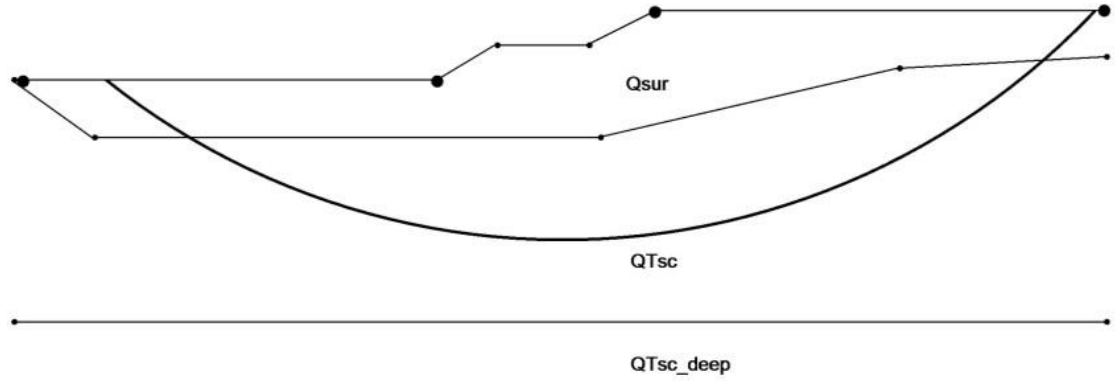

Figure 4.9 Critical failure surface with low shear strengths under static condition

With shear wave velocity and thickness of failure mass, The site period T_s, is computed from the average thickness of the failure mass (H_{avg}) and the average shear wave velocity over that thickness using $T_s = 4H/V_s$. The uncertainty in T_s is due to uncertainty in the shear wave velocity, as well as uncertainty in the thickness of the failure mass, as predicted for different shear strengths. Table 4.4 summarizes the different values of T_s that result from different combinations of H_{avg} and V_s. The resulting T_s values range from 0.22 s to 0.52 s.

Table 4.4 Variation of T_s with shear strengths and V_s predictions

Thickness (ft)		Uncertainty In Shear Strength	Uncertainty in V_s Predictions					
			Average V_s (m/s)			T_s (s)		
			High	Mean	Low	High V_s	Mean V_s	Low V_s
H_{avg}	116.3	High	384	329	274	0.37	0.43	0.52
	90.4	Best-Estimate	317	272	226	0.35	0.41	0.49
	32.2	Low	179	153	128	0.22	0.26	0.31

One thing to be noted is that the site period calculation and dynamic response prediction in this study are based on one-dimensional (1D) site response analysis. However, the site and critical failure surfaces described here are two-dimensional (2D) problems. Rathje and Bray (2001) found that the dynamic response predicted by 1D analysis is generally greater than for 2D analysis, although the 1D sliding displacement is not always greater than the 2D result. Nonetheless, a 1D site period using an average thickness is selected for analysis.

Intuitively, materials with smaller shear strength are associated with smaller stiffness (i.e., V_s), which was the basis for the shear strength and V_s relationships used in Section 4.2.2. A failure mass with lower shear strengths should be treated as softer in

the dynamic response analysis. However, in Table 4.4, the failure mass with low shear strengths has a smaller T_s than the failure masses with idealized and high shear strengths, indicating that low shear strengths give a more rigid failure mass for this special case. The reason of this unusual observation is that the reduction of the failure mass thickness dominates the change of T_s, when low shear strengths are used. In another word, a thin soft soil mass may have a more rigid seismic performance than a thick hard soil mass.

4.2.4 Ground Motion Hazard

The ground motion seismic hazard curve and seismic hazard deaggregation are required for the computation of the dynamic response and sliding displacements. The PGA hazard curve can be obtained from the hazard curve application tools developed by the 2008 National Seismic Hazard Map Project (NSHMP, http://geohazards.usgs.gov/hazardtool/). This tool provides the ground motion hazard for 19 levels of ground shaking. For PGA, these 19 levels range from 0.005 to 2.13 g. The USGS website also provides the 2008 Interactive Deaggregations, which contains seismic hazard deaggregation information (i.e., distribution of magnitude and distances contributing to the selected ground motion hazard) of the 48 continental states in the United States (http://geohazards.usgs.gov/deaggint/2008/). There are 36 seismic hazard levels available for generating seismic hazard deaggregation. The deaggregation information is used to identify the dominant earthquake magnitude or magnitudes corresponding to a given ground motion, and it is also used to develop vector hazard information (Section 3.2.2).

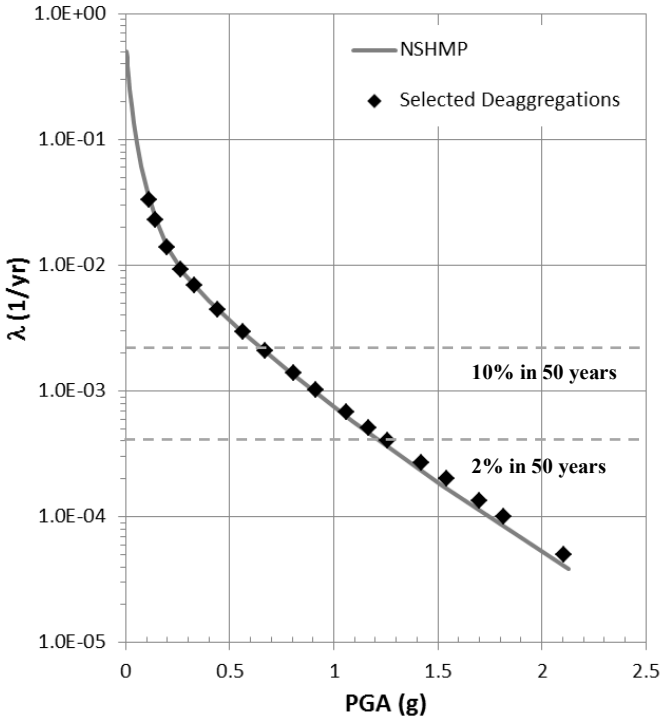

Figure 4.10 PGA hazard curve and selected hazard levels of deaggregation

Figure 4.10 shows the NSHMP PGA hazard curve of the Lexington school site and the hazard levels of deaggregation. It is not necessary to use all 36 hazard levels of deaggregation because some hazard levels are very close to each other. Therefore, 18 seismic hazard levels (Table 4.5) are selected for generating seismic hazard deaggregation information. Figure 4.10 shows that the selected seismic hazard levels are evenly distributed along the PGA hazard curve.

As seen in Table 4.5, the maximum PGA level is 2.11 g at 1% probability of exceedance in 200 years (19,900 year return period), and the minimum PGA level is 0.11 g at 50% probability of exceedance in 21 years (30 year return period). The two most

commonly used seismic hazard levels in design are 10% and 2% probabilities of exceedance in 50 years, which correspond with 475 year and 2,475 year return periods, respectively. The corresponding PGA levels for the Lexington School site are 0.67 g and 1.26 g. The mean annual probability of occurrence, P[PGA], as derived from differencing the hazard values (Equation 3.3), is also presented in Table 4.5.

Table 4.5 Selected hazard levels of deaggregation for Lexington Elementary School

Probability	Years	λ (1/yr)	Return Period (yr)	PGA (g)	P[PGA]
50%	21	3.301E-02	30	0.1115	4.951E-03
50%	30	2.310E-02	43	0.14093	9.572E-03
50%	50	1.386E-02	72	0.1975	6.931E-03
50%	75	9.242E-03	108	0.2629	3.466E-03
50%	100	6.931E-03	144	0.3278	2.390E-03
20%	50	4.463E-03	224	0.4428	1.978E-03
20%	75	2.975E-03	336	0.5647	1.178E-03
10%	50	2.107E-03	475	0.6709	7.852E-04
10%	75	1.405E-03	712	0.8074	5.407E-04
5%	50	1.026E-03	975	0.9142	3.604E-04
5%	75	6.839E-04	1462	1.0614	2.565E-04
5%	100	5.129E-04	1950	1.1678	1.399E-04
2%	50	4.041E-04	2475	1.2593	1.218E-04
2%	75	2.694E-04	3712	1.4217	1.015E-04
1%	50	2.010E-04	4975	1.5425	6.768E-05
1%	75	1.340E-04	7462	1.6979	5.025E-05
1%	100	1.005E-04	9950	1.8146	4.188E-05
1%	200	5.025E-05	19900	2.1081	7.538E-05

Three types of seismic hazard deaggregation are provided by the USGS website: geographic deaggregation, deaggregation bins and text-format deaggregation,. As explained later, the text-format deaggregation data are used in subsequent calculations, but the other forms of deaggregation allow for a better visualization of the magnitude and distance distributions.

The geographic deaggregation plots the source contribution deaggregation on a map, which allows for a magnitude and distance deaggregation to be related to the fault in the area. Figure 4.11 plots the sources of ground motion hazard and their contributions for the Lexington school site for the 475 year and 2,475 year return period ground motions. The yellow dot at the center of the blue circle is the Lexington school site. The orange lines represent faults, and the fault closest to the school site is the San Andreas Fault. Figure 4.11 shows that the major source of ground motion hazard is the San Andreas Fault and the associated magnitude is about 7.5.

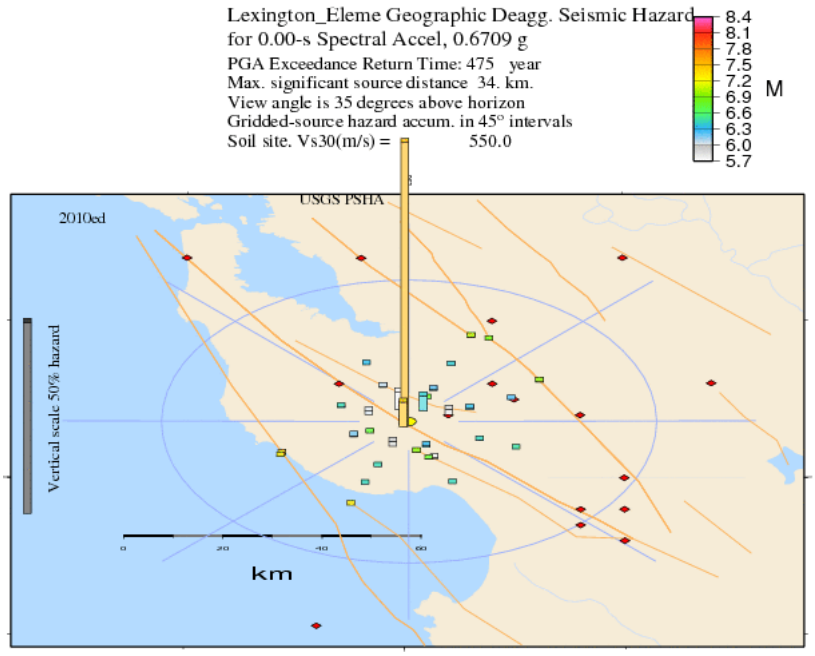

(a)

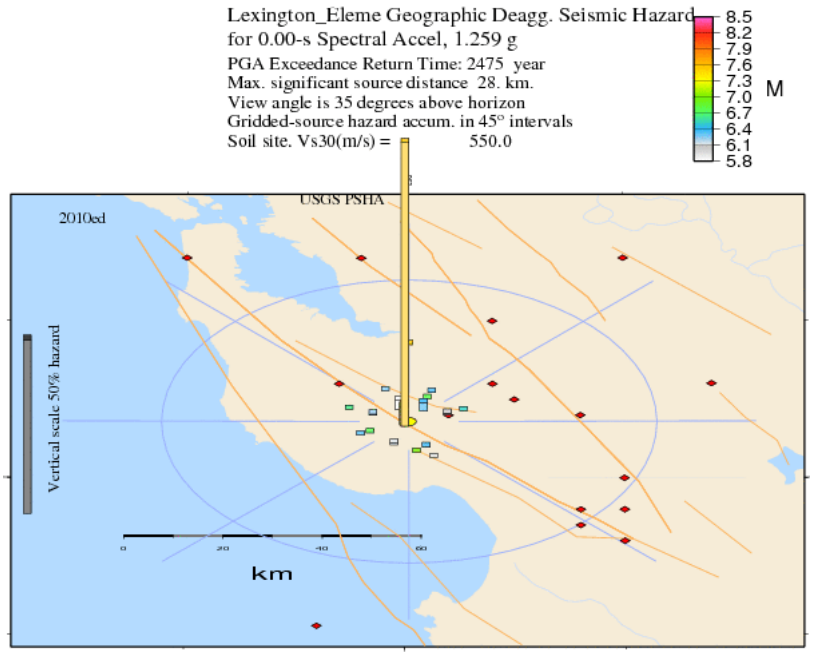

(b)

Figure 4.11 Geographic seismic hazard deaggregation for Lexington Elementary School at (a) 10% in 50 years, and (b) 2% in 50 years

Deaggregation bins, as shown in Figure 4.12, can visually display the contributions of all sources with respect to magnitude and site-to-source distance. The ε value represents the difference, in terms of the number of standard deviations, between the considered PGA level (e.g. 0.67 g at the 475 year return period) and the predicted median PGA value given each combination of M and R. In another words, the ε value shows the probability of exceedance of the considered PGA level given a combination of M and R. Therefore, ε values are larger for smaller magnitudes and longer distances, because such M and R values predict lower median PGA values. The mean magnitude for 2475-year return period is 7.46, higher than the magnitude 7.33 for 475-year return period. The modal events (i.e. largest source contribution) in both cases represent a magnitude of 8.0 and a distance of 1.2 km. Most of the events with large source contributions have magnitude values between 7.0 and 8.0, and these events are all about 1.0 km away from the school site. This reveals the same trend as observed in Figure 4.11; i.e., the source contribution is dominated by events on the San Andreas Fault.

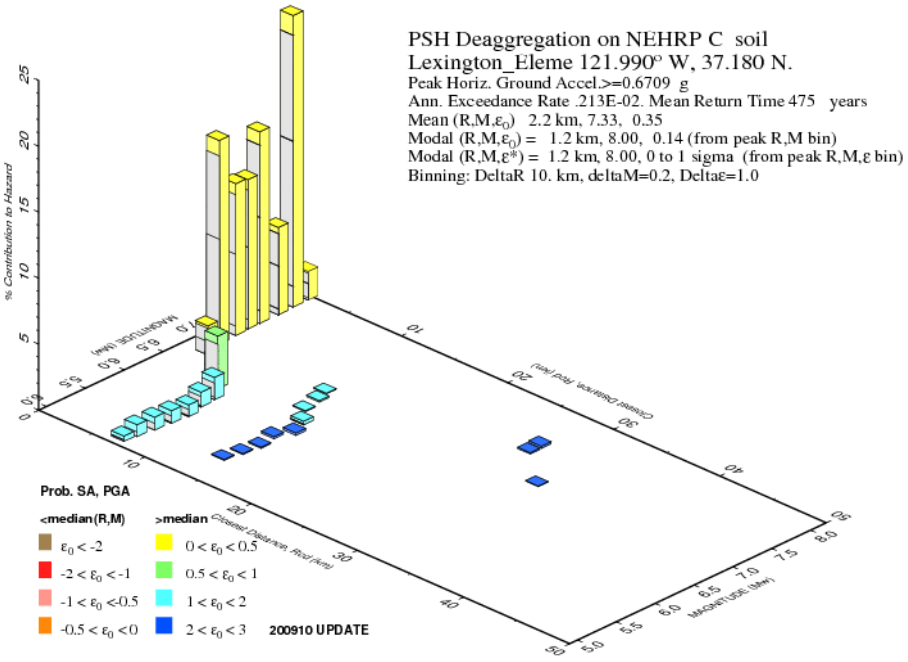

(a)

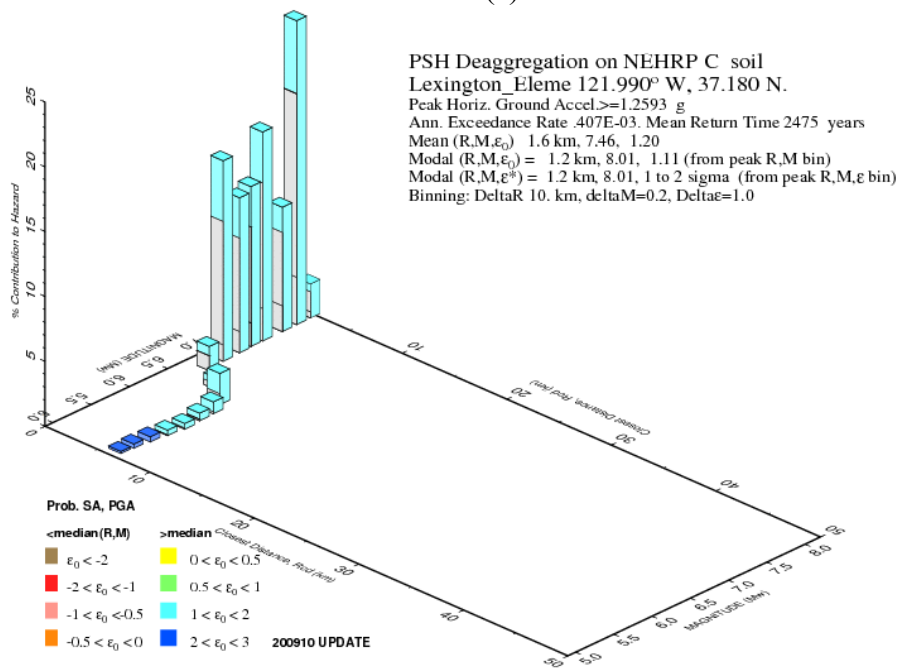

(b)

Figure 4.12 Seismic hazard deaggregation bins for Lexington Elementary School at (a) 475-year return period, and (b) 2,475-year return period

One thing to be noted is that there are some ambiguities in the definition of the site-to-source distance reported in the seismic hazard deaggregation because multiple ground motion prediction equations (GMPE) .are used in the seismic hazard calculation. On the USGS website it explains that the reported site-to-source distance has the same metric as the GMPE used for ground motion predictions. However, different GMPEs use different distance definitions, yet the deaggregation plot only uses a single distance definition (i.e., closest distance). For instance, the seismic hazard calculation and associated deggregation for the Lexington school site use the GMPEs of Boore and Atkinson (2008, BA08), Campbell and Bozorgnia (2008, CB08), and Chiou and Youngs (2008, CY08). BA08 uses R_{JB}, which is the closest distance from the site to the ground surface projection of a fault rupture, while the others use R_{rup}, which is defined as the closest distance from the site to the fault rupture plane. For an event that ruptures the ground surface on a vertical, strike-slip fault, these distance metrics are the same. However, for dip-slip faults and ruptures that do not break the ground surface, the distance metrics will be different. This issue is most important when developing the vector ground motion hazard from the scalar ground motion hazard (i.e., Equation 3.11 in Chapter 3).

The text-format deaggregation contains more details of the deaggregation. Each M, R, and ε scenario is listed in a table along with its contribution to the hazard at each ground motion level, and such a table can be converted into a matrix of magnitude bins and distance bins. The M values are taken every 0.01 magnitude units and the R values every 0.1 km. Using this information we can combine the contribution of defined magnitude and distance bins. The magnitude bins are defined by the lower end of the magnitude bins (e.g. 4.0, 5.0, 5.5, 6.0, 6.5, 7.0, 7.5, 8.0 and 8.4), and the bin sizes are about 0.5 magnitude units wide. The distance bins are also defined by the lower end of

the distance bin (e.g. 0, 2, 5, 10, 20, 50, 100, 200 and 500 km), but these bin sizes increase with distance to account for the large distances considered and the logarithmic decay of amplitude with distance. For instance, an event with M=7.3 and R=1.4 km is put into the magnitude bin 7-7.5 and the distance bin 0-2 km, and its contribution will be summed up with all other events in the same bin. The sum of the contributions for each magnitude bin M_k and distance bin R_l represents $P[M_k, R_l | PGA > PGA_i]$, which is used to develop the vector ground motion hazard (e.g., Equation 3.8).

As mentioned above, three GMPEs (BA08, CB08, and CY08) were used for the computation of the seismic hazard and associated deaggregation. Each GMPE contributes a part of the total deaggregation, and the contribution of each GMPE varies with different return periods. For instance, the contribution of the CY08 model decreases from 62% to 33% when the hazard changes from 1% probability in 200 years to 50% probability in 21 years. Nonetheless, these three GMPEs predict very similar ground motions for the school site, and therefore the variation of the model contributions will not significantly influence the vector hazard calculation. As a result, the percent contribution of each GMPE is assumed constant and taken as equal to the average contribution over all return periods. The model contributions of BA08, CB08, and CY08 are assigned as 33%, 19% and 48%, respectively. The percent contributions are required to take into account the different GMPE when computing the vector ground motion hazard. In particular, it is used in the calculation of $P[PGV_j | PGA_i, M_k, R_l]$, as required in Equation 3.11. Here, the median values and standard deviations of PGA and PGV used for computing $P[PGV_j | PGA_i, M_k, R_l]$ are computed for each GMPE given M_k and R_l, and they are weighted based on the percent contribution of each GMPE. An alternative approach is to only use the deaggregation from one attenuation model, and thus the percent contribution for the different GMPEs is not an issue.

With the PGA hazard curve and the seismic hazard deaggregation, the joint annual probability of occurrence P[PGA,PGV], as shown in Figure 4.13, can be computed using Equations 3.10 and 3.11. Generally, pairs of larger PGA and PGV have smaller annual probabilities of occurrence, while pairs of smaller PGA and PGV have larger probabilities of occurrence. In addition, the probability of a small PGA occurring with a large PGV is very small, and vice versa, because of the relatively high correlation between PGA and PGV (i.e., $\rho = 0.6$). The total annual probability of occurrence summed across all P[PGA,PGV] bins is 0.033 1/yr, which is equal to the mean annual rate of exceedance of the smallest PGA level considered in the analysis (Table 4.5). The P[PGA,PGV] information will be ultimately used to compute the displacement hazard using the vector approach (Equation 3.9).

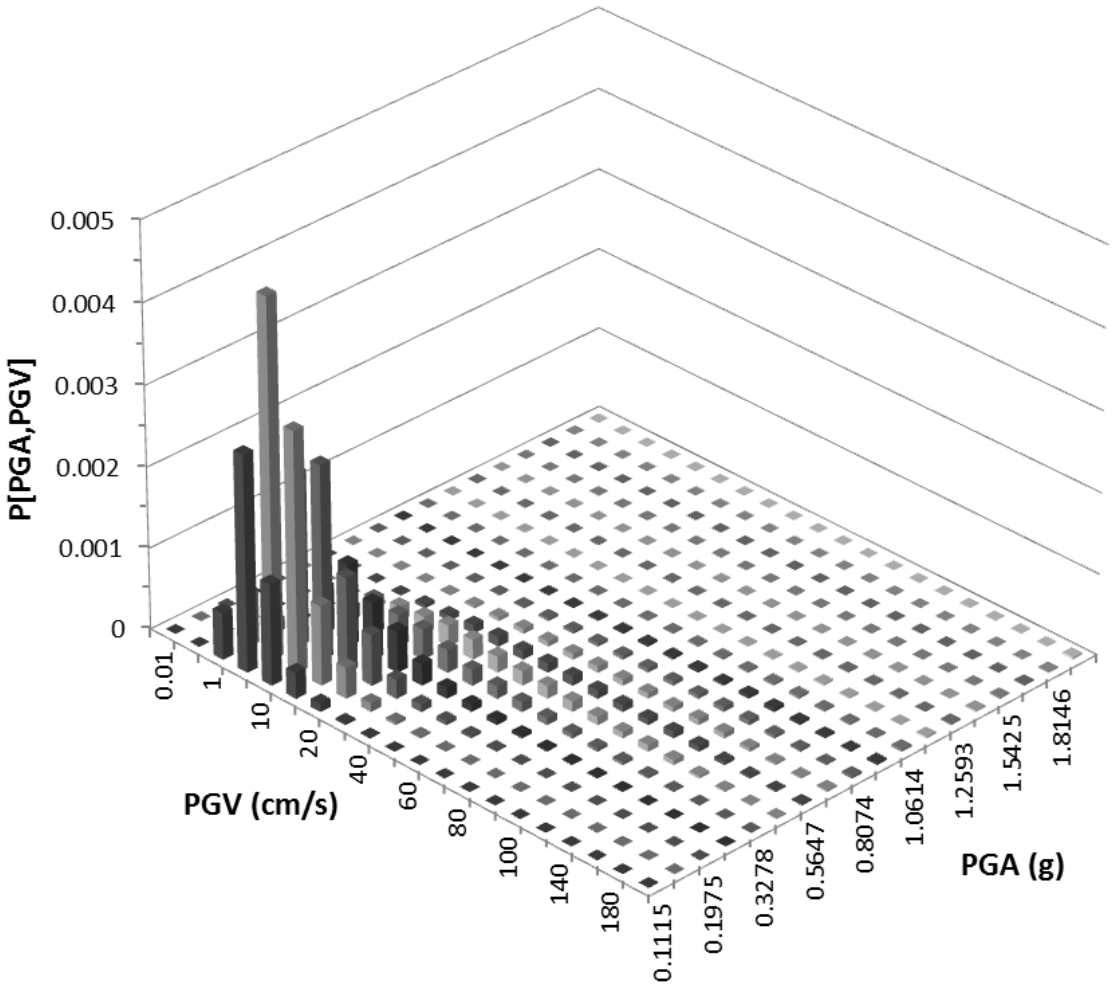

Figure 4.13 Joint annual probabilities of occurrence for (PGA, PGV) pairs for the Lexington school site

For the probabilistic analysis of flexible sliding masses, the mean period of ground motion T_m is required. Rathje et al. (2004) proposed an empirical model for predicting T_m (Equation 2.6) by using magnitude, distance, site class and forward directivity. As seen in the seismic hazard deaggregation, many earthquake sources can contribute to the seismic hazard of a site. Such earthquake sources have different values of M and R, and this variability coupled with the aleatory variability associated with the prediction of T_m results in significant variability in the mean period of ground motion. The rigorous approach to incorporating the variability in T_m would be to include it in the vector of ground motion parameters required for the displacement hazard calculation. This approach requires the estimation of the joint probability of occurrence of PGA, PGV, and T_m (i.e., P[PGA, PGV, T_m]) and the 3x3 covariance matrix between these three parameters. Extension of the vector hazard approach to 3 parameters increases the complexity of the calculations significantly, therefore in this study the uncertainty in T_m is taken into account through a logic tree approach, as described below.

Given a PGA level, the median T_m is predicted using the mean M and R from the seismic hazard deaggregation. Table 4.6 summarizes the mean M and R values for all seismic hazard levels at the Lexington School site. In computing T_m, the site class is assigned as C (i.e., $V_{s,30} = 1800$ ft/s) and Forward Directivity is taken into account because the school site is very close to a major earthquake source . The best estimate T_m for the school site may be approximated as:

1) The weighted mean of the median T_m values, or
2) The weighted mean of all mean $\ln T_m$ values, or
3) The median T_m value predicted by using the weighted mean M and R.

where the weight is taken as the mean annual probability of occurrence of each PGA level, P[PGA]. The smaller ground motions have the larger weights and will overly influence the predicted T_m, but such low PGA levels cannot induce landslide movement because they are unlikely to exceed the k_y values (Table 4.3). Considering the smallest k_y in Table 4.3, the ground motion levels with PGA < 0.26 g should be excluded from the prediction of T_m.

Table 4.6 T_m predictions for Mean M and R at each hazard level

Probability	Years	PGA (g)	P[PGA]	Mean M	Mean R (km)	Median T_m (s)
50%	21	0.1115	4.951E-03	6.44	25.2	0.427
50%	30	0.14093	9.572E-03	6.53	20.6	0.468
50%	50	0.1975	6.931E-03	6.72	14.0	0.538
50%	75	0.2629	3.466E-03	6.90	9.1	0.602
50%	100	0.3278	2.390E-03	7.03	6.2	0.646
20%	50	0.4428	1.978E-03	7.18	3.7	0.691
20%	75	0.5647	1.178E-03	7.27	2.6	0.712
10%	50	0.6709	7.852E-04	7.33	2.2	0.717
10%	75	0.8074	5.407E-04	7.37	1.9	0.721
5%	50	0.9142	3.604E-04	7.40	1.8	0.722
5%	75	1.0614	2.565E-04	7.43	1.7	0.723
5%	100	1.1678	1.399E-04	7.44	1.6	0.724
2%	50	1.2593	1.218E-04	7.46	1.6	0.724
2%	75	1.4217	1.015E-04	7.48	1.5	0.725
1%	50	1.5425	6.768E-05	7.49	1.5	0.725
1%	75	1.6979	5.025E-05	7.50	1.4	0.726
1%	100	1.8146	4.188E-05	7.52	1.4	0.726
1%	200	2.1081	7.538E-05	7.54	1.4	0.726
Weighted mean for PGA>0.26 g				7.12	5.3	0.66

T_m values were predicted using the three approaches. For approach three, the weight mean M and R values considering only PGA ≥ 0.26 g are 7.12 and 5.3 km. The three methods provide very similar results (0.664 s, 0.662 s, and 0.666 s). As a result, the best-estimate T_m value is taken as 0.66 s. The other branches of the logic tree are taken as the 5th and 95th percentiles (i.e., -1.6σ and +1.6σ), and using the $\sigma_{\ln T_m}$ value of 0.416 reported in Rathje et al. (2004) the resulting values of T_m are 0.34 s and 1.29 s. The associated weights for the logic tree are equal to 0.2, 0.6, and 0.2. The two most commonly used seismic hazard levels (i.e., 10% and 2% probabilities of exceedance in 50 years) have large and similar T_m values ($T_m \cong 0.72$ s), which are about 10% greater than the best-estimate T_m adopted above. However, because a large level of uncertainty in T_m has already been considered through the logic tree, the small difference between the different approaches to select a best-estimate T_m is not significant.

4.2.5 Summary of Logic Tree for Lexington School Site

Summarizing all of the above discussions, the logic tree for the Lexington School site is shown in Figure 4.14. The logic tree consists of three sections representing the uncertainties in k_y, T_s, and T_m. The k_y values and T_s values are correlated, because different shear strengths lead to different thicknesses of the failure mass. The T_m values are not correlated to the k_y and T_s values. There are 27 branches in the logic tree, and the best-estimate branch has $k_y = 0.34$ g, $T_s = 0.41$ s and $T_m = 0.66$ s.

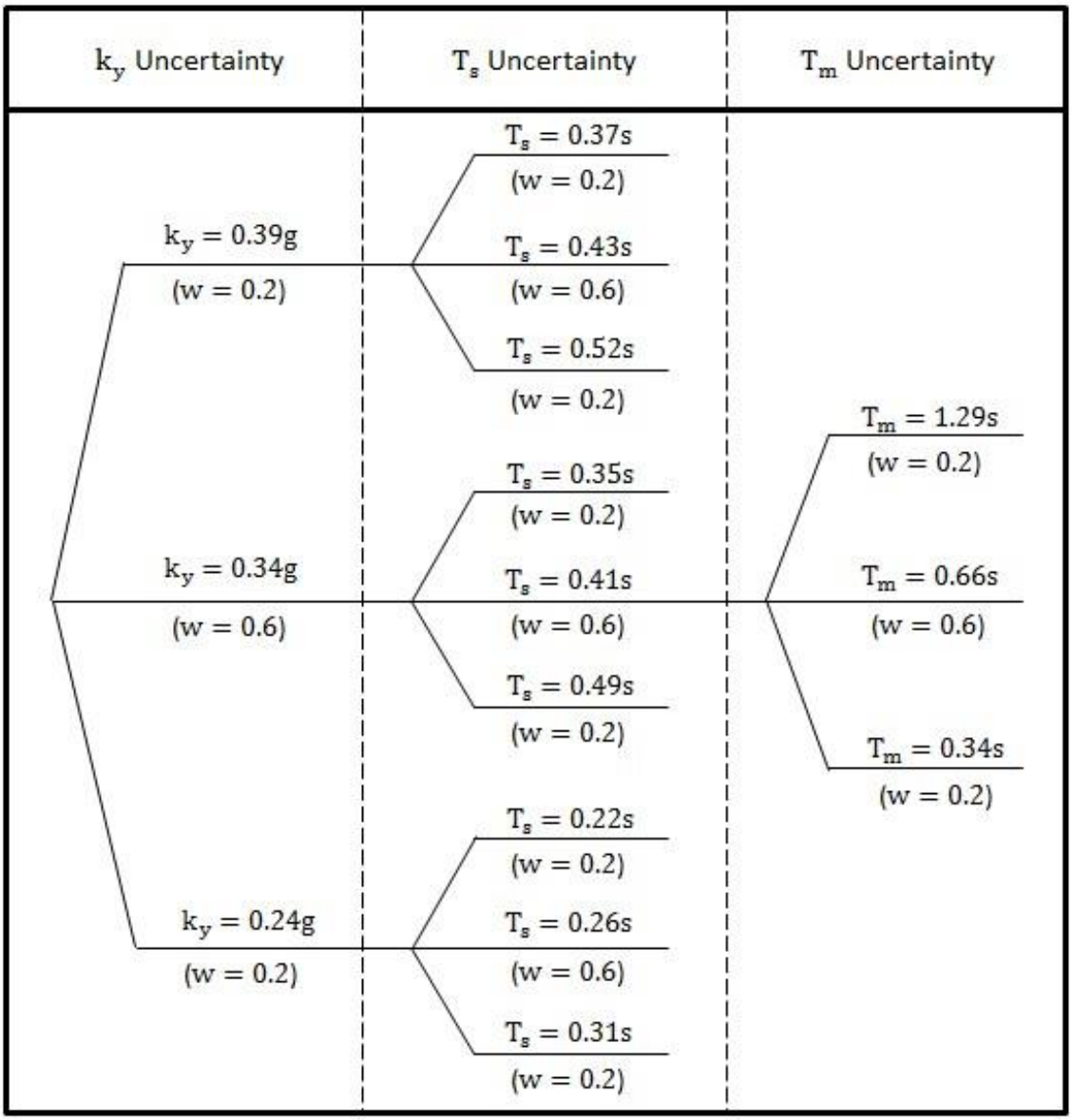

Figure 4.14 Logic tree of Lexington Elementary School

4.3 PROBABILISTIC ESTIMATE OF SEISMIC STABILITY

4.3.1 Dynamic Response

The dynamic response of the flexible sliding mass, as characterized by k_{max}, will have widely distributed amplitudes due to the large uncertainties in the site period (T_s) and the mean period of the ground motion (T_m), as seen in the logic tree above. The k_{max} hazard curves for the Lexington school site are shown in Figure 4.15. The 27 k_{max} hazard curves have T_s/T_m ratios from 0.17 to 1.53. The probabilistic k_{max} values range from 0.19 to 0.68 g at 10% probability of exceedance in 50 years (λ = 0.0021 1/yr), and range from 0.24 to 1.06 g at 2% probability of exceedance in 50 years (λ = 0.0004 1/yr). The 27 k_{max} hazard curves are weighted by their associated weights to generate a mean k_{max} hazard curve. Note that the weights are applied to the hazard (i.e., λ) at each k_{max} value, and not to the k_{max} values themselves. Also shown in Figure 4.15 is the k_{max} hazard curve using the best-estimate soil properties and T_m characterization (i.e., Ts = 0.41 s and Tm = 0.66 s from Figure 4.14). Note that this curve falls below the mean hazard curve showing that incorporating uncertainty in the soil properties and T_m generally leads to a larger seismic hazard. The difference between these curves increases as λ decreases.

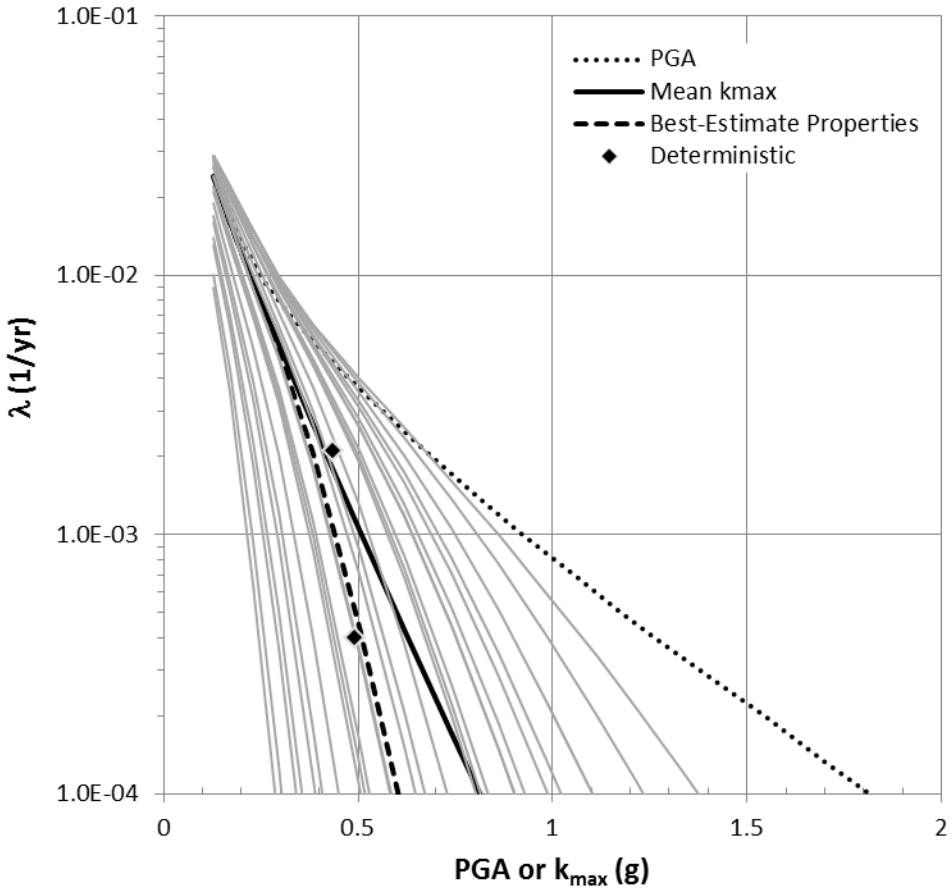

Figure 4.15 k_{max} hazard curves for Lexington School site

Deterministic values of k_{max} for 10% and 2% probabilities of exceedance in 50 years are also shown in Figure 4.15. These values are calculated by using the mean M and R from the seismic hazard deaggregation (Table 4.6), the associated median T_m, and the best estimate T_s. The resulting deterministic values of k_{max} are 0.436 g and 0.491 g at 10% and 2% probabilities of exceedance in 50 years, respectively. At 10% probability of exceedance in 50 years, the deterministic k_{max} is close to the values from the probabilistic approach. At 2% probability of exceedance in 50 years, the deterministic k_{max} is much lower than the probabilistic k_{max}, because it reaches a limiting

value at large PGA as discussed in Section 3.3, while the probabilistic k_{max} can take on values larger than the limiting value due to the consideration of the variability in the k_{max} prediction (i.e., σ_{lnkmax}).

To further investigate the influence of different sections of the logic tree on the probabilistic estimates of dynamic response, k_{max} hazard curves associated with each section of the logic tree (Figure 4.14) are shown in Figure 4.16. For the hazard curves shown, the best-estimate values associated with other sections of the logic tree are used while varying the parameters within the selected section of the logic tree. It should be noted that although the k_{max} hazard curve does not explicitly depend on k_y , the different k_y values are derived from different shear strength and shear wave velocity profiles that result in different thicknesses of the failure mass and average Vs over the thickness of the failure mass. As a result, the best-estimate T_s is different for each k_y value (Table 4.4). Figure 4.17a shows the k_{max} hazard curves for the three best-estimate Ts values associated with the k_y section of the logic tree, while Figure 4.17b shows the k_{max} hazard curves for the three central Ts values within the Ts section of the logic tree, which are associated with the best-estimate k_y. For all of these hazard curves, Tm is taken as 0.66 s. The hazard curves in Figure 4.17 (a) and (b) indicate that uncertainties in Ts associated with the k_y and T_s sections of the logic tree generate small variations in k_{max}, which is about 10 ~ 20% of the mean values. Figure 4.17c shows the kmax hazard curves for the three potential values of Tm, assuming the best-estimate Ts. It is clear that the uncertainty of T_m generates a larger variation in k_{max} predictions because T_m varies over a wider range than T_s in the logic tree.

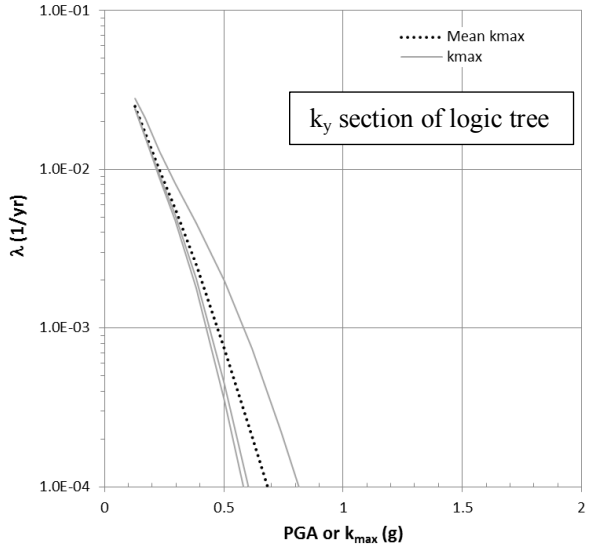

(a)

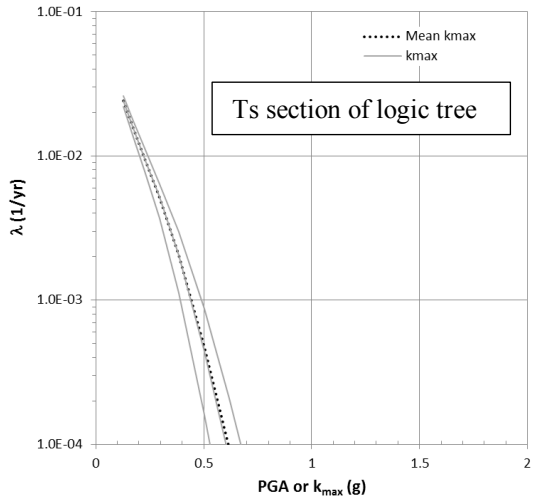

(b)

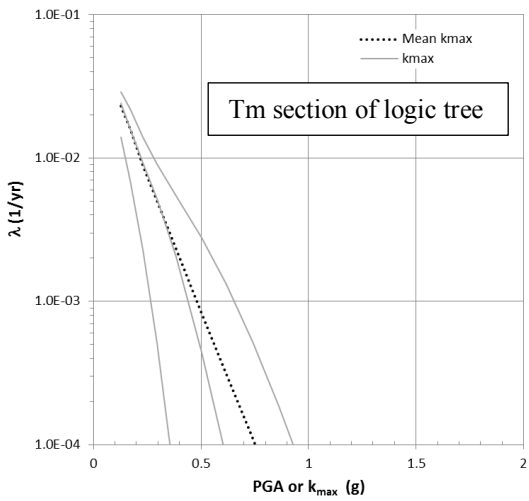

(c)

Figure 4.16 Influence of different sections of the logic tree on the k_{max} hazard curves

Hazard curves for k-vel_{max} are not created due to the fact that they are not used in the vector probabilistic analysis. Instead, the joint annual probability of occurrence of k_{max} and k-vel_{max} is computed from P[PGA, PGV] by using Equation 3.21. The resulting P[k_{max}, k-vel_{max}] for the best-estimate branches of the logic tree is shown in Figure 4.17. Comparing Figure 4.13 and Figure 4.17, P[k_{max}, k-vel_{max}] and P[PGA, PGV] have a similar shapes. However, the P[k_{max}, k-vel_{max}] values are more widely distributed than the P[PGA, PGV] values, and the k_{max} and k-vel_{max} values associated with the peak P[k_{max}, k-vel_{max}] are smaller that PGA and PGV values associated with the peak P[PGA, PGV]. Figure 4.18 plots the difference between P[k_{max}, k-vel_{max}] and P[PGA, PGV] for each bin. As seen in Figure 4.18, the difference is negative (i.e., P[k_{max}, k-vel_{max}] < P[PGA, PGV], colored blue) for the bins that represent the peaks in P[PGA, PGV]. This means that the dynamic response has reduced the probability of occurrence of these values. The difference becomes positive (i.e., P[k_{max}, k-vel_{max}] > P[PGA, PGV], colored red) for bins associated with combinations of large/small k_{max} and k-vel_{max} levels. As a result, P[k_{max}, k-vel_{max}] is distributed over a wider range of (k_{max}, k-vel_{max}) combinations.

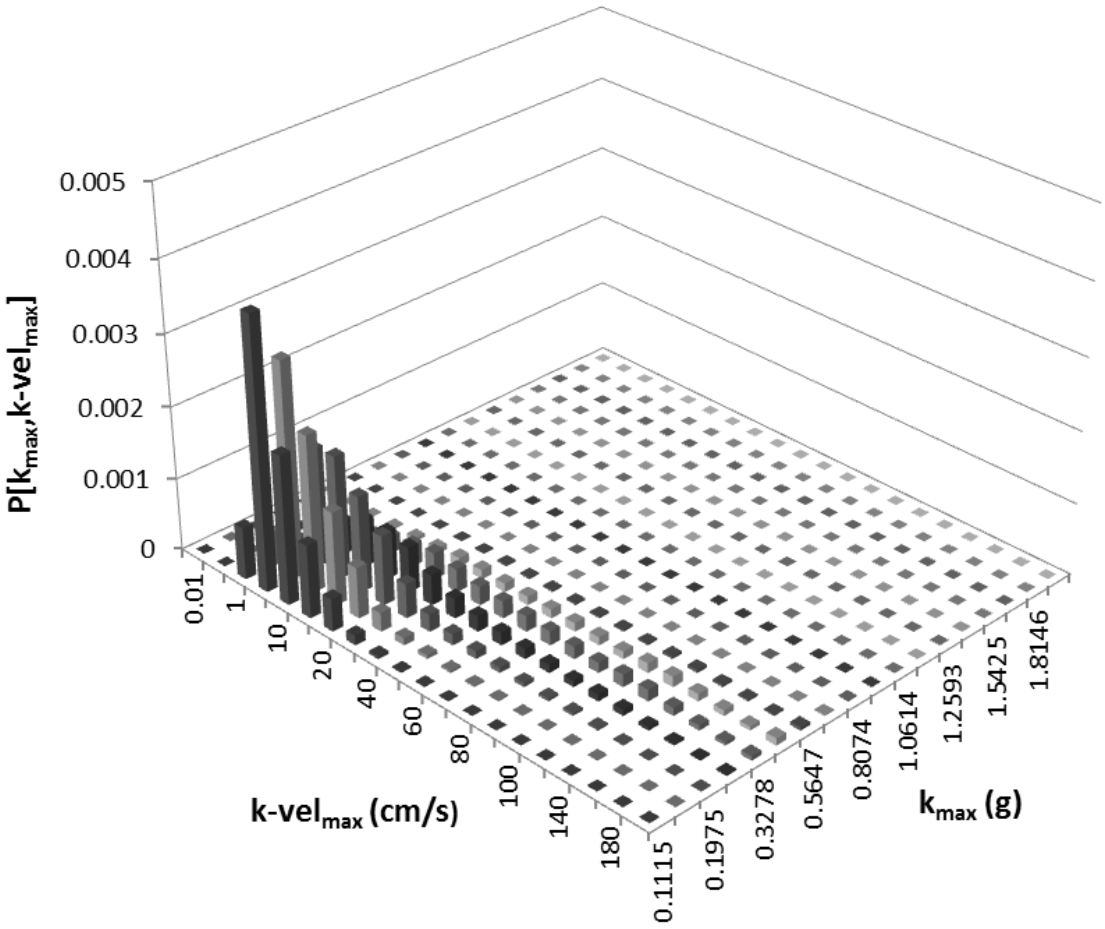

Figure 4.17 Joint annual probabilities of occurrence for (k_{max}, k-vel_{max}) pairs for the best-estimate branches of the logic tree

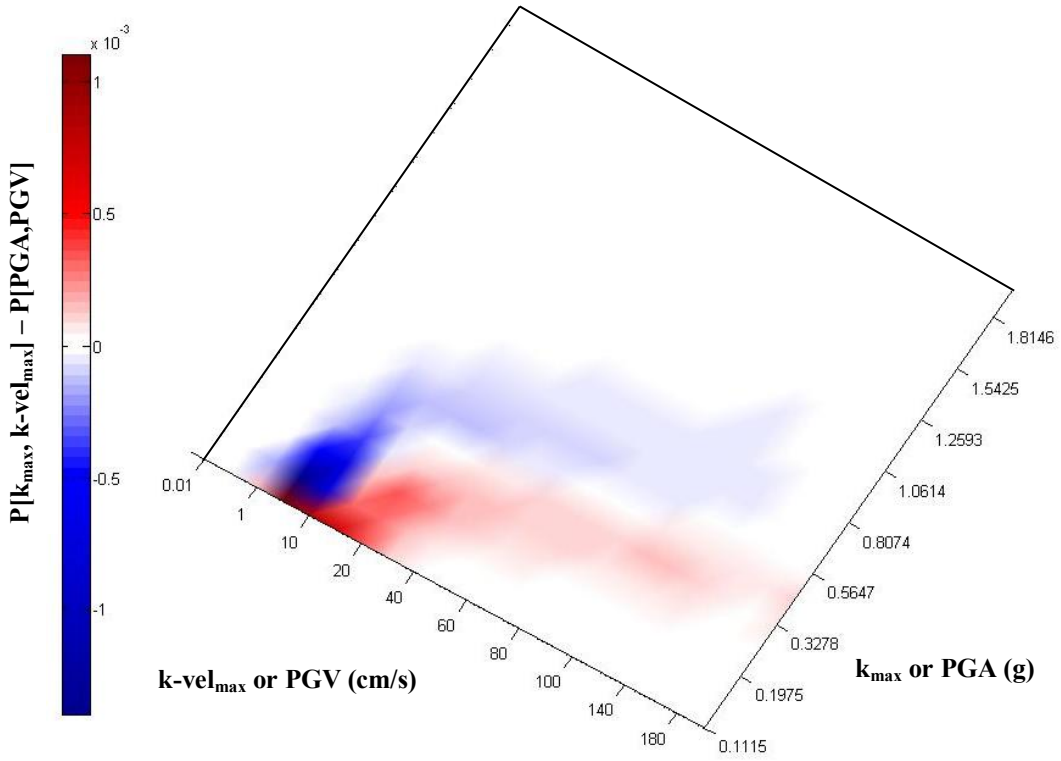

Figure 4.18 Difference between joint annual probabilities of occurrence for (PGA, PGV) pairs and (k_{max}, k-vel_{max}) pairs for the best-estimate branches of the logic tree

4.3.2 Displacement Hazard Curves

Through the steps described in Sections 3.2 and 3.4, displacement hazard curves for the Lexington School site are constructed using both the scalar and vector approaches. Figure 4.19a shows the displacement hazard curves from the (k_{max}, M) scalar model and Figure 4.19b shows the displacement hazard curves from the (k_{max}, k-vel_{max}) vector model. Table 4.7 summarizes the predicted sliding displacements along with the ground motions and dynamic responses at λ = 0.0021 1/yr and 0.0004 1/yr. The conditional

PGV correlated with PGA is used to compute k-vel_{max} in the deterministic approach, and it can be derived from Equation 3.12. For both of these models, the displacement from the mean hazard curve is larger than the displacement from the hazard curve associated with the best-estimate properties and significantly larger than from the deterministic approach. The mean hazard curve produces larger displacements than the best-estimate hazard curve because it accounts for uncertainty in the site properties and T_m. These differences are most significant at longer return periods (i.e., smaller λ). At $\lambda = 0.0021$ 1/yr, the difference between the deterministic value and the mean hazard curve may be on the order of a factor of 4 to 6, but at $\lambda = 0.0004$ 1/yr the difference may be larger than a factor of 10. This large difference is caused by the fact that the k_{max} predictive model has a limiting mean value at large input PGA, which cannot be exceeded when this model is used deterministically. However, the k_{max} data shows variability about this limiting value and when this variability is taken into account in the probabilistic approach larger displacements develop.

Figure 4.19c shows the mean hazard curves from the scalar and vector models. Generally, the mean hazard curve for the vector model predicts smaller displacements than the scalar model at each seismic hazard level because the (k_{max}, k-vel_{max}) vector displacement model generally predicts smaller displacements with less variability.

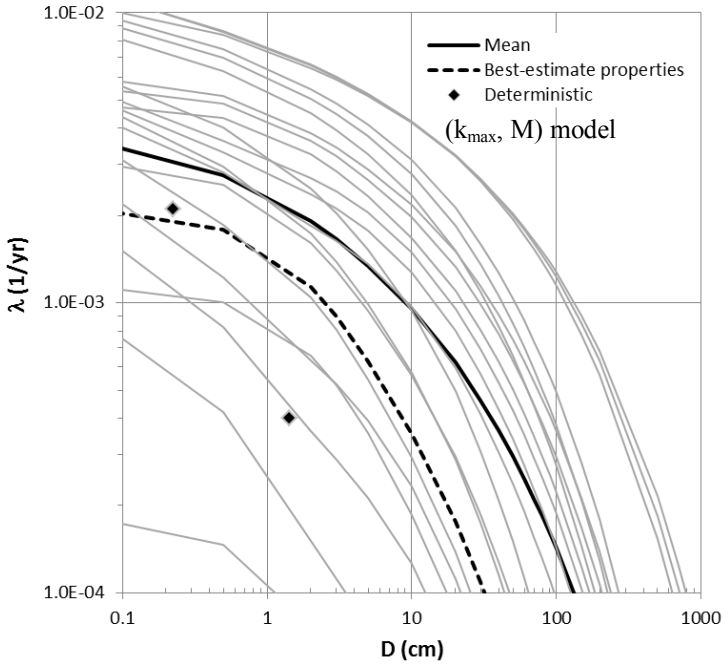

(a)

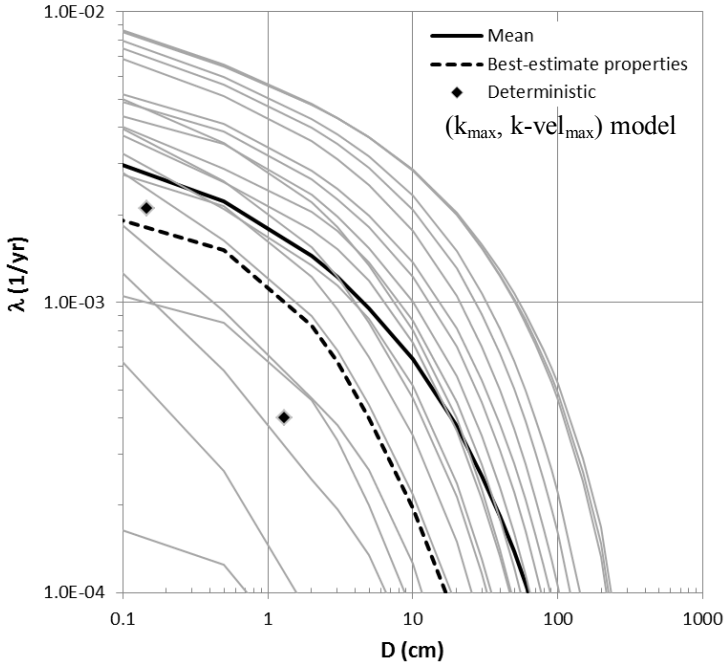

(b)

Figure 4.19

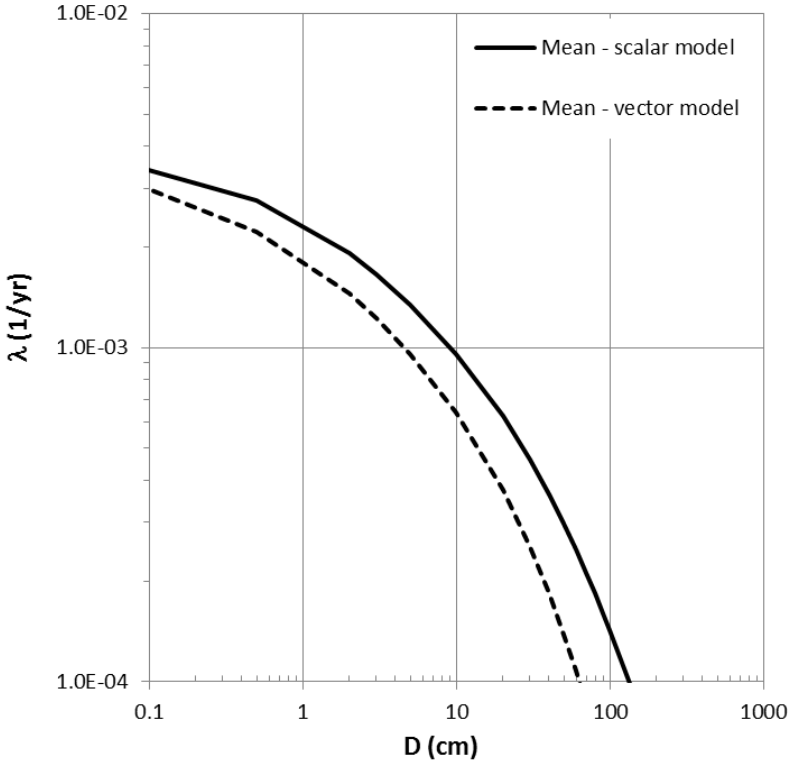

(c)

Figure 4.19 Displacement hazard curves of Lexington Elementary School (a) (k_{max}, M) model, (b) (k_{max}, k-vel_{max}) model and (c) mean hazard curves

Table 4.7 Deterministic and probabilistic predictions of sliding displacements

	λ (1/yr)	Ground Motions		Dynamic Response		Sliding Displacement (cm)	
		PGA (g)	Conditional PGV (cm/s)	k_{max} (g)	k-vel_{max} (cm/s)	Deterministic	Probabilistic with Logic Tree
Scalar Model	0.0021	0.67	-	0.44	-	0.22	1.4
	0.0004	1.26	-	0.49	-	1.4	34
Vector Model	0.0021	0.67	72	0.44	77	0.15	0.61
	0.0004	1.26	112	0.49	111	1.3	18

*T_m and M are shown in Table 4.6

The seismic landslide hazard categories of the Lexington school site determined from the deterministic results are low hazard at λ = 0.0021 1/yr and moderate at λ = 0.0004 1/yr. Instead, the probabilistic approach predicts low/moderate hazard and very high hazard at 10% and 2% probabilities of exceedance in 50 years, respectively. The increment of hazard is significant with uncertainties in input parameters, thus the results of the probabilistic analysis should be accepted to better estimate the seismic performance of the Lexington school site. Further dynamic slope stability analyses using numerical methods and ground motion records must be performed to fully evaluate the landslide potential of the Lexington school site.

The influence of k_y, T_s and T_m on sliding displacements are individually illustrated in Figure 4.20 using displacement hazard curves derived from the (k_{max}, M) model. Only the parameters within the selected section of the logic tree are varied while all other parameters are set to the best-estimate values. The different k_y values within the logic-tree explicitly affect the displacement hazard curves, and the resulting variation of sliding displacement is significant (Figure 4.20a), with the displacement at a given hazard value varying by about an order of magnitude for the lower and upper k_y values. The uncertainty of T_s (Figure 4.16b) leads to a relatively smaller variation in predicted sliding displacements, about a half of an order of magnitude. Figure 4.20c shows that the variation of sliding displacements caused by the uncertainty of T_m can be very large, several orders of magnitude. The large difference is driven by the very small displacements predicted by the lower bound $T_m = 0.34$ s in the logic tree. The displacements are extremely small because the corresponding k_{max} values are very close to or even smaller than the best-estimate $k_y = 0.34$ g. The uncertainties of k_y and T_m together dominate the variation of predicted sliding responses. Similar observations can

be made about the influence of each section in the logic tree when using the (k_{max}, k-vel_{max}) model.

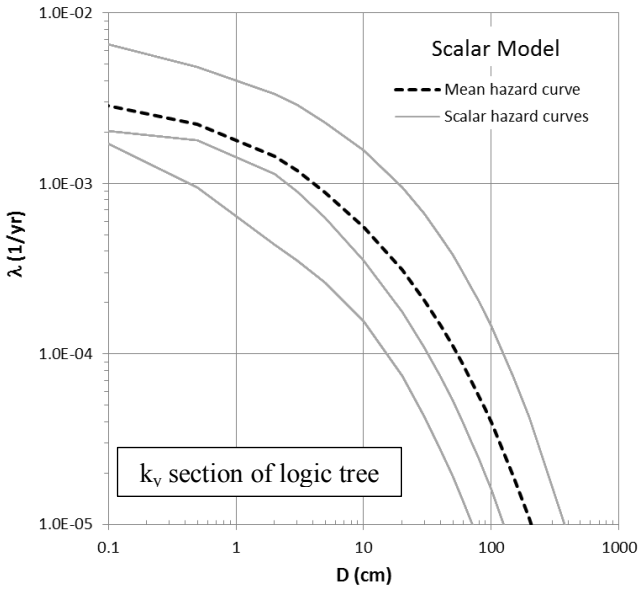

(a)

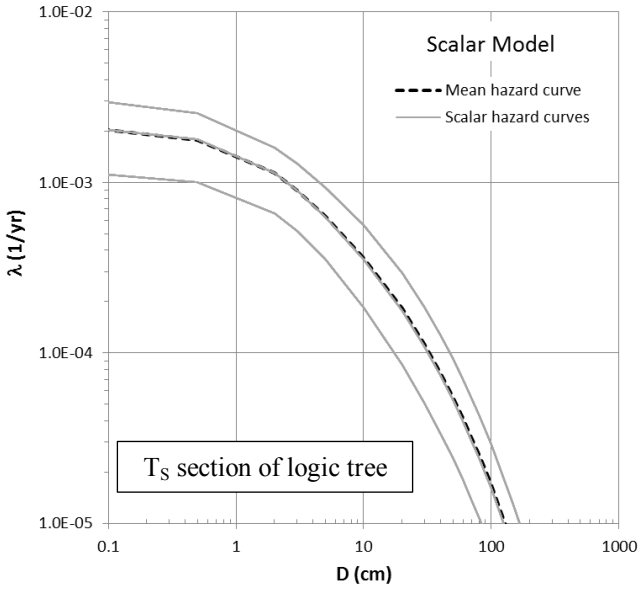

(b)

Figure 4.20

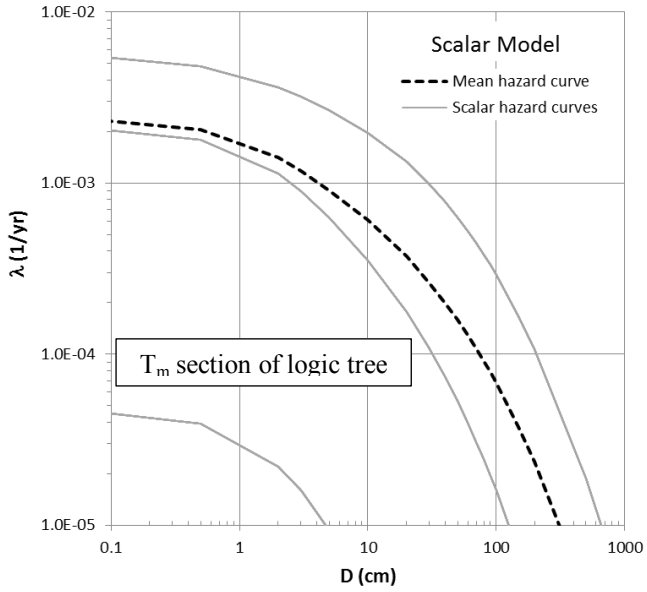

(c)

Figure 4.20 Influence of different sections of the logic tree on the displacement hazard curves

The ground motions used in the above analysis are the geometric mean of two orthogonal horizontal components of motions. The maximum component could be 20% on average higher than the geometric mean. Since the Lexington school site is very close to the the San Andreas Fault, the effect of using maximum components of ground motions may be taken into account for the probabilistic analysis.

A scale factor equal to 1.2 is applied to the PGA levels shown in Figure 4.10, and the associated seismic hazard deaggregation is assumed to be the same as before. The median PGA and PGV values predicted by GMPEs are also scaled up by 20%, so that the P[PGA, PGV] and P[k_{max}, k-vel_{max}] used in the vector approach can be accordingly updated.

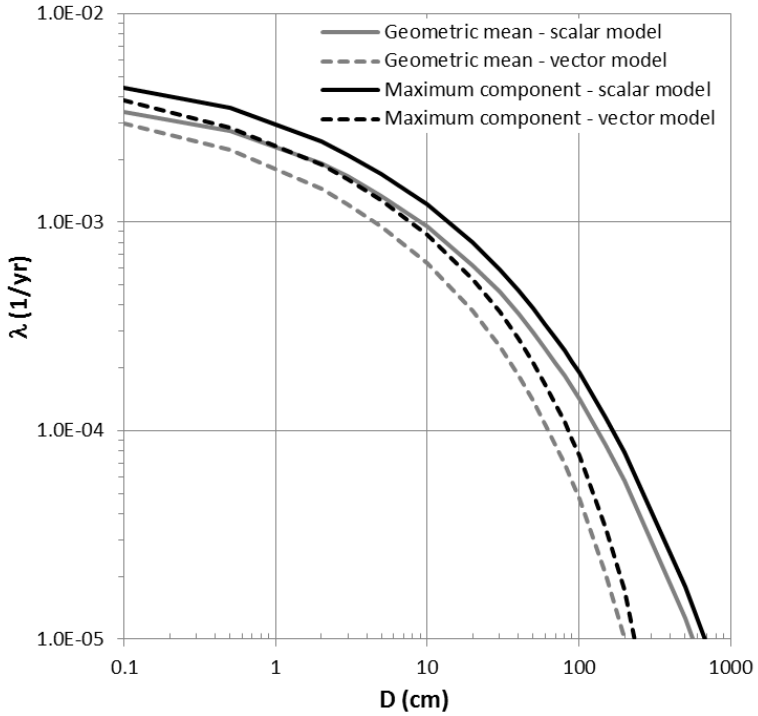

Figure 4.21 Displacement hazard curves using geometric mean and maximum component of ground motions

The effect of using the maximum component of ground motions on sliding displacements is illustrated in Figure 4.21 for both the scalar and vector displacement models. After applying the scale factor, the sliding displacements predicted by the scalar and vector models are 1.4 cm (vector) and 1.9 cm (scalar) at $\lambda = 0.0021$ 1/yr, and 26 cm (vector) and 44 cm (scalar) at $\lambda = 0.0004$ 1/yr. These predicted displacements are generally 30 ~ 40% larger than those predicted with the original ground motions.. Although the maximum components of ground motions may lead to conservative predictions of sliding displacements, such an unfavorable condition may be considered for the Lexington school site due to the short site-to-source distance. However, the best approach to incorporating this effect would be to model it within the ground motion

hazard calculation such that the effect is only modeled for near-fault earthquake scenarios. The approach utilized above assumes each earthquake scenario represents a near-fault scenario.

4.4 SUMMARY

This chapter demonstrated the application of the probabilistic framework for flexible sliding masses by investigating the Lexington Elementary School site. The uncertainty in soil shear strengths influences not only the yield acceleration, but also the shape of the critical failure surface, which affects the thickness of failure mass and associated site period. The uncertainty in yield acceleration, k_y, is determined from the different shear strengths, and the uncertainty in the site period T_s is determined from the different failure mass thicknesses and different shear wave velocity profiles. The mean period of the ground motion T_m also has significant uncertainty, as indicated from the empirical predictive model for T_m. A logic tree analysis is applied to incorporate all uncertainties in k_y, T_s and T_m. The results show that the uncertainty in T_m dominates the variation of dynamic response and sliding displacements. The deterministic analysis may considerably under-estimate the dynamic response and sliding response of flexible sliding masses.

Chapter 5 Probabilistic Seismic Landslide Hazard Mapping

5.1 INTRODUCTION

Seismic landslides have been responsible for a tremendous amount of economic losses in earthquakes. For instance, the 2008 Sichuan Earthquake (Mw = 7.9) in China induced significant landslides and these landslides not only buried dozens of towns, but also blocked roads, which are the lifelines connecting those ruined towns and nearby large cities. Knowledge of the locations and scale of potential seismic landslides is essential for reducing losses caused by earthquakes.

Regional maps of potential seismic landslides are used in land-use planning and emergency-response planning, and are used to identify zones that require detailed, site-specific studies. Current seismic landslide hazard mapping efforts utilize empirical predictions of sliding displacement based on the expected ground shaking and the general slope properties (e.g. Jibson el al. 2000). The seismic landslide hazard is assigned qualitatively as high, medium, or low based on the different displacement thresholds (Table 2.1). However, these maps typically utilize a deterministic approach that does not consider the aleatory variability in predictions of ground shaking or sliding displacement; nor do they consider the epistemic uncertainty in the slope properties (i.e., soil shear strengths, ground water table and thickness of sliding blocks).

A recently developed probabilistic approach, as discussed in Chapter 3, uses a sliding displacement hazard curve to quantify the seismic landslide hazard. The

displacement hazard curve incorporates aleatory variability to compute the annual frequency of exceedance (i.e., hazard) of different displacement levels, and it is used to identify the displacement associated with a specified hazard level (Saygili and Rathje 2009). Using the displacements associated with the specified hazard level (typically 10% or 2% probability of exceedance in 50 years), a seismic landslide hazard map is produced using the same displacement thresholds used in deterministic approaches. However, this probabilistic approach does not incorporate any epistemic uncertainty in the slope properties. Yet, at a regional scale the uncertainties in the slope properties are significant and should be taken into account.

In Chapter 3, the logic-tree analysis was introduced to incorporate the epistemic uncertainties in the slope properties into the probabilistic framework. This chapter describes the probabilistic approach to seismic landslide hazard mapping and the incorporation of a logic-tree to account for various sources of epistemic uncertainties. An efficient computational scheme is described that allows the logic-tree approach to be applied more easily to regional analysis.

5.2 SEISMIC LANDSLIDE HAZARD MAPPING

5.2.1 Input Parameters

To produce a seismic landslide hazard map, either the deterministic or probabilistic approach must be applied to a regional area containing hundreds of thousands to millions of sites. The input parameters for the analysis (e.g., slope angle, shear strength) take on different values at different locations. In a Geographic Information System (GIS), such location-dependent data is stored as raster data (Figure

5.1), which is made of small square grid cells (typical cell sizes are the scale of meters). An entire study area can be divided into millions of grid cells, each storing a single value. The resolution of a raster data describes the detail level of the data. Finer resolution means smaller grid cells, more detail and larger storage space.

The spatial distribution of the yield acceleration k_y, which represents the sliding resistance of a slope, is the critical slope parameter for predicting sliding displacement and needs to be computed for each grid cell in the study area. As discussed in Chapter 2, the most common type of earthquake-induced landslide is a thin, veneer slope failure, so the infinite slope model can be used to calculate k_y (Equations 2.1 and 2.2). This approach allows the k_y of each grid cell to be computed easily. Each grid cell is treated as an independent infinite slope, which may not be realistic for all types of landslides but it is the most practical way to perform a regional analysis. Slope stability analysis of finite slopes using circular or non-circular failure surfaces would be too difficult to be applied for seismic landslide hazard mapping, because 1) it requires much more site information (e.g. soil profiles), 2) the geometry of slopes are different from one location to another, and 3) the number of slopes is incredibly large in a region. However, slope stability analysis of detailed geometries of finite slopes can be used in site-specific analysis of the slopes that are identified by the seismic landslide hazard mapping.

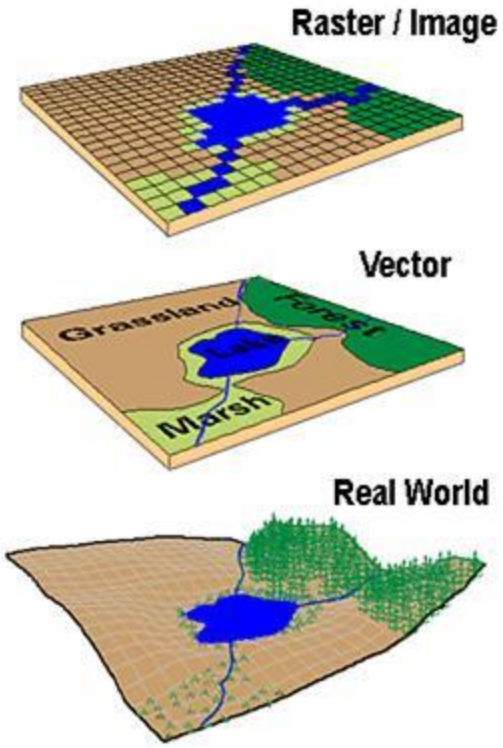

Figure 5.1 Convert the real world into raster and vector data (http://www.sfu.ca/rdl/GIS/tour/gis_wrk.html)

The infinite slope model requires slope angle, shear strength and ground water condition for the computation of k_y. Each of these input parameters are stored in raster format so that k_y can be computed for each grid cell. The calculation of the input parameters within the GIS is described below. A region within Niigata Prefecture, Japan is used to demonstrate the process.

A Digital Elevation Model (DEM), which contains the elevation at the center of each grid cell (e.g. Figure 5.2), is used to compute the slope angle of each grid cell. The slope angle is computed for a center grid cell by using its elevation data and its eight adjacent grid cells. A slope map (e.g. Figure 5.3) can be created using this slope

algorithm as incorporated within the Slope tool in the ArcGIS© software developed by the Environmental Systems Research Institute (ESRI).

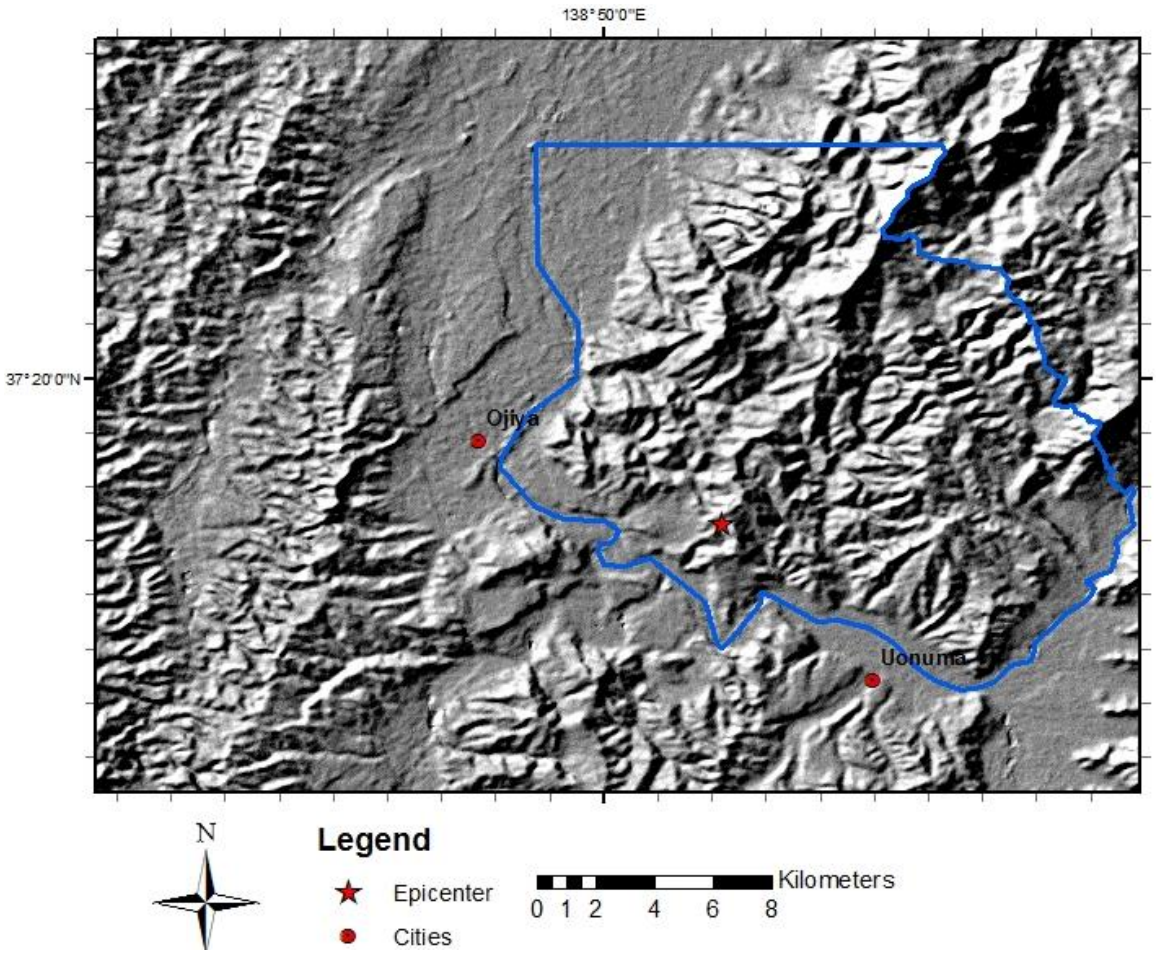

Figure 5.2 Hillshade DEM in Niigata Prefecture, Japan

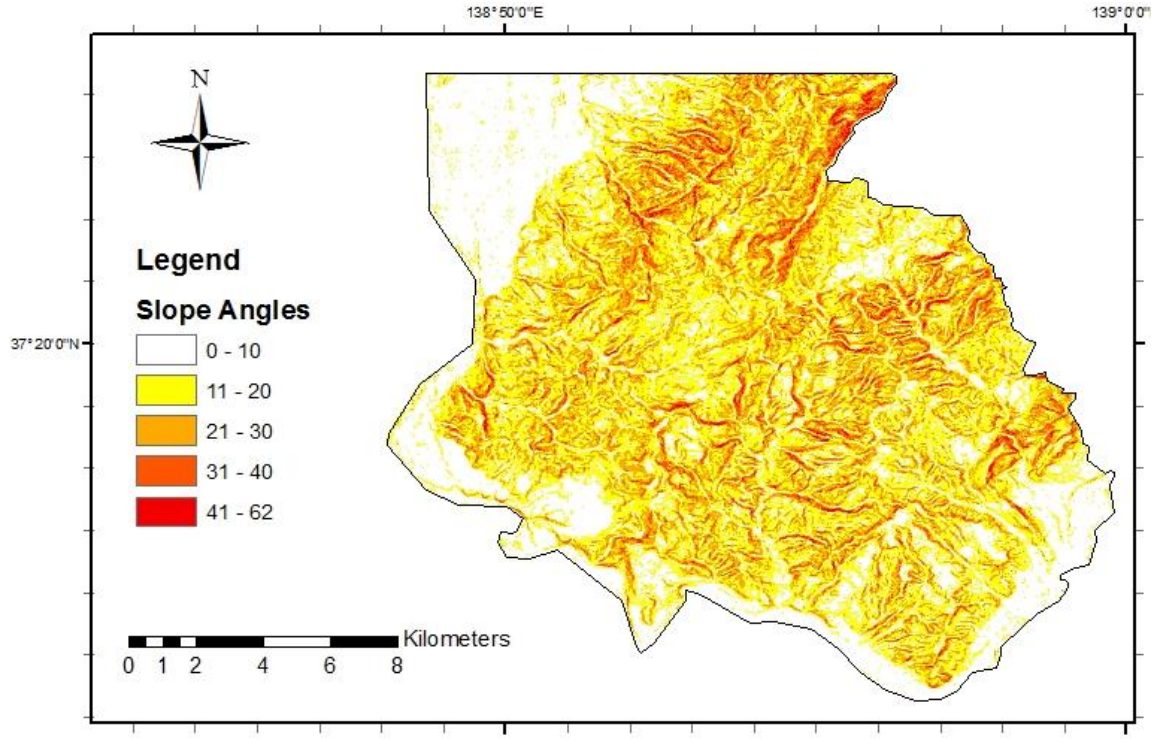

Figure 5.3 Slope map in Niigata Prefecture, Japan

The shear strength data required for the k_y calculation are usually derived from a geologic map. A geologic map (Figure 5.4a) is made of polygons, and each polygon represents a single geologic unit. Polygons are vector data in the GIS framework (Figure 5.1), and they need to be converted into raster data for further computation. The conversion divides polygons into raster grid cells, and each grid cell obtains a single value from the polygon to which it belongs. Shear strengths are assigned to each geologic unit prior to the conversion. Because there are two shear strength parameters (c and ϕ), a separate cohesion map and friction angle map are developed from the geologic map (Figure 5.4b and c).

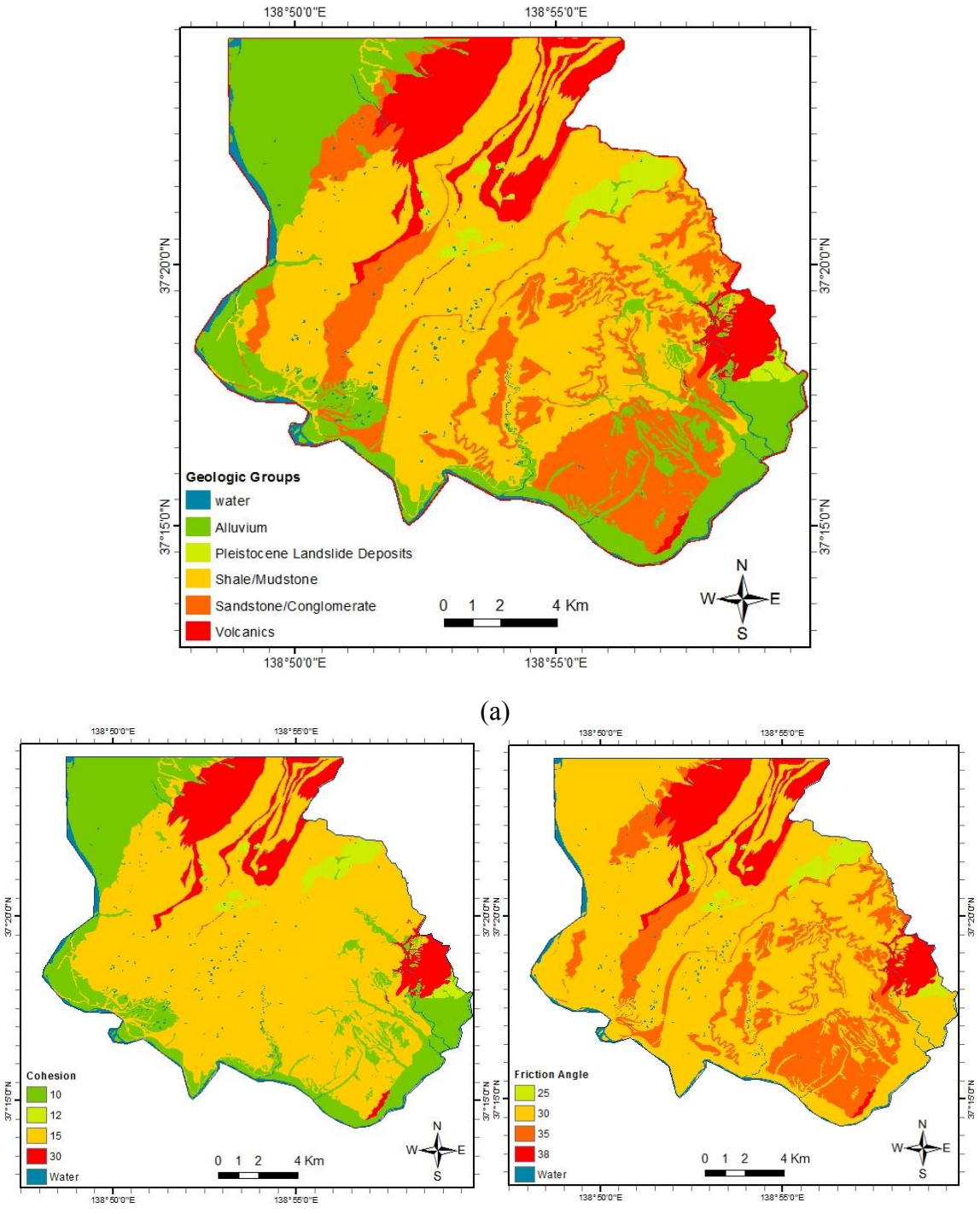

Figure 5.4 (a) Geologic map, (b) cohesion map, and (c) friction angle map in Niigata Prefecture, Japan

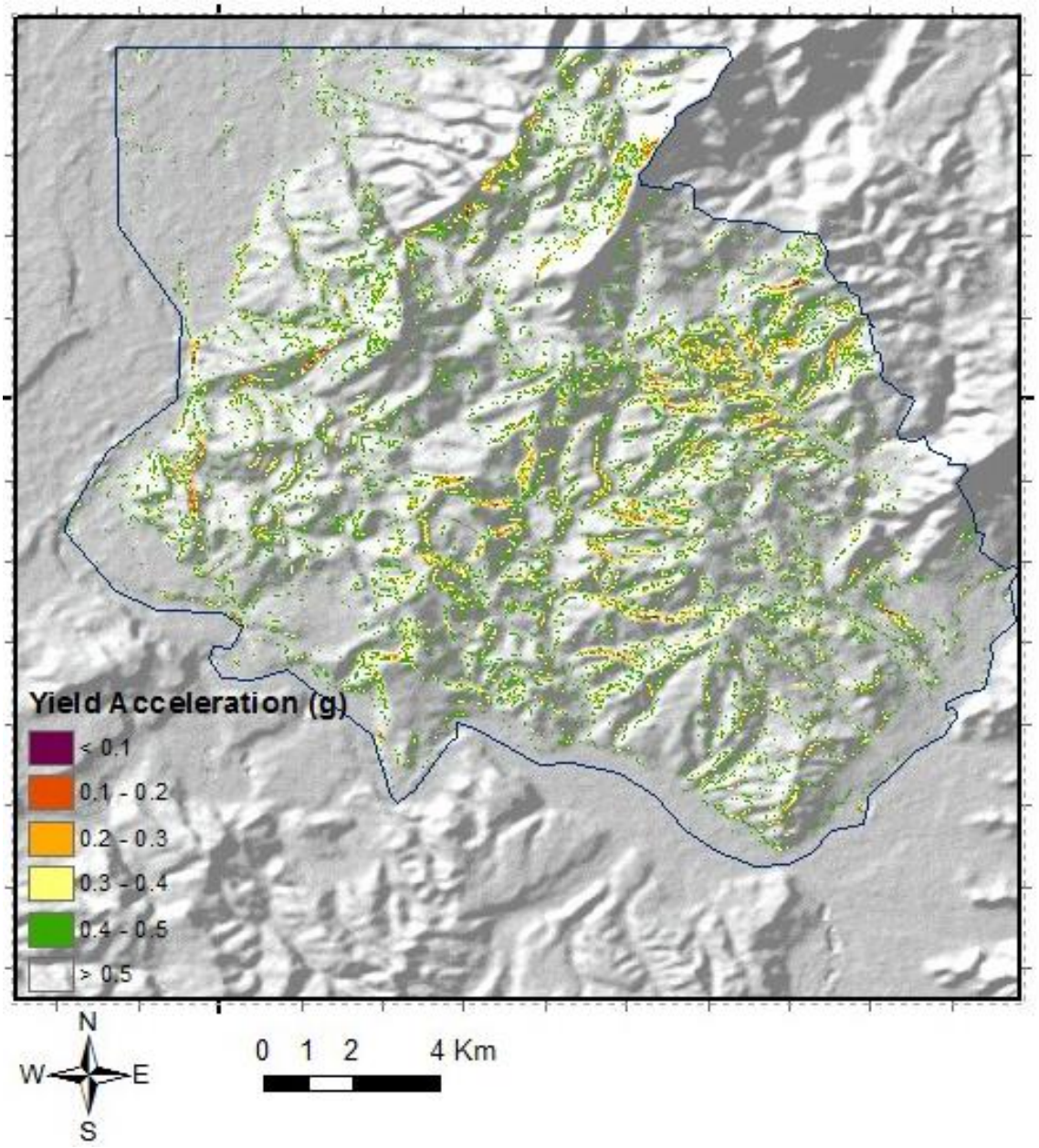

Figure 5.5 Yield acceleration map of Niigata, Japan

The other inputs for the calculation of k_y are t (slope normal thickness), m (proportion of block thickness that is saturated), and γ (unit weight of soil). These values commonly are assigned as constant values across the study area in the deterministic approach. The t value, which represents the failure depth of shallow landslides, is typically up to several meters as discussed in Chapter 2. It can be determined from the thickness of surficial weak soils underlain by stiff soil or rock layer, or from observations of local shallow failures. The m value, which represents the pore water pressure on the failure surface, depends on the ground water table and may fluctuate due to seasonal change and precipitation. In deterministic analysis, the selected m value often is selected to represent the most unfavorable conditions for seismic landslides, so that seismic landslide hazard map is conservative. The unit weight of soil γ can be assigned differently to each geologic unit if there are available testing results. However the difference in γ values is usually small, so that using a constant γ value across the study area is convenient for the k_y computation. Jibson el al. (2000) used t = 2.4 m, m = 0 and γ = 15.7 kN/m^3 for the Oak Mountain quadrangle in southern California, because such values are representative for local conditions.

With all above-mentioned input data, a yield acceleration map (e.g. Figure 5.5) is created by applying Equations 2.1 and 2.2 to each grid cell. Combined with ground motion parameters, the sliding displacement in each grid cell is predicted by empirical models.

For ground motion parameters, it is not practical to obtain a ground motion hazard curve for each grid cell due to the heavy computation required; additionally there will be almost no difference in the hazard curves for adjacent cells and little difference within a study area (typically smaller than 25 km by 25 km). The seismic hazard curves provided by USGS are based on the NSHM 2008 Gridded Data, which has 0.05 degree increments

in longitude and latitude. It means that the seismic hazard curve is assumed to be the same within a distance range of several kilometers. Using the same seismic hazard across a study area may not be rigorous, but it simplifies the analysis without introducing large errors. Therefore, ground motion hazard curves are selected at a representative location within the study area and the same curves are used for the entire study area. Of course, if the area to be analyzed is too large to have a consistent seismic hazard, such area should be divided into several smaller areas and one set of ground motion hazard curves assigned to each smaller area.

Overall, the selected input parameters for seismic landslide hazard mapping are not as accurate as those used in site-specific analysis. However, the purpose of seismic landslide hazard mapping is to quantitatively assign hazard categories to grid cells, to distinguish zones with high hazard from other low-hazard zones, and to identify high-hazard zones that require further site-specific analysis.

5.2.2 Deterministic Approach

A deterministic seismic landslide hazard map is created for ground shaking associated with a given seismic hazard level. An example of a deterministic seismic landslide map is shown in Figure 5.6 for Anchorage, Alaska for 2% probability of exceedance in 50 years. To develop this type of map, a sliding displacement map is computed by applying an empirical displacement model to the yield acceleration map. Such computation can be carried out by the Map Algebra tool in the ArcGIS© software. The ground motion parameters required by empirical models are obtained from ground motion hazard curves at a given seismic hazard level (e.g. PGA=0.69 g for Figure 5.6).

Only one set of ground motion hazard curves is used for the entire study area. Finally, a deterministic seismic landslide hazard map is produced by comparing the predicted sliding displacement map with the displacement thresholds that define the seismic hazard categories (Table 2.1). An example of a deterministic seismic landslide hazard map is given in Figure 5.6 for the Anchorage, Alaska area.

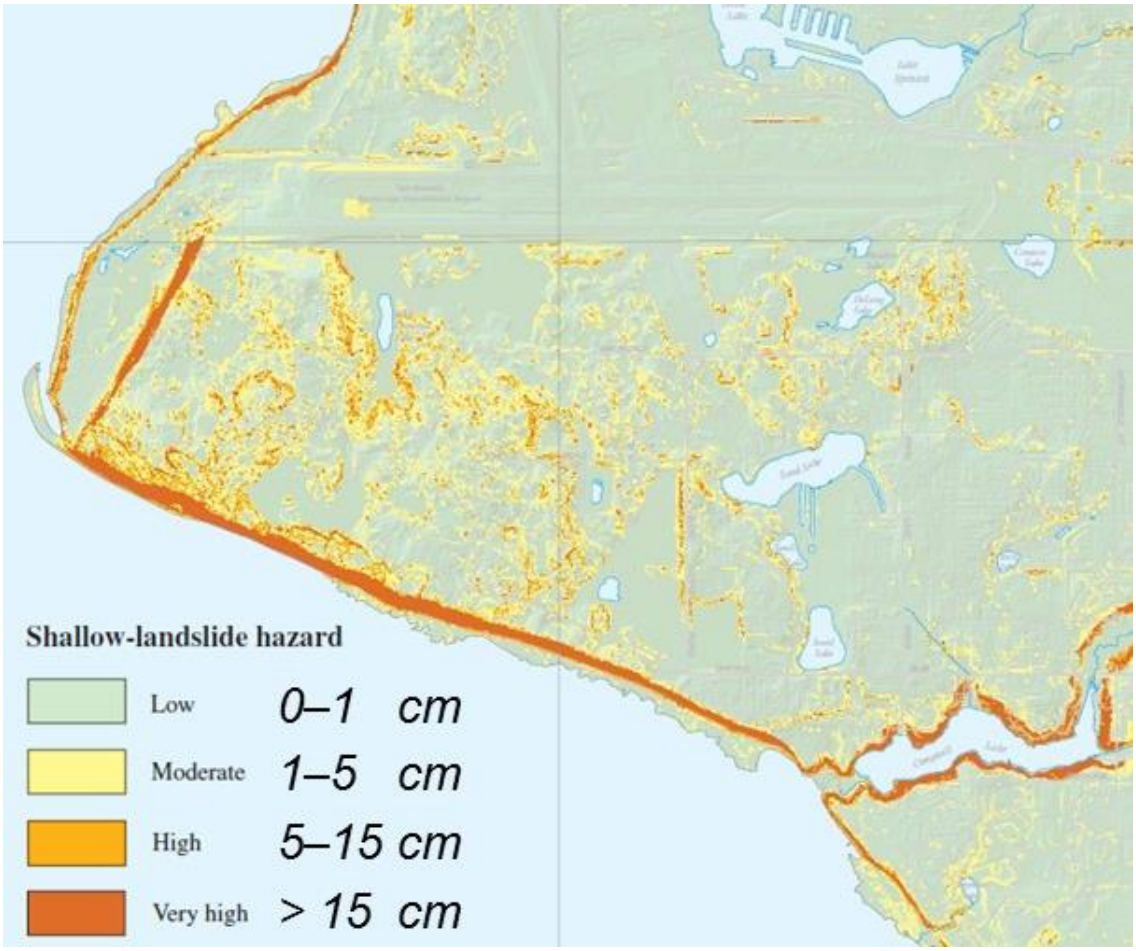

Figure 5.6 Deterministic Seismic Landslide Hazard Map at 2% probability of exceedance in 50 years in Anchorage, Alaska (Jibson and Michael 2009)

The deterministic approach ignores aleatory variability and epistemic uncertainty, which may significantly influence the seismic landslide hazard prediction. Table 5.1 shows median and plus one standard deviation (σ_{lnD}) displacements predicted by four different empirical models for k_y = 0.18 g using a deterministic scenario with ground motions of PGA = 0.54 g, PGV = 43 cm/s, and M=6.75 at 10% probability of exceedance in 50 years. These ground motions were adopted from a site in the San Francisco Bay Area (Rathje and Saygili 2011). The median predicted displacements mostly indicate high seismic landslide hazard (5 cm < D < 15 cm). For the median plus one standard deviation displacements, the seismic landslide hazard increases to very high (D > 15 cm). However, these displacements are less likely than the median displacements. This issue can be taken into account through a probabilistic analysis that incorporates the aleatory variability in predicted displacement. There are also significant differences between the displacements predicted by each of the empirical models, which represents a source of epistemic uncertainty. This issue can be taken into account through logic-tree analysis.

Table 5.1 Predicted Newmark Displacements with Standard Deviation

Predictive Model		Median D (cm)	+1σ D (cm)
Scalar	Rathje and Saygili 2009	12.6	32.0
	Jibson 2007	2.8	4.4
	Bray and Travasarou 2007	8.7	16.8
Vector	Saygili and Rathje 2008	8.2	14.6

*PGA = **0.54 g, PGV = 43 cm/s, M = 6.75, k_y = 0.18 g**

5.2.3 Probabilistic Approach Incorporating Aleatory Variability

The probabilistic approach incorporating aleatory variability utilizes a displacement hazard curve to define the displacement associated with a given hazard level (Chapter 3). This approach utilizes only one representative set of ground motion hazard curves for an entire region and ignores epistemic uncertainties in the slope properties. Ignoring epistemic uncertainties allows the probabilistic approach to be applied through the use of yield acceleration thresholds that correspond to the displacement thresholds associated with each seismic landslide hazard category. Yield acceleration thresholds were originally used by the CGS for regional mapping using the deterministic approach (McCrink 2001).

Given a representative ground motion, the predicted sliding displacement from an empirical model is a function of k_y. CGS identifies the k_y value that produces each of the displacement thresholds associated with a seismic landslide hazard category (e.g. Table 2.1). These k_y values are defined as k_y thresholds, and they are equivalent to the displacement thresholds. These k_y thresholds are used with a yield acceleration map, in which k_y is computed for each grid cell, to identify the seismic landslide hazard category for each grid cell. This approach provides the same result as computing the deterministic displacement for each grid cell and applying the displacement thresholds.

When epistemic uncertainty is not taken into account, the k_y-threshold approach can also be applied to the probabilistic framework (Saygili and Rathje 2009). In this case, displacement hazard curves are computed for a range of k_y values using the representative ground motions hazard curves and seismic hazard deaggregation for the study area. The displacement hazard curves are used to identify the k_y values that produce a given displacement threshold (e.g. 15 cm) for a specified seismic hazard level

(e.g. 10% probability of exceedance in 50 years). These k_y values are defined as the k_y thresholds. For example, Figure 5.7 shows displacement hazard curves for three k_y values (0.21g, 0.16g and 0.12g), which exactly produce the displacement thresholds of 5cm, 15cm and 30cm associated with a 10% probability of exceedance in 50 years. These k_y thresholds are applied to the yield acceleration map to create a probabilistic seismic landslide hazard map. For example, grid cells with k_y between 0.16g and 0.21g will have predicted sliding displacements between 5cm and 15cm, and they assigned a high seismic landslide hazard. Since only hazard categories, not the exact predictions of sliding displacements, are shown on a seismic landslide hazard map, the k_y-threshold approach is equivalent to the displacement-threshold approach.

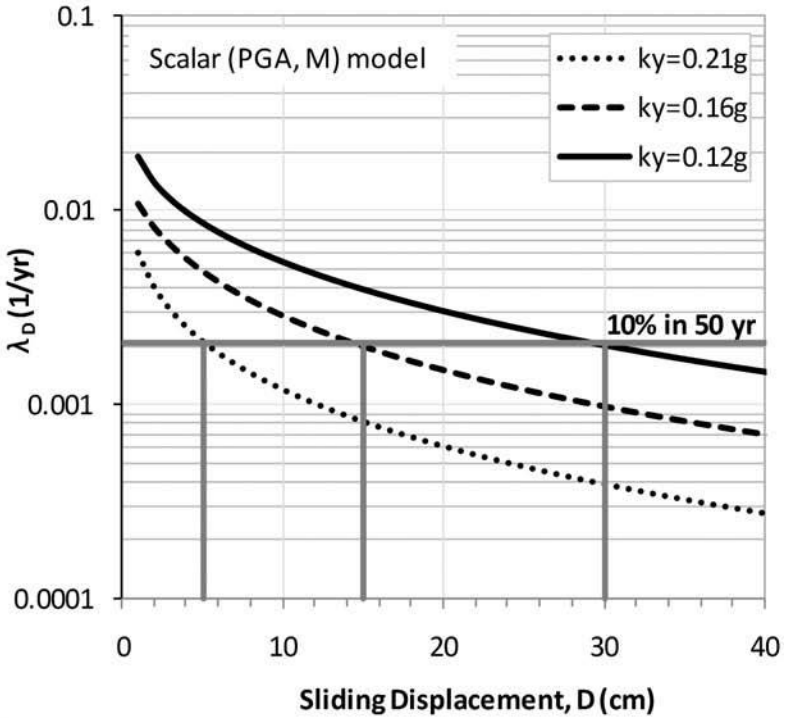

Figure 5.7 Displacement hazard curves for determining k_y thresholds (from Saygili and Rathje 2009)

The k_y-threshold approach avoids the computation of displacement hazard curves for each grid cell, thus it saves huge computational efforts in the probabilistic seismic landslide hazard mapping. However, the epistemic uncertainties in slope properties cannot be taken into account in this approach.

5.3 LOGIC TREE APPROACH FOR SEISMIC LANDSLIDE HAZARD MAPPING

To incorporate epistemic uncertainties in slope properties, a logic-tree analysis is introduced into the probabilistic seismic landslide hazard mapping. Specifically, the epistemic uncertainty in the shear strengths, *m* value and *t* value should be considered in the logic-tree analysis, because such parameters are used to determine the k_y value of each grid cell. Additionally, the epistemic uncertainty among empirical displacement models should also be considered in the logic-tree analysis.

5.3.1 Development of Logic Tree

The uncertainty in shear strengths can be estimated from lab and field testing results. However, at a regional scale the most practical way to assign uncertainty may be through published uncertainty estimates or, if available, through the variability in in situ test parameters, such as SPT blow count, across a geologic unit. As an example of published uncertainty estimates, Phoon and Kulhawy (1999) summarized that the coefficient of variance is about 10 to 50% for undrained shear strength and 5 to 15% for effective friction angle. If enough testing results are not available to evaluate the uncertainty in shear strengths, one may refer to the above coefficients of variance and use

engineering judgment to develop specific values to be used in the logic-tree analysis. The weights of branches can be determined based on three-point estimation of a normal distribution, as discussed in Chapter 4.

The thickness of sliding block *t* is typically several meters for shallow failures. It depends on the thickness of surficial weak soil, and it is also correlated with the shear strengths of underlying soil layers. If the underlying soil layers are strong enough, the failure will be restrained in the surficial weak layer. Smaller shear strengths of underlying layers may lead to deeper landslides. Slope stability analysis may be necessary to determine the critical failure depth for complicated slope geometries. Nevertheless, the shallow-failure assumption is generally valid and convenient for regional mapping. The selection of representative *t* values should be based on the knowledge of local geology and engineering observations. In the logic tree, three branches can be used to represent a typical range of *t* values, and a uniform distribution should be used to assign weights unless there is specific information indicating that some depths are more likely than others.

The *m* value, defined as the proportion of the block thickness that is saturated, is calculated by the ground water table and the *t* value. The ground water table will fluctuate due to seasonal changes and precipitation. Topography, seepage, and artesian water can cause complicated spatial variations of the ground water table in a region. The estimation of the ground water table relies on survey records and precipitation forecasts. Because of these complications, a uniform distribution is most likely applied to the ground water table levels. The selected ground water table levels, and corresponding *m* values, should represent the likely range of values indicated by observations. If one wants to incorporate the most unfavorable location of the ground water table, it can be

included in the logic tree with a corresponding weight that indicates its likelihood of occurrence.

The unit weight of soil γ generally has a small variation in the same soil and a small difference between different soils. The coefficient of variance in γ is less than 10% according to Phoon and Kulhawy's study (1999). Therefore, using a constant γ value across the study area is acceptable.

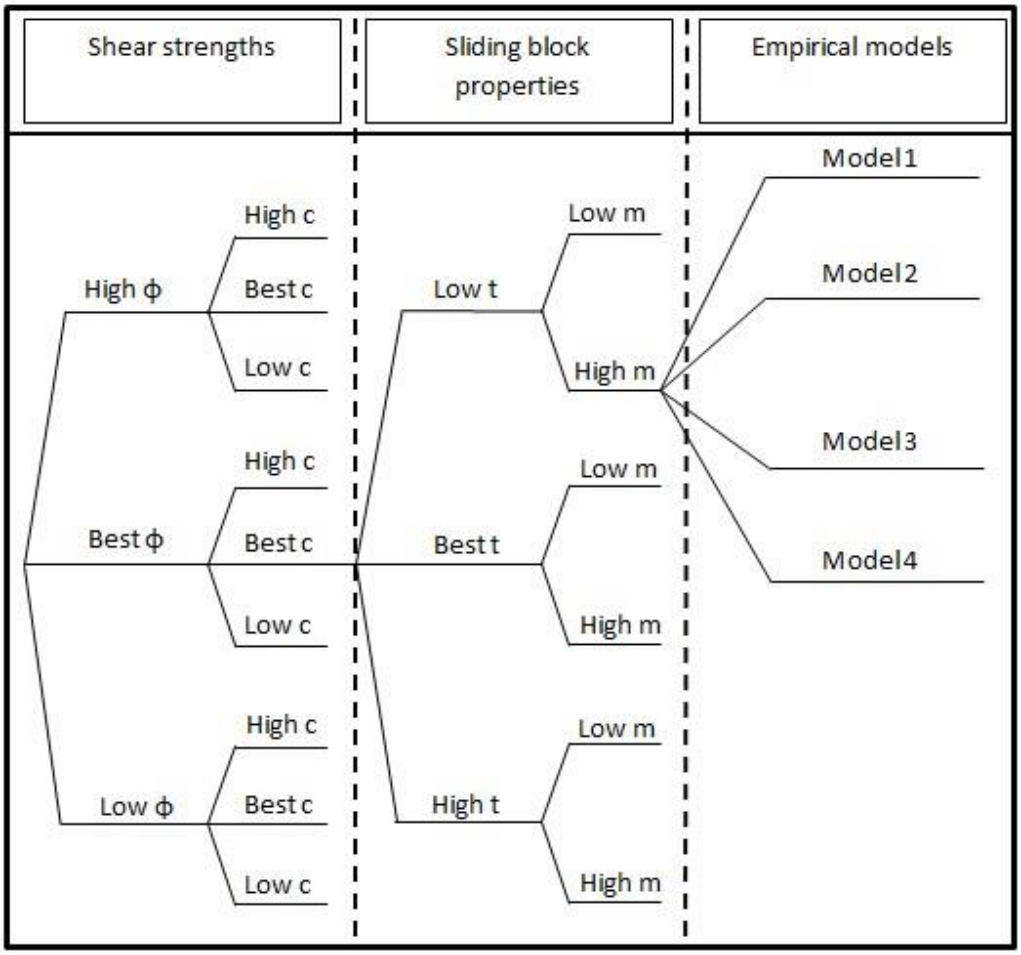

Figure 5.8 Example logic tree for probabilistic seismic landslide hazard mapping

Several empirical displacement models should be adopted, rather than only one model, to incorporate the epistemic uncertainty among the different models. All empirical models should be equally weighted unless some models are believed to be more accurate than others. For instance, a vector model (e.g. SR08) may be assigned a higher weight than scalar models because the vector model takes more ground motion information in the calculation and, theoretically, should provide a more accurate prediction of displacement.

Considering all uncertainties discussed above, a logic tree may have dozens to hundreds of branches. Each branch leads to one k_y value for a grid cell and each k_y has a corresponding displacement hazard curve. As a result, each grid cell has dozens to hundreds of displacement hazard curves associated with the weights from the logic tree. A mean displacement hazard curve is computed from the individual hazard curves by summing the weighted hazard values at each displacement level. Considering a logic tree with *n* values of k_y, the mean hazard for displacement x can be computed as:

$$\overline{\lambda_D}(x) = \sum_{i=1}^{n} w_i \cdot \lambda_D(x)_i \tag{5.1}$$

where $\overline{\lambda_D}(x)$ is the weighted mean annual rate of exceedance for displacement x, $\lambda_D(x)_i$ is the displacement hazard from the i^{th} branch of the logic tree for displacement x, and w_i is the weight associated the i^{th} branch of the logic tree.

5.3.2 Applying Logic-Tree Analysis to Seismic Landslide Hazard Mapping

When the logic-tree analysis is applied to seismic landslide hazard mapping, each grid cell has dozens of possible k_y values with associated weights. Therefore, the approach of using k_y thresholds to define seismic landslide hazard categories is no longer applicable. A mean displacement hazard curve could be computed for each grid cell across an entire region but this would require a large amount of computation and is not practical. To address this issue, an efficient computational scheme is developed which does not sacrifice any accuracy.

The approach to applying the logic tree to regional analysis is based on computing the weighted mean annual rate of exceedance $\overline{\lambda_D}(x)$ at each grid cell for the displacement thresholds associated with the seismic landslide hazard categories. This approach is called the Mean λ_D Threshold approach. Comparing $\overline{\lambda_D}(x)$ of each grid cell and for each displacement threshold with the hazard level under consideration (target hazard level λ^*) allows each grid cell to be assigned to an appropriate seismic landslide hazard category. An example is given in Figure 5.9. At $\lambda^* = 0.0021$ 1/yr, the sliding displacement is 8 cm for a grid cell, and this grid cell should be categorized as high seismic landslide hazard (5 cm < D < 15 cm). Instead, comparing λ^* with $\overline{\lambda_D}(5\text{cm})$ and $\overline{\lambda_D}(15\text{cm})$ can also provide the same result. If $\overline{\lambda_D}(5\text{cm})$ for a grid cell is greater than $\lambda^* = 0.0021$ 1/yr, then the sliding displacement for that grid cell associated with $\lambda^* = 0.0021$ 1/yr is greater than 5 cm. If $\overline{\lambda_D}(15\text{cm})$ is less than $\lambda^* = 0.0021$ 1/yr for the same cell, then the sliding displacement for that cell associated with $\lambda^* = 0.0021$ 1/yr is smaller than 15 cm. Therefore, this grid cell would be placed in the 5 to 15 cm bin, which corresponds with the high seismic landslide hazard category. Similar as the k_y-threshold approach, only hazard categories, not exact predictions of sliding

displacements, are assigned to grid cells to create a seismic landslide hazard map. The Mean λ_D Threshold approach is equivalent to the displacement-threshold approach.

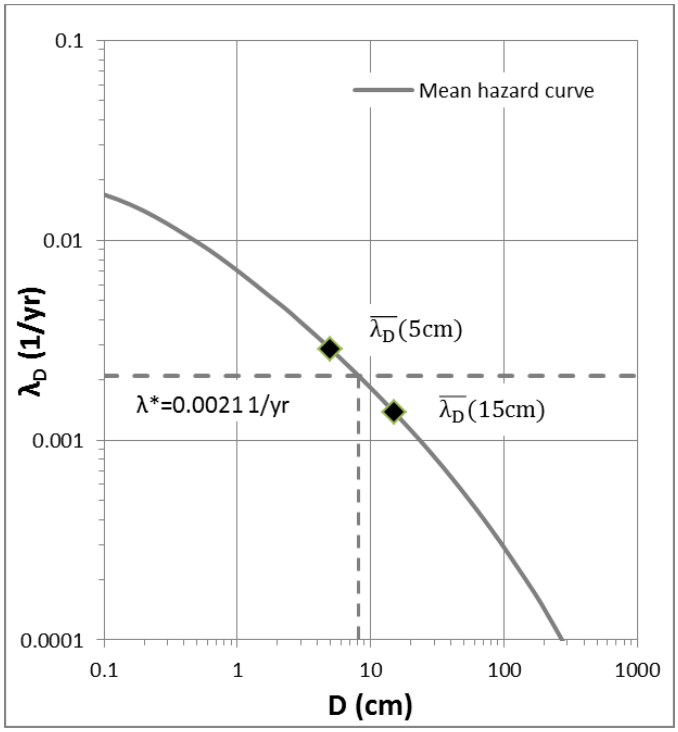

Figure 5.9 Illustration of Mean λ_D Threshold approach

The key to applying the Mean λ_D Threshold approach to each cell is the efficient computation of $\overline{\lambda_D}(x)$ from Equation 5.1 for each displacement threshold so that it can be compared with λ^*. Equation 5.1 requires the $\lambda_D(x)$ values associated with each k_y value. An interpolation relationship between k_y and $\lambda_D(x)$ is used to efficiently compute the $\lambda_D(x)$ values for Equation 5.1. The development of this interpolation relationship is described below.

For a single empirical displacement model (e.g. RS09) and single ground motion hazard curve, one k_y value leads to one displacement hazard curve. At a displacement

threshold of x cm (e.g. 5 cm), one k_y value corresponds to one $\lambda_D(x)$ value. This concept is demonstrated in Figure 5.10 for x = 5 cm. To establish a relationship between k_y and $\lambda_D(5cm)$ for this case, $\lambda_D(5cm)$ is compiled for a range of k_y values from the associated displacement hazard curves, and the data are fit with a 4th order polynomial regression model in log-log space (Figure 5.11). This relationship can then be used to quickly calculate $\lambda_D(5cm)$ for a given k_y value.

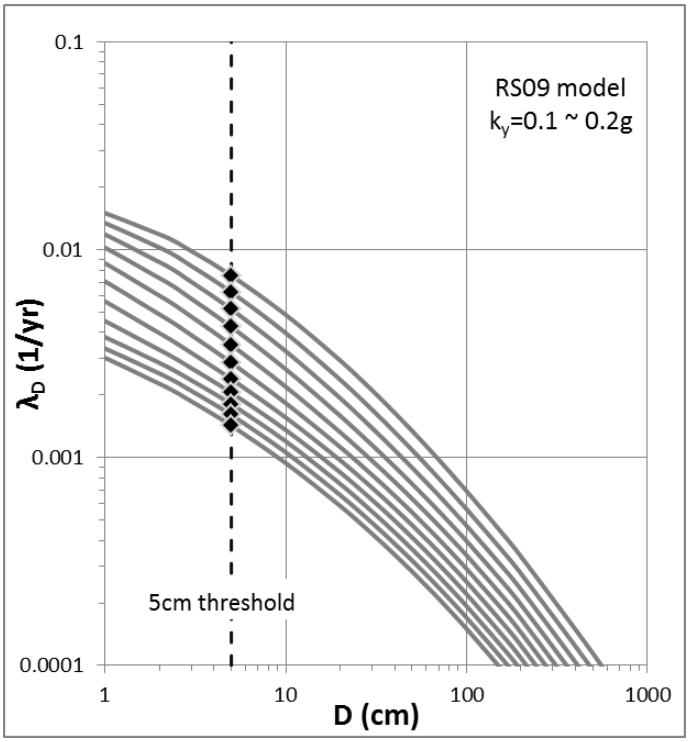

Figure 5.10 Displacement hazard curves for k_y values between 0.1 and 0.2 g

The typical range of k_y values of slopes that are potentially unstable during earthquakes is from 0.01 to 0.70 g. Any slope with k_y below 0.01g is essentially statically unstable (FS ≤ 1.0) and slopes with k_y larger than 0.70 g are either very flat or

are made of strong soils/rocks, meaning that such slopes can be assumed as seismically stable. Using a small k_y increment (e.g. 0.01g) and assuming all k_y values are between 0.01 to 0.70 g, there are only several dozens of possible k_y values to consider within a study area, despite the presence of millions of grid cells. Additionally, the difference between two displacement hazard curves is very small for a small change in k_y. Figure 5.10 shows a series of displacement hazard curves for k_y values between 0.1 and 0.2 g using an increment of 0.01 g, and these curves change gradually. Therefore several dozens of displacement hazard curves and interpolation between these hazard curves can be used to approximate all possible displacement curves in a region.

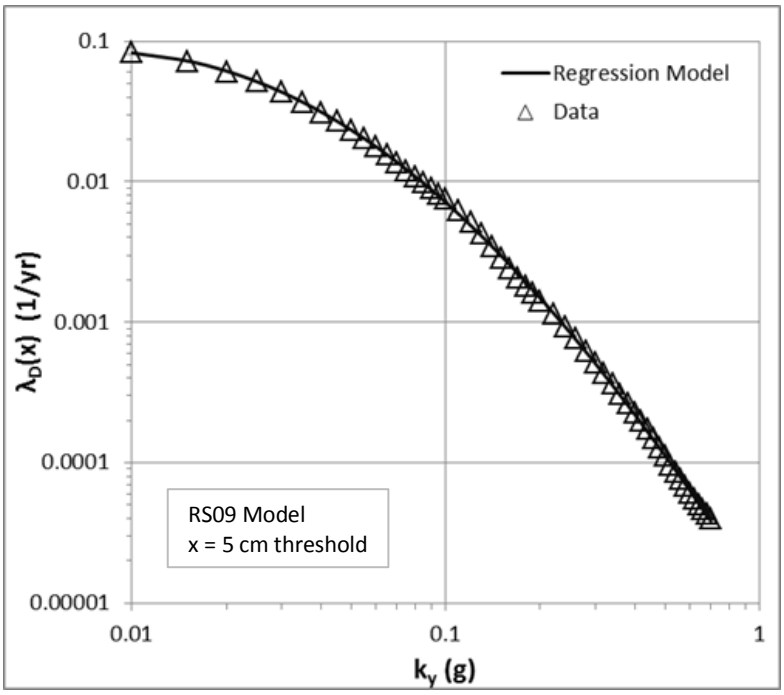

Figure 5.11 $\lambda_D(x)$ vs. k_y for x= 5 cm and 54 k_y values between 0.01 and 0.7 g.

Relationships between $\lambda_D(x)$ and k_y can be derived for each empirical displacement model and each displacement threshold. The general form of the regression relationships is expressed as:

$$\ln(\lambda_D(x)) = a_1(\ln(k_y))^4 + a_2(\ln(k_y))^3 + a_3(\ln(k_y))^2 + a_4\ln(k_y) + a_5 \quad (5.2)$$

where a_1 to a_5 are coefficients of the regression model. Using the regression relationships, the multiple k_y values associated with each grid cell can be quickly related to the associated $\lambda_D(x)$ values needed for Equation 5.1 and the $\overline{\lambda_D}(x)$ of each grid cell calculated. By comparing $\overline{\lambda_D}(x)$ values for the displacement thresholds of x = 1, 5 and 15 cm with the target hazard level (λ^*), the seismic landslide hazard category can be determined for each grid cell.

5.3.3 Screening Analysis

To further reduce the computation time for the regional analysis incorporating epistemic uncertainties, a screening analysis using the worst-case scenario of the logic tree is carried out. The worst-case scenario is associated with the minimum k_y, and is represented by the smallest shear strength and the largest *m* and *t* values. This analysis can highlight the grid cells that have low seismic landslide potential because if the displacement hazard for 1 cm (i.e., the lower bound displacement threshold for the moderate landslide hazard category) is less than λ^* for the minimum k_y, then the displacement hazard computed using the full logic tree will also be less than λ^*. Therefore, the full logic-tree analysis does not need to be performed for these grid cells.

The screening analysis can be performed for all displacement thresholds. For larger displacement thresholds, more grid cells are excluded from the full logic-tree analysis. The screening analysis may remove as many as 70% to 90% (or even more) of the grid cells from the full logic-tree analysis.

5.4 SUMMARY

This chapter discussed the development of probabilistic seismic landslide hazard maps. These maps represent an improvement from current deterministic approaches so that they incorporate the aleatory variability and epistemic uncertainties in the displacement predictions. A logic-tree analysis is introduced to incorporate the epistemic uncertainties associated with the slope properties and among empirical displacement models. A weighted mean displacement hazard curve is computed from the branches of the logic tree for each grid cell.

To reduce the computational efforts, an efficient approach to computing the weighted mean displacement hazard was developed. This Mean λ_D Threshold approach computes the weighted mean hazard at each displacement threshold ($\overline{\lambda_D}(x)$) directly from the k_y values through regression models that relate the displacement hazard at the displacement threshold ($\lambda_D(x)$) to k_y. The $\overline{\lambda_D}(x)$ values are compared with the target hazard level to determine the seismic landslide hazard category for each grid cell. A screening analysis using the worst-case scenario of the logic tree can further reduce the computational effort.

Chapter 6 Application of Regional Probabilistic Framework: Anchorage Seismic Landslide Hazard Map

6.1 INTRODUCTION

To implement the regional probabilistic framework described in Chapter 5, Anchorage, Alaska is selected as the study area. This location was selected based on the history and occurrence frequency of earthquakes, the availability of the required data in GIS format, access to databases of soil properties in the study area, and the availability of PGV ground motion prediction models for the tectonic region.

Anchorage has experienced several large earthquakes in the past, such as the 1964 Alaska earthquake (M=9.2). Seismic landslides caused most of the deaths and economic losses during the 1964 earthquake in Anchorage (Keefer, 1984). Since then, many studies have been conducted to identify areas susceptible to potential landslides in future earthquakes. Jibson and Michael (2009) recently created seismic landslide hazard maps for Anchorage using the deterministic approach, and thus this is an ideal study area because the data required for analysis are available.

The Anchorage, Alaska study area is about 24 km by 25 km (Area = 301 km^2, Figure 6.1) and represents the extent of the recently developed seismic landslide hazard map by Jibson and Michael (2009). The northern, western and central areas are mostly plains, and downtown Anchorage is located at the northwestern corner. The study area boundaries along the northwest to southwest are mostly coastlines. The Chugach

Mountains cover the eastern and southern parts and extend beyond the boundaries of the study area.

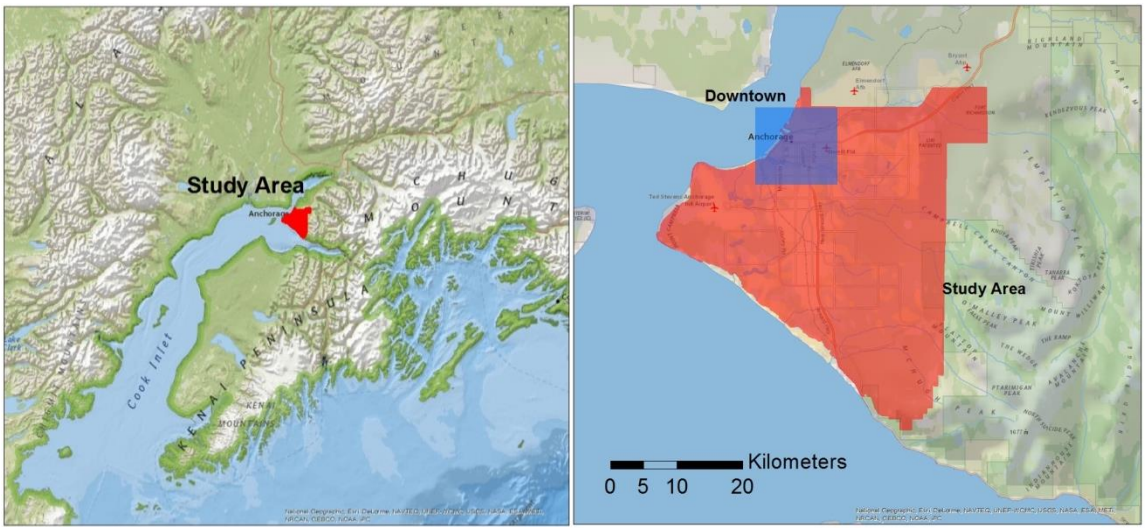

Figure 6.1 Overview of the study area in Anchorage, Alaska (based on National Geographic, ESRI)

6.2 CURRENT SEISMIC LANDSLIDE HAZARD MAP

Jibson and Michael (2009) produced seismic landslide hazard maps for Anchorage using sliding displacements predicted from a deterministic approach. The maps are based on ground motions associated with two different seismic hazard levels, 2% probability of exceedance in 50 years and 10% probability of exceedance in 50 years, which correspond to PGA values of 0.69 g and 0.43 g respectively (Wesson et al. 2007). In defining the slope properties for the calculation of the infinite slope k_y the slab thickness (t) was assumed to be 15 meters (50 ft), which is the upper bound of commonly observed landslides in Anchorage (personal communication with Dr. Randall W. Jibson).

By assuming a groundwater table at 3-meter (10 ft) depth, the saturation factor (*m*) is relatively large at 0.8. The combination of the large slab thickness and high groundwater level is very conservative and results in small values of k_y. The unit weight of soil was held constant at 18.8 kN/m^3 (120 lb/ft^3), and used for the entire study area. The friction angle and cohesion intercept were assigned across the study area based on geologic units. Displacements were computed across the study area using yield acceleration values determined at 6-m (20 ft) intervals, and the empirical displacement model of Jibson (2007) that uses only PGA, without magnitude, to characterize the ground motion.

Figure 6.2 shows the Jibson and Michael (2009) seismic landslide hazard map given a PGA with a 2% probability of exceedance in 50 years. The landslide hazard categories are assigned from displacements using the displacement thresholds previously described in Table 2.1. For this map, about 1.5% and 2.7% of the study area are classified as high hazard (5cm < D < 15cm) and very high hazard (D > 15cm), respectively. Another 5.5% of the study area was defined as moderate hazard (1cm < D < 5cm). Most areas with high or very high hazard are within colluvium units along the coastal bluffs and stream valleys in the lowland, colluvium units within the inland Chugach Mountains, and alluvium units along abandoned or modern stream-banks. A similar hazard map with 10% probability of exceedance in 50 years was also produced through the deterministic approach, and the results are summarized in Table 6.1. The smaller ground motions associated with this hazard level results in less of the study area assigned to the moderate, high, and very high hazard categories.

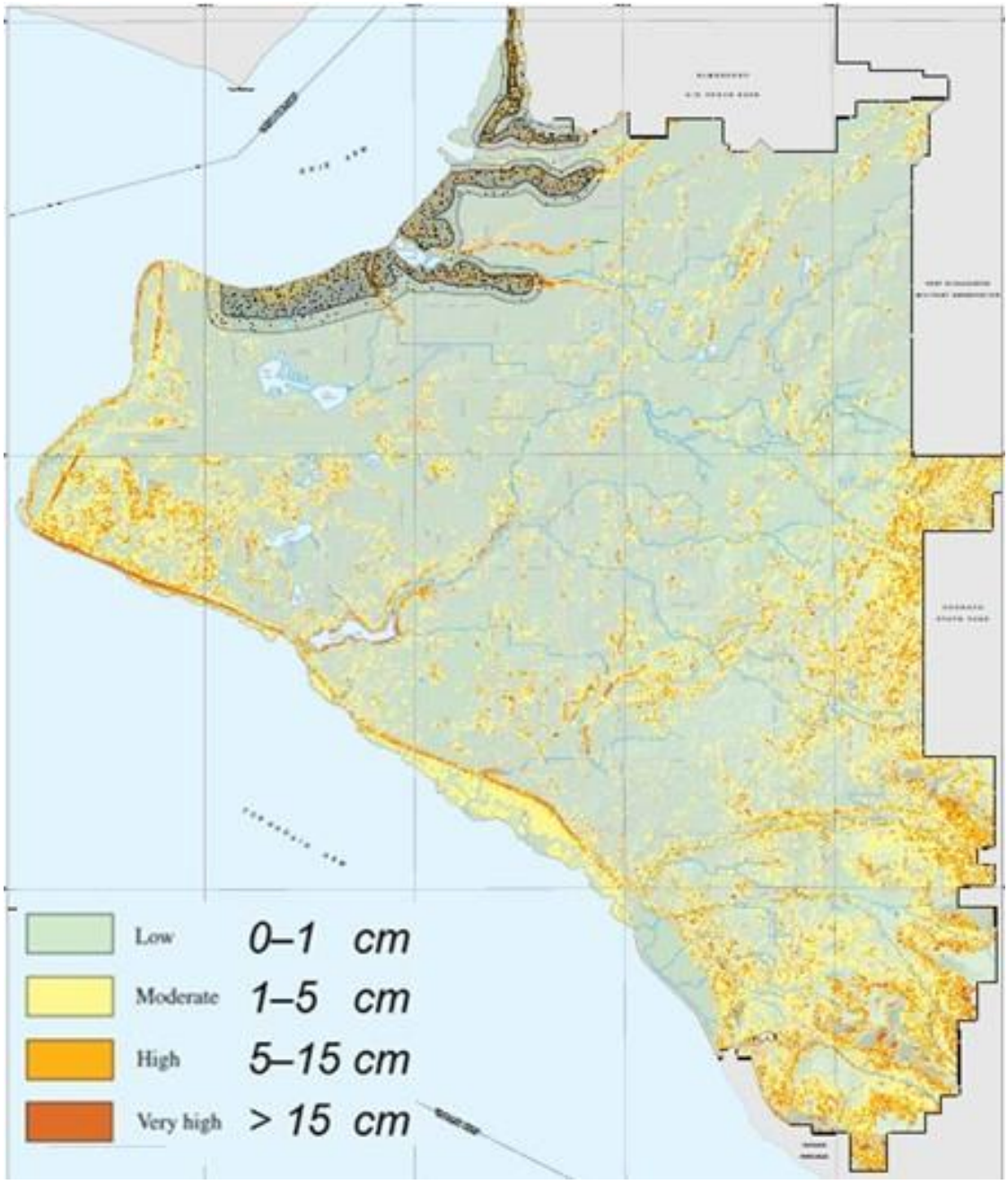

Figure 6.2 Deterministic seismic landslide hazard map at 2% probability of exceedance in 50 years of Anchorage, Alaska (Jibson and Michael 2009)

Table 6.1 Percentage of study area in hazard categories from deterministic maps

Hazard Category	Sliding Displacement (cm)	Percentage of Study Area	
		2% in 50 years	10% in 50 years
Low	0 - 1	90.31%	95.69%
Moderate	1 - 5	5.53%	1.63%
High	5 - 15	1.48%	0.75%
Very High	> 15	2.68%	1.93%

6.3 INPUT PARAMETERS

6.3.1 Topography and Geology

Figure 6.3 is a shaded relief map of the study area derived from a DEM. The entire study area is about 301 km^2 (8,370,622 grid cells), with a width of 24 km and a length of 25 km. The highest elevation is 1,026 m (3,363 feet) and the largest slope angle is 77^o. The DEM was derived from Light Detection and Ranging (LIDAR) data produced by the Municipality of Anchorage in 2004. The original LIDAR DEM was at 1.5 m (5 ft) resolution and the vegetation and buildings had been removed. Jibson and Michael (2009) resampled the LIDAR data to a 6-m (20 ft) resolution DEM and used this DEM to generate a slope map (Figure 6.4).

The original DEM with very fine resolution provides too many details about the local topography, with very small, steep surfaces on generally flat slopes identified. The influence of the DEM resolution the slope distribution across the study area is shown in Figure 6.5. Using a higher resolution DEM results in more steep slopes, and the increase is most significant for slope angles above 40°. These small, steep surfaces, which include earth retaining structures, are not a significant seismic slope stability hazard, but

they will be predicted to experience large sliding displacements during an earthquake. Therefore, we found it unnecessary to preserve the very fine resolution for seismic landslide hazard mapping purposes. Additionally, the using the 6-m resolution DEM instead of the 1.5-m resolution DEM will accelerate the speed of computation by approximately 16 times and decrease the required storage capacity of data. Finally, if one considers the 6-m resolution DEM in Figure 6.3, it is clear that this DEM captures the important topographic features across the study area. For example, the stream channels associated with the creeks north and south of downtown Anchorage area are clearly observed, as the Anchorage International Airport located to the southwest of the downtown area.

The 6-m resolution DEM is used to develop the slope map (Figure 6.4) required to compute the yield acceleration information across the study area. Most of the steep terrain is along the coastal bluffs, stream valleys, and in the southern and eastern mountain areas. These locations of steep terrain are, of course, more susceptible to seismic landslides than other areas, as also seen in the deterministic seismic landslide hazard map (Figure 6.2). The distribution of slope angles derived from the 6-m resolution DEM is shown in Figure 6.5. About 1.0% of the study area has slope angles greater than 30^{o}, and about 4.6% of the area is steeper than 20^{o}.

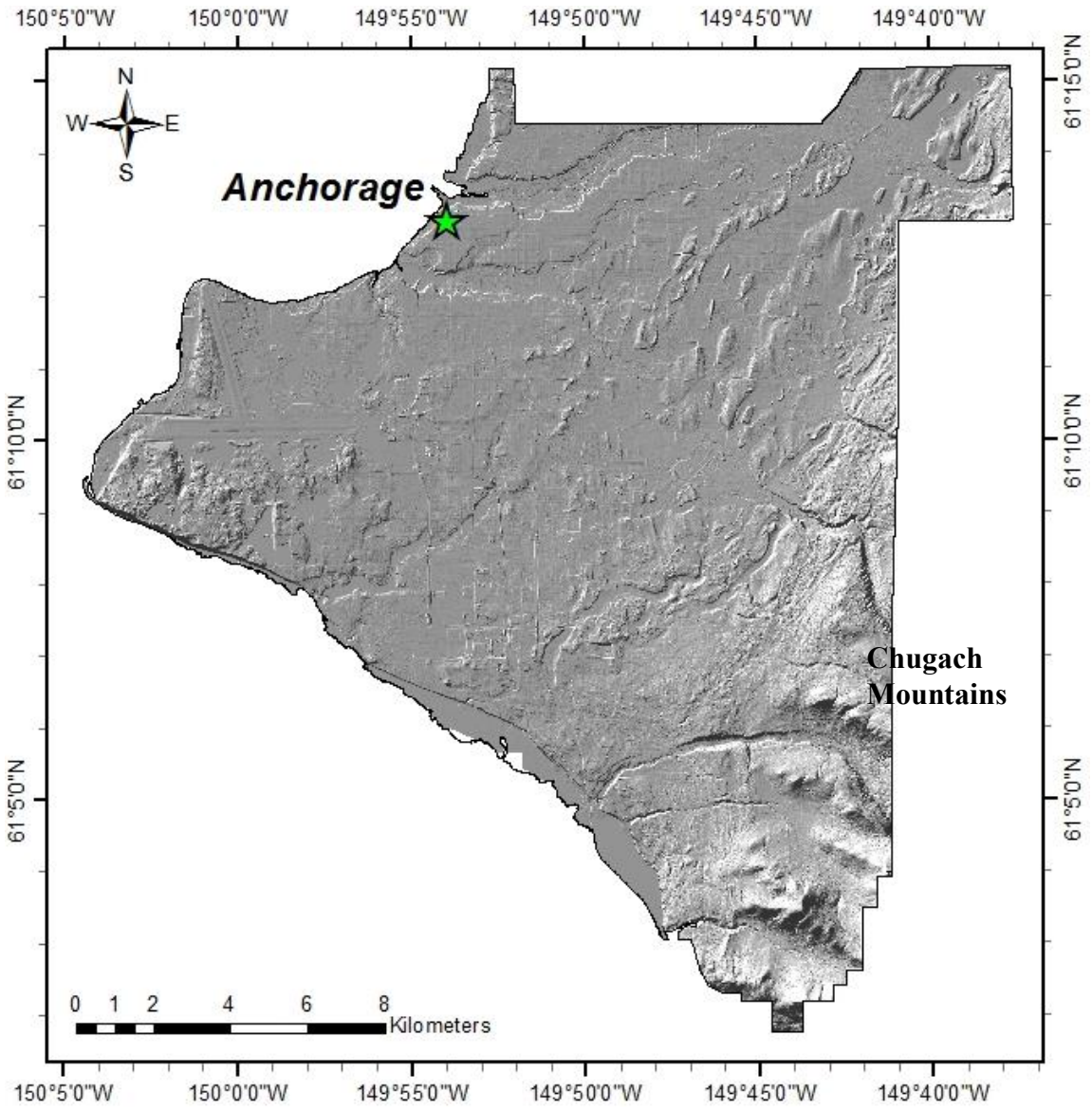

Figure 6.3 Shaded relief map of Anchorage, Alaska

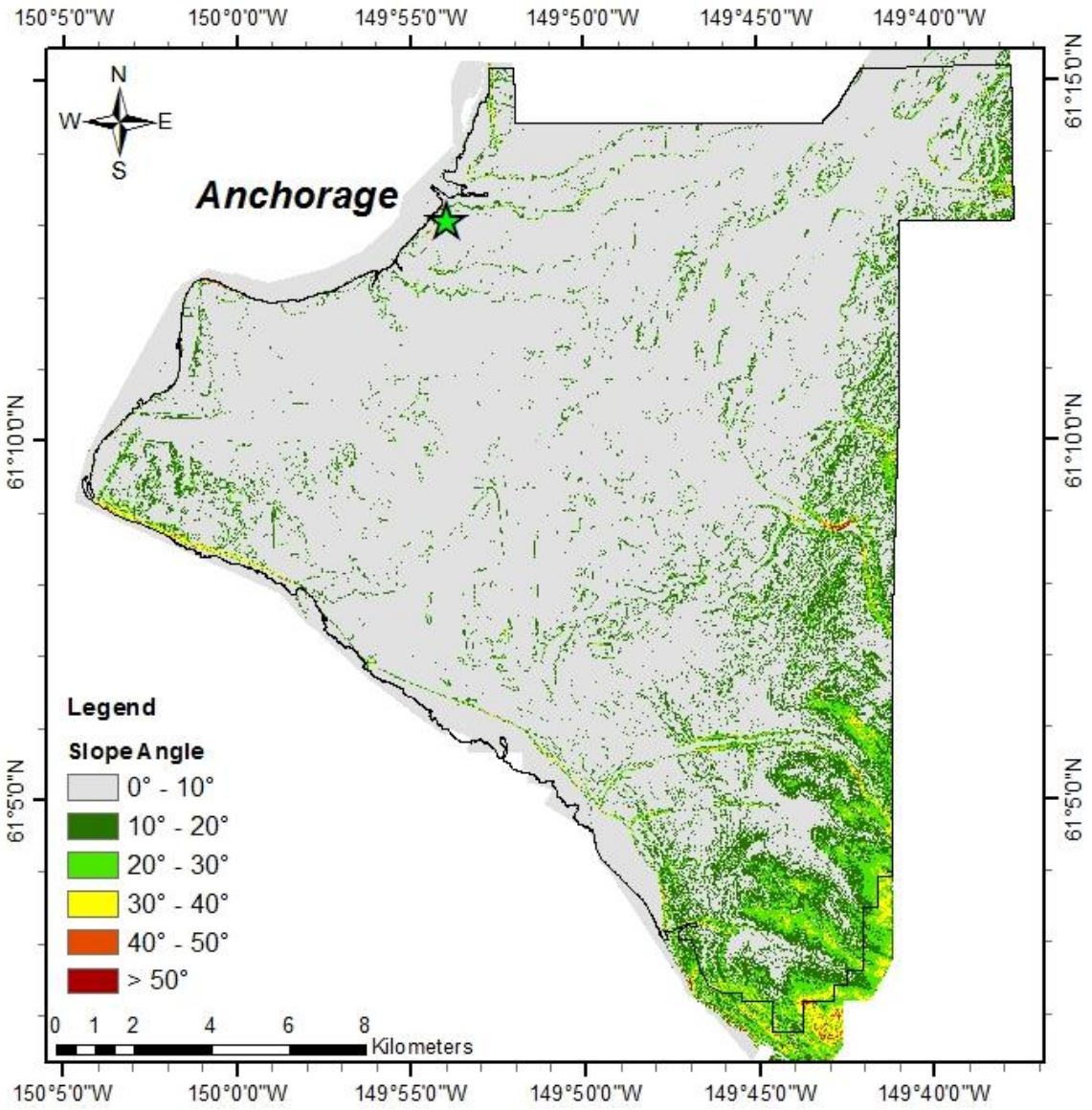

Figure 6.4 Slope map of Anchorage, Alaska

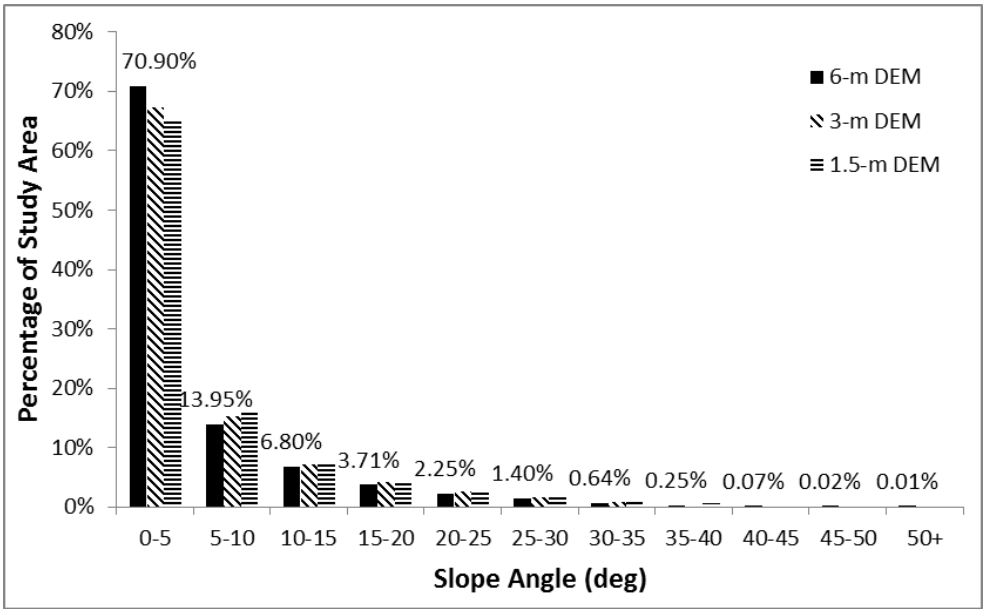

(a)

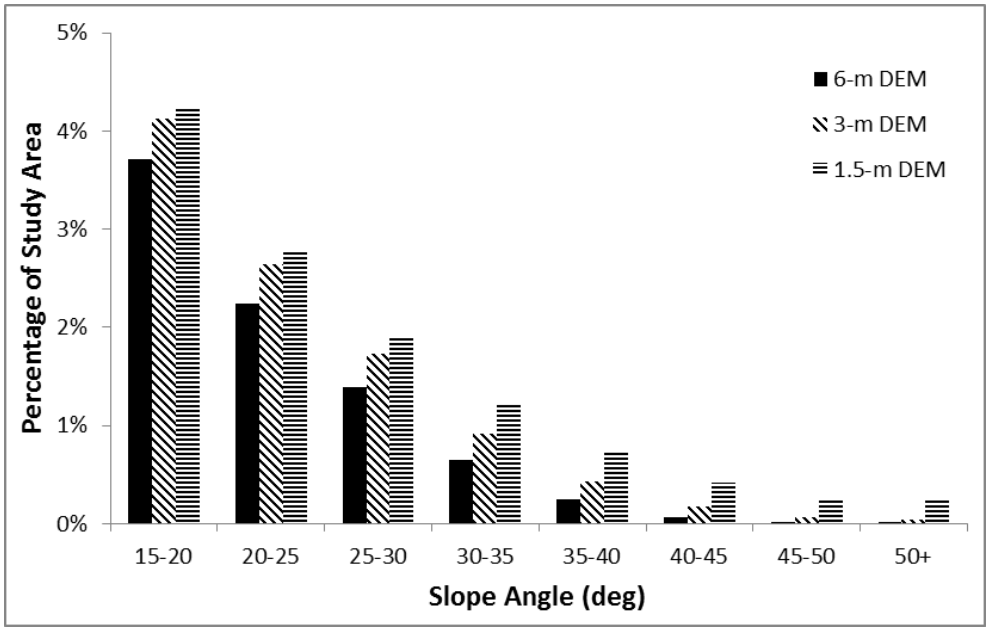

(b)

Figure 6.5 Slope angle distributions of the study area with different DEM resolutions (a) all slopes (b) slopes > 15^{o}

Jibson and Michael (2009) used digitized versions of the surficial geologic maps of Schmoll and Dobrovolny (1972) and Yehle et al. (1992) to assign shear strengths across the study area. There are 17 geologic units across the study area: a map of these units is shown in Figure 6.6 and the shear strength properties from Jibson and Michael (2009) are listed in Table 6.2.

The famous Bootlegger Cove Clay (bc unit) is related to the deeper landslides from the 1964 earthquake, because at depth it is weak with the potential for cyclic degradation of shear strength. However, the Bootlegger Cove Clay was assigned relatively larger shear strength when exposed at the ground surface based on the relatively larger values of SPT blowcount indicated near the surface as compared to at depth. Although the Bootlegger Cove Clay is not widely shown on the surficial geologic map, it is the main underlying soil layer of man-made fills and sand deposits.

Silt deposits (s) are along the coastal lines. The units af, al and an are alluvium on plains and along stream channels with similar shear strengths, and the glacial alluvium (ga) on irregular-shaped hills has higher shear strength. Glacial material units (gm, m and mg) all have high shear strength, and they form the underlying soil layer of most surficial geologic units in Anchorage. Sand deposits (sl and sh) cover the central west part of the study area. The colluvium unit c-bl mostly covers coastal bluffs and valley walls in the lowland. The other colluvium unit c-br is distributed in the eastern area on the slopes of the Chugach Mountains.

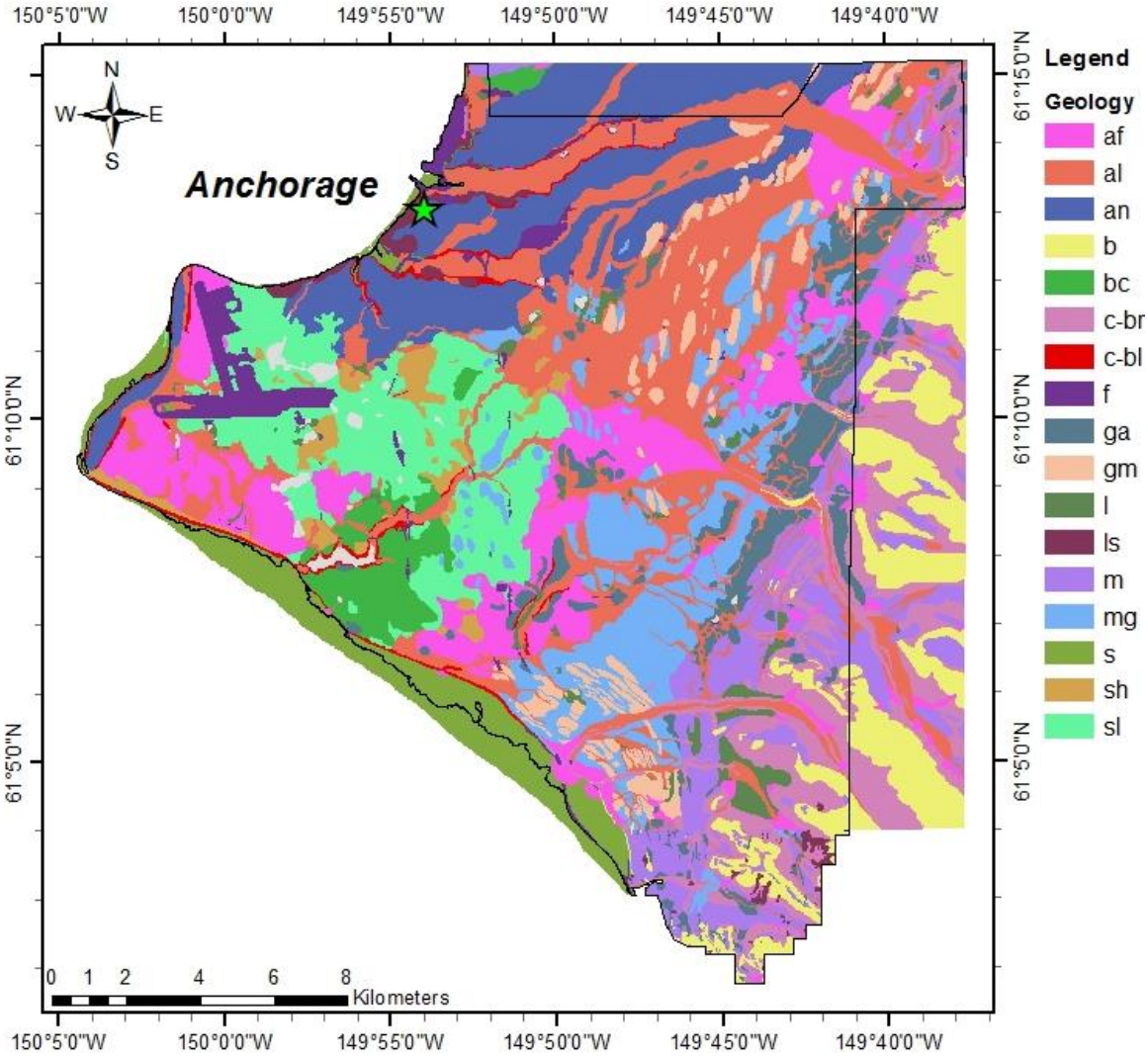

Figure 6.6 Surficial Geologic Map of Anchorage, Alaska

Table 6.2 Geologic Units and Shear Strengths (Jibson and Michael 2009)

units	Friction Angle (deg)	Cohesion (kPa)	Compositions
af	36	24	Deposits in alluvial fans, alluvial cones, and emerged deltas
al	36	19	Alluvium in abandoned stream channels and in terraces along modern streams
an	36	24	Coarse-grained surficial deposits
b	40	192	Bedrock
bc	0	120	Bootlegger Cove Clay
c-br	38	38	Colluvium derived from bedrock on slopes of the Chugach Mountains
c-bl	0	38	Colluvium derived from glacial materials along coastal bluffs
f	34	48	Manmade fill
ga	32	38	Glacial alluvium in irregular-shaped hills (including kames, eskers, and kame terraces)
gm	38	48	Glacial and (or) marine deposits, typically in elongate hills
l	0	144	Lake and pond deposits
ls	30	24	Landslide deposits, similar to an unit
m	38	43	Morainal deposits, generally in long ridges marking the margins of former glaciers
mg	37	38	Marine, glacial, and (or) lacustrine deposits
s	0	72	Silt
sh	34	24	Sand deposits in broad, low hills, and windblown sand deposits in cliffhead dunes near Point Campbell
sl	34	19	Sand deposits in a wide low-lying belt around Connors Lake

Sands and gravels were characterized using effective (drained) shear strengths. Clays and silts were characterized as total (undrained) shear strengths with zero friction angle. The shear strengths in Table 6.2 are considered best estimates and were compiled by Jibson and Michael (2009) using triaxial test, direct shear, vane shear and standard penetration test (SPT) results.

The variability in shear strengths can be estimated from the study of Phoon and Kulhawy (1999). They summarized that the coefficient of variation (COV, equal to the standard deviation divided by the mean) is about 10 to 50% for undrained shear strength and 5 to 15% for effective friction angle. For this study, the COV for the undrained shear strength is taken as 30%, and for the effective friction angle it is taken as 10%. The COV for the effective cohesion is taken as 20%, so that the total uncertainty in the drained shear strength is similar to the undrained shear strength. Dr. Randall W. Jibson from the USGS (personal communication) also suggested similar levels of uncertainty for shear strength based practical experience and engineering judgment in Anchorage, Alaska.

Assuming that shear strengths follow a normal distribution, the weights of the logic tree branches assigned to the high, mean and low shear strengths are determined based on a three-point estimation of the normal distribution. To approximate a standard normal distribution the three points are taken at 10%, 50%, and 90% (i.e., $\mu - 1.3\sigma$, μ, $\mu + 1.3\sigma$), the corresponding weights are 0.3, 0.4, and 0.3. The weights of the logic tree branches for shear strengths are summarized in Table 6.3.

Table 6.3 Weights of logic tree branches for shear strengths

Shear Strength	No. of σ	CDF	Weight
High	1.3	90%	0.3
Mean	0	50%	0.4
Low	-1.3	10%	0.3

The typical thickness and the underlying soil layers of the different surficial geologic units are summarized from the studies of Schmoll and Dobrovolny (1972) and Combellick (1999), as shown in Table 6.4. The underlying units are listed in order of their predominance across the main geologic unit. Such information will be used in the 2-D slope stability analyses in the next section to determine failure surfaces and associated failure depths of each geologic unit.

Table 6.4 Thickness and underlying soil layers of surficial geologic units

Units	Thickness (m)	Underlying Soil Layers
al	3 ~ 9	m, gm, mg, ga, bc
an, af, ga	6 ~ 15	m, gm, mg, bc
bc	up to 18 in the sea bluffs up to 60 in the central part of lowland area	m, gm, mg
c-bl	up to 3	m, gm, mg, ga, bc
c-br	up to 3	b
f	3 ~ 6	bc, l, an, af, ga, al
l	6 ~ 20	m, gm, mg
ls	6 ~ 9	bc
m, gm, mg	mostly > 30 6 ~ 15 on mountains	b
sl, sh	6 ~ 18	m, gm, mg, bc, l

6.3.2 Sliding Block Properties

As discussed in Section 2.2, the thickness of seismic landslides is typically shallow, on the order of several meters. Jibson and Michael (2009) used t = 15 m (50 ft) for the seismic landslide hazard maps in Anchorage, Alaska. Such a large thickness was used because $t \leq 15$ m is the typical range of landslide depths observed in Anchorage and it was decided to use the larger value because it leads to smaller k_y and thus is conservative (personal communication, Dr. Randall W. Jibson). In this study, instead of using a large and conservative t value, the epistemic uncertainty in t values is considered.

Shallow landslides usually occur within the surficial weak soils or on the contact surface between the surficial soil and underlying stiff soil/rock. Table 6.4 lists the general thickness of surficial geologic units, and it provides an initial estimate of failure depths. To further investigate failure depths for the most critical geologic units, the landslide hazard distribution across geologic units according to the Jibson and Michael (2009) deterministic map are used. The number of grid cells with high or very high hazard (D > 5 cm) in each geologic unit from the Jibson and Michael (2009) study is summarized in Table 6.5. In this table, Landslide Cells are grid cells with predicted displacement greater than the 5-cm threshold. The % of Study Area represents the percentage of study area covered by each geologic unit. The % of Geo Unit is the percentage of grid cells with D > 5 cm for each geologic unit. The % of Landslide Cells is the contribution of each geologic unit to all landslide cells in the study area. Identified in Table 6.5 are the geologic units that are covered with more than 5% landslides (% of Geo Unit > 5%) and the geologic units that contribute more than 5% to the total number of landslide cells (% of Landslide Cells > 5%). Seven geologic units fit into these categories and represent about 87% of the landslide cells. The other geologic units,

which have high shear strength and are underlain by stiff soil/rock (e.g. gm, m and mg) or exist mostly on flat terrain (e.g. an, f and l), do not contribute significantly to the seismic landslide hazard. The seven geologic units are investigated in detail to identify representative slope geometries that will help guide the selection of an appropriate range of slab thicknesses, *t*, through 2-D slope stability analysis.

Table 6.5 Deterministic landslide prediction in geologic units (5 cm threshold, 2% probability of exceedance in 50 years)

Geo Units	Landslide Cells	% of Study Area	% of Geo Unit	% of Landslide Cells
af	21441	11.4%	2.2%	**6.1%**
al	24446	22.0%	1.3%	**7.0%**
an	4982	9.8%	0.6%	1.4%
b	812	2.2%	0.4%	0.2%
bc	4373	2.8%	1.9%	1.2%
c-br	95859	6.1%	**18.9%**	**27.4%**
c-bl	98628	1.3%	**93.0%**	**28.2%**
f	1666	3.0%	0.7%	0.5%
ga	33788	5.3%	**7.7%**	**9.6%**
gm	2917	3.9%	0.9%	0.8%
l	1051	1.8%	0.7%	0.3%
ls	19434	1.0%	**22.4%**	**5.6%**
m	14729	6.0%	3.0%	4.2%
mg	6379	9.5%	0.8%	1.8%
s	4731	2.0%	2.8%	1.4%
sh	10378	2.1%	**5.8%**	3.0%
sl	4527	10.0%	0.5%	1.3%
Total	350141	100.0%		100.0%

First we consider the slope angle distribution for the seven geologic units (Figure 6.7). Alluvium units af and al are widely spread on flat plains in Anchorage, which results in a significant portion of these units on flatter slopes (about 80% < 5°). Nonetheless, these units contribute to the landslide hazard at locations of stream-banks covered by af and al which have steeper slopes. Glacial Alluvium (ga) exists on moderate slopes and contains significantly more steeper slopes than af and al. For the colluvium units, c-bl is mostly on coastal bluffs and valley walls, and c-br covers steep slopes of the Chugach Mountains. Sand deposits (sh) are found in low hills that have some landslide hazard under ground shaking. Landslide deposits (ls) cover bluffs and slopes along stream valleys in the central and western study area, and moderate to steep slopes in the southern mountainous area.

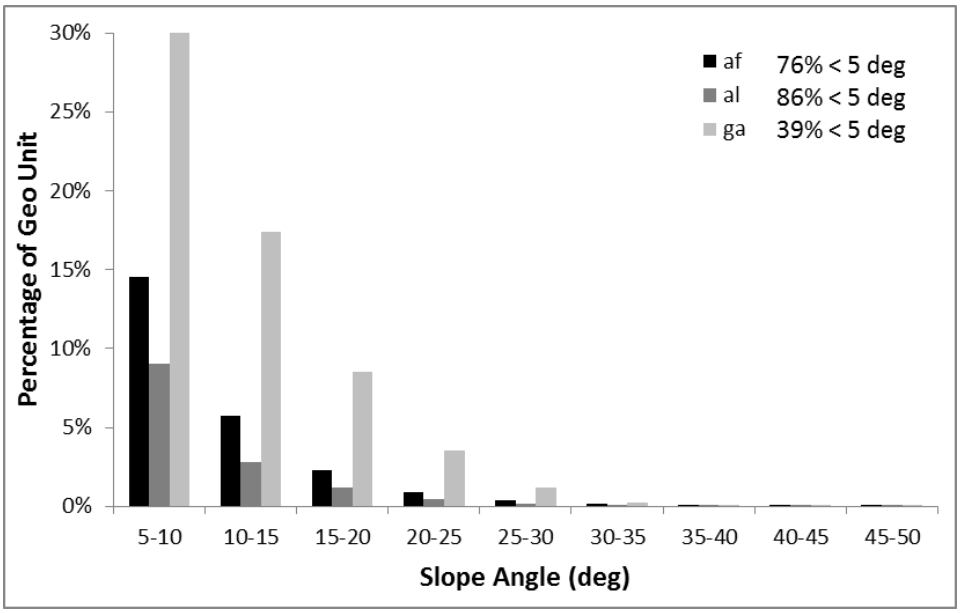

(a)

Figure 6.7

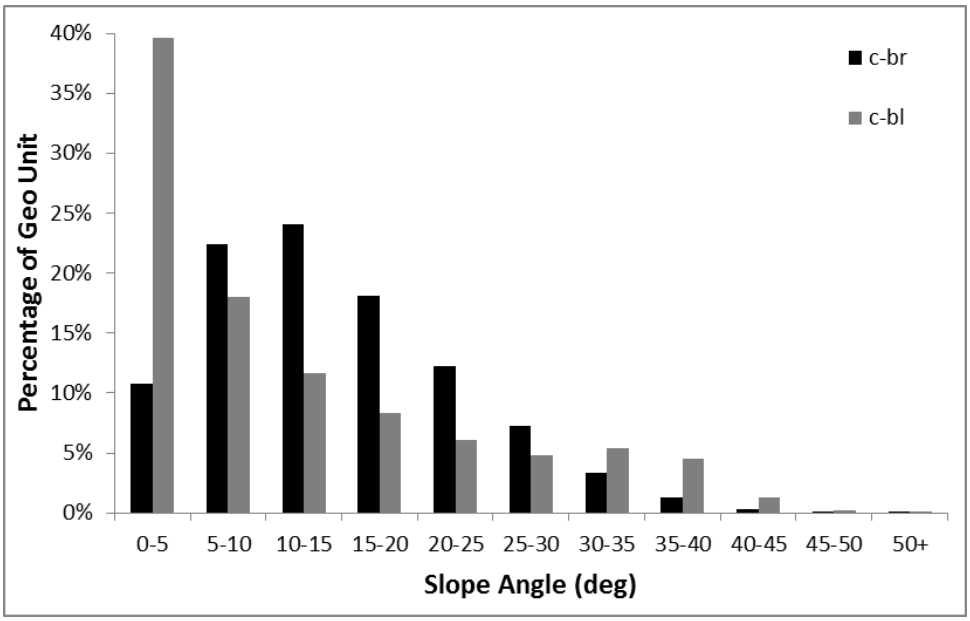

(b)

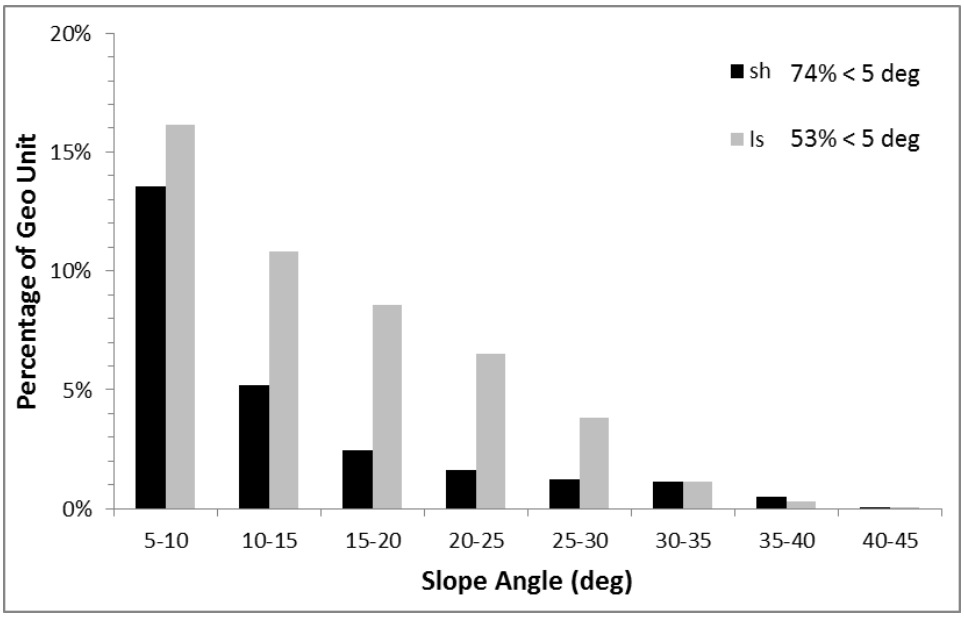

(c)

Figure 6.7 Slope angle distributions of (a) af, al and ga (b) c-br and c-bl (c) sh and ls

In Anchorage, slopes are found at two different spatial scales. The geologic units in the eastern and southern mountainous areas, (e.g. ga and ls) mostly exist as large-scale slopes (i.e., extend for significant distance uphill) with strong underlying soils, and the failure surfaces in these geologic units are typically shallow and extend long distances. The slopes on low hills and along coastal bluffs and stream valleys usually have smaller spatial scales, and the underlying soils may not be significantly stronger. It is impossible to illustrate all of the slopes for different surficial soils and underlying layers in such a large study area. However, some typical slopes can be analyzed using 2-D slope stability analysis to assist in the selection of *t* values used in seismic landslide hazard mapping.

Large-scale slopes commonly have failure depths equal to a few meters, up to the thickness of the surficial weak soil. The c-br unit is selected for 2-D slope stability analysis, because it exists in the southern mountainous area and a large portion of this unit is categorized as high hazard and above. Figure 6.8 shows a typical slope within the c-br unit, as developed from cross-sections provided in the geologic map of Combellick (1999). The surficial c-br unit has a thickness of 3 m and is underlain by the bedrock (b), as indicated in Table 6.2. The groundwater table (blue line) is placed at 3-m depth. Three slope configurations, representing moderate (3H:1V), moderately steep (2H:1V) and steep (1.3H:1V) slopes are analyzed with UTEXAS4 Educational Version to compute the critical failure depths. The results indicate that all critical failure surfaces are restrained by the contact surface between the surficial weak soil and underlying bed rock.

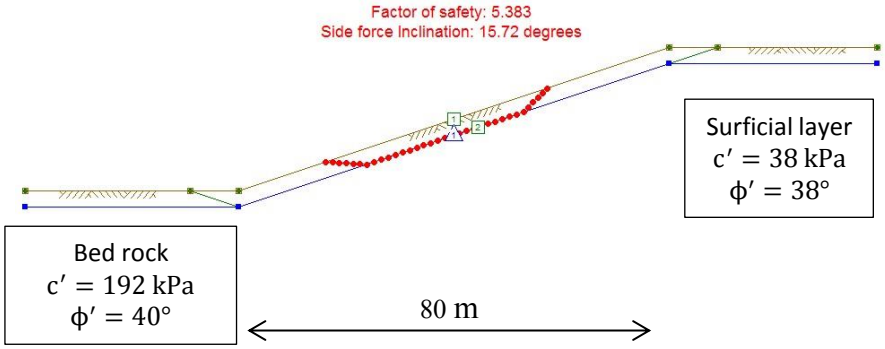

(a)

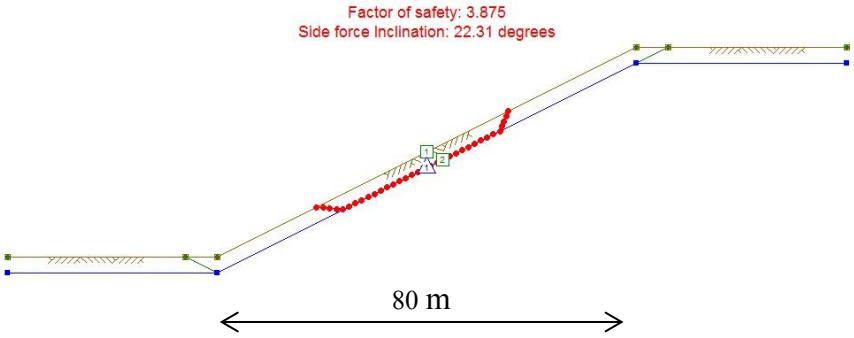

(b)

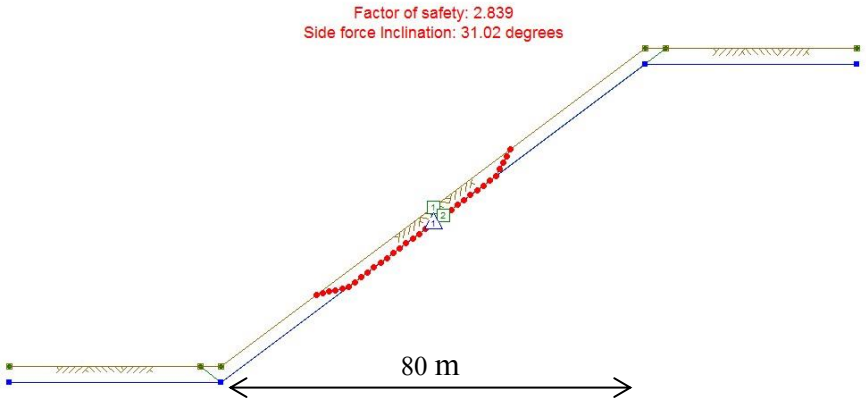

(c)

Figure 6.8 Critical failure surface of ls unit on (a) a 3H:1V slope (18^{o}), (b) a 2H:1V slope (27^{o}), and (c) a 1.3H:1V slope (37^{o}) in mountainous areas.

Glacial Alluvium (ga) is another unit that exists widely in the eastern mountain area and is investigated through 2-D slope stability analysis (Figure 6.9). Based on geologic information (Table 6.4), the surficial layer of ga can be characterized with a thickness of 6 to 9 m and it is underlain by morainal deposits (m). A 3H:1V slope is analyzed based on the slope histogram in Figure 6.9, the slab thickness is taken as 9 m, and the groundwater table is placed at about 3-m depth. The slope stability analysis shows a shallow failure within the surficial layer. The 2-D slope stability analyses for c-br and ga indicate that failures are constrained within the surficial unit. This is not surprising considering that the underlying material is stronger than the surficial unit. These analyses indicate for the thickness of the surficial unit can be used to guide the selection of slab thickness when the underlying unit is stronger than the surficial unit.

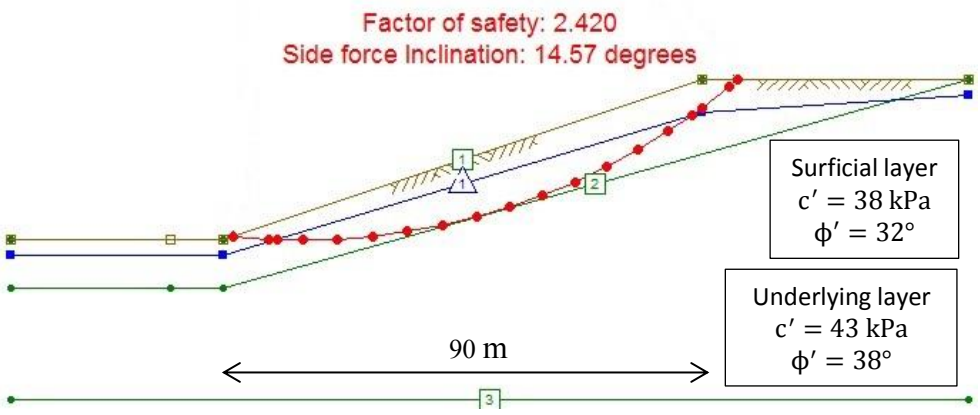

Figure 6.9 Critical failure surface of ga unit on a 3H:1V slope (18^{o})

The sub-surface geometry of small-scale slopes on low hills or along coastal bluffs and stream valleys is more complex than those associated with large-scale slopes. In these cases, the failure may extend into an underlying layer with lower shear strength.

These types of geometries are common in the c-bl unit, as well as the ls unit. Figure 6.10 shows a moderate steep slope (2H:1V) with about 30-m horizontal distance from toe to crest. Such a slope is very common along the stream valleys. The surficial ls unit has a thickness of 6 m and is underlain by the coarse-grained deposits (an) and Bootlegger Cove clay (bc). The groundwater table is at 3-m depth. This cross-section was developed from a cross-section shown on the geologic map of Combellick (1999). Analyses were performed with the undrained shear strength of the bc unit assigned at its mean and lower values. The critical failure surface is constrained to the surficial landslide deposits when the mean strength is assigned to the bc unit, but a deeper failure (> 30 m deep) surface occurs when the lower shear strength is used for the bc unit. The Bootlegger Cove Clay exposed at the ground surface has relatively high shear strength, as assigned in Table 6.2. However, the shear strength can be lower at depth due to the presence of weaker facies that are prone to cyclic degradation and sensitivity of shear strength (Jibson and Michael 2009). Low shear strength in the bc layer may cause deep failures, as shown in Figure 6.10b. Seismic landslide hazard mapping do not typically focus on predicting deep-seated landslides because their failure is a function of the 2-D geometry which cannot be modeled at regional scale. Nonetheless, seismic landslide hazard maps can identify dangerous zones that require site-specific analysis for deep failures.

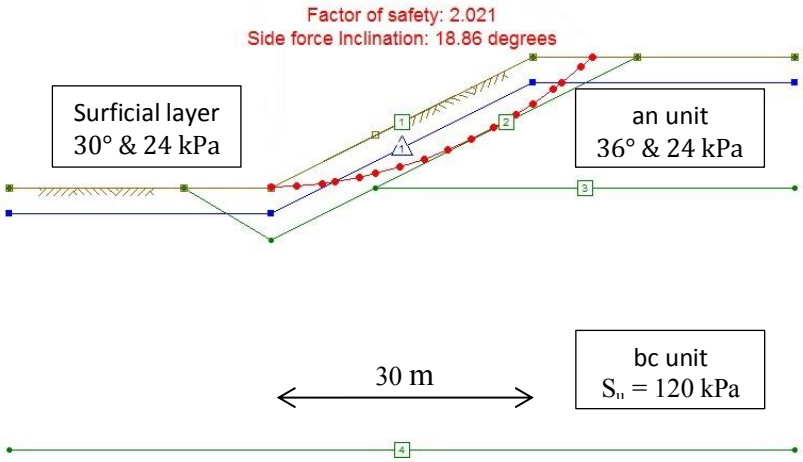

(a)

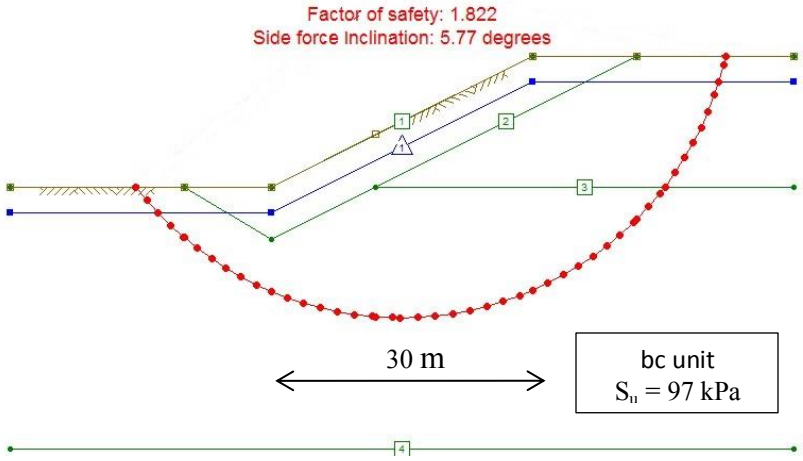

(b)

Figure 6.10 Critical failure surface of ls unit on a 2H:1V slope (28°) with (a) mean shear strength in bc unit and (b) low shear strength in bc unit

Another type of small-scale slope that occurs around Anchorage is a coastal bluff, which consists of a thin layer (3 m) of colluvium (c-bl) derived from glacial materials (e.g. m unit) underlain by the Bootlegger Cove Formation. Coastal bluffs are usually steep (greater than 30°), and this slope geometry is illustrated in Figure 6.11. Because

the surficial colluvium has low shear strength, the critical failure surface is a thin, veneer failure within the surficial layer. However, if the shear strength of the Bootlegger Cove Clay is smaller than about 100 kPa, a deeper failure (> 30 m deep) may become the critical failure mode.

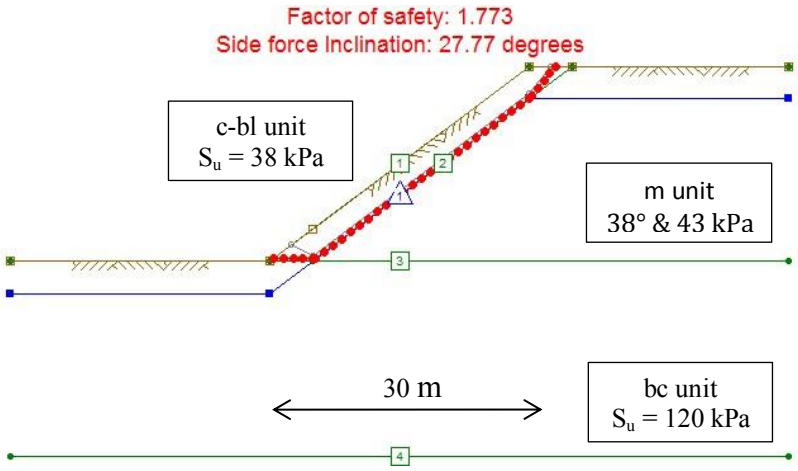

(a)

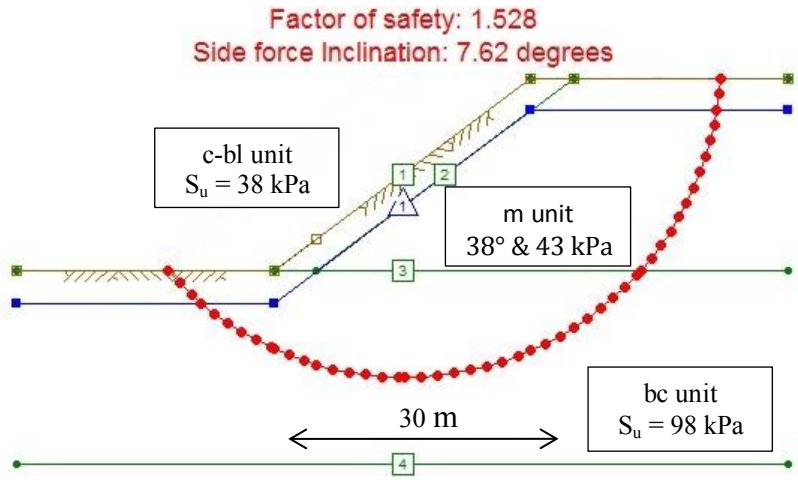

(b)

Figure 6.11 Critical failure surface of c-bl unit on a 1.3H:1V slope (37^o) with (a) mean shear strength in bc unit and (b) low shear strength in bc unit

One thing to be noted is that the true effective cohesion of surficial soils at shallow depths (i.e., small confining pressures) may be smaller than the assigned value due to the curvature of the failure envelope at small confining pressures. If the surficial soils have lower shear strength, then the failure surface should stay in the surficial layer rather than extend into underlying layers.

Overall, 2-D static slope stability analysis indicates that both large-scale and small-scale slopes have shallow critical failure surfaces that stay within surficial weak soils, except when the Bootlegger Cove clay at depth is assigned a low shear strength. As noted earlier, regional seismic landslide maps do not typically account for deep seated failures and therefore they will not be considered here. As a result, for shallow failures the thickness of the surficial soil is the main controlling factor of the *t* values. The data summarized in Table 6.4 describe typical thickness values for the different geologic units. These values are based on limited information, such that the actual surficial soils may be thinner or thicker across the study area, but these values are the best estimates available and appropriate for regional analysis. Generally, the surficial soil layers are thicker in flat terrain, and thinner in steep terrain. Based on this information and the thicknesses in Table 6.4, the thickness of surficial soils in the landslide-prone units can range from between 3 to 15 m. Thicknesses between 3 to 9 m are considered the most representative for moderate steep to steep slopes because the soil layers should be thinned on steeper slopes. Such estimates are consistent with the engineering observation that landslide depths in Anchorage can extend to a depth of 15 m (Jibson and Michael 2009). The colluvium units (c-br and c-bl) are treated differently based on the thickness estimates shown in Table 6.4. These units are assigned a thickness of 3 m with no uncertainty. The resulting logic-tree for *t* values is summarized in Table 6.6.

Table 6.6 *t* values and associated weights in logic-tree analysis

t value (m)	weights for c-br and c-bl	weights for other units
3	1	0.3
6	0	0.4
9	0	0.3

The *m* value, which is the proportion of the block thickness that is saturated, depends on the groundwater conditions, subsurface hydraulic conductivity, and precipitation, as these parameters influence the groundwater table location. Topography and artesian conditions can cause complicated spatial variations in the ground water table across a region. The estimation of ground water table relies on survey records and average annual precipitation. Jibson et al. (2000) used $m = 0$ to characterize the pore water pressure for slopes in the Oat Mountain quadrangle during the 1994 Northridge earthquake. This value was selected because the coarse-grained surficial slope material was very dry due to no rainfall over the preceding several months, and therefore the groundwater table was below the defined failure depth ($t = 2.4$ m).

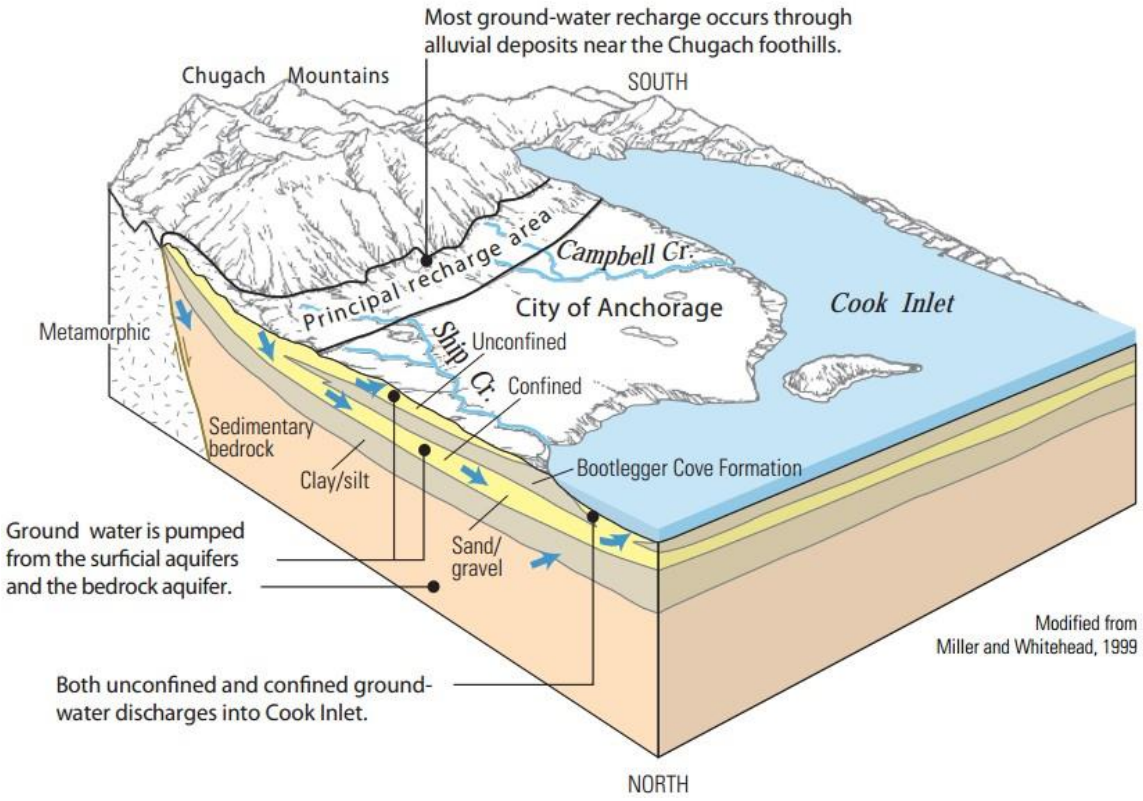

Figure 6.12 Conceptual models of the aquifer systems in Anchorage area (updated by Moran and Galloway, 2006)

The groundwater in Anchorage mostly comes from the Chugach Mountains as illustrated in Figure 6.12. In the eastern study area in the foothills of the mountains, the groundwater table should be high because this area is the so-called "Principal recharge area" which is close to the Chugach Mountains. In the central and western study area, slopes along stream valleys and coastal bluffs should also have relatively high groundwater table. Some groundwater data, collected from wells or borings in or around the downtown area, show that the groundwater table is tens of meters below the ground surface, but these data cannot represent the groundwater condition outside the urban area,

in which groundwater table is significantly reduced by heavy pumping (Moran and Galloway 2006).

The most commonly observed groundwater table in the Anchorage area is about 3 to 6 m (personal communication, Dr. Randall W. Jibson), and Jibson and Michael (2009) used a 3-m deep groundwater table to calculate their *m* value. For this study, a uniform distribution is used to simply describe the uncertainty in the groundwater table between 3 and 6 m. We assign 50% probability to the 3-m depth, and another 50% probability to the 6-m depth. The logic tree branches for *t* and *m* values are shown in Figure 6.13. The two *m* values associated with each *t* value represent 3-m depth and 6-m depth groundwater table, respectively. For colluvium units (c-bl and c-br), a constant *t* = 3 m is used, and *m* is set equal to 0 with the shallowest ground water table at 3 m. Thus, there are not logic tree branches for the colluvium units.

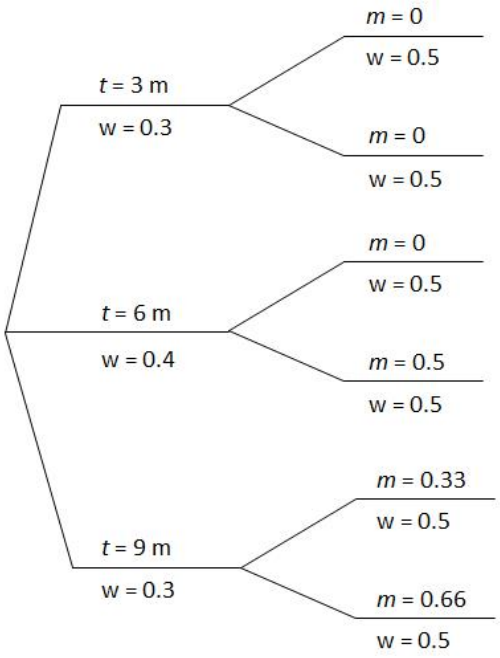

Figure 6.13 Logic tree branches for *t* and *m* values except for colluvium units (*t* = 3 m and *m* = 0)

6.3.3 Static Factor of Safety

The shear strengths and sliding block properties assigned to geologic units should satisfy slope stability under static conditions. For surficial soils on very steep slopes, the thicknesses are inherently thin and the shear strengths are usually high, so that the worst slope properties are unlikely to be present on very steep slopes. Therefore, instead of using the maximum slope angle, the slope angle at 99.5 percentile in each geologic unit is selected to calculate the static factor of safety.

As shown in Table 6.7, the static factors of safety using the best estimates of the slope properties (i.e. mean shear strengths, t = 6 m and m = 0.25) are all greater than 1.0, meaning that static slope stability is satisfied in each geologic unit. For the worst-case condition (i.e. low shear strengths, t = 9 m and m = 0.67), most geologic units still have static factors of safety greater than or approximately equal to 1.0. The probability of the worst-case condition is only about 1% according to the assigned weights in Table 6.3 and Figure 6.13, and such condition may be even rarer on very steep slopes as discussed above. The negative k_y values associated with static factors of safety less than 1.0 are set to 0.01 g.

Table 6.7 Static factor of safety

units	Slope angle at 99.5 percentile (deg)	Static FS (best estimate)	Static FS (worst case)
af	28	1.64	0.97
al	23	1.92	1.15
an	20	2.36	1.40
b	52	2.72	1.42
bc	29	2.19	**0.89**
c-br	40	1.99	1.56
c-bl	43	1.00	**0.61**
f	23	2.47	1.41
ga	29	1.68	0.97
gm	27	2.27	1.29
l	21	3.55	1.44
ls	34	1.12	**0.66**
m	30	1.94	1.11
mg	24	2.31	1.33
s	22	1.70	**0.69**
sh	35	1.21	**0.71**
sl	17	2.50	1.50

6.3.4 Ground Motion Hazard

The PGA seismic hazard for Anchorage is obtained from the 2008 National Seismic Hazard Mapping (NSHM) project (http://geohazards.usgs.gov/hazardtool/, Petersen et al. 2008). USGS provides a NSHM application through which a PGA hazard curve can be calculated at any location within the United States. Figure 6.14 shows the PGA hazard curve (solid line) from the 2008 NSHM project for Anchorage (N61.22, W149.90).

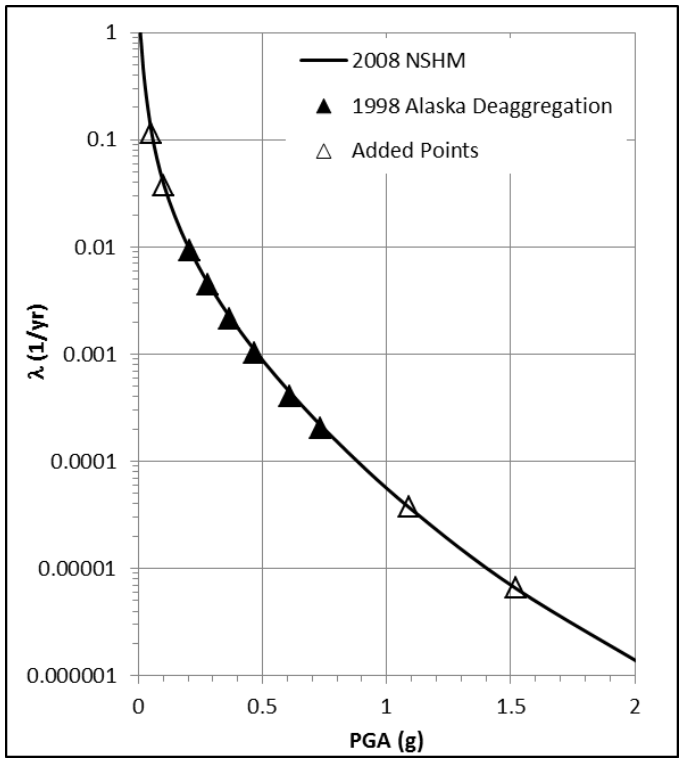

Figure 6.14 PGA Hazard Curve and deaggregation hazard levels in Anchorage (N61.22, W149.90)

The seismic hazard deaggregation data required by Equations 3.5 through 3.8 can also be downloaded from the USGS website. As seen in Figure 6.15, the geographic seismic hazard deaggregation presents the spatial distribution of all earthquake sources, providing a more intuitive representation of the seismic hazard deaggregation. The yellow dot, representing the location for which seismic hazard deaggregation is created, is downtown Anchorage. The red line north of Anchorage is the Castle Mountain Fault. The areas enclosed by orange lines at the southeast are megathrust subduction zones, where the northwestward-moving Pacific plate is subducting beneath the North American plate.

These maps show that the deaggregation contributions generally come from two major sources. Much of the hazard comes from earthquake events close to Anchorage, which are shallow crustal events with magnitude generally less than 7.0. Subduction zone events further away also have significant contributions.

The PGA values from the deaggregation are 0.61 g and 0.37 g at 2% and 10% probabilities of exceedance in 50 years, respectively. These PGA levels are smaller than the values used by Jibson and Michael (2009) (i.e., 0.690 g and 0.433g), because the seismic hazard deaggregation for Alaska was published by the USGS in 1998 while Wessen et al. (2007, 2008) updated the PGA seismic hazard in Alaska a decade later. Because the deaggregation information is required to compute the displacement hazard curves, the PGA hazard curve used in the analyses is derived from the PGA values reported in the deaggregation. This maintains consistency between the ground motion values and the deaggregation.

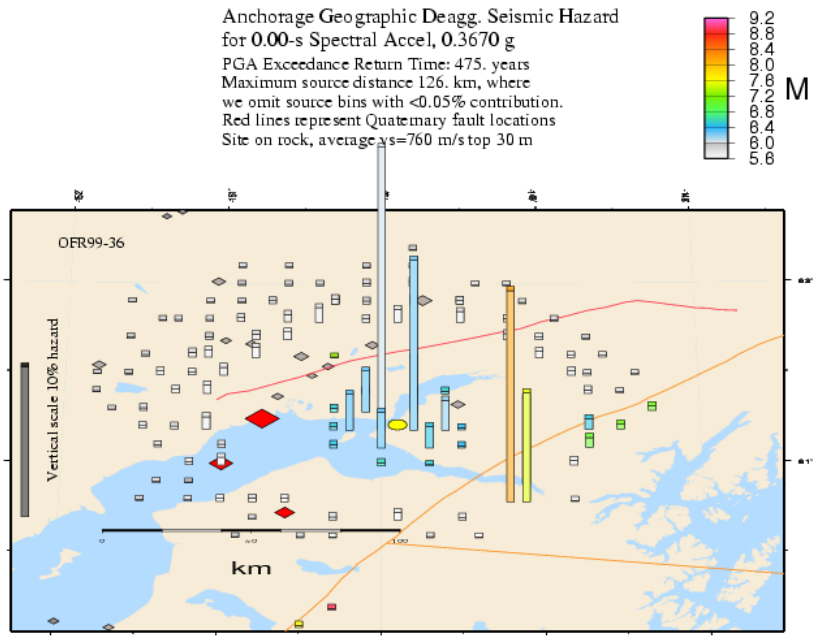

(a)

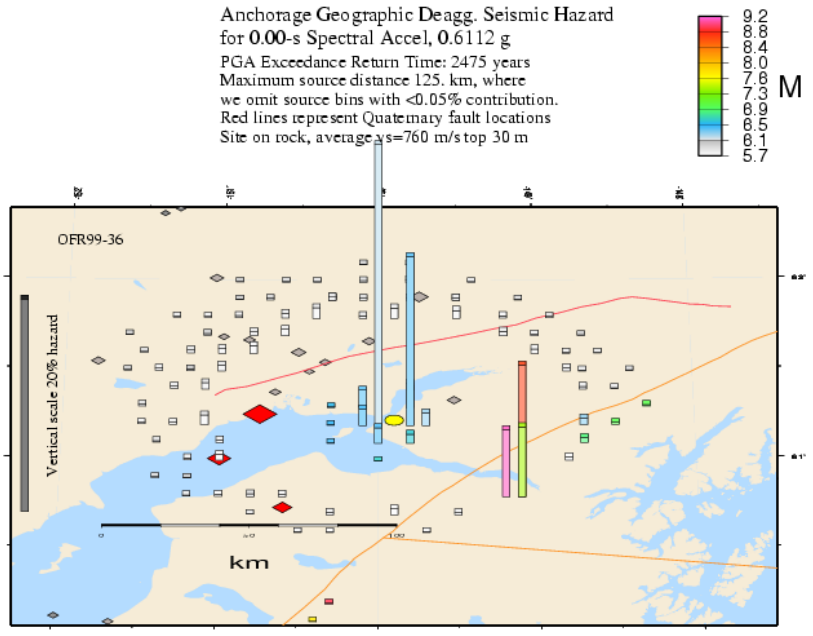

(b)

Figure 6.15 Geographic seismic hazard deaggregation in Alaska at (a) 10% in 50 years and (b) 2% in 50 years

Figure 6.16 shows the same deaggregation information in terms of percent contribution to the hazard for discrete magnitude and distance bins. The percent contribution represents $P[M_k, R_l | PGA > PGA_i]$, as used in Equations 3.5 through 3.8. Similar to Figure 6.15, this deaggregation shows that significant contributions from the hazard come from smaller/closer events and larger/farther events. The binning process sums the contributions of sources within each bin, and assigns the average M and R to that bin. For example, all sources with M = 6 ~ 6.5 and R = 10 ~ 20 km are combined and their contributions are summed together for this bin. This bin is then assigned a mean magnitude (M_k = 6.25) and a mean distance (R_l = 15 km). The mean magnitude and distance are 6.74 and 36.7 km for 2% probability of exceedance in 50 years, and 6.66 and 41.7 km for 10% probability of exceedance in 50 years. However, these mean M, R combinations contribute almost nothing to the hazard. The identification of mean M, R scenarios that contribute little hazard occurs when the deaggregation is bi-modal, which is the case in Figure 6.16. Because the probabilistic approaches developed in this work incorporate the entire deaggregation, this issue will not be a problem for our results.

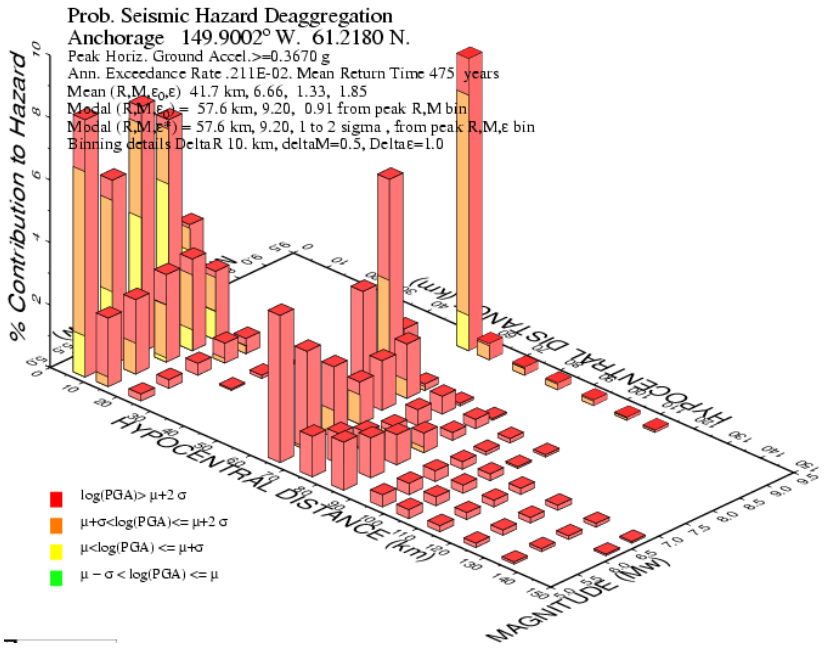

(a)

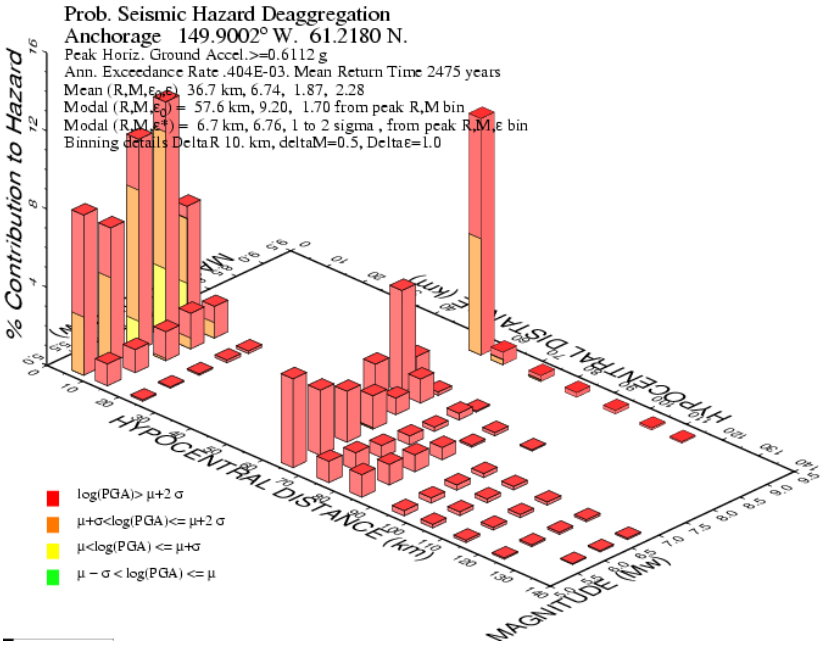

(b)

Figure 6.16 Seismic hazard deaggregation bins in Anchorage at (a) 10% in 50 years and (b) 2% in 50 years

The USGS published seismic hazard deaggregation data in 1996 for the continental 48 states. In the following decade, two updated versions were published in 2002 and 2008. The 2008 version provides deaggregation data for dozens of seismic hazard levels, but the previous versions only provided deaggregation data for 6 seismic hazard levels. For the State of Alaska, seismic hazard deaggregation data was only published in 1998 and it represents an extension of the 1996 analysis for the continental 48 states. The seismic hazard deaggregation for Alaska was never updated in 2002 or 2008. Therefore, as shown in Figure 6.14, the 1998 Alaska deaggregation only covers a range of hazard levels from 1% probability of exceedance in 50 years (λ = 0.0002 1/yr and PGA = 0.73 g) to 50% probability of exceedance in 75 years (λ = 0.009 1/yr and PGA = 0.21 g). This range does not represent the entire seismic hazard curve.

The deaggregation information is used to compute $P[M_k, R_l|PGA_i]$ for use in the calculation of the sliding displacement. To deal with the limited amount of deaggregation information, the $P[M_k, R_l|PGA_i]$ for hazard values outside the range available is assumed to be the same as for the closest hazard level. For example, the $P[M_k, R_l|PGA_i]$ for $\lambda < 0.0002$ 1/yr is assigned the values from $\lambda = 0.0002$ 1/yr and the $P[M_k, R_l|PGA_i]$ for $\lambda > 0.009$ 1/yr is assigned the values from $\lambda = 0.009$ 1/yr. Such assumption ignores the tendency that shallow crustal events close to Anchorage have more contributions at smaller λ, while subduction zone events contribute more to the seismic hazard at larger λ. Nonetheless, the associated errors should be small.

6.3.5 Vector Ground Motion Hazard

As discussed in Section 3.2.2, the vector approach requires the computation of $P[PGV_j|PGA_i]$. This calculation requires ground motion prediction equations (GMPEs) for PGA and PGV for use in Equations 3.12 and 3.13. When selecting appropriate GMPEs, the most important issue to consider is the tectonic environment (e.g., active crustal earthquakes vs. subduction earthquakes). The Anchorage study area is complicated by the fact that active crustal events occur close to Anchorage, yet there is also a large subduction zone located as close as 60 to 70 km southeast of the city (Figure 6.15). Therefore, GMPEs for both active crustal and subduction events must be used and these two types of earthquakes must be distinguished from each other in the seismic hazard deaggregation data. The distinction of these events and the GMPEs used to model them are described below.

The shallow crustal events around Anchorage typically have magnitudes smaller than 7.0 (Wesson et al. 1999 and 2007) and are mostly within 50 km of the city. Thus, all events closer than 50 km are considered shallow crustal events and all events at distances larger than 50 km are considered subduction events. Subduction events are generally distinguished between intraslab and interface events using the focal depth (Youngs et al. 1997, Kanno et al. 2006). Youngs et al. (1997) summarized that: (1) interface earthquakes are typically shallow (focal depth < 50 km) and occur at the interface between the subducting oceanic plate and overriding continental plate (Figure 6.17), and (2) intraslab earthquakes are relatively deeper (focal depth > 50 km) and occur within the subducting oceanic plate. Similarly, Wesson et al. (1999 and 2007) classified subduction zone events with focal depth greater than 50 km as intraslab events, which typically have magnitude smaller than 7.0. They also classified earthquakes with M >

7.0 as interface events. There is no focal depth information provided with the deaggregation data, therefore magnitude is used distinguish between intraslab and interface events. Events with magnitudes less than 7.0 and distance greater than 50 km are considered intraslab events and events with magnitudes greater than 7.0 and distance greater than 50 km are considered interface events.

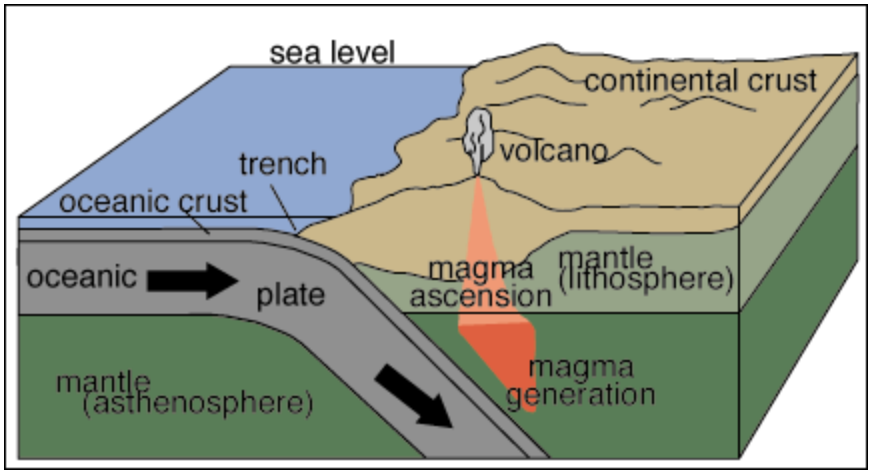

Figure 6.17 Illustration of subduction zone (http://www.platetectonics.com/)

The GMPEs for PGA were selected based on the GMPEs used in the hazard calculations. The USGS open-file report by Wesson et al. (1999) listed the GMPEs used in the 1998 hazard and deaggregation analysis and we selected one shallow crustal GMPE (Boore et al. 1997) and one subduction GMPE (Youngs et al. 1997) from that list for use in this study (Table 6.8). The GMPEs for PGV was selected based on the currently availability relationships. The Boore and Atkinson (2008) GMPE for PGV was selected for shallow crustal events because it is the most simply of the Next Generation Attenuation (NGA) relationships. The availability of a PGV GMPEs for subduction zone events is very limited, because PGV was not considered an important

ground motion parameter until relatively recently. The most recent GMPE for PGV for subduction zone events was developed by Kanno et al. (2006) using ground motion data in Japan and this relationship is used in this study (Table 6.8).

Table 6.8 GMPEs for PGA and PGV in Anchorage

Seismic event categories	PGA GMPEs	PGV GMPEs	Distance metrics
R<50 km Shallow Crustal Events	BJF97	BA08	R_{JB}
R>50 km, M<7 Subduction Intraslab Events	Youngs97	Kanno06	R_{rup}
R>50 km, M>7 Subduction Interface Events	Youngs97	Kanno06	R_{rup}

The correlation coefficient between PGA and PGV also is required to calculate the conditional probability $P[PGV_j|PGA_i, M_k, R_l]$. The correlation coefficient has been estimated as 0.6 (Rathje and Saygili 2008, Baker 2007). Thus, the joint probability $P[PGA_i, PGV_j]$ can be calculated for the vector approach, as shown in Figure 6.18. Generally, pairs of larger PGA and PGV have smaller annual probabilities of occurrence, while pairs of smaller PGA and PGV have larger probabilities. In addition, the probability of a small PGA occurring with a large PGV is very small, and vice versa.

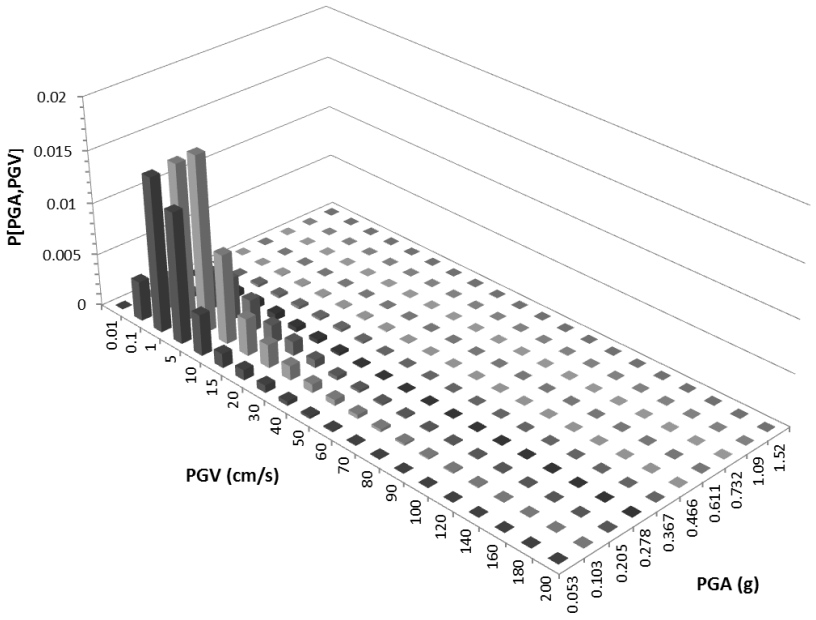

Figure 6.18 Joint annual probabilities of occurrence for (PGA, PGV) pairs

6.4 LOGIC TREE

To incorporate the epistemic uncertainties into the seismic landslide hazard mapping, a logic-tree analysis is applied to the various sources of uncertainties. The logic tree is separated into three parts, representing epistemic uncertainties in shear strength, slope properties, and displacement prediction models. The logic tree is shown in Figure 6.19 and its components are explained below.

Part 1 of the logic tree shows possible combinations of shear strengths and associated weights. Best estimate properties (c_{best} and φ_{best}) as well as high (c^+ and φ^+) and low (c^- and φ^-) values were assigned to each geologic unit based on the discussion in Section 6.3.1. The best estimates of shear strength for all geologic units are shown in Table 6.2. The undrained shear strength has a coefficient of variation (COV) equal to

30%, and the effective friction angle has a COV equal to 10%. The COV for effective cohesion is assumed to be 20% so that the total uncertainty in drained shear strength is similar to undrained shear strength. Therefore, for those geologic units with $\phi = 0$, the cohesion assigned as an undrained shear strength varies +/-39% (i.e., +/-1.3·COV) above/below (c^+/c^-) the best estimate value. For those units with drained shear strengths, the effective friction angle is varied +/-13% based on its COV, and the effective cohesion has is varied +/-26% based on its COV. The weights are assigned first to friction angle as: (1) 0.4 to the best estimate and (2) 0.3 to the values above/below the best estimates as shown in Table 6.3. When assigning weights to the associated cohesion values, it is considered that the combinations of (c^+, φ^+) or (c^-, φ^-) are less likely than (c^+, φ^-) or (c^-, φ^+). Therefore, the weights for cohesion values associated with (c^+, φ^+) or (c^-, φ^-) are taken as 0.25 and the weights for cohesion values associated with (c^+, φ^-) or (c^-, φ^+) are taken as 0.35. The weight for the cohesion values associated with (c_{best}, φ_{best}) is equal to 0.4.

The epistemic uncertainties for the *t* and *m* values are presented in Part 2 of the logic tree. The best estimate *t* value is 6 m for all geologic units except the collvium units of c-br and c-bl. Additional values of 3 m and 9 m are selected to represent the potential range of landslide depths across Anchorage, and the associated weights are 0.3, 0.4 and 0.3 as noted in Section 6.3.2. Because the colluvium units (c-br and c-bl units) exist on the surface of slopes as a thin layer, their depths were assumed as 3 m, and no variability was considered in the logic-tree analysis. Two groundwater depths (i.e. 3 m and 6 m) are selected to calculate *m* values for each of the *t* values. For example, if the *t* value is 6 m, the two corresponding *m* values are 0 and 0.5 for the different groundwater depths. The two *m* values for each *t* value are equally weighted.

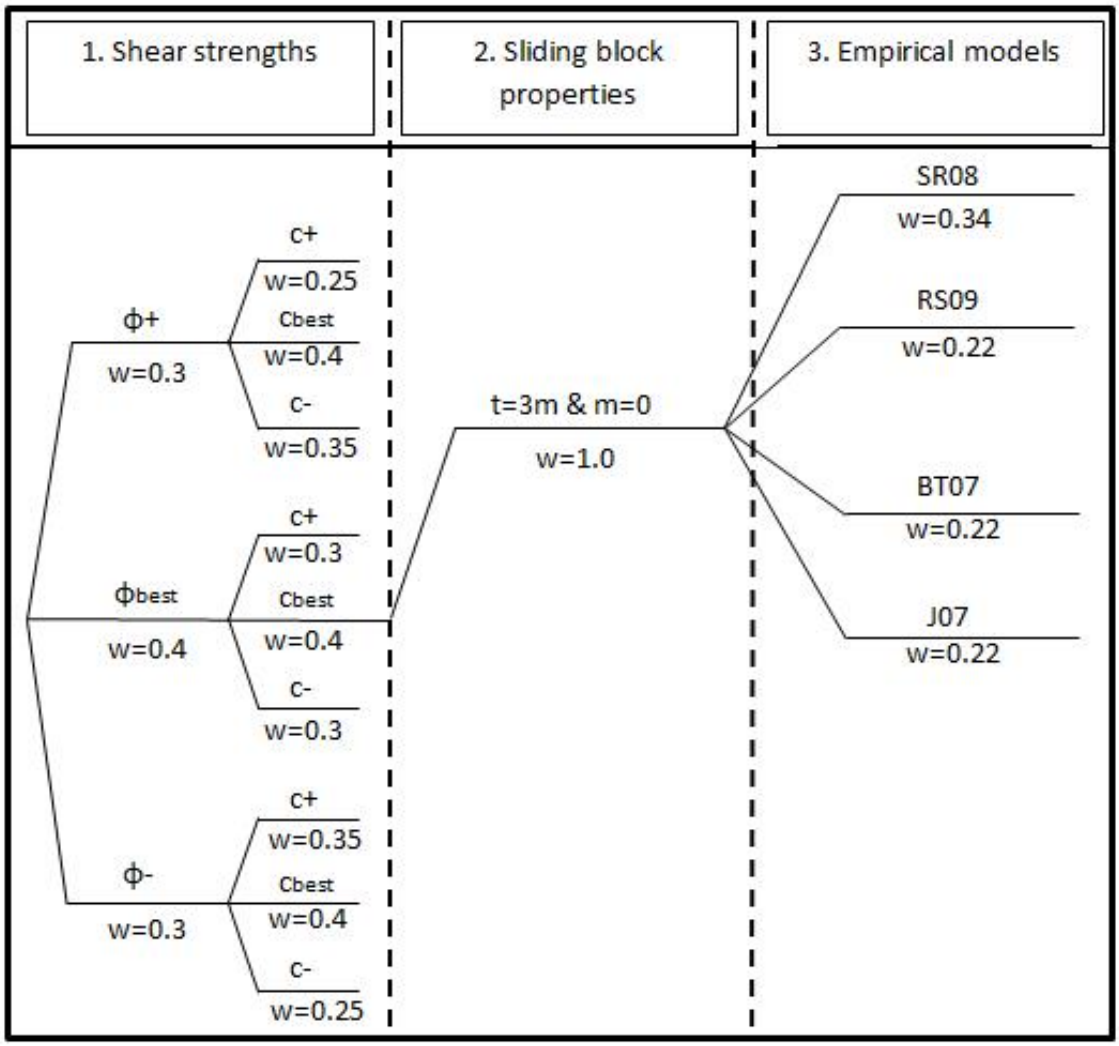
1. Shear strengths
2. Sliding block properties
3. Empirical models
ϕ+
w=0.3
c+
w=0.25
Cbest
w=0.4
c-
w=0.35
ϕbest
w=0.4
c+
w=0.3
Cbest
w=0.4
c-
w=0.3
ϕ-
w=0.3
c+
w=0.35
Cbest
w=0.4
c-
w=0.25
t=3m & m=0
w=1.0
SR08
w=0.34
RS09
w=0.22
BT07
w=0.22
J07
w=0.22

(a)

Figure 6.19

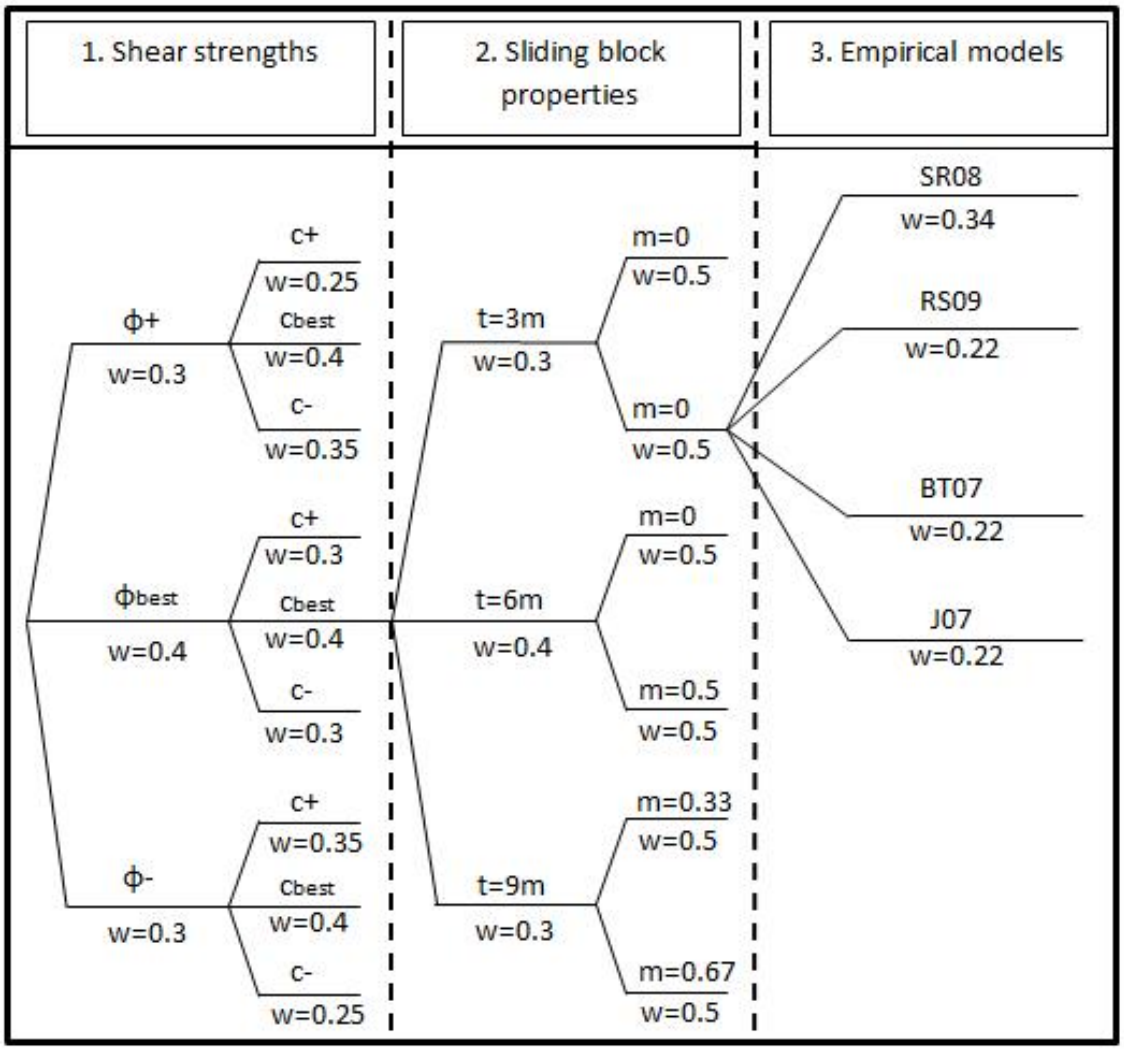

(b)

Figure 6.19 Logic tree with weights of (a) colluvium units (c-bl and c-br) and (b) all other geologic units for Anchorage

The first two parts of the logic tree are related to the calculation of the yield acceleration using the infinite slope model. The different branches result in 56 different values of k_y and corresponding weights associated with each grid cell. These 56 values of k_y will be used to define the mean displacement hazard curve using the procedure outlined in Section 5.3.

Finally, the epistemic uncertainty associated with the different empirical displacement models is incorporated in Part 3 of the logic tree. Three scalar models that use PGA and earthquake magnitude are selected for use (Rathje and Saygili 2009, Jibson 2007, Bray and Travasarou 2007) as well as one vector model that uses PGA and PGV (Saygili and Rathje 2008). These models are labeled RS09, J07, BT07, and SR08. Figure 6.20 shows the predicted sliding displacements as a function of k_y/PGA for the four empirical models for M = 6.74, PGA = 0.61 g, and PGV = 34 cm/s. The PGA and M values come directly from the hazard information for Anchorage, while the PGV represents the conditional value given PGA = 0.61 g and correlation coefficient $\rho_{PGA,PGV} = 0.6$. The four empirical models in Figure 6.20 predict displacements the range by a factor of about 4 for this scenario. For other scenarios there may be more or less difference between these models. Such difference is the epistemic uncertainty to be captured. To assign the weights, the scalar models are equally weighted at 0.22 and the vector model is weighted at 0.34. The vector model is more heavily weighted because the use of a second ground motion parameter provides a better estimate of sliding displacement.

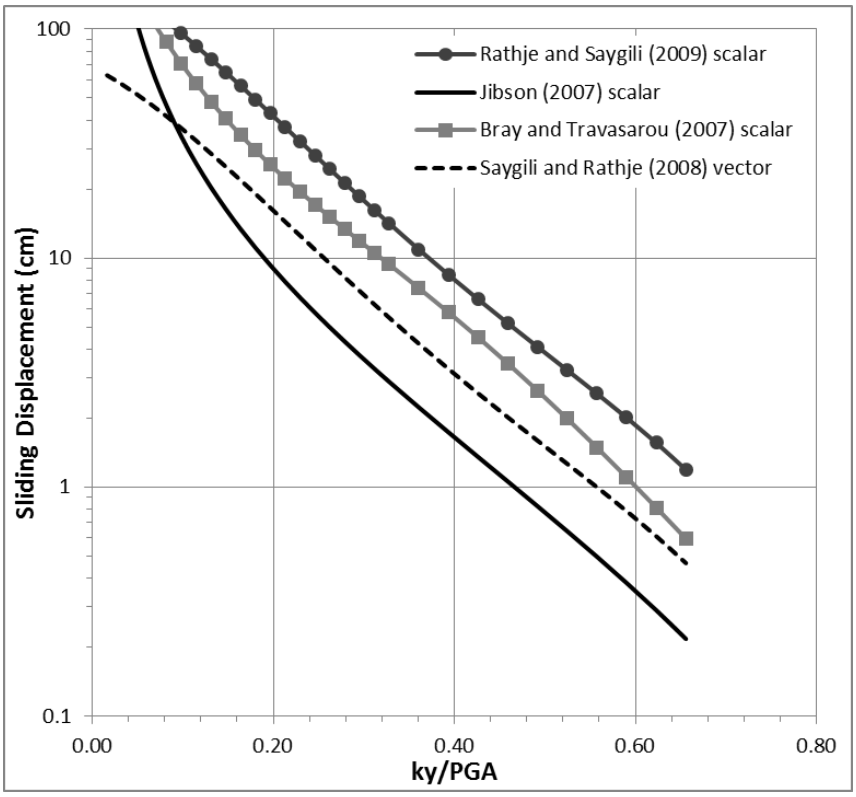

Figure 6.20 Comparison of Predictive Models for a scenario of M = 6.74, PGA = 0.61 g and PGV = 34 cm/s

Combining the 54 k_y values and four displacement models within the logic tree, 216 displacement hazard curves can be computed for each grid cell across the study region. A weighted mean displacement hazard curve is calculated from the 216 curves and their weights through Equation 5.1. To illustrate this calculation, Figure 6.21 shows displacement hazard curves computed for the 9 branches associated with the shear strength part of the logic tree (i.e., all other parameters held constant at the values indicated in Figure 6.21), as well as the mean displacement hazard curve. The mean displacement hazard curve is above the hazard curve associated with the best estimate k_y, indicating that the seismic slope performance may be underestimated when one does not

incorporate the uncertainties in the soil properties. The mean displacement hazard curve indicates D = 2.1 cm at 10% probability of exceedance in 50 years (λ = 0.0021 1/yr) and D = 25 cm at 2% probability of exceedance in 50 years (λ = 0.0004 1/yr). Thus, at these hazard levels this cell would be considered moderate hazard (1 cm < D < 5 cm) and very high hazard (D > 15 cm) respectively.

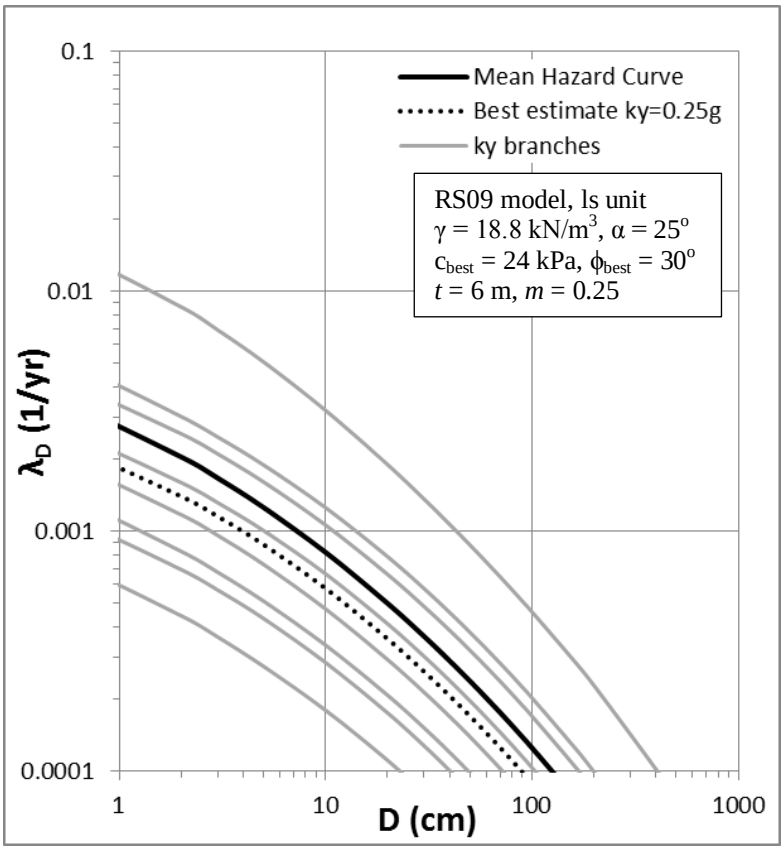

Figure 6.21 Displacement hazard curves associated with the shear strength part of the logic tree.

6.5 REGRESSION MODELS

As mentioned in Section 5.3, the Mean λ_D Threshold approach to applying the logic tree analysis on a regional scale requires an interpolation relationship between k_y and $\lambda_D(x)$, which can be expressed as a 4th order polynomial regression model in the form of:

$$\ln(\lambda_D(x)) = a_1(\ln(k_y))^4 + a_2(\ln(k_y))^3 + a_3(\ln(k_y))^2 + a_4\ln(k_y) + a_5 \qquad (6.1)$$

The regression relationship is specific to a specified ground motion hazard, a specified level of displacement x, and a specified empirical displacement model. The coefficients used in Equation 6.1 are provided in Table 6.9 for the Anchorage ground motion hazard, three displacement thresholds, and the four empirical displacement models considered. The three displacement thresholds (1cm, 5 cm and 15 cm) represent moderate, high and very high seismic landslide hazard categories (Table 2.1).

Table 6.9 Coefficients of regression models

Displacement Threshold	Empirical Displacement Models		a_1	a_2	a_3	a_4	a_5
1 cm	Scalar	RS09	0.0067	0.0673	-0.2122	-3.5961	-10.7348
		J07	0.0089	0.1051	-0.0672	-3.7699	-11.8035
		BT07	0.0116	0.1377	0.0984	-3.2727	-11.0939
	Vector	SR08	-0.0024	-0.0088	-0.3859	-3.7557	-11.4605
5 cm	Scalar	RS09	0.0044	0.0529	-0.1717	-3.4082	-11.3582
		J07	-0.0013	0.0061	-0.3379	-4.1157	-13.0937
		BT07	-0.0036	-0.0161	-0.3892	-3.9692	-12.2431
	Vector	SR08	-0.0139	-0.1396	-0.8389	-4.3842	-12.7071
15 cm	Scalar	RS09	-0.0029	-0.0212	-0.3917	-3.6514	-12.1558
		J07	-0.0224	-0.2211	-1.1387	-5.3158	-14.6797
		BT07	-0.0512	-0.5404	-2.35	-7.037	-15.0673
	Vector	SR08	-0.0397	-0.4348	-2.0095	-6.3164	-14.6476

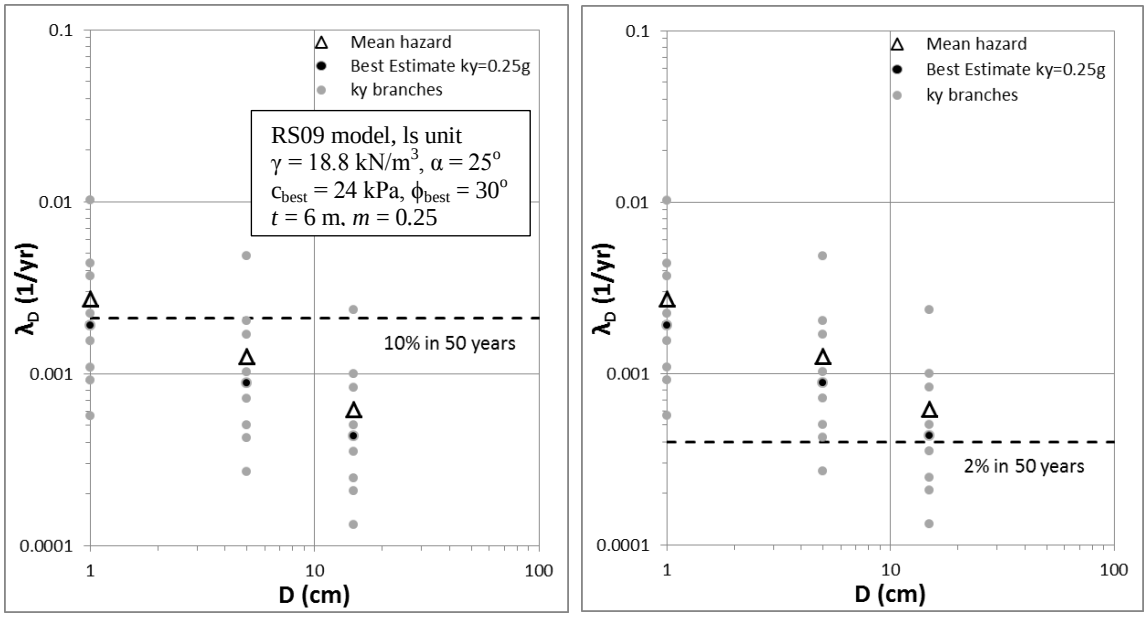

(a) (b)

Figure 6.22 Comparison between displacement hazards from regression models at (a) 10% and (b) 2% probabilities of exceedance in 50 years

With these regression models and Equation 5.1, the mean annual rate of exceedance for a specific displacement threshold ($\overline{\lambda_D}(x)$, where x is the displacement threshold) at each grid cell can be computed from the 216 branches in the logic tree and the associated weights. After comparing the computed $\overline{\lambda_D}(x)$ with the hazard level under consideration (λ^*), the seismic landslide hazard category of each grid cell can be determined. Figure 6.22 demonstrates this approach to assigning seismic landslide hazard categories at 10% and 2% probabilities of exceedance in 50 years (λ^* = 0.0021 1/yr and 0.0004 1/yr). For this example, a slope angle of 25° is assumed along with the properties of the ls unit. Only the shear strength part of the logic tree is considered, which is the same as shown in Figure 6.21. The gray dots in Figure 6.22 represent the

$\lambda_D(x)$ values for the 9 k_y values for each of the three displacement thresholds (x = 1, 5, and 15 cm), and the triangles represents $\overline{\lambda_D}(x)$ computed from the $\lambda_D(x)$ values for each displacement threshold. At 10% probability of exceedance in 50 years, the associated λ^*=0.0021 1/yr falls between $\overline{\lambda_D}(1\text{cm})$ and $\overline{\lambda_D}(5\text{cm})$, which indicates that the displacement at this hazard level is between 1 cm and 5 cm and this cell should be assigned to the moderate seismic landslide hazard category. At 2% probability of exceedance in 50 years, $\overline{\lambda_D}(15\text{cm})$ is greater than the associated λ^*=0.0004 1/yr, resulting in very high hazard category assigned to this cell. These are the same results that were obtained when computing the full hazard curves (Figure 6.21).

6.6 SCREENING ANALYSIS

To further reduce the computation time, a screening analysis is performed first using the worse-case scenario of the logic tree. The lowest shear strengths (c^- and φ^-) and the largest *m* and *t* values (0.67 and 9 m for drained units, 0 and 3 m for undrained units) are used to compute the minimum factor of safety for each grid cell. The RS09 scalar model is selected for the screening analysis because it generally predicts the largest sliding displacement relative to the other three models, as seen in Figure 6.20. All grid cells in which λ_D(5cm) is greater than λ^* = 0.0004 1/yr (i.e., 2% probability of exceedance in 50 years) are colored red in Figure 6.23. All non-red grid cells are excluded from the full logic-tree analysis for a hazard level greater than 2% in 50 years, because these grid cells do not have landslide potential for the 5-cm threshold even under the worst-case condition. Similar screening analysis is carried out for the 1-cm and 15-cm thresholds.

For the 5-cm threshold, only 9.0% of grid cells in the study area are colored red, which means that about 91% of the study area is removed from the full logic-tree analysis. For the 1-cm and 15-cm thresholds, about 73% and 95% of study area is removed from analysis by applying the screening analysis first. Therefore, the full logic-tree analysis for a specified displacement threshold performed using Python codes in ArcGIS® can be completed within an hour for the Anchorage study area.

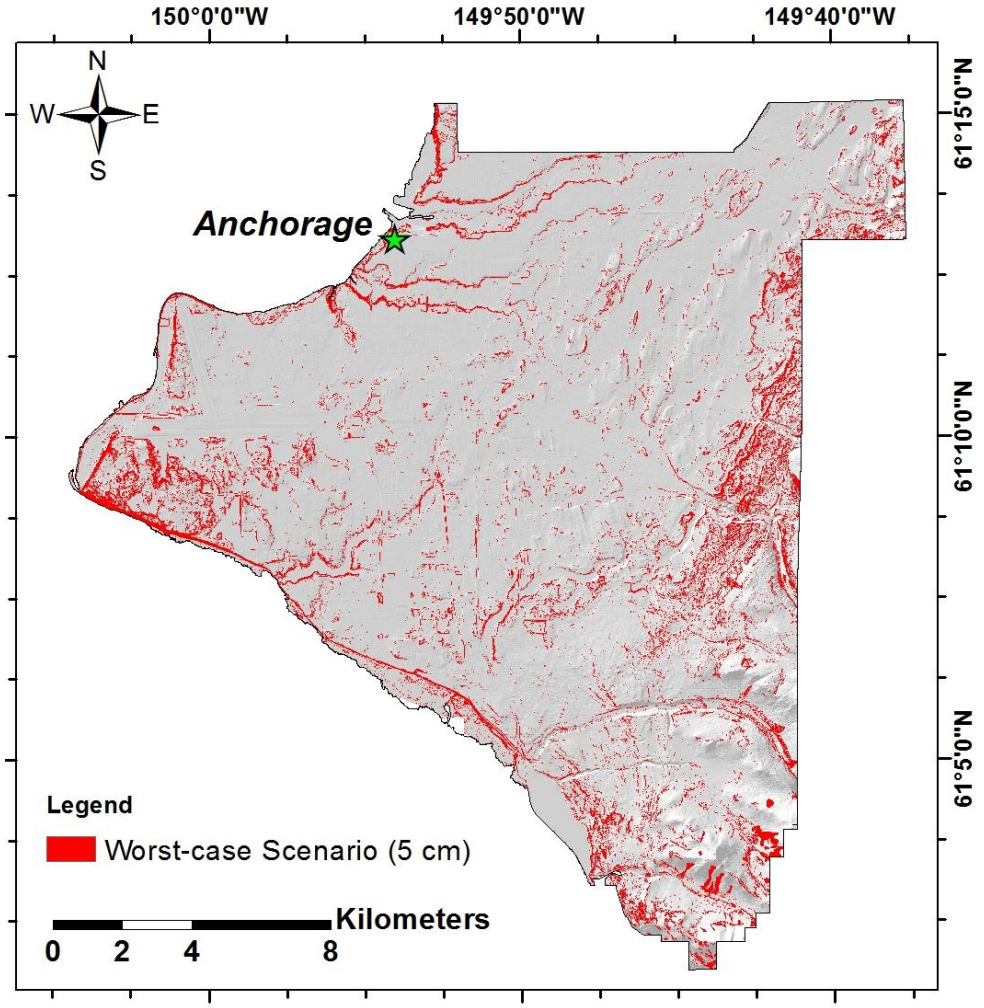

Figure 6.23 Cells with $\lambda_D(5cm) > 0.0004$ 1/yr for worst-case condition (5-cm threshold, 2% in 50 years)

6.7 RESULTS

Using the procedures described above, a probabilistic seismic landslide hazard map was created by running Python codes in ArcGIS®. Figure 6.24 plots such a hazard map of Anchorage for a 2% probability of exceedance in 50 years ($\lambda^* = 0.0004$ 1/yr) and the three seismic landslide categories (moderate, high, and very high). The area with moderate hazard (1 cm < D < 5 cm, colored orange) and high hazard (5 cm < D < 15 cm, colored red) are about 0.85% and 0.33% of the entire study area respectively, and the area with very high hazard (D > 15 cm, colored blue) covers 0.96% of the entire study area. These results cannot be compared directly with the current deterministic map developed by Jibson and Michael (2009), because the deterministic map assumed a worst-case scenario (t = 15 m and m = 0.8).

As seen on the map, most areas with high or very high hazard are along coastal bluffs, stream valleys or in mountainous areas. More detailed landslide predictions are shown on Figure 6.24b for downtown Anchorage, located between Ship Creek to the north and Chester Creek on the south. Colluvium and landslide deposits on slopes along coastal bluffs and stream valleys are most susceptible to seismic landslides around the downtown area. Figure 6.25 plots the seismic landslide hazard for a 10% probability of exceedance in 50 years ($\lambda^* = 0.0021$ 1/yr). The area with moderate, high and very high hazard are about 0.18%, 0.14% and 0.60% of the entire study area, respectively. The seismic landslide hazard at this smaller hazard level is significantly reduced across the study area, except for the c-bl unit along coastal bluffs and stream valleys.

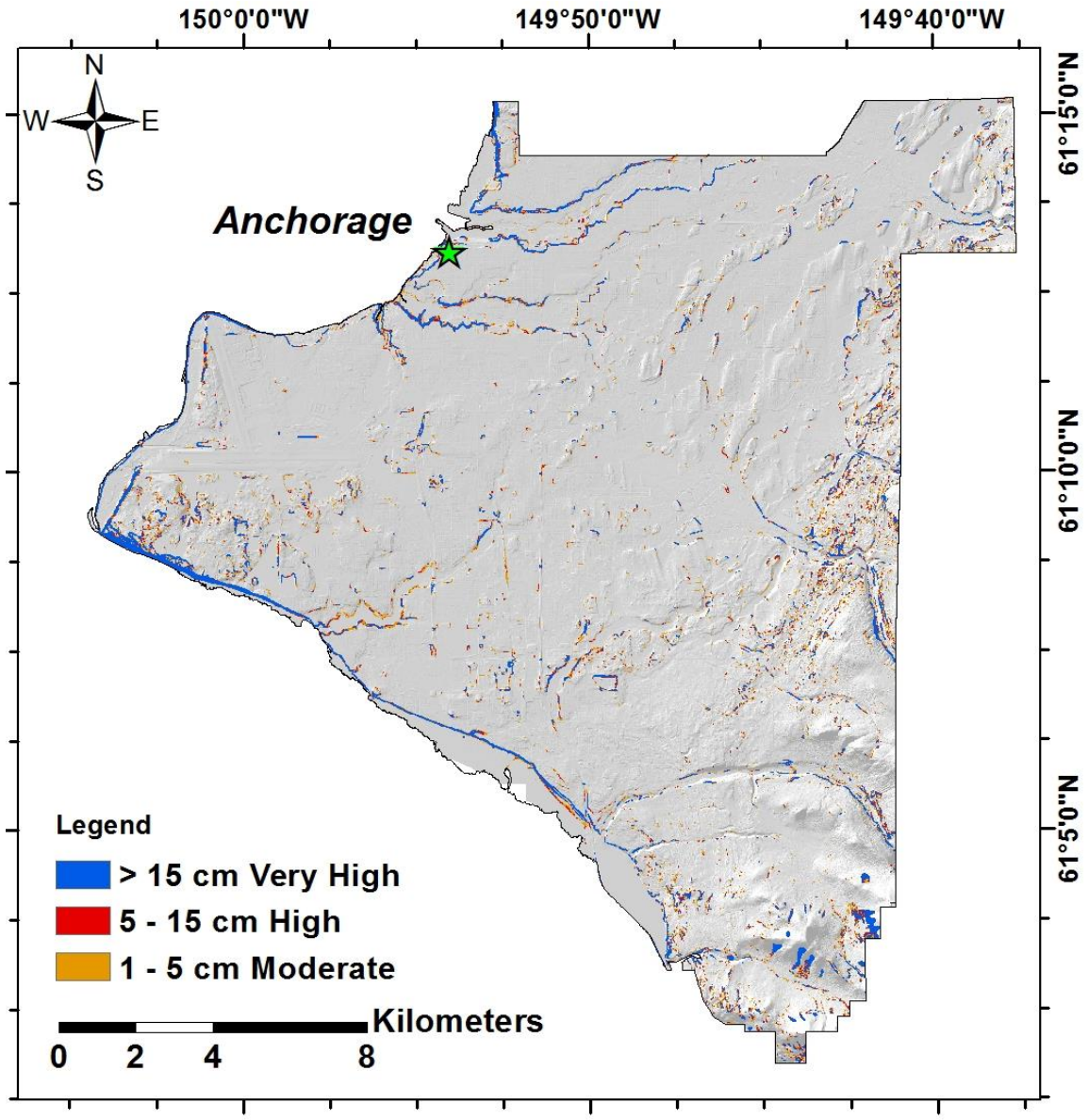
150°0'0"W
149°50'0"W
149°40'0"W
61°15'0"N
61°10'0"N
61°5'0"N
N
W
E
S
Anchorage
Legend
> 15 cm Very High
5 - 15 cm High
1 - 5 cm Moderate
Kilometers
0
2
4
8

(a)

Figure 6.24

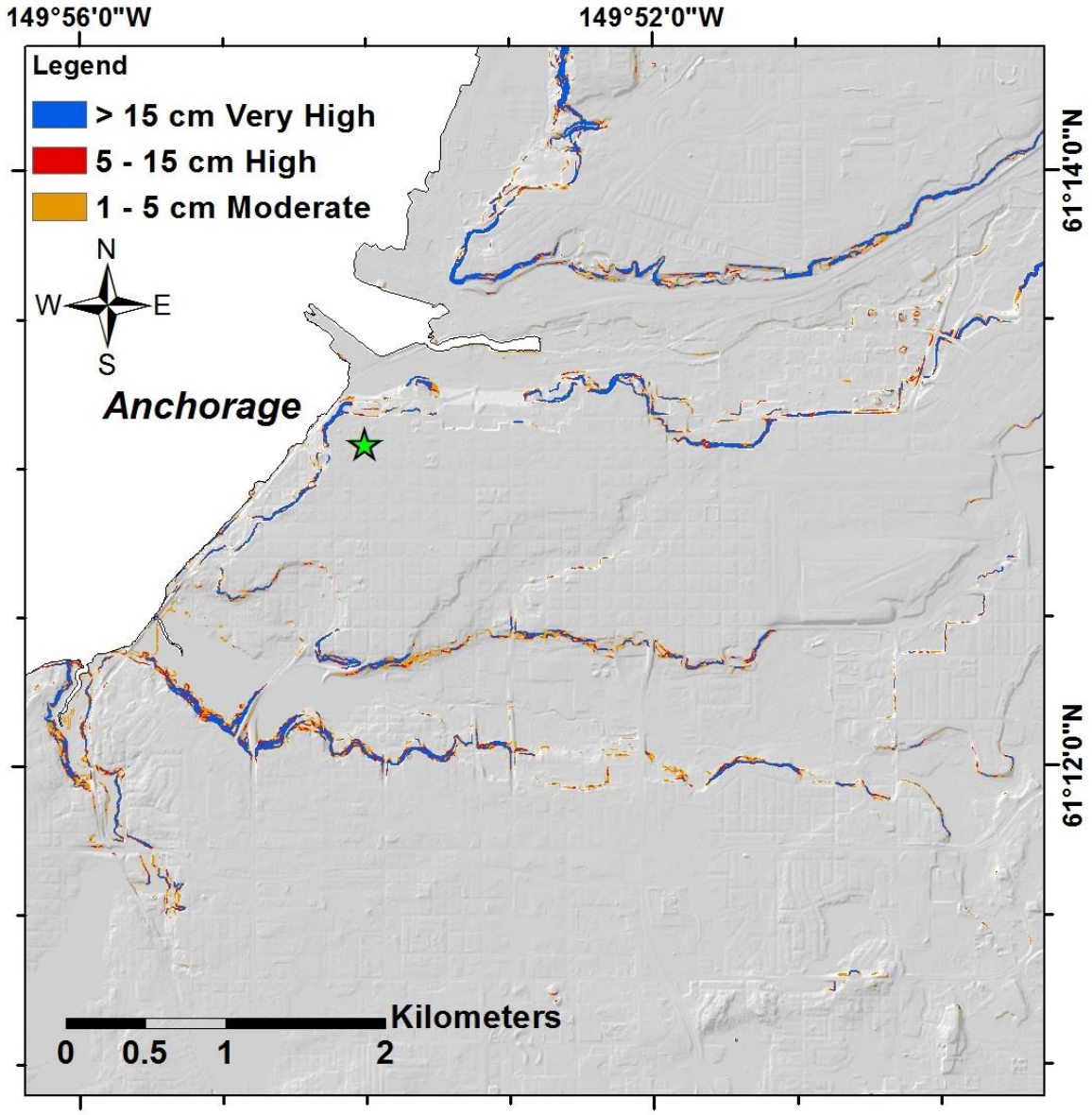

(b)

Figure 6.24 Probabilistic seismic landslide hazard map of Anchorage at 2% probability of exceedance in 50 years (a) entire study area and (b) downtown area

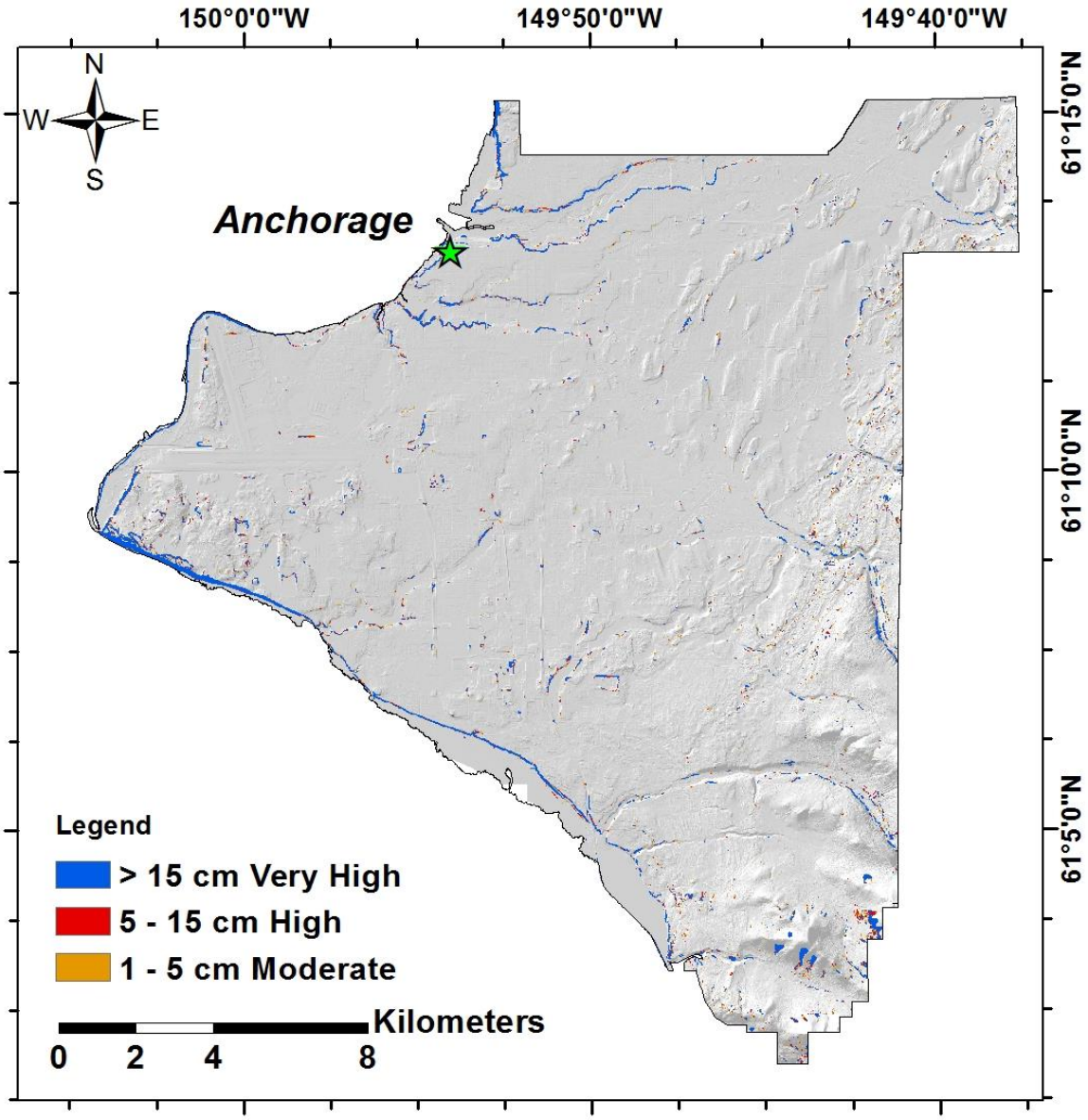
150°0'0"W
149°50'0"W
149°40'0"W
61°15'0"N
61°10'0"N
61°5'0"N
N
W
E
S
Anchorage
Legend
> 15 cm Very High
5 - 15 cm High
1 - 5 cm Moderate
Kilometers
0
2
4
8

(a)

Figure 6.25

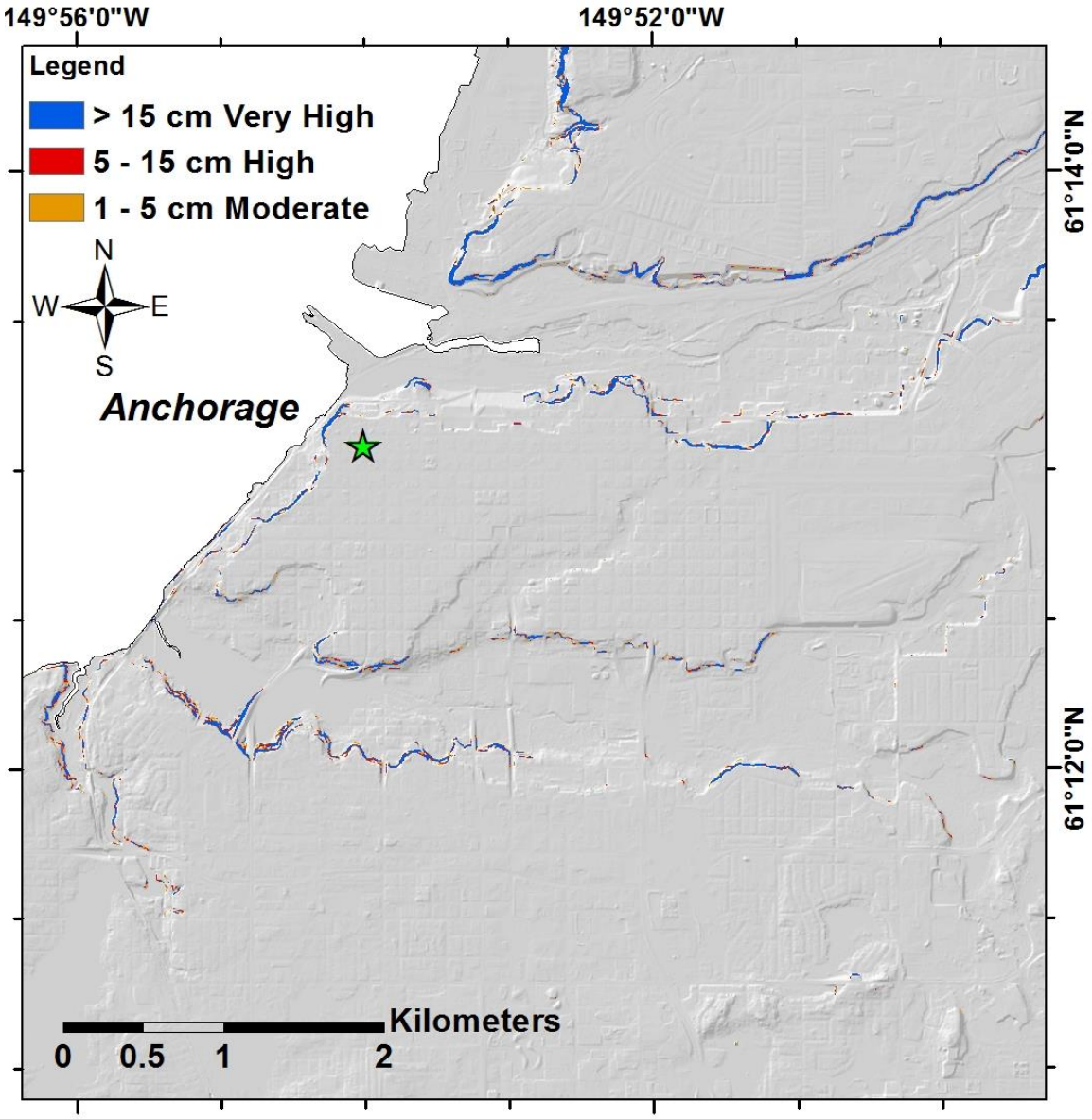

(b)

Figure 6.25 Probabilistic seismic landslide hazard map of Anchorage at 10% probability of exceedance in 50 years (a) entire study area and (b) downtown area

To investigate the influence of each part of the logic tree on the seismic landslide hazard, a series of displacement maps were created by implementing different parts of the logic tree (i.e., epistemic uncertainty). Also analyzed is the deterministic approach in which the 2% in 50 year PGA was used to compute sliding displacements. This deterministic approach is essentially the approach used by Jibson and Michael (2009), although with different assumed slope properties.

The percentage of the study area exceeding different displacement thresholds when incorporating different parts of the logic tree is summarized in Table 6.10 and Figure 6.26. Ten different cases are shown. Cases 1 to 5 only use one empirical displacement model (RS09 scalar model), while all four models are applied to Cases 6 to 10. The deterministic cases (Cases 1 and 6) use the best estimates of all slope properties for the k_y computation. The probabilistic cases (Cases 2-5, 7-10) all incorporate aleatory variability but different components of epistemic uncertainty.

Table 6.10 Implementing different parts of the logic tree (2% in 50 years)

Case		Aleatory Variability	Epistemic Uncertainty	% of Study Area		
				D > 1 cm	D > 5 cm	D > 15 cm
RS09 scalar model	1	No	No	1.22%	0.54%	0.30%
	2	Yes	No	1.33%	0.72%	0.43%
	3	Yes	Shear Strength	1.90%	1.09%	0.73%
	4	Yes	Sliding Block	2.13%	1.16%	0.74%
	5	Yes	Shear Strength and Sliding Block	2.96%	1.69%	1.13%
All four models	6	No	No	0.82%	0.37%	0.21%
	7	Yes	No	0.91%	0.49%	0.32%
	8	Yes	Shear Strength	1.35%	0.81%	0.59%
	9	Yes	Sliding Block	1.52%	0.84%	0.55%
	10	Yes	Shear Strength and Sliding Block	2.14%	1.29%	0.96%

The results is Table 6.10 are summarized in Figure 6.26a for the RS09 model. The area of high/very high hazard (i.e., D > 5 cm) increases by 33% when aleatory variability is included (i.e., 0.72% for Case 2 vs. 0.54% for Case 1), and increases by more than a factor of 3 when all of the sources of epistemic uncertainty in k_y are included (i.e., 1.69% for Case 5 vs. 0.54% for Case 1). The influence of the epistemic uncertainty in the sliding block properties (Case 4) is generally greater than the influence of the epistemic uncertainty in the shear strengths (Case 3) because the uncertainties in *m* and *t* are larger than the uncertainties in c and ϕ (Figure 6.19). However, the difference between these two sources of uncertainty is smaller at larger displacement threshold. The reason is that the c-bl unit is not assigned uncertainties in *t* and *m* values (Figure 6.19) while it contributes significantly to the landslide hazard in the very high hazard category (Figure 6.24).

The combined influence of the epistemic uncertainties in the shear strength and sliding block properties (Case 5) is slightly greater than the simple summation of individual influences (Cases 3 and 4), indicating that the combined effect of uncertainties may amplify the increase in the seismic landslide hazard. The same trend is observed for 1 cm and 15 cm thresholds.

Comparing Figure 6.26a and Figure 6.26b, the analyses using all four empirical displacement models always predict less area within each seismic landslide hazard level than the corresponding analyses using the RS09 model. This difference is a result of the RS09 model generally predicting the largest sliding displacements among all four models (Figure 6.20).

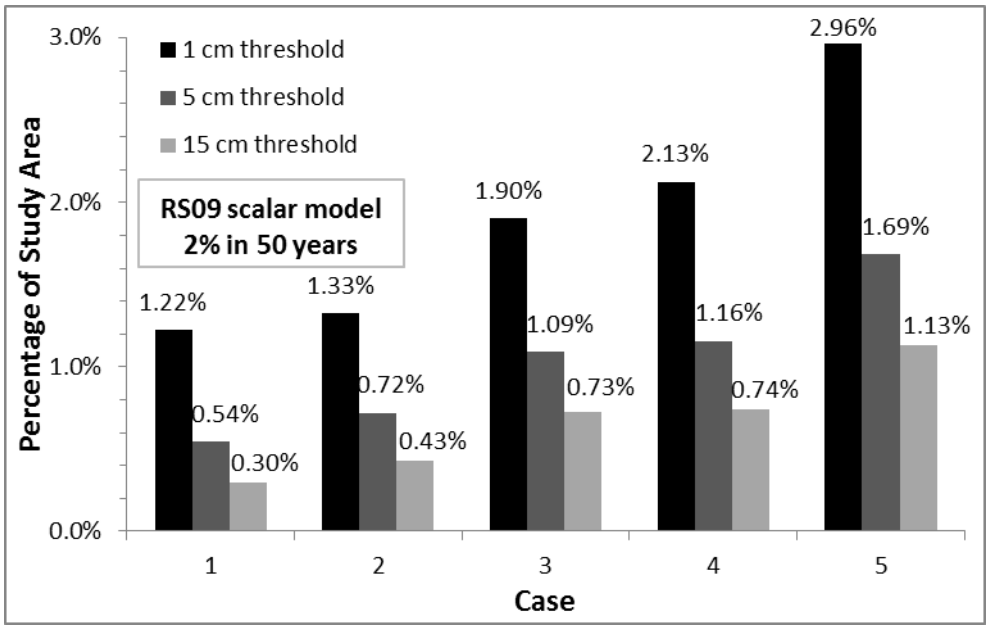

(a)

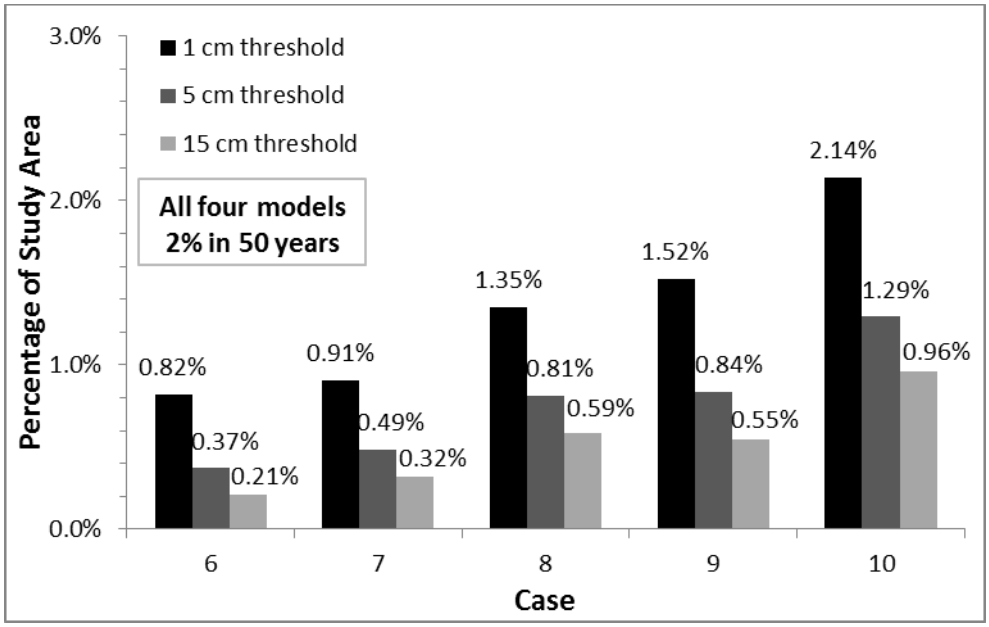

(b)

Figure 6.26 The influence of different parts of the logic tree on the computed seismic landslide hazard at 2% probability of exceedance in 50 years using (a) RS09 scalar model and (b) all four empirical displacement models

To further investigate the hazard distribution among geologic units, the number of grid cells with high/very high hazard (D > 5 cm) in each geologic unit is summarized and shown in Table 6.11. Landslide Cells are grid cells with predicted displacements greater than the 5-cm threshold, the % of Study Area represents the percentage of the study area covered by each geologic unit, the % of Geo Unit is the percentage of grid cells with D > 5 cm for each geologic unit, and the % of Landslide Cells is the contribution of each geologic unit to all landslide cells in the study area. Also shown in Table 6.11 are the corresponding values from the Jibson and Michael (2009) map.

With 35% of its area predicted as high/very high hazard, the colluvium unit c-bl is most susceptible to landslides, because this unit has low undrained shear strength and mostly covers steep coastal bluffs and valley walls (Figure 6.6). Landslide deposits (ls), mostly distributed on coastal bluffs, valley walls and the Chugach Mountains, also has a large portion of its area (about 15%) classified as high/very high hazard. Glacial alluvium (ga) and sand deposits (sh) in low hills, both having more than 2.5% of their area with D > 5 cm, also contribute to the landslide hazard. Although the alluvium units, af and al, contribute more than 20% of all landslide cells (each about 10%), they are relatively stable because only 1.1% and 0.6% of these units are classified as high/very high hazard. The only reason these units contribute so much to the overall landslide hazard is because they cover a large percentage of the study area. The other geologic units, which either have high shear strength underlain by stiff soil/rock (e.g. m, gm and mg) or exist mostly on flat terrain (e.g. an, f and l), do not represent a significant seismic landslide risk.

Table 6.11 Probabilistic landslide prediction in geologic units (5 cm threshold, 2% probability of exceedance in 50 years)

	This Study				Jibson and Michael (2009)	
Geo Units	Landslide Cells	% of Study Area	% of Geo Unit	% of Landslide Cells	% of Geo Unit	% of Landslide Cells
af	10486	11.4%	1.1%	**9.7%**	2.2%	6.1%
al	11327	22.0%	0.6%	**10.5%**	1.3%	7.0%
an	2536	9.8%	0.3%	2.3%	0.6%	1.4%
b	18	2.2%	0.0%	0.0%	0.4%	0.2%
bc	3071	2.8%	1.3%	2.8%	1.9%	1.2%
c-br	65	6.1%	<0.1%	0.1%	18.9%	27.4%
c-bl	36796	1.3%	**34.7%**	**34.0%**	93.0%	28.2%
f	362	3.0%	0.1%	0.3%	0.7%	0.5%
ga	11535	5.3%	**2.6%**	**10.7%**	7.7%	9.6%
gm	491	3.9%	0.2%	0.5%	0.9%	0.8%
l	471	1.8%	0.3%	0.4%	0.7%	0.3%
ls	13061	1.0%	**15.0%**	**12.1%**	22.4%	5.6%
m	3262	6.0%	0.7%	3.0%	3.0%	4.2%
mg	1666	9.5%	0.2%	1.5%	0.8%	1.8%
s	2966	2.0%	1.8%	2.7%	2.8%	1.4%
sh	7404	2.1%	**4.2%**	**6.8%**	5.8%	3.0%
sl	2626	10.0%	0.3%	2.4%	0.5%	1.3%
Total	108143	100.0%		100.0%		

Table 6.11 also summarizes the results from the Jibson and Michael (2009) deterministic map that uses the 2% in 50 year ground motions. The colluvium unit in the mountainous area (c-br) was predicted as one of the most landslide-susceptible unit in the Jibson and Michael (2009) deterministic map (Table 6.5), but it has almost no seismic landslide hazard according to the probabilistic analysis. The use of conservative sliding block properties in the deterministic map leads to an overprediction in the landslide

hazard for this unit. In fact, the conservative sliding block properties used by Jobson and Michael (2009) resulted in a much larger area of seismic landslide hazard than predicted in this study. This result demonstrates that is may be more useful to use a logic-tree approach to assign a range of possible model parameters rather than using conservative parameters.

6.8 SUMMARY

In this chapter, probabilistic seismic landslide hazard mapping is applied to Anchorage, Alaska. The shear strengths of the geologic units are assigned based on a previous study that created a deterministic seismic landslide map (Jibson and Michael 2009), and the associated uncertainties are determined from judgment and published values (e.g., Phoon and Kulhawy 1999). The thicknesses of the surficial soils, described or roughly estimated from geologic maps, are used to assist the selection of *t* values in the logic tree. Additionally, 2-D static slope stability analysis is performed for typical slopes that are susceptible to seismic landslides, indicating that potential failures will not extend into underlying strong soils and, thus the thickness of surficial layer is the main controlling factor of failure depths. *m* values are determined from the groundwater table, representing relatively unfavorable conditions for seismic landslides. The ground motion hazard comes from the hazard calculations performed by USGS and these data indicate that both shallow crustal events and subduction zone events affect ground shaking at the site. In developing the vector hazard information for PGA and PGV, GMPEs for both shallow crustal events and subduction zone are required.

The logic-tree analysis is applied to the study area through the Mean λ_D Threshold approach introduced in Chapter 5. The results show that incorporating epistemic uncertainties significantly increases the seismic landslide hazard. The combined influence of different sources of epistemic uncertainties is greater than the simple summation of individual influences. The geologic units distributed on coastal bluffs, valley walls, low hills and Chugach Mountains are most susceptible to seismic landslides.

Chapter 7 Summary, Conclusions and Recommendations for Future Work

7.1 SUMMARY AND CONCLUSIONS

Accurate evaluations of the potential for earthquake-induced landslides and slope failures are essential for reducing losses caused by earthquakes. This assessment involves a prediction of the sliding displacements induced by ground shaking. The predicted sliding displacements are used to indicate the likelihood of landslide occurrence and to assign seismic landslide hazard categories.

Current practice uses a deterministic approach to predict sliding displacement. The deterministic approach ignores the aleatory variability in the predictions of ground shaking or displacements, as well as the epistemic uncertainties in the slope properties. A probabilistic framework was developed that computes a displacement hazard curve using: (1) a ground motion hazard curve from a probabilistic seismic hazard analysis, (2) a model for predicting the dynamic response of the sliding mass, (3) a model for predicting the sliding response of the sliding mass, and (4) a logic tree analysis that incorporates the uncertainties in the various input parameters. Both scalar and vector approaches to the probabilistic analysis were developed. The probabilistic framework was applied to site-specific analysis of a real slope in California and to regional analysis for seismic landslide mapping around the Anchorage, Alaska area. For both of these applications, the ground motion hazard was derived from the seismic hazard data from

the USGS and the logic-tree was derived from available field/laboratory data and engineering judgment.

The development of the probabilistic framework for flexible sliding masses involved first the calculation of the annual rate of occurrence of the seismic loading parameters for the flexible slope and then the calculation of a hazard curve for sliding displacement. A logic-tree analysis was used to incorporate the epistemic uncertainties regarding the slope properties. This framework can be easily implemented in engineering practice using available empirical models for the dynamic response and sliding response of sliding masses. The influence of incorporating the various sources of epistemic uncertainty was investigated. The probabilistic approach to predicting sliding displacements for flexible sliding masses results in larger displacements than a deterministic approach because the probabilistic approach incorporates the variability in the seismic response prediction and the displacement prediction. The probabilistic approach can predict displacements 1.5 to 5 times larger than the deterministic approach, with the largest difference occurring for sliding masses with large site periods. Incorporating epistemic uncertainties further increases the predicted displacements. Although incorporating uncertainty consistently increases the displacement hazard, acknowledging and accounting for uncertainties provides for a better assessment of the potential for slope deformations during earthquakes.

To demonstrate the probabilistic approach for an actual site and realistic site characterization data, the Lexington Elementary School site in California was selected. The available site characterization data was used to develop the epistemic uncertainties in the shear strength and shear wave velocity profiles. These uncertainties resulted in uncertainties in the yield acceleration (k_y) and site period (T_s). An additional source of uncertainty was the mean period of the ground motion (T_m). The computed

displacement hazard curves were used to predict displacements at 10% and 2% probabilities of exceedance in 50 years, and these values were compared with deterministic estimates. The probabilistic displacements were as much as 4 to 6 times larger than the deterministic values at 10% in 50 years, and they were more than 10 times larger at 2% in 50 years. The uncertainty in T_m resulted in the largest effect on the displacements, while the uncertainty in T_s had the smallest effect. Again, these results indicate that accounting for uncertainty produces displacements that are larger than those predicted using deterministic methods and best-estimate properties. However, efforts to reduce the epistemic uncertainties can reduce the displacements, and thus there is an incentive for engineers and owners to collect data to reduce uncertainties, where possible.

The probabilistic framework developed in this research can also be applied to regional seismic landslide mapping. The level of epistemic uncertainty in a regional analysis is more significant than for a site-specific analysis, and thus it is even more critical to incorporate these uncertainties in regional analysis. An impediment to incorporating epistemic uncertainty in regional mapping is the computational effort required to apply logic-tree analysis at hundreds of thousands to millions of grid cells. In this research, an efficient scheme (i.e., the Mean λ_D Threshold approach) for the computation of the weighted mean displacement hazard was developed to reduce the computational efforts. To further reduce the computational effort, a screening analysis using the worst-case scenario of the logic tree was introduced into the mapping approach. The screening analysis removes as many as 73% to 95% of the grid cells from the full logic-tree analysis.

Anchorage, Alaska, which has a significant seismic landslide hazard, was selected as an example study area to implement the developed probabilistic approaches to seismic landslide hazard mapping. A previous study provided the best-estimate shear strengths

of the geologic units, and the associated epistemic uncertainties were determined from the literature. The reported thicknesses of the surficial geologic units and 2D slope stability analyses were used to select the failure surface thicknesses used in the logic tree. The saturation thickness values were estimated from reported locations of the groundwater table, representing generally unfavorable conditions for seismic landslides. The ground motion hazard data and deaggregation data from the USGS were used as input into the probabilistic analyses. A series of seismic landslide maps were created to investigate the influence of each part of the logic tree on the seismic landslide hazard and to identify the geologic units contributing most to the seismic landslide hazard.

The resulting seismic landslide hazard maps indicated that 1.29% of the study area has high or very high seismic landslide hazard (i.e., displacements greater than 5 cm) at 2% probability of exceedance in 50 years. At 10% probability of exceedance in 50 years the high/very high seismic landslide hazard areas represents 0.74% of the study area. Most of the areas with high or very high hazard are along coastal bluffs, stream valleys or in mountainous areas. The probabilistic map that includes aleatory variability and epistemic uncertainties identified the area with high/very high hazard that is 3 times larger than identified through the deterministic approach. The influence of the epistemic uncertainty in the sliding block properties on the computed displacements is generally greater than the influence of the epistemic uncertainty in the shear strengths because the uncertainties in sliding block properties are larger than the uncertainties in shear strength. The combined influence of the epistemic uncertainties in the shear strength and sliding block properties is slightly greater than the simple summation of individual influences, indicating that the combined effect of uncertainties may amplify the increase in the seismic landslide hazard. Finally, comparison with a previous deterministic seismic landslide map developed by the USGS indicates that the seismic landslide hazard from

the probabilistic analyses is smaller because the deterministic map used very conservative (and in some cases unrealistic) assumptions with respect to the sliding block properties. This comparison indicates that the logic-tree approach provides an alternative way to rigorously account for uncertainties in slope properties, and it can avoid using overly conservative input parameters to capture these uncertainties in a deterministic approach.

7.2 RECOMMENDATIONS FOR FUTURE WORK

The developed probabilistic approaches to evaluate the seismic stability of slopes represent an important step forward in accounting for variability and uncertainty in the assessment of seismic landslide hazards. Nonetheless, additional improvements can still be made and some recommendations for future work are outlined below.

The site-specific analysis using the probabilistic approach with a logic tree was performed for a slope at a site in California. The detailed slope geometry and soil profile allows a thorough evaluation of the seismic performance of the slope. However, the empirical models for the seismic loading parameters and flexible sliding displacements were derived solely from numerical analysis assuming all deformations are localized on a failure plane. Thorough validation of these empirical models should be performed. This validation could be achieved through comparisons with well-documented case histories in which ground motions and deformations are recorded during earthquakes. Additionally, physical model testing (e.g., centrifuge tests) of slopes excited by earthquake shaking could be used to validate the models.

The logic-tree analyses performed for flexible sliding masses showed that the mean period of ground motion T_m has a significant influence on the predicted

displacements. The uncertainty of T_m was considered through the logic-tree approach, but T_m is a ground motion parameter and should be rigorously incorporated as part of the ground motion hazard. In this approach, the joint annual probability of occurrence of PGA, PGV, and T_m combinations would be used to predict the joint annual probability of occurrence of k_{max} and k-vel_{max}, which in turn would be used in the computation of displacement hazard curves. To develop this approach, the correlations between T_m and other ground motion parameters are required, and the computation of displacement hazard curves becomes more complex due to the higher dimension of correlation.

Finally, an important factor that influences the distribution of seismic landslides is the spatial variation of the soil shear strength. For probabilistic seismic landslide hazard mapping (and all seismic landslide hazard mapping performed to date), the same shear strength parameters are used across an entire geologic unit, which ignores this important factor. The characterization of the spatial variation of shear strength is a difficult task, it requires a large amount of field testing data, which may be difficult to obtain in mountainous areas. Alternative approaches to develop the spatial variation in shear strength should be considered, including various type of remote sensing.

Reference

Baker, J. W. (2007). Correlation of ground motion intensity parameters used for predicting structural and geotechnical response. 10th international conference on applications of statistics and probability in civil engineering. Tokyo, Japan.

Bazzurro, P. and Cornell, C. A. (2002). Vector-valued probabilistic seismic hazard analysis. Proceedings, 7th U.S. National Conference on Earthquake Engineering, Boston, MA. 10 p.

Boore, D. M. and Atkinson, G. M. (2008). Ground-motion prediction equations for the average horizontal component of PGA, PGV, and 5%-damped PSA at spectral periods between 0.01 s and 10.0 s. Earthquake Spectra, 24(1), 99–138.

Boore, D. M., Joyner, W., and Fumal T. (1997). Equations for estimating horizontal response spectra and peak acceleration from Western North American earthquakes—a summary of recent work. Seismological Research Letters, 68(1), 128–153.

Bradley, B. A. (2010). A generalized conditional intensity measure approach and holistic ground motion selection. Earthquake Engineering and Structural Dynamics, 39(12), 1321–1342.

Bray, J. D. and Rathje E. M. (1998). Earthquake-induced displacements of solid-waste landfills. J. Geotech. Geoenviron. Eng., ASCE, 124(3), 242-253.

Bray, J. D. and Travasarou, T. (2007). Simplified procedure for estimating earthquake-induced deviatoric slope displacements. J. Geotech. Geoenviron. Eng., 133(4), 381–392.

Campbell, K. W. and Bozorgnia, Y. (2008). NGA ground motion model for the geometric mean horizontal component of PGA, PGV, PGD and 5% damped linear elastic response spectra for periods ranging from 0.01 to 10 s. Earthquake Spectra, 24(1), 139-171.

Chiou, B. J. and Youngs, R. R. (2008). An NGA model for the average horizontal component of peak ground motion and response spectra. Earthquake Spectra, 24(1), 173-215.

Close, U. and McCormick, E. (1922). Where the mountains walked. National Geographic, 41(5), 445-464.

Dickenson, S. E. (1994), Dynamic response of soft and deep cohesive soils during the Loma Prieta earthquake of October 17, 1989. Doctoral dissertation, University of California, Berkeley.

Fugro Consultants, Inc. (2011). Dynamic slope stability analyses for cross section A-A of Lexington Elementary School, Santa Clara County. Dec. 2011.

Fugro Consultants, Inc. (2012). Dynamic slope stability analyses for Lexington Elementary School with long duration ground motions and reduced strength properties, Santa Clara County. June 2012.

Harp, E. L. and Jibson, R. W. (1996). Landslides triggered by the 1994 Northridge, California earthquake. Seismological Society of America, 86, S319-S332.

Jibson, R. W. (2007). Regression models for estimating coseismic landslide displacement. Engineering Geology, 91(2007), 209-218.

Jibson, R. W. (2011). Methods for assessing the stability of slopes during earthquakes—A retrospective. Engineering Geology, 122(2011), 43-50.

Jibson, R. W. and Michael, J. A. (2009). Maps showing seismic landslide hazards in Anchorage, Alaska: U.S. Geo¬logical Survey Scientific Investigations Map 3077, scale 1:25,000, 11-p. pamphlet. [Available at URL http://pubs.usgs.gov/sim/3077]

Jibson, R. W., Harp, E. L., and Michael, J. A. (1998). A method for producing digital probabilistic seismic landslide hazard maps - an example from the Los Angeles, California area. U.S. Geological Survey Open-File Report 98-113.

Jibson, R. W., Harp, E. L., and Michael, J. A. (2000). A method for producing digital probabilistic seismic landslide hazard maps. Engineering Geology, 58(2000), 271-289.

Kanno, T., Narita, A., Morikawa, N., Fujiwara, H., and Fukushima, Y. (2006). A new attenuation relation for strong ground motion in Japan based on recorded data. Bulletin of the Seismological Society of America, 96(3), 879–897.

Keefer, D. K. (1984). Landslides caused by earthquakes. Geological Society of America Bulletin, 95.

Keefer, D. K. (1999). Earthquake-induced landslides and their effects on alluvial fans. Journal of Sedimentary Research, 69(1), 84-104

Keefer, D. K. (2002). Investigating landslides caused by earthquakes - a historical review. Surveys in Geophysics, 23, 473-510.

Kieffer, D. S., Jibson, R. W., Rathje, E. M. and Kelson, K. (2006). Landslides triggered by the 2004 Niigata Ken Chuetsu, Japan, Earthquake. Earthquake Spectra, 22(S1), S47–S73.

Kobatashi, Y. (1981). Causes of fatalities in recent earthquakes in Japan. Journal of Disaster Science, 3, 725-730

Makdisi, F. I. and Seed, H. B. (1978). Simplified procedure for estimating dam and embankment earthquake-induced deformation. Journal of the Geotechnical Engineering Division, 104, 849-867.

McCrink, T. P. (2001). Regional earthquake-induced landslide mapping using Newmark displacement criteria, Santa Cruz County, California. In H. Ferriz, & R. Anderson (Eds.). Engineering Geology Practice in Northern California. California Division of Mines and Geology Bulletin 210 / Association of Engineering Geologists Special Publication 12, 77-92.

McCrink, T. P., & Real, C. R. (1996). Evaluation of the Newmark method for mapping earthquake-induced landslide hazards in the Laurel 7-1/2 minute quadrangle, Santa Cruz County, California. California Division of Mines and Geology Final Technical Report for the U.S. Geological Survey Contract 143-93-G-2334. U.S. Geological Survey, Reston, Virginia.

Moran, E. H. and Galloway, D. L. (2006). Ground-water in the Anchorage area, Alaska - meeting the challenges of ground-water sustainability. U.S. Geological Survey Fact Sheet 2006-3148.

Newmark, N. (1965). Effects of earthquakes on dams and embankments. Geotechnique, 15(2), 139-160.

Pacific Crest Engineering, Inc. (2011). Geotechnical investigation and engineering geology report for modernization project, Lexington Elementary School, Los Gatos, California. prepared for Los Gatos Union School District, April.

Parise, M. and Jibson, R. W. (2000). A seismic landslide susceptibility rating of geologic units based on analysis of characteristics of landslides triggered by the 17 January, 1994 Northridge, California earthquake. Engineering Geology, 58(2000), 251–270.

Petersen, M. D., Frankel, A. D., Harmsen, S. C., Mueller, C. S., Haller, K. M., Wheeler, R. L., Wesson, R. L., Zeng, Y., Boyd, O. S., Perkins, D. M., Luco, N., Field, E. H., Wills, C. J., and Rukstales K.S. (2008). Documentation for the 2008 Update of the United States National Seismic Hazard Maps. U.S. Geological Survey Open-File Report 2008-1128.

Phoon, K. K. and Kulhawy, F. H. (1999). Characterization of geotechnical variability. Can. Geotech. J., 36, 612–624.

Rathje, E. M. and Bray, J. D. (2001). One- and two-dimensional seismic analysis of solid-waste landfills. Can. Geotech. J. 38, 850–862.

Rathje, E. M. and Saygili, G. (2008). Probabilistic seismic hazard analysis for the sliding displacement of slopes: scalar and vector approaches. J. Geotech. Geoenviron. Eng., ASCE, 134(6), 804-814.

Rathje, E. M. and Saygili, G. (2009). Probabilistic assessment of earthquake-induced sliding displacements of natural slopes. Bulletin of the New Zealand Society for Earthquake Engineering, 42(1), 18-27.

Rathje, E. M. and Saygili, G. (2011). Estimating fully probabilistic seismic sliding displacements of slopes from a pseudoprobabilisitc approach. J. Geotech. Geoenviron. Eng., 137(3), 208–217.

Rathje, E. M., Abrahamson, N. A., and Bray, J. D. (1998). Simplified frequency content estimates of earthquake ground motions. J. Geotech. Geoenviron. Eng., ASCE, 124 (2), 150–159.

Rathje, E. M., Antonakos, G. (2011). A unified model for predicting earthquake-induced sliding displacements of rigid and flexible slopes. Engineering Geology, 122(2011), 51–60.

Rathje, E. M., Faraj, F., Russell, S., and Bray, J. D. (2004). Empirical relationships for frequency content parameters of earthquake ground motions. Earthquake Spectra, Earthquake Engineering Research Institute, 20(1), 119-144.

Rathje, E. M., Wang, Y., Stafford, P., Antonakos, G., and Saygili, G. (2013). Probabilistic Assessment of the Seismic Performance of Slopes. Bulletin of Earthquake Engineering, doi: 10.1007/s10518-013-9485-9.

Rodriguez-Marek, A., Bray, J. D., and Abrahamson, N. A. (2001). An empirical geotechnical seismic site response procedure. Earthquake Spectra, 17(1), 65–87.

Saygili, G. (2008). A probabilistic approach for evaluating earthquake-induced landslides. Doctoral Dissertation, University of Texas at Austin, Austin, TX.

Saygili, G. and Rathje, E. M. (2008). Empirical predictive models for earthquake-Induced sliding displacements of slopes. J. Geotech. Geoenviron. Eng., 134(6), 790–803.

Saygili, G. and Rathje, E. M. (2009). Probabilistically based seismic landslide hazard maps: An application in Southern California. Engineering Geology, 109(2009), 183-194.

Schmoll, H. R. and Dobrovolny, E. (1972). Generalized geologic map of Anchorage and vicinity, Alaska. U.S. Geological Survey Miscellaneous Investigation Map I-787-A, scale 1:24,000.

Spencer, E. (1967). A method of analysis of the stability of embankments assuming parallel inter-slice forces. Geotechnique, 17, 11-26.

Terzaghi, K. (1950). Mechanisms of landslides. Engineering Geology (Berkey) Volume, Geological Society of America.

Vrymoed, J. L. and Calzascia, E. R. (1978). Simplified determination of dynamic stresses in earth dams. Proceedings, Earthquake Engineering and Soil Dynamics Conference, ASCE, NY, 991–1006

Wesson, R. L., Boyd, O. S., Mueller, C. S., Bufe, C. G., Frankel, A. D., and Petersen, M. D. (2007). Revision of time-independent probabilistic seismic hazard maps for Alaska. U.S. Geological Survey Open-File Report 2007-1043, 41 p.

Wesson, R. L., Frankel, A. D., Mueller, C. S., and Harmsen, S., (1999), Probabilistic seismic hazard maps of Alaska. U.S. Geological Survey Open-File Report 99–36, 43 p.

Wilson, R. C. and Keefer, D. K. (1985). Predicting areal limits of earthquake-induced landsliding. in Evaluating Earthquake Hazards in Los Angeles Region, Zinoy, J.L., ed., U.S. Geological Survey, Reston, Virginia, Professional Paper 1360, 317-345.

Wilson, R. C., Keefer, D. K. (1983). Dynamic analysis of a slope failure from the 6 August 1979 Coyote Lake, California, earthquake. Bulletin of Seismological Society of America, 73, 863–877.

Yahle, L. A., Schmoll, H. R., and Dobrovolny, E. (1992). Surficial geologic map of the Anchorage A-8 SE quadrangle, Alaska. U.S. Geological Survey Open-File Report 92-350, scale 1:25,000.

Youd, T. L. (1978). Major cause if earthquake damage is ground failure. Civil Engineering, ASCE, 48(4), 47-51.

Youngs, R. R., Chiou, S. J., Silva, W. J., and Humphrey, J. R., (1997). Strong ground-motion attenuation relationships for subduction zone earthquakes. Seismological Research Letters, 68(1), 58–73.

Vita

Yubing Wang was born in Tangshan, China in January, 1987. After completing his study at Tangshan No. 1 High School in 2005, he was admitted by Tongji University, Shanghai, China. He chose Civil Engineering as his major. He earned his Bachelor degree from Tongji University in June 2009. In August 2009, he entered the Department of Civil, Architectural and Environmental Engineering at The University of Texas at Austin. He was conferred the Master of Science in Dec 2010.

Permanent email: wangyubing1987@hotmail.com

This dissertation was typed by the author.